# Investigation of Trilinear Vector Boson Couplings Through W Boson Pair Production in Dilepton Decay Channels

By

Paul Craig Bloom

March 1998

DISSERTATION

Submitted in partial satisfaction of the requirements for the degree of

DOCTOR OF PHILOSOPHY

in

Physics

in the

GRADUATE DIVISION

of the

UNIVERSITY OF CALIFORNIA

DAVIS

Approved:

.....

.....

.....

# Abstract

An investigation of the interactions between the $W$ boson and the $Z$ boson and photon through the pair production of $W$ bosons is presented. This has been accomplished via a study of the reaction $p\bar{p} \rightarrow \ell\bar{\nu}_\ell\bar{\ell}'\nu_{\ell'} + X$ ($\ell$, $\ell' = e, \mu$) at $\sqrt{s} =$ 1.8 TeV, using the DØ detector at Fermilab. In a data sample corresponding to an integrated luminosity of 82 pb$^{-1}$, four candidate events were observed with an expected background of $2.5 \pm 0.4$ events, which is consistent with the Standard Model prediction of $1.5 \pm 0.1$ signal events. This results in a 95% confidence level upper limit on the $W$ pair production cross section at $\sqrt{s} = 1.8$ TeV of 44.1 pb. Limits on anomalous $WWZ$ and $WW\gamma$ couplings are obtained for equal and HISZ coupling relations using both the total cross section and a maximum likelihood fit to the lepton transverse momentum distribution. Assuming a form factor scale of 1.5 TeV, the lepton fit yields 95% CL limits of $0.68 < \Delta\kappa < 0.83$ ($\lambda = 0$) and $0.57 < \lambda < 0.62$ ($\Delta\kappa = 0$) for equal couplings, and $1.02 < \Delta\kappa_\gamma < 1.30$ ($\lambda_\gamma = 0$) and $0.60 < \lambda_\gamma < 0.62$ ($\Delta\kappa_\gamma = 0$) for HISZ coupling relations.

# Acknowledgments

This text and the work described within represents the culmination of my formal education. It has been a process undertaken of my own curiosities and desires, but is a journey that would not have been possible without the help and encouragement of many people. It is therefore incumbent upon me to demonstrate comprehension of one more lesson - knowing how to give credit and thanks as they are due.

When it is difficult to know where to begin, it is often helpful to start at the beginning. As far as my education in the sciences, that would have start with my junior high school science teacher, Thor Hansen, who took the time to encourage my curiosities and got me to enter the science fair, and my algebra teacher, Edith Sonke, who let me go at my own pace, and encouraged me to explore. In high school, it was not science, but my Latin teacher, Francis Goshawk, who pushed me the hardest, and refused to let me get by on cruise control. It has been a lesson that served me well.

The most profound effect on my education came from my time at Reed College. There I encountered many fine physicists and teachers, including Professors Nick Wheeler, Dennis Hoffman, and Robert Reynolds. At Reed, Johnny Powell and Mary James (under who's tutelage I had the pleasure of writing my undergraduate thesis) introduced me to the world of experimental physics. But it was my chance encounter with David Griffiths, first as a freshman academic advisee hell bent on being a biology major, and then as a student in his introductory physics course, which changed my future. After one semester in that class, I knew I was going to be a physicist. Four years later, after taking his elementary particles course, I was hooked for good. To David, all I can say is that this is your fault. The thanks I owe the members of the Reed Physics faculty cannot be understated, for they taught not only the equations, but the beauty underlying the physical world. Also deserving of great thanks from my Reed days is Professor Steven Wasserstrom, for making me realize the importance of incorporating my theological beliefs into my view of the physical universe, and helping me take the first steps in making peace between my beliefs as a Jew and my studies as a scientist.

In graduate school, it has been my good fortune to have worked under the guidance of Sudhindra Mani. Over the last few years, he has provided me with support - both financial and moral, guidance when required, and perhaps most importantly, the freedom to explore and find my own way. I am indebted to him not only for this, but for his taking a risk by accepting me as a thesis student when

his plate was already full, and my prospects weren't so great.

The last stage of my formal education has taken place at Fermilab, on the great plains just west of Chicago. It is safe to say that when I arrived, brain packed with the clichés of course work, I knew next to nothing. Over the span of three years I was somehow transformed into a functioning experimental physicist who was actually capable of making a contribution to a large collaboration. Given the size and the complexity of the DØ experiment and the Tevatron accelerator, the number of people collectively involved in my work numbers in the hundreds. I am indebted to them all. There are some, however, who are more guilty that others, and I shall attempt to name names - even if they can't all be brought to justice for their crimes. First, it was my good fortune to have shared the Davis cubicle with Steven Glenn for much of my time at FNAL. He had the misfortune of arriving at Fermilab about a year before I did, so he ended up being my "live in" tutor - helping me get up to speed much more quickly than I might have on my own. Steve helped with several parts of this analysis, and more importantly, was a good friend. Others who have aided and abetted include Jamal Tarazi - the keeper of the data and occasional tennis opponent, and Erich Varnes - who when not working on one of my backgrounds (that pesky top quark) was usually good for a day trip to Wrigley or Comisky. Jim Cochran (another one of those top people) provided many useful discussions and was a never ending source of background Monte Carlo. Paul Quintas provided many useful discussions about muon identification and triggering,

while Meenakshi Narain, Uli Heinz and the rest of the electron ID group developed the likelihood test used in this analysis. Joey Thompson was ever ready and reliable to help with the calculation of the luminosities. The editorial board - Fritz Bartlett, Tom Trippe, Sue Blessing and Cecilia Gerber gave useful suggestions and took the time to review the analysis. The members of the Electroweak and Diboson groups also provided suggestions - Darien Wood, Marcel Demarteau, Harry Melanson, Greg Landsberg, Mike Kelly, Tom Fahland, Brajesh Chourdhary, Tom Diehl and Taka Yasuda to name as many as memory permits. Brajesh deserves special mention for providing much needed guidance during the early days of the analysis, and I am particularly indebted to Tom Diehl and Taka Yasuda. Tom gave much help in the muon related parts of the analysis, and was always available for advice, or more often, to act as a sounding board for whatever crisis I was having on a particular day. Taka performed the analysis on the lepton spectrum and was always good for advice. His biweekly visits also provided a periodic deadline to force me to get things done. I would also be remiss if I did not mention Hossein Johari, who performed to 1A analysis.

Special mention must be made of two people. First is my good friend Michael Begel. Fellow Reedie and physicist, his friendship has always been a prized asset - but especially so in the stressful times of the last few years when I have been so far from home and there seemed so much to do. I shall be every thankful for his offer to kill me should the "senior thesis" incident seem likely to recur. The second

person is relatively new to my life. Karen's arrival could not have been anticipated, nor could it have come in a more unlikely way. She has most unexpectedly turned much of my life upside down, in many of the most hoped for ways. The joy she has brought into my life is incalculable. I look forward with great anticipation to seeing what the future holds in store for us.

Finally, nothing can be said of my education without mentioning my family. The process of my education has been a long one, but made more bearable by the constant and unlimited support and encouragement from my brothers, my parents, and my grandparents (not to mention aunts, uncles and cousins galore). From the beginning, my parents and grandparents instilled in me the importance of education - not as a means, but as an end. Whatever I have become, they and that which they have taught me are at the core. My gratitude to them, as my love for them, is beyond measure.

If I have learned nothing else, it is that the quest for knowledge - all knowledge - is at the heart of my people's beliefs. That the universe exists, and that humanity has been gifted with the faculty to ask, places upon us the requirement to do so.

In honor of my grandparents.

# Forward

What is it made of and how does it work? This is a very old question. At least as long ago as ancient Greece, the school of Atomists posited that one could deduce a fundamental list of materials from which all other things were made. This is the underlying principal of the modern science of elementary particle physics, also known as high energy physics. Today we ask the question in the following way; what are the fundamental constituents of matter, and how do they interact with each other? Over the course of the last 100 years, physicists have, through great experimental and theoretical effort, developed the modern answer, the Standard Model. The work discussed here is the work of the experimentalist; to test, through empirical investigation, the predictions of the theory, and to search for deficiencies in those predictions.

The Standard Model (SM) is a phenomenology based on the mathematical construct of a locally gauge invariant quantum field theory, which describes the motions of fermions (particles of half integer intrinsic angular momentum - spin) and

bosons (particles of integer spin), and the interactions between them. The theory has acquired its name because to this point it has correctly predicted every experimentally observable quantity which is with the predictive power of the theory. The predictive power of the SM comes from the formalism of quantum field theory, along with the application to that formalism of certain symmetries which are observed to be true in nature. The details of the field theory underlying the SM are far beyond the scope of this work (the interested reader is urged to refer to the many fine works devoted to the description of quantum field theory and its application to elementary particles - for example [1, 2, 3, 4, 5]), however we can still describe the players involved. This forward is provided to initiate the uninitiated; first, by providing an introduction the Standard Model from a historical perspective, and further by describing the present state of high energy physics and by providing a brief overview of the business of doing a high energy physics experiment.

## 100 Years of Elementary Particles

The history of this field since the turn of the century is one of brilliant insight, frustrating blunders, and lots of dedicated hard work. It is populated by an assortment of characters which the best fiction would have trouble conjuring. It is sadly beyond the scope of this text to give this history the proper illumination it deserves, and the reader is again urged to refer to the fine works which celebrate

this era of physics (for example [6, 7, 8, 9]). Here we shall have to be content with just the highlights.

## The Early Years - Atoms and Nuclei

From a historical perspective, the modern era of particle physics began in 1897 with J.J. Thomson's discovery of the electron. He determined that cathode rays were in fact very light, negatively charged particles. He dubbed them corpuscles, and the charge the electron - the name which has stuck. He then proposed a model of atomic structure in which electrons were suspended in a sort of positively charged paste, which would account for atoms being electrically neutral. This model was shortly repudiated by Rutherford, who demonstrated that the positive charge of the atom, and most of its mass, was concentrated in a small dense core or nucleus. He called the nucleus of the lightest atom (hydrogen) the proton. Thus the hydrogen atom could be thought of as a system of one electron and one proton, bound together by electromagnetism (the rules of which were know since the 1870's from the work of Faraday, Maxwell and others) and the basic rules of quantum mechanics.

While fine for hydrogen, the simple Rutherford model fails for all the heavier elements. For instance, while helium does have two electrons, it weighs four times as much as hydrogen, and so on up the periodic table. This problem was resolved in 1932 by Chadwick's discovery of the neutron - an electrically neutral partner to the proton. This completed the picture of the atom. They were all composed of

an equal number of electrons and protons (determining the element) and a variable number of neutrons (determining the isotope).

Meanwhile, in 1900, Planck was attempting to explain the blackbody spectrum for electromagnetic radiation using statistical mechanics. He found that only way he could fit the experimental data was to assume that electromagnetic radiation is quantized, that is, comes in discrete packets of energy. He did not profess to know why, but thought that this had something to do with the process of the emission of the radiation. In 1905 however, Einstein posited that it was the electromagnetic field itself that was quantized, and then went on to use this information to explain the photoelectric effect - the work for which he eventually received his Nobel prize. The idea that the electromagnetic field was quantized was poorly received by the physics community until 1923, when Compton showed that the wavelength shift observed when light scatters off a particle at rest is precisely what is predicted when you assume that light is a particle of zero mass and apply Planck's energy formula and the kinematics of special relativity. We call this particle the photon. Thus, electromagnetism can be viewed as the mass exchange of photons streaming between two charged objects - messengers which tell them to come a little closer, or go away - depending on the charges involved. In most cases, this point of view is unnecessary as the numbers of photons are so great that the lumpiness of the field is smoothed out and the classical theory of electromagnetism is sufficient. But where individual photons are involved, their quantum nature must be taken into account.

So by the mid 1930's the atom was well understood territory. Protons and neutrons in the nucleus, electrons roaming the region beyond, bound to the nucleus by the electromagnetic attraction to the protons. But what holds the nucleus together? By all rights, when you pack lots of positively charged objects that close together, they ought to violently repel each other. Gravity wasn't the answer, as it is much to feeble a force for such tiny masses. The answer was that there was some hitherto undiscovered force at work. Yukawa was the first to make a significant contribution in this area. He posited that there was some sort of field which attracted the neutron and the proton (just like the electromagnetic field attracts the proton and electron). Since we don't see the effects of this force outside the nucleus, Yukawa assumed it must be a short range force (gravity and electromagnetism have infinite range), and hence the quanta of field must be reasonably heavy (he calculated about 300 times heavier than the electron). At about the same time, detailed studies of cosmic rays were showing that just such a particle existed, it's called the pion, and everything seemed to be in order.

## "Who Ordered That?"

Those same cosmic ray studies, however, also found something quite unexpected (prompting the above quote from I.I Rabi). In addition to the pion, there was what appeared to be a heavier version of the electron (about 200 times heavier), which was dubbed the muon. And there were further complications. In 1931

Anderson discovered the positron, a positively charged twin of the electron. This discovery rescued Dirac's relativistic theory of electrons, which had predicted the positron (although nobody realized it at the time). But when Stuckelberg and Feynman reformulated the theory in the forties, they came to the conclusion that the existence of the positron is an example of a dualism found throughout quantum field theory - every particle has a corresponding anti-particle. By 1955, the antiproton was observed at the Berkeley Bevatron [10, 11], with the antineutron coming the following year.

A third complication came from the prediction and subsequent discovery of the neutrino [12]. In the early thirties, the study of beta decay (the process by which a radioactive nucleus transforms into a different, lighter nucleus through the emission of an electron) was yielding confusing results. The spectrum of electrons indicated that either energy conservation was being violated (a very bad thing), or that there was an undetected particle carrying away some of the energy. Pauli proposed that there was such a neutral particle, and wanted to call it the neutron (Chadwick preempted the name in 1932). In 1933, Fermi devised a theory describing beta decay, which incorporated Pauli's particle (which Fermi dubbed the neutrino). The theory predicted the observed spectra so well that the neutrino had to be taken seriously despite having never been observed. Circumstantial evidence, such as bubble chamber pictures of particle decays which seemed to wildly violated momentum conservation hinted at it's existence, but direct evidence of the neutrino did not

come until the mid fifties when Cowan and Reines observed inverse beta decay at the Savannah River nuclear reactor [13]. It turned out that neutrinos are ghost-like in their interactions with matter. Massless (or almost), they can pass through light-years of lead before being absorbed or scattered. Hundreds of billions of them (mostly from the sun) pass through every square inch of your body every second. Further studies showed that there were in fact two kinds of neutrinos, one associated with the electron, the other with the muon [14]. They also showed that neutrinos and antineutrinos were distinct particles (some electrically neutral particles - like the photon - are their own antiparticles) [15].

## The Middle Years - Mesons and Baryons

By the late the late forties, things seemed to be fairly stable. The atom was well explained. Yukawa's pion was found, Pauli's neutrino was under control (although at the time still un-apprehended), and the positron had been found. The muon, while seemingly unnecessary in the picture, was reasonably well understood. It didn't last. Within a few years, a plethora of additional mesons (heavier versions of the pion) and baryons (heavier versions of the proton and neutron) were discovered, first in cosmic ray studies, then in the laboratory as the modern particle accelerator came into being. Some of these were dubbed 'strange' particles because although produced copiously, they decayed very slowly (relatively speaking). To many this suggested that the mechanism for these particles' decay was very different from that

of their production (as it turned out, they are produced by the strong force - the same one that holds the nucleus together, but decay via the weak force - the force that governs beta decay). In 1961 Gell-Mann found that by suitable application of a new property (which he called 'strangeness') to these particles, they fell into a sort of periodic table for mesons and baryons which he called the eightfold way [16, 17]. This allowed him to successfully predict the existence of a hitherto undiscovered baryon called the omega-minus, clinching the correctness of his scheme.

Of course, the success of the eightfold way begged the question: why do the hadrons (the collective name for baryons and mesons - anything which interacts via the strong force) fit into those patterns? An answer came in 1964 from Gell-Mann and Zweig [18]. They proposed that all hadrons are made up of fundamental constituents they called quarks. These particles carry fractional electric charge (where the unit charge is the charge of the positron) and come in three types - up (u), down (d) and strange (s). In the quark model, baryons are made of three quarks, while mesons are made of quark - antiquark pairs. By taking suitable combinations of quarks and antiquarks it was possible to produce all the observed hadrons, and deduce which ones should not be observed (and weren't). The only flaw to this theory was that, in spite of all experimental effort, no one had (or has) ever seen a quark. It was thought that if hadrons were really made of quarks, then a sufficiently violent collision should cause them to come out. They would be easy to identify because they carried fractional charge, and they would be stable

because of charge conservation (there is nothing lighter which also carries fractional charge, so they would have nothing to decay into). There was indirect evidence for quarks, however. So called deep inelastic scattering experiments (analogous to Rutherfords experiment with the atom nearly seventy years earlier) were conducted in the sixties [19]. Researchers found that when one scatters high energy electrons off of a proton, the results are consistent with the electric charge of the proton being concentrated in three lumps.

Those who favored the quark model attempted to rescue the theory by proposing that for some reason quarks are confined inside hadrons. This seemed to be a desperate maneuver at the time, but in fact turns out to be a feature of the strong force, although it is only recently that the modern theory which describes the strong interactions - quantum chromodynamics (QCD) - has given us clues that confinement really is a feature of the theory. A further difficulty is that the quark model requires the assignment of an additional quantum number - color charge - to the quarks in order for them to obey the Pauli exclusion principal of quantum mechanics. There would have to be three different kinds of this charge, and the result would be that each baryon would have a one quark of each charge, while mesons would have one unit of plus and minus charge of the same kind. This implied that all hadrons would be "colorless" (either the total charge is zero or there is the same amount of each kind of charge). This also nicely ruled out other combinations of quarks and antiquarks because they would in general have some net color.

## The November Revolution

In 1974, the situation was largely unchanged. The quark model explained the Eightfold Way and predicted the lumpy structure of the proton, but no free quarks had been observed, and the model seemed to violate the exclusion principle. The proposed theoretical fixes seemed rather unmotivated, and general attitudes about the quark model were demonstrated by the naming of the lumps in the protons as 'partons', rather than calling them quarks. It was left to the completely unexpected discovery of the Psi meson in 1974 to rescue the quark model [20, 21]. This particle turned out to be unique because it's lifetime was one thousand times longer that other hadrons of its approximate mass. It had been noticed by many that there were four leptons ($e$, $\mu$, $\nu_e$, $\nu_\mu$), but only three quarks ($u$, $d$, $s$), and that perhaps a fourth quark would make things more symmetric (physicists like symmetries). Work by Glashow, Iliopoulos, and Maiani in 1970 offered compelling theoretical reasons why another quark might be needed [22]. Soon after the Psi was discovered, it was identified as the quark - antiquark combination of the fourth quark - 'charm' (c). Now if there really was a fourth quark (or any quarks at all) then one expected to find all manner of 'charmed' baryons and mesons. Sure enough, these particles started being discovered [23, 24, 25] as particle accelerators became more powerful, and the quark model was now impossible to ignore.

In 1975, however, Perl discovered another lepton - the tau [26]. It had it's own

neutrino (the existence of which has been inferred through indirect measurements, but has not actually been directly observed as of this writing), so that meant that there were now six leptons, ruining the symmetry. The fix came in 1977 with the discovery of the Upsilon meson, which was identified as the quark - antiquark combination of the fifth quark - 'bottom' [27]. This in turn led to the prediction for the sixth quark - 'top' (t) - to restore the symmetry, but it was not observed directly until 1995 because of it's extremely large mass [28, 29]. Precision measurements have shown that there are only three species of light neutrinos [30] so, perhaps, this is where it ends.

## Electroweak Unification - $W$'s and $Z$'s

For the last pieces, we must return to Fermi's theory of beta decay. In solving the problem, Fermi treated the interaction as a contact interaction - requiring no mediating particle to transmit the force. The problem with this formulation is that it fails at high energies, and it was recognized that a theory describing the weak interactions must have a particle which acts as a mediator. The answer was provided by the electroweak theory of Glashow, Weinberg and Salam [31, 32, 33]. In this theory, there were two kinds of mediators, the $W$, which was to come in plus and minus electric charges, and the $Z$, which was to be electrically neutral. They were predicted to be extremely heavy - about one hundred times the mass of the proton. This was why Fermi's theory was so good at low energies, but failed

in more energetic regions. These particles were seen for the first time in 1983 at CERN, and the measured masses turned out to be almost precisely as they had been predicted [34, 35, 36, 37].

Aside from providing a theory of weak interactions that was good at high energies, the GWS electroweak theory has other nice features. It supplants the separate electromagnetic and weak interactions, and replaces them with a single unified interaction. Electromagnetism and the weak force turn out to be different manifestations of the same phenomenon. In addition, the GWS theory provides an apparatus - the so call Higgs mechanism - which generates the masses of all the fermions (quarks and leptons) and electroweak gauge bosons. This results in the prediction of one last - and as yet unobserved particle - the Higgs boson.

## The Current State of Particle Physics

As we understand things today, all matter is made of three kinds of particles: leptons, quarks and mediators (also called gauge bosons). Their groupings and some of their properties are summarized in tables 1.1, 1.2 and 1.3. There are six kinds of leptons, which fall into three families or generations, and there are also six kinds of quarks, which also fall into three generations. All the leptons and quarks are accompanied by their antiparticle counterparts. The quarks and antiquarks also come in three different colors each.

All these particles can interact with each other via the exchange of gauge bosons. Electrically charged particles interact through the electromagnetic force by exchanging photons. All the quarks and leptons can interact through the weak force by exchanging $W$'s or $Z$'s. The weak force and electromagnetism are unified into a single electroweak interaction, requiring the existence of at least one Higgs boson, and allowing the $W$, $Z$ and photon (and Higgs) to interact amongst themselves. Finally, quarks can interact through the strong force with other quarks by exchanging gluons - the gauge bosons (there turn out to be eight of them) in QCD - and the gluons also interact amongst themselves. Table 1.4 summarizes these interactions. Of the four fundamental forces found in nature, only gravity is not incorporated into the Standard Model, as no suitable quantum description of gravity has been found.

## Physics Beyond the Standard Model

While the Standard Model is a marvelously successful theory, it has its shortcomings and limitations. The most glaring is the number of parameters which have to be input into the theory by hand. No feature of the SM allows you to predict what the mass of the top quark should be, or what the the weak mixing angle is. These numbers have to be extracted from experiment and put into any calculation in order to give the theory numerically predictive power. Any theory that would go beyond the SM would have to address this issue. Another problem is that even with

electroweak unification, there are still two forces to contend with. The unification of the electroweak and strong forces is another primary issue that future theories have to contend with, not to mention the eventual incorporation of gravity. There are candidates for the successor, or at least the extension of the SM, the most promising of which is called supersymmetry. But as of this writing, there is no experimental evidence in support of any of these theories.

On the experimental front, there are many tasks remaining. The foremost of which is to discover the Higgs boson, or any alternate mode of electroweak symmetry breaking (the reason why the weak force looks separate from electromagnetism). Other tasks include testing the self interactions of the gauge bosons (the purpose of the work described in this text), and the precision measurements of various quantities such as the $W$ boson and top quark masses. Beyond this, however, is a philosophical point: there is no such thing as a correct theory, just one in which there have been found no deficiencies. It is therefore the main goal of the experimenter (and the most exciting) to search for something which is either beyond the scope of the SM, or in violation of its predictions. The former would likely require extensions to the theory as described above. The latter has the possibility to turn the physics world on its head.

# Particle Physics Experiment

So, you want to study elementary particles in an experiment? The everyday world made almost exclusively of electrons and protons and photons, so they are easy. Cosmic rays (primarily muons) and nuclear reactors (mostly neutrinos) can provide a few other types of particles. But if you want to study something more exotic, more extreme efforts are required. To produce the rarest and heaviest particles, you must arrange for them to be created from the energy liberated by a violent collision of the more everyday particles. This is the purpose of the particle accelerator. The skillful application of electric and magnetic fields can be used to accelerate charged particles to velocities comparable with the speed of light, and hence to energies many orders of magnitude greater than that associated with their mass. The reason for desiring high energies is twofold. First, if you want to discover more massive particles, you must arrange a collision energetic enough to produce them. The top quark for instance, weighs 170 times as much as the proton (as much as a whole gold atom!). So to make one, you must produce a collision with at least that much energy. In fact, many particles can often only be produced in pairs, so you need twice as much energy. The second reason has to do with the ability to resolve detail when examining a structure. The higher the energy of the collision, the closer the two particles come together. So if you want to study an interaction at short range, you must arrange for a very energetic collision. A different way of

looking at this is expressed by the de Broglie relationship of quantum mechanics. A particle of momentum p has a wavelength given by ($\lambda$=h/p). If you wish to resolve fine detail of something, you must look with wavelengths smaller than the detail you wish to resolve, and hence large momenta are required. Alternately, this is a manifestation of the uncertainty principle ($\Delta x \cdot \Delta p \geq \hbar/2$ or $\Delta E \cdot \Delta t \geq \hbar/2$). To see something that happens at small scales (small $\Delta x$) you must be at large momenta, or to see something that happens quickly (small $\Delta t$), you must be at high energies. The bottom line is that to probe small distances, you need to use high energies.

Today, accelerators are used to perform two basic types of experiments; fixed target and collider. As the name suggests, in a fixed target experiment a beam of particles is made to collide with some target. Interaction rates in such experiments are typically very high, and they have the advantage that particles that are produced in the collision tend to be highly relativistic, which means they take longer to decay due to time dilation and can be measured more easily. Fixed target experiments can also take advantage of techniques for producing secondary beams of particles such as pions, photons and neutrinos. In collider experiments, two counter rotating beams of particles are made to collide with each other, generally in a storage ring synchrotron. Such experiments are more technically challenging to run (you need better aim for one thing), and require the use of stable particles such a electrons, protons and their antiparticles (some are considering the use of muons). While they tend to produce lower interaction rates, the energy of the collisions is much higher,

and if the particles don't collide, they come around for another try.

Once you have a source of high energy collisions, you need a way to see what happened. Any apparatus used in experimental high energy physics can really only do one thing: measure the passage of a charged particle through matter. This measurement can be done in many ways, and in combination with electric and magnetic fields allows one to infer various properties of a particle, including its charge, mass, energy and momentum. Often, processes of interest occur so quickly that the particles you are looking for don't make it into the detector, only the relatively stable particles make it that far. So after one interprets the electronic signals that come from the detector as electrons or pions or muons and so forth (the process of event reconstruction), one must then work backwards to deduce what process has taken place in a particular event by looking at the contents of the detector as the decay products of whatever happened. An additional complication is that for many processes, nature is reluctant to show you what you want to see. Figure D.2 shows the ISAJET [38] Monte Carlo predictions for the cross sections (a measure of how often something happens) for various processes to produce an object of increasing transverse momentum in proton-antiproton collisions. At all transverse momenta, the dominant process (by orders of magnitude) is multijet production by the strong force. So if one recorded just any event with a high $p_T$ object, one would end up with almost nothing but multijet events. The solution to this problem is twofold. First, look for manifestations of the process of interest which are unique.

For example, when searching for $W$ boson decays, one could look for $W$'s which decay into two jets. The problem is that even though a majority of $W$'s decay hadronically, the background from dijet production is many orders of magnitude larger, making detection of signal a difficult job. By looking for $W$'s which decay into leptons one reduces the backgrounds substantially, even at the cost of seeing a smaller percentage of the $W$'s actually produced. The other part of the solution is to design a trigger system which requires topological and particle identification cuts to select which events are recorded. Leptons from $W$ and $Z$ production tend to be unique in that they are both high $p_T$ and well isolated (no energy deposited in the detector around lepton). The work discussed later involves the study of pairs of $W$'s, with the focus being on leptonic decay modes for the above reasons.

After all this, there only a few things that can be measured. First, we can, for a particular process, measure the cross section. Second, we can measure various properties of a particle, including its mass, charge and lifetime - how long it takes (on average) to decay. Last, we can measure the relative frequency with which the particle decays into whatever it can decays into. We call this the branching ratio. From these properties, it is often possible to use calculated results from the Standard Model to infer the values of input parameters to the model, such as the Weinberg angle or the CKM matrix elements. This interplay between the empirical and the theoretical is at the heart of doing good science.

# Into the Abyss

The text that follows describes work done at the Fermi National Accelerator Laboratory between 1994 and 1997 - a study of the self-couplings of the electroweak gauge bosons via the hadroproduction of $W$ boson pairs which decay in purely leptonic modes. In chapter 1, a brief summary of the Standard Model is followed by a more detailed description of the electroweak theory of Glashow, Weinberg and Salam. The ramifications of both Standard Model and non-Standard Model physics on the pair production of $W$ bosons is then discussed, followed by a summary of relevant experimental measurements. Chapter 2 is devoted to the description of the experimental apparatus used - the Tevatron collider complex used to produce high energy collisions, and the DØ detector used to observe the results of those collisions. Chapter 3 describes the processing of raw data from the detector into usable physics information - event reconstruction, and begins the discussion of the data selection process by describing the methods and criteria used for the identification of particles. Chapter 4 offers a brief discussion of event modeling, detailing event generation and detector simulation. A description of the remainder of the $W$ pair event selection criteria and the computation of the detection efficiencies and expected Standard Model event yields can be found in chapter 5. Chapter 6 is devoted to the discussion of backgrounds to the $W$ pair process, and the computation of expected event yields. The works described in chapters 5 and 6 are employed to produce results for the

$W$ pair production cross section, and limits on anomalous gauge boson couplings in chapter 7. Finally, chapter 8 summarizes the results, and attempts to place those results within the context of contemporary experimental efforts.

# Contents

**Abstract** ii

**Acknowledgments** iii

**Forward** x

**List of Tables** xxxiii

**List of Figures** xxxvi

**1 The Standard Model and the Physics of $W$ Pairs** 1
- 1.1 The Standard Model of Elementary Particle Interactions . . . . . 2
- 1.2 The GWS Theory of Electroweak Interactions . . . . . 7
  - 1.2.1 $SU(2)_L \times U(1)_Y$ . . . . . 7
  - 1.2.2 Local Gauge Invariance . . . . . 10
  - 1.2.3 Symmetry Breaking and the Higgs Mechanism . . . . . 13
- 1.3 $W$ Pairs in the Standard Model . . . . . 15
  - 1.3.1 Standard Model $WW$ Production Mechanisms . . . . . 16
  - 1.3.2 Standard Model Predictions for $WW$ Production . . . . . 17
  - 1.3.3 Experimental Signature for $WW$ Production . . . . . 19
- 1.4 $W$ Pairs Beyond the Standard Model . . . . . 24
  - 1.4.1 Mechanisms for non-SM $WW$ Production . . . . . 25
  - 1.4.2 Formalism . . . . . 27
  - 1.4.3 Experimental Signatures of non-SM $WW$ Production . . . . . 34
- 1.5 Previous Experimental Results . . . . . 38

**2 Experimental Apparatus** 41
- 2.1 The FNAL Collider Complex . . . . . 42
- 2.2 The DØ Detector . . . . . 47
  - 2.2.1 Central Detector . . . . . 49

2.2.2 Calorimeter . . . . . 61
2.2.3 Muon Spectrometer . . . . . 71
2.2.4 Trigger . . . . . 76
2.2.5 Main Ring Effects and Beam Vetos . . . . . 81
2.2.6 Data Acquisition . . . . . 82
2.3 Detector Operation and Data Collection . . . . . 82

**3 Event Reconstruction and Particle Identification 84**
3.1 DØRECO . . . . . 85
3.1.1 Tracking Reconstruction . . . . . 85
3.1.2 Vertex Determination . . . . . 87
3.1.3 Calorimeter Reconstruction . . . . . 88
3.1.4 Electron Reconstruction . . . . . 89
3.1.5 Muon Reconstruction . . . . . 89
3.1.6 Missing $E_T$ Reconstruction . . . . . 90
3.1.7 Jet Reconstruction . . . . . 92
3.1.8 Energy Calibrations . . . . . 93
3.2 Particle Identification . . . . . 95
3.2.1 Electron Identification . . . . . 95
3.2.2 Muon Identification . . . . . 111

**4 Event Modeling 116**
4.1 Monte Carlo Event Generators . . . . . 117
4.1.1 Full Event Generators . . . . . 117
4.1.2 Fast Event Generators . . . . . 118
4.2 Detector Simulation . . . . . 119
4.2.1 First Principle Detector Simulation . . . . . 120
4.2.2 Parametric Detector Simulation . . . . . 122

**5 Event Selection and Detection Efficiencies 127**
5.1 Data Samples . . . . . 128
5.2 Event Selection . . . . . 128
5.2.1 Online Event Selection and Luminosity . . . . . 129
5.2.2 Offline Event Selection . . . . . 133
5.3 Detection Efficiencies and Standard Model Expectations . . . . . 141

**6 Backgrounds 145**
6.1 Instrumental Backgrounds . . . . . 146
6.1.1 Misidentification of Photons as Electrons . . . . . 147
6.1.2 Misidentification of Jets as Electrons . . . . . 151
6.1.3 Production of Isolated Muons in Association with Jets . . . . 156

6.2 Dilepton Backgrounds . . . . . 164
6.2.1 $Z \to ee, \mu\mu$ . . . . . 164
6.2.2 Drell Yan Dileptons . . . . . 166
6.2.3 $Z \to \tau\tau$ . . . . . 168
6.2.4 $t\bar{t}$ production . . . . . 169
6.3 Background Summaries . . . . . 172

**7 Results** **174**
7.1 $p\bar{p} \to W^+W^- + X$ Cross Section . . . . . 175
7.2 Coupling Limits from the $W$ Pair Cross Section . . . . . 176
7.3 Coupling Limits from the Candidate Lepton Spectrum . . . . . 180
7.4 Results from the Combined Run 1 Analysis . . . . . 187

**8 Conclusions** **191**
8.1 Summary . . . . . 191
8.2 Comparison With Other Results . . . . . 193
8.3 Future Prospects . . . . . 195
8.4 Final Remarks . . . . . 196

**A Candidate Event Displays** **198**

**B Measurement of $P_{j\to e}$** **211**
B.1 Introduction . . . . . 212
B.2 Data Sample and Event Selection Criteria . . . . . 213
B.3 Trigger Bias . . . . . 214
B.4 Direct Photon Subtraction . . . . . 216
B.5 Fake Probabilities . . . . . 217

**C Cross Check of the $ee$ Background from Jet Fakes** **221**

**D Physics at a Hadron Collider** **225**

**Bibliography** **229**

# List of Tables


1.1 Summary of the quarks and some of their properties . . . . . 3
1.2 Summary of the leptons and some of their properties . . . . . 3
1.3 Summary of the Standard Model gauge bosons and some of their properties . . . . . 4
1.4 Summary of Standard Model interactions. . . . . 6
2.1 Selected TeVatron parameters . . . . . 47
2.2 Selected parameters of the Vertex Drift Chamber . . . . . 55
2.3 Selected parameters of the Central Drift Chamber . . . . . 57
2.4 Selected parameters for FDC $\Phi$ modules . . . . . 59
2.5 Selected parameters for FDC $\Theta$ modules . . . . . 60
2.6 Selected properties of uranium . . . . . 65
3.1 Track-in-road efficiency, method 1 . . . . . 108
3.2 Track-in-road efficiency, method 2 . . . . . 109
3.3 Combined track-in-road efficiency . . . . . 109
3.4 Likelihood + isolation efficiencies . . . . . 110
3.5 Final likelihood + isolation efficiencies . . . . . 110
3.6 Combined electron ID efficiencies (per electron) . . . . . 110
3.7 Muon ID efficiencies (per muon) . . . . . 115
5.1 Single muon trigger efficiencies. Uncertainties are statistical only. . . 132
5.2 Dimuon trigger efficiencies and luminosities. . . . . 132
5.3 Kinematic and topological event selection cuts . . . . . 133
5.4 Characteristics of dielectron candidate . . . . . 139
5.5 Characteristics of $e-\mu$ candidate one. . . . . 139
5.6 Characteristics of $e-\mu$ candidate two. . . . . 140
5.7 Characteristics of dimuon candidate . . . . . 140
5.8 Detection efficiencies for the dielectron channel . . . . . 141
5.9 Detection efficiencies for the $e-\mu$ channel . . . . . 142
5.10 Detection efficiencies for the dimuon channel. . . . . 142

5.11 Sources of systematic uncertainty for the prediction of $WW \rightarrow$ dilepton detection efficiencies. . . . . 142
5.12 Predicted event yields for Standard Model $WW$ production. . . . . 144
6.1 Relative electron ID efficiencies for photons with tracks . . . . . 149
6.2 Jet misidentification probabilities for electrons. Uncertainties are statistical (fit) only. . . . . 153
6.3 Relative luminosities and trigger efficiencies for $e - \mu$ fake candidate sample. . . . . 156
6.4 Secondary muons surviving all cuts. . . . . 159
6.5 Secondary muons surviving all cuts (heavy quark enhanced). . . . . 160
6.6 Parameters for Drell-Yan backgrounds. For the dimuon channel, the number of passing events is for pre (post) shutdown MUSMEAR parameterizations. . . . . 167
6.7 Number of events passing selection cuts in $Z \rightarrow \tau\tau \rightarrow \ell\ell$ Monte Carlo samples. For the $e - \mu$ and $\mu\mu$ channels, the first number is for pre-shutdown and the second for post-shutdown MUSMEAR parameterizations respectively. . . . . 169
6.8 Number of events passing selection cuts in $t\bar{t} \rightarrow \ell\ell$ Monte Carlo sample. For the $e - \mu$ and $\mu\mu$ channels, the first number is for pre-shutdown and the second for post-shutdown MUSMEAR parameterizations. . . . . 172
6.9 Background summary for dielectron channel. . . . . 173
6.10 Background summary for $e - \mu$ channel. . . . . 173
6.11 Background summary for dimuon channel. . . . . 173
7.1 Anomalous coupling limits for various coupling schemes . . . . . 180
7.2 Binning for $ee$ channel lepton spectrum fit. . . . . 182
7.3 Binning for $e\mu$ channel lepton spectrum fit. . . . . 183
7.4 Binning for $\mu\mu$ channel lepton spectrum fit. . . . . 183
7.5 Fitted parameters for the number of expected $ee$ signal events with "equal" couplings. . . . . 184
7.6 Fitted parameters for the number of expected $e\mu$ signal events with "equal" couplings. . . . . 184
7.7 Fitted parameters for the number of expected $\mu\mu$ signal events with "equal" couplings. . . . . 184
7.8 Summary of Run 1a $WW \rightarrow$ dilepton analysis. . . . . 188
7.9 Anomalous coupling limits for various coupling schemes using Run 1a+1b data. . . . . 189
8.1 Summary of anomalous coupling limits. . . . . 192
8.2 Summary of decay channels. Errors are combined in quadrature. . . . 193
8.3 Summary of anomalous coupling limits. All results assume equal couplings. . . . . 195

B.1 Summary of $E_T$ thresholds used in measuring fake rates. Units are GeV. . . . . 215
C.1 Parameters in Fake Background Calculation . . . . . 223

# List of Figures


1.1 A plot of the Higgs potential both as a function of the complex scalars $\phi^+$ and $\phi^0$ (left) and as a function of $\phi^0$ only. . . . . 15

1.2 Standard Model Feynman Diagrams for tree level hadro-production of $W$ pairs decaying into purely leptonic final states. . . . . 17

1.3 Kinematic distributions for Standard Model $W$ pair production. . . . 20

1.4 Distributions of $e^+e^-$ invariant mass, $\not\!\!E_T$ , $|\vec{E}_T^{Had}|$, and electron $E_T$ for $W$ pair Monte Carlo events in the dielectron channel. The solid line indicates PYTHIA+ DØGEANT+DØRECO v11.19, the dashed fast Monte Carlo+DIPS. The discrepancy in the $\vec{E}_T^{Had}$ and $\not\!\!E_T$ distributions is due to the inclusion of underlying event in the fast Monte Carlo. . . . . 23

1.5 Feynman Diagrams involving anomalous couplings for the tree level hadro-production of $W$ pairs decaying into purely leptonic final states. 27

1.6 The cross section as a function of anomalous couplings for the three sets of events generated. The left figure is for "equal coupling" relations and $\Lambda = 1000$ GeV. The middle figure is for "equal couplings" with $\Lambda = 1500$ GeV. The right figure is for couplings with the HISZ relations and $\Lambda = 1000$ GeV. . . . . 30

1.7 The cross section ratio for events generated with the "equal coupling" relations and $\Lambda = 1500$ vs. $\Lambda = 1000$ GeV (left). The cross section ratio for events generated with the "usual couplings" relations and the HISZ coupling relations, both with $\Lambda = 1000$ GeV (right). . . . . 31

1.8 Unitarity surface and limit contours. (Right) The surface generated by the unitarity condition on dipole form factors. The vertical scale is $\Lambda$ in units of TeV. (Left) Coupling limit contours from the unitarity condition for various values of $\Lambda$. . . . . 33

1.9 $W$ boson transverse momentum distribution for Standard and non-Standard Model Couplings. . . . . 36

1.10 Final state lepton transverse momentum distribution for Standard and non-Standard Model Couplings. . . . . 37
2.1 Schematic of the FNAL facility (not to scale). . . . . 43
2.2 Isometric cutaway view of the DØ detector. . . . . 48
2.3 End view of one quadrant of the VTX chamber. . . . . 54
2.4 End view of three CDC modules. Sense wires are indicated by small dots, guard (field shape) wires by large dots, and delay lines by open circles. . . . . 56
2.5 Exploded isometric view of one half of the FDC tracking system. . . . 59
2.6 Structure of a calorimeter readout cell. . . . . 65
2.7 Side view of one quadrant of the calorimeter and central detector. The lines of constant pseudorapidity intervals are with respect to $z = 0$. . . . . 67
2.8 Total material in the calorimeter and muon toroid, as a function of polar angle. . . . . 72
2.9 End view of the proportional drift tubes used in the muon spectrometer. 74
2.10 Schematic of data acquisition at DØ. . . . . 83
3.1 Fractional Isolation Distributions. (a) CC distributions of fractional energy isolation for electrons from $Z \to ee$ candidate events (hashed) and highly electromagnetic showers from multijet events. (b) EC distributions of fractional energy isolation for electrons (hashed) and jets. The electrons are from the dielectron data used in $WW \to e^+e^-$ search, while the jets are from the multijet data sample used to study the electron fake probabilities. . . . . 98
3.2 Definition of the track match significance in terms of the cluster centroid in EM3 and the projection of a track to this radius. Track projects which fall within the indicated ellipse are considered good matches. . . . . 101
3.3 Electron Likelihood Distributions. (a) 4-variable electron likelihood for CC electrons from $Z \to ee$ candidate events (hashed) and highly electromagnetic showers from multijet events. (b) 4-variable electron likelihood for EC electrons (hashed) and jets. The electrons are from the dielectron data used in $WW \to e^+e^-$ search, while the jets are from the multijet data sample used to study the electron fake probabilities. . . . . 103
3.4 Ratio of weighted electron ID efficiency to background event yield for jets misidentified as electrons. . . . . 105
4.1 Distributions of Dielecton mass, $\not\!\!E_T$ , $\vec{E}_T^{Had}$ and Electron $E_T$ for $Z \to e^+e^-$ events from Data (solid), Standard (ISAJET, DØRECO v11.19) (dashed) and Fast Monte Carlo (dotted). . . . . 125

4.2 Distributions of Dimuon mass, $E_T^{\eta}$, $\vec{E}_T^{Had}$ and Muon $p_T$ for $Z \to \mu^+\mu^-$ events from Data (solid), Standard (ISAJET, DØRECO v12.20) (dashed) and Fast Monte Carlo (dotted). The data have been background subtracted. . . . . 126
5.1 Level 2 trigger turn-on curves. (a) Missing $E_T$ turn on for events with an electron in the CC with $E_T > 25$ GeV. (b) Missing $E_T$ turn on for events with an electron in the EC with $E_T > 25$ GeV. (c) Electron $E_T$ turn for CC electrons in events with $\not\!\!E_T > 25$ GeV. (d) Electron $E_T$ turn for EC electrons in events with $\not\!\!E_T > 25$ GeV. . . . . 130
5.2 Distributions of $\Delta\phi(E_T^{e_2}, \not\!\!E_T)$ vs $\not\!\!E_T$ for $Z$, $Z \to \tau^+\tau^-$, Standard Model $W$ pair (PYTHIA, DØRECO v11.19) and non-Standard Model $W$ pair (fast Monte Carlo, DIPS) events in the dielectron channel. . . 135
5.3 Distributions of $\Delta\phi(p_T^{\mu}, \not\!\!E_T)$ vs $\not\!\!E_T$ for $Z \to \tau^+\tau^-$, Standard Model $W$ pair (PYTHIA, DØRECO v12.20) and non-Standard Model $W$ pair (fast Monte Carlo, DIPS) events in the $e-\mu$ channel. . . . . 136
5.4 Distributions of $\Delta\phi(p_T^{\mu_2}, \not\!\!E_T)$ vs $\not\!\!E_T$ for $Z$, $Z \to \tau^+\tau^-$, Standard Model $W$ pair (PYTHIA, DØRECO v12.20) and non-Standard Model $W$ pair (fast Monte Carlo, DIPS) events in the dimuon channel. . . . 138
6.1 Jet $E_T$ distribution for dielectron fake candidate sample events passing all selection cuts. . . . . 155
6.2 Jet $E_T$ distribution for $e-\mu$ fake electron candidate sample events passing all selection cuts. . . . . 157
6.3 Jet $E_T$ distribution for dimuon fake candidate sample. . . . . 163
6.4 Transverse hadronic energy distributions for $t\bar{t}$ (shaded) and $W$ pair events in dilepton channels. The samples are from generator level Monte Carlo. . . . . 171
7.1 The grids in $\lambda$ and $\Delta\kappa$ for the events generated with the "equal" coupling relations (left) and the HISZ coupling relations (right). . . . 177
7.2 $W$ pair cross section as a function of anomalous couplings for the three sets of events generated. The left figure is for couplings with the "equal" relations and $\Lambda = 1000$ GeV. The middle figure is for couplings with the "equal" relations and $\Lambda = 1500$ GeV. The right figure is for couplings with the HISZ relations and $\Lambda = 1000$ GeV. . . 179
7.3 Surfaces of 95% confidence level Limit $WW$ cross section. The left figure is for couplings with the "equal" relations and $\Lambda = 1000$ GeV. The middle figure is for couplings with the "equal" relations and $\Lambda = 1500$ GeV. The right figure is for couplings with the HISZ relations and $\Lambda = 1000$ GeV. . . . . 179
7.4 Anomalous coupling limit contour for "equal" couplings with $\Lambda = 1000$ GeV. . . . . 181

7.5 Anomalous coupling limit contour for "equal" couplings with $\Lambda$ = 1500 GeV. . . . . 181
7.6 Anomalous coupling limit contour for HISZ couplings with $\Lambda = 1000$ GeV. . . . . 182
7.7 Lepton Spectra for the $W$ pair signal and background. The solid histograms are the candidates, the shaded histograms are the estimated background, and the dashed are the sum of the SM signal prediction plus background. . . . . 186
7.8 Run 1b anomalous coupling limits. a) Limits for the "equal" coupling relationships with $\Lambda$ = 1.5 TeV. b) Limits for the HISZ coupling relationships. For each plot, the innermost contour is the 1 degree of freedom contour, the middle is the 2 degree of freedom contour, and the outermost contour the unitarity limit. . . . . 188
7.9 Run 1 anomalous coupling limits. a) Limits for the "equal" coupling relationships with $\Lambda$ = 1.5 TeV. b) Limits for the HISZ coupling relationships. For each plot, the innermost contour is the 1 degree of freedom contour, the middle is the 2 degree of freedom contour, and the outermost contour the unitarity limit. . . . . 190
A.1 $R - Z$ View of Dielectron Candidate. . . . . 199
A.2 $R - \Phi$ View of Dielectron Candidate. . . . . 200
A.3 Lego Display of Dielectron Candidate. . . . . 201
A.4 $R - Z$ View of $e\mu$ Candidate One. . . . . 202
A.5 $R - \Phi$ View of $e\mu$ Candidate One. . . . . 203
A.6 Lego Display of $e\mu$ Candidate One. . . . . 204
A.7 $R - Z$ View of $e\mu$ Candidate Two. The muon in the upper right quadrant is the primary muon associated with the $W$ pair candidate. The remaining two muons (upper left) are low pt (see lego of this candidate) and result from either the underlying event, or combinatoric fakes associated with the WAMUS EF region. . . . . 205
A.8 $R - \Phi$ View of $e\mu$ Candidate Two. . . . . 206
A.9 Lego Display of $e\mu$ Candidate Two. . . . . 207
A.10 $R - Z$ View of Dimuon Candidate. . . . . 208
A.11 $R - \Phi$ View of Dimuon Candidate. . . . . 209
A.12 Lego Display of Dimuon Candidate. . . . . 210
B.1 Distributions of jet misidentification as electron probability - direct photon subtraction applied. (a) Fake probability in the CC for a likelihood cut of 0.20 (b) Fake probability in the EC for a likelihood cut of 0.25. . . . . 218
B.2 Distributions of jet misidentification as electron probability - no direct photon subtraction. (a) Fake probability in the CC for a likelihood cut of 0.20 (b) Fake probability in the EC for a likelihood cut of 0.25. 220

C.1 $\not{E}_T$ distributions for Good (top) and Fake (bottom) dielectron samples. 224
D.1 (a) Parton distributions from the MRSD'_ set evaluated at $\mu = M_Z$.
(b) Sensitivity of the up and down quark distributions to the scale $\mu$.
Typical $x$ values for gauge boson production are indicated by $x_{WZ}$. . 227
D.2 Cross sections for various processes at the Tevatron as predicted by the ISAJET Monte Carlo. . . . . 228

# Chapter 1

# The Standard Model and the Physics of $W$ Pairs

This study involves a search for new physics indirectly manifested as interactions between the $W$ boson and the $Z$ boson or photon beyond those predicted by the Standard Model. Specifically, evidence for anomalous trilinear $WW\gamma$ or $WWZ$ vertices would signal new physics. In this chapter, we review the Standard Model, followed by a more detailed examination of the Electroweak theory of Glashow, Weinberg and Salam, covering it's most crucial features. This is followed by a discussion of the pair production of $W$ bosons in the Standard Model. Next, we discuss the consequences of $W$ pair production from non-Standard Model mechanisms, and introduce the necessary formalism to quantitatively account for such production. Finally, we review relevant measurements from previous and current experiments.

## 1.1 The Standard Model of Elementary Particle Interactions

The Standard Model is the modern description of all elementary particle processes. Developed over the last 100 years, it provides a description of nature at distance scales of order $10^{-15}$ m, and energy scales ranging up to order $10^{11}$ eV, a regime where the worlds of quantum mechanics and relativity overlap. Built on the mathematical foundation of quantum field theory, the Standard Model is a theory of interacting quantum fields. The excitations of these fields are identified as particles, and are grouped into three categories: quarks and leptons, mediators, and Higgs particles. The quarks and leptons are spin $\frac{1}{2}$ fermions. Each can be further divided into three generations containing two particles each. The mediators, also called gauge bosons, are spin 1 particles. These particles are the quanta of the interactions in the Standard Model - Electromagnetic, Weak and Strong[1]. Finally, the Higgs particle is a spin 0 boson which results from the spontaneous breaking of Electroweak gauge symmetry.

There are six kinds each of quarks and leptons. Each generation of quarks contains one charge $\frac{1}{3}$ quark and one charge $\frac{2}{3}$ quark. Each generation of leptons contains one charged lepton and one neutral lepton. The groupings and some of the

[1]The fourth force in nature is Gravity, however there is currently no suitable quantum description of this interaction to incorporate into the Standard Model. At energy and distance scales for which the Standard Model is valid, gravity is many orders of magnitude more feeble than the other forces and may be safely ignored.

properties of the quarks and leptons are summarized in tables 1.1 and 1.2 (from [39]). The quarks and electrically charged leptons experience the Electromagnetic interaction. All the quarks and leptons experience the Weak interaction. Only the quarks experience the Strong interaction.

| | Flavor | Mass (GeV/$c^2$) | Elect. Charge |
|---|---|---|---|
| u | up | 0.005 | $+\frac{2}{3}$ |
| d | down | 0.01 | $-\frac{1}{3}$ |
| c | charm | 1.5 | $+\frac{2}{3}$ |
| s | strange | 0.2 | $-\frac{1}{3}$ |
| t | top | 180 | $+\frac{2}{3}$ |
| b | bottom | 4.7 | $-\frac{1}{3}$ |

Table 1.1: Summary of the quarks and some of their properties

| | Flavor | Mass (GeV/$c^2$) | Elect. Charge |
|---|---|---|---|
| $\nu_e$ | e neutrino | $< 7 \times 10^{-9}$ | 0 |
| $e^-$ | electron | 0.000511 | -1 |
| $\nu_\mu$ | $\mu$ neutrino | $< 0.0003$ | 0 |
| $\mu^-$ | muon | 0.106 | -1 |
| $\nu_\tau$ | $\tau$ neutrino | $< 0.03$ | 0 |
| $\tau^-$ | tau | 1.7771 | -1 |

Table 1.2: Summary of the leptons and some of their properties

The gauge bosons are the quanta of the forces of the Standard Model, and are responsible for the interactions between particles. Particles which can experience a

particular force do so via the exchange of gauge bosons, which are said to *mediate* the interaction. The quanta of the electromagnetic force is the photon. The weak force has three quanta, the charged $W^{\pm}$ and the neutral $Z$. The quanta of the strong force are the gluons, which come in eight different types. A summary of these particles along with some of their properties can be found in table 1.3 (also from [39]).

| Boson | Force | Mass (GeV/c$^2$) | Elect. Charge |
|---|---|---|---|
| $\gamma$ | Electromagnetism | 0.0 | 0.0 |
| $W^+$ | Weak | 81 | +1 |
| $W^-$ | Weak | 81 | -1 |
| $Z$ | Weak | 91 | 0 |
| Gluon | Strong | 0 | 0 |

Table 1.3: Summary of the Standard Model gauge bosons and some of their properties

The simplest of the forces is the electromagnetic force. The theory describing this interaction is called Quantum Electrodynamics (QED). In this theory, all particles which carry electric charge may interact with each other via the exchange of photons. The strength of the electromagnetic force, which can be parameterized by a coupling constant, increases as the interaction energy increases (alternately, as the interaction distance decreases).

The strong interaction is described by Quantum Chromodynamics (QCD).

As the name suggests, the quantum number of this interaction is color charge. Particles with non-zero color charge can interact with each other via the exchange of gluons. QCD differs from QED in three important ways. First, instead of just one kind of charge as in QCD, there are three kinds of color charge. Second, because of the non-abelian nature of QCD, the gluons also carry color charge (one unit each of color and anticolor). This results in additional types of interactions in which gluons can couple to other gluons. The final difference between QCD and QED is that the QCD coupling decreases at large energies (short distances) and increases at small energies (large distances). The consequences of this are twofold. First, at high energies quarks (especially those bound up in baryons - QCD bound states) behave as if they were free particles. This is known as "asymptotic freedom" [40], and allows the use of perturbative calculations at large energies. At large distances however, the strong coupling grows rapidly. This results in the phenomenon known as "confinement" [40], which requires quarks (or any object with a net color charge) to remain only in bound states with no net color.

The weak force is a short range interaction due to the large mass of the $W$ and $Z$ bosons. A key element of the Standard Model is that this force is unified with the electromagnetic force to form a single "electroweak" interaction. Similar to QCD, the electroweak interaction has a non-abelian gauge structure, implying that the gauge bosons of the theory may interact with each other as well as with the fermions of the theory. Table 1.4 summarizes the Standard Model interactions.

A more detail discussion of the electroweak interaction follows in the next section.

| Interaction | Weak | Electromagnetic | Strong |
|---|---|---|---|
| Acts on: | Flavor Charge | Electric Charge | Color Charge |
| Particles Experiencing it: | Leptons, Quarks, EW Gauge Bosons | Quarks, charged Leptons | Quarks, Gluons |
| Force Carriers | $W^+$, $W^-$, $Z$ | $\gamma$ | Gluons |

Table 1.4: Summary of Standard Model interactions.

The final piece to the Standard Model is the Higgs boson. The underlying principle to all the theories of the Standard Model is "local gauge invariance". This invariance requires that the Lagrangian of the theory be invariant under a generalized phase transformation which may vary as a function of space-time. The specifics of the transformation are determined by the symmetry (gauge) group associated with the interaction. Unfortunately, the imposition of this requirement means that all the particles (both fermions and gauge bosons) in the theory must be massless. This is clearly a problem since most of the particles observed in nature are massive. The solution to this problem is called the Higgs mechanism [41]. Through

spontaneous local symmetry breaking, it generates the masses of the appropriate fermions and gauge bosons, but at the price of introducing one (more in Standard Model extensions) new particle - the Higgs boson.

## 1.2 The GWS Theory of Electroweak Interactions

A principal feature of the Standard Model is the unification of the electromagnetic and weak interactions. In the theory of Glashow, Weinberg and Salam, both forces are described as manifestations of a single electroweak interaction. This unification is based on the assertion that both quarks and leptons carry internal quantum numbers which transform under the $SU(2)_L \times U(1)_Y$ symmetry group, where the $L$ subscript denotes the fact that only left handed particles transform under the SU(2) weak isospin symmetry group, whereas both left and right handed particles transform under the U(1) weak hypercharge group. This assertion, along with the principal of local gauge symmetry and the application of the Higgs mechanism result in a theory which describes both the electromagnetic and weak interactions observed in nature.

### 1.2.1 $SU(2)_L \times U(1)_Y$

The first step in writing an electroweak theory is to re-identify the fundamental fermions as left and right handed particles. This step is motivated by the

fact that while the electromagnetic interaction is observed to conserve parity, the weak interaction is observed to violate parity (maximally). In order to unify the two observed interactions, we must place ourselves in a framework which allows us to work easily with both. The choice of 'handed' particles accomplished this task. We define left and right-handed particle states via helicity projection operators [40]

$$\psi_L = \frac{1}{2}(1-\gamma_5)\psi \text{ and } \psi_R = \frac{1}{2}(1+\gamma_5)\psi,$$

which pick out the left and right handed helicity components of the fermion spinors. It should be noted that these operators only pick out states of definite helicity when the particles of interest are massless. After this procedure, the left handed particles are arranged into iso-doublets, whereas the right handed particles are arranged into iso-singlets as there is no right handed neutrino (as observed in nature). For example, the first generation fermions can be classified in the following way:

$$(e_L, \nu_{eL}), (d_L, u_L), e_R, d_R, u_R,$$

for the particles, and

$$(\bar{e}_R, \bar{\nu}_{eR}), (\bar{d}_R, \bar{u}_R), \bar{d}_L, \bar{u}_L, \bar{e}_L$$

for the anti-particles.

The SU(2) transformation rule for the left handed doublets is

$$\psi'_L = e^{-ig\vec{\alpha}\cdot\vec{\tau}/2}\psi_L,$$

where $g$ is a constant, $\vec{\alpha}$ a vector in weak isospin specifying the transformation, and $\vec{\tau}$ is a vector of the SU(2) generator matrices (the Pauli spin matrices) for the $j = \frac{1}{2}$ representation. In this representation, $\frac{\vec{\tau}}{2}$ is the weak isospin operator. This transformation mixes the components of the left handed doublets. The SU(2) transformation rule for the right handed singlets is the trivial

$$\psi'_R = \psi_R.$$

The U(1) transformations for the left and right handed states are given by

$$\psi'_L = e^{-ig'Y\beta/2}\psi_L$$

and

$$\psi'_R = e^{-ig'Y\beta/2}\psi_R$$

respectively, where $g'$ is a constant, $\beta$ an arbitrary value in hypercharge space specifying the transformation, and $Y$ the weak hypercharge operator. Both these transformations are a simple overall phase change.

From the above, it is straightforward to see that this structure results in a left-handed interaction which transmutes one fermion doublet member into another. This will turn out to be the charged current weak interaction. It also contains an interaction independent of handedness which transmutes singlet and doublet elements into themselves. This will turn out to contain both the neutral current weak and electromagnetic interactions[2]. It is also important to note that given the

[2]It should be noted that we ignore the issue of generational mixing in the quarks. In nature,

above definitions of $\psi_L$ and $\psi_R$, the fermion mass term in the Lagrangian density ($m\bar{\psi}\psi$) is not invariant under SU(2)$_L$, so for the time being, the fermions must be taken as massless.

### 1.2.2 Local Gauge Invariance

The next step in constructing the theory requires the application of the principal of local gauge invariance. A feature of all modern particle theories, local gauge invariance requires that the theory produce the same results when the fields are changed according to the above prescriptions at all space-time points. In this case, $\vec{\alpha}$ and $\beta$ become functions of the space-time four vector $x$. This principle was first applied for the case of SU(2) by Yang and Mills [43] in an unsuccessful attempt to describe the strong interaction. The first successful application came when Glashow added an independent U(1) symmetry and applied the combined symmetry to the weak + electromagnetic interactions [31]. The fermions in this theory carried both weak isospin ($\vec{T} = (T_1, T_2, T_3)$) and weak hypercharge ($Y$) quantum numbers. These quantities are related to the electromagnetic charge ($q$), by $q = T_3 + Y/2$.

The general procedure for writing a theory which is invariant under local gauge transformations begins with writing the Lagrangian density for the fermion

the first generation doublet, for example, appears to be ($d'_L$,$u_L$) where d′ is a mixture of d, s and b and the mixing angles are given by the Cabbbio, Kobayashi, Maskawa matrix elements [42]. This allows any charge changing transition to occur via $W$ exchange, but does not affect the gauge structure which we concern ourselves with here. Generational mixing amongst the leptons is not observed in nature, but is possible if neutrinos are found to have a non-zero mass.

fields of the theory. Since we are considering massless fermions, there is no mass term, and we are left with the "free" or "kinetic" term of the Dirac Lagrangian [44]

$$\mathcal{L} = \bar{\psi}\gamma^{\mu}\partial_{\mu}\psi \tag{1.1}$$

where we work in units $\hbar = c = 1$. The generic procedure to make equation 1.1 invariant under some transformation on the fields $\psi$ is to replace $\partial_\mu$ with the "covariant derivative" $D_\mu$, whose form is determined by the gauge symmetry group. This derivative generally requires the introduction of one or more "gauge fields" (spin 1), again depending on the symmetry group, which also transform under the local gauge transformations.

For Glashow's theory, the covariant derivative takes the form [40]

$$D_\mu = \partial_\mu + ig\vec{W}_\mu \cdot \vec{\tau} + i\frac{1}{2}g'B_\mu Y \tag{1.2}$$

where $\vec{W} = (W_1, W_2, W_3)$ is an $\mathrm{SU}(2)_L$ isotriplet, and $B$ is a $\mathrm{U}(1)_Y$ singlet. To maintain the invariance of the Lagrangian, these field must have the following transformations: [40]

$$\vec{W}'_\mu = \begin{cases} \vec{W}_\mu, & \mathrm{U}(1)_Y \\ \vec{W}_\mu + \partial_\mu\vec{\alpha} + g\vec{\alpha} \times \vec{W}_\mu, & \mathrm{SU}(2)_L \end{cases} \tag{1.3}$$

and

$$B'_\mu = \begin{cases} B_\mu + \partial_\mu B_\mu, & \mathrm{U}(1)_Y \\ B_\mu, & \mathrm{SU}(2)_L \end{cases} \tag{1.4}$$

where the cross product in (1.3) is evaluated in weak isospin space. Because we have added new fields to the Lagrangian, we must also add a free field term for

each of these fields (which by necessity turns out to be invariant under local gauge transformations). It is important to note however, that the mass term in the spin 1 particle (Procca) Lagrangian, $\frac{1}{4}M^2 A_{\mu\nu}A^{\mu\nu}$, is not invariant under any of the above transformations, so to keep the total Lagrangian invariant, the gauge fields must be massless [9]. Substitution of equation 1.2 into equation 1.1 results in interaction terms between the fermion and $\vec{W}$ and $B$ fields.

It is now possible to re-identify the bosons as states with definite electromagnetic charge $q$. These are given by

$$W_\mu^\pm = (W_\mu^1 \mp iW_\mu^2)/\sqrt{2}$$

for the charged ($W$) bosons, and

$$Z_\mu = W_\mu^3 \cos\theta_w - B_\mu \sin\theta_w$$

$$A_\mu = W_\mu^3 \sin\theta_w + B_\mu \cos\theta_w$$

for the neutral bosons, anticipating their eventual identification as the $Z$ and the photon ($A_\mu$). The mixing of the neutral bosons is determined by the electroweak mixing or Weinberg angle ($\theta_w$). Using these definitions, the free Lagrangian we started with now contains three currents

$$q\bar{\psi}\gamma^\mu\psi A_\mu$$

$$g(\bar{\psi}\gamma^\mu T_L^+\psi W_\mu^+ + \bar{\psi}\gamma^\mu T_L^-\psi W_\mu^-)$$

$$g_Z \bar{\psi} \gamma^\mu [T_{3L} - q sin^2\theta_w] \psi Z_\mu$$

where

$$g = \frac{e}{sin\theta_w} \quad and \quad g_Z = \frac{e}{sin\theta_w cos\theta_w}.$$

These are precisely the electromagnetic, charged weak, and neutral weak interactions. So a theory that started only with fermions now has, through the application of local gauge invariance, the full structure of the electromagnetic and weak interactions. 'T Hooft's 1971 [45] proof that all gauge theories are renormalizable, provided additional motivation to try to make this theory work as a description of a unified electroweak interaction.

### 1.2.3 Symmetry Breaking and the Higgs Mechanism

Despite it's success in generating the correct structure, Glashow's theory had one major flaw - all the particles were massless. The problem was to somehow generate all the gauge boson and fermion masses, while retaining the renormalizability of the theory. The solution to this problem, provided by Weinberg and Salam [32, 33], is achieved by spontaneous symmetry breaking and the Higgs Mechanism [41].

In the Standard Model, we introduce an SU(2) doublet of scalar fields

$$\Phi = \begin{pmatrix} \phi^+ \\ \phi^0 \end{pmatrix}.$$

The fields $\phi^+$ and $\phi^0$ are assigned quantum numbers $(T_3, Y, Q)$ of $(\frac{1}{2}, \frac{1}{2}, 1)$ and

$(-\frac{1}{2}, \frac{1}{2}, 0)$ respectively [44]. This field must have a term in the Lagrangian

$$\mathcal{L}_\Phi = (\partial_\mu \Phi)^\dagger (\partial^\mu \Phi) - \mu^2 \Phi^\dagger \Phi - \lambda (\Phi^\dagger \Phi)^2, \tag{1.5}$$

where the first term is the free field term term for $\Phi$ and the second two terms represent the most general renormalizable form for a scalar potential. As illustrated in figure 1.1, for $\mu^2 < 0$ the physical vacuum (corresponding to the minimum of the potential) does not occur at $|\Phi| = 0$, but at $|\Phi| = \sqrt{-\frac{1}{2}\mu^2/\lambda}$. Alternately, this means that the vacuum expectation value of $|\Phi|$ is non-zero. The "vev" selects a direction in weak isospin plus hypercharge space and "spontaneously breaks" the $\mathrm{SU}(2)_L \times \mathrm{SU}(1)_Y$ symmetry. Conventional field theory is formulated as fluctuations about the physical vacuum, so it is appropriate (in unitary gauge) to redefine $\Phi$ as

$$\Phi = \frac{1}{\sqrt{2}} \begin{pmatrix} 0 \\ v + H(x) \end{pmatrix} \tag{1.6}$$

where $H$ now represents fluctuations above the minimum of the potential. Substituting this new definition of equation 1.6 into equation 1.5, and following the example of the previous section to impose local gauge symmetry yields terms in the Lagrangian which can be identified as mass terms for the Higgs, $W$ and $Z$ bosons. The photon remains massless. This procedure also produces terms which define trilinear and quartic self interactions between the gauge and Higgs boson. Additionally, by allowing a Yukawa type interaction between the Higgs boson and the fermion fields, terms are generated in the Lagrangian which can be identified as

fermion masses. So after the application of the principal of local gauge symmetry and the Higgs mechanism, what began as a theory of massless fermions, has become a theory which fully describes a unified electroweak interaction of massive fermions and gauge bosons.

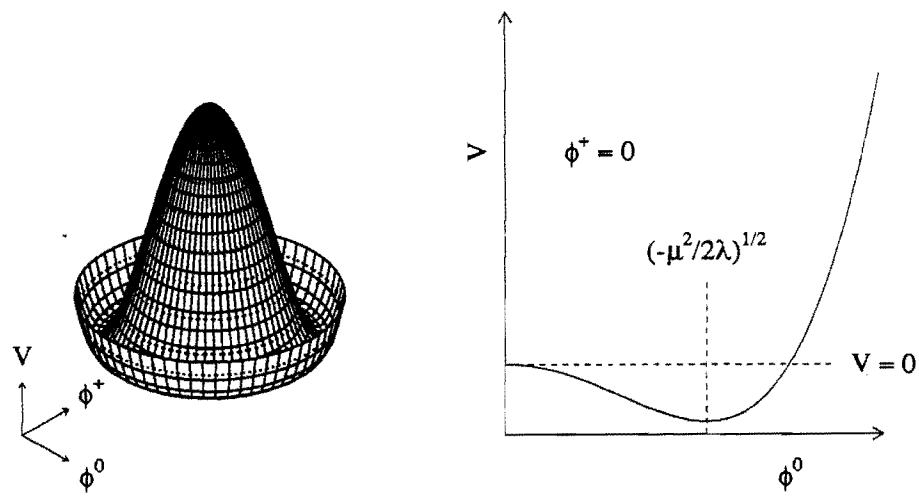


Figure 1.1: A plot of the Higgs potential both as a function of the complex scalars $\phi^+$ and $\phi^0$ (left) and as a function of $\phi^0$ only.

## 1.3 $W$ Pairs in the Standard Model

Of particular interest to this analysis are the terms in the SM Lagrangian which describe the trilinear interactions involving the $W$ boson with either the $Z$

boson or the photon. These terms are [44]

$$+ig\sin\theta(W_\mu^- W_\nu^+ A^{\mu\nu} + W_\mu^+ W^{-\mu\nu} A_\nu - W^{+\mu\nu} W_\mu^- A_\nu) \tag{1.7}$$

$$+ig\cos\theta(W_\mu^- W_\nu^+ Z^{\mu\nu} + W_\mu^+ W^{-\mu\nu} Z_\nu - W^{+\mu\nu} W_\mu^- Z_\nu) \tag{1.8}$$

which describe the $WW\gamma$ and $WWZ$ vertices respectively. These terms are a direct consequence of the non-abelian gauge structure of the theory. Along with the terms describing the fermion couplings to the $W$'s, these terms describe all the mechanisms by which $W$'s can be pair produced at the tree level in the Standard Model. In this section, we describe the SM production mechanisms for $W$ pairs. We then discuss the theoretical predictions which result from these mechanisms, along with the experimental signature expected.

### 1.3.1 Standard Model $WW$ Production Mechanisms

There are four diagrams which describe tree level hadroproduction of $W$ pairs in the Standard Model. Shown in figure 1.2, the first two diagrams (t and u-channel) are fully described by the couplings of the quarks to the $W$ boson. These couplings are well measured from studies of the hadroproduction of single $W$ bosons. The second two diagrams (s-channel) involve the trilinear couplings of the $W$ boson to the $Z$ boson and photon. Thus a measurement of $W$ boson pair production can lead to a direct measurement of the trilinear gauge boson couplings by deconvoluting the contribution from the t and u-channel diagrams from the overall signal.

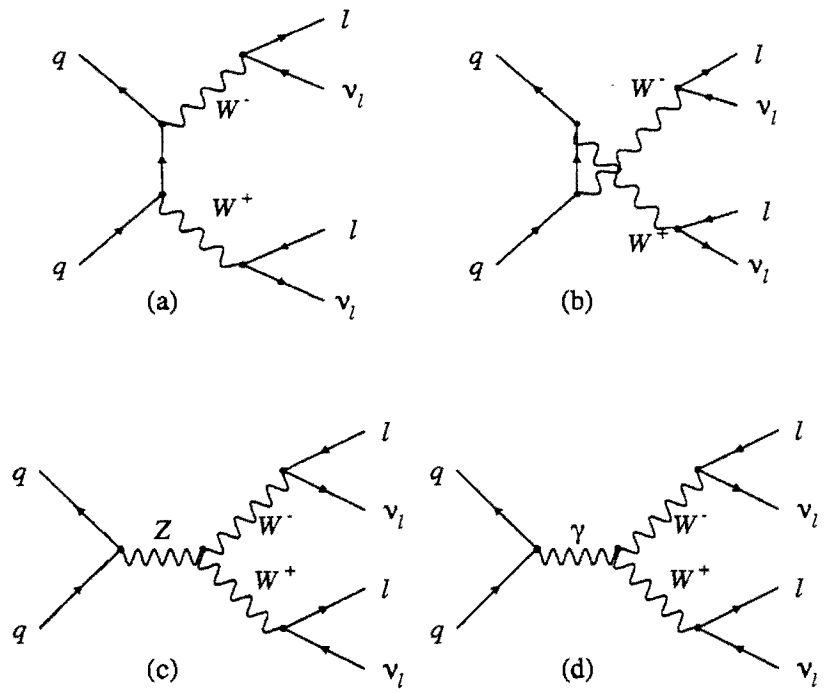


Figure 1.2: Standard Model Feynman Diagrams for tree level hadro-production of $W$ pairs decaying into purely leptonic final states.

### 1.3.2 Standard Model Predictions for $WW$ Production

With tree level diagrams in hand, we can now ask the SM for predictions of observables. The first of these is the cross section. The calculation of the $W$ pair cross section offers insight into one of the special features of the Standard Model. If, for example, one were to calculate the total cross section from only t-channel

quark exchange diagram, the result would be linear in $\hat{s}$ (the subprocess collision energy) [40]. This in turn implies that partial wave unitarity will be violated at sufficiently large energies [3]. It is only by the inclusion of the s-channel diagrams (involving the triple boson couplings), and the cross terms which result from squaring all the summed amplitudes, that the unitarity condition is restored. In fact, both the $WW\gamma$ and $WWZ$ diagrams are required to produce the full cancellation [40]. This is often referred to as "delicate" gauge cancellation, and is a requirement of the SM. It is the very nature of the construction of the SM which provides the gauge boson self-interaction terms which, although unnecessary to describe the weak current interactions for which the construction is motivated, restores the physical consistency of the model as a whole. As will be discussed later, this balance will have important consequences in the search for deviations from the SM predicted values for the couplings.

Because of the composite nature of the proton (see appendix D), a numerical result for the cross section for the hadroproduction of $W$ pairs cannot be produced analytically. An analytic computation can be performed to determine the parton subprocess cross section, but this must be summed over all possible pairs of participating partons in the initial state hadrons, and additionally integrated over the parton momentum distributions. These problems lend themselves most easily to solution via a Monte Carlo approach. Event generators such as PYTHIA [46] and

[3]Formally, this is the violation of the conservation of probability flux in quantum mechanics.

HERWIG [47] are capable of fully modeling the hadroproduction of Standard Model $W$ pairs, and can be used to produce a numerical result for the cross section. Another Monte Carlo, written by the authors of reference [48] uses a fast Monte Carlo approach to model the hadroproduction of both Standard and non-Standard Model $W$ pairs. These programs are discussed in more detail in Chapter 4. Using the MRSD'_ parton distribution function set [49, 50], the fast Monte Carlo predicts a Standard Model cross section of 9.4 pb. Monte Carlos can also be used to model the kinematic characteristics of $W$ pair events. Of interest to an analysis at a hadron collider are the transverse momentum distribution of the $W$'s, and the transverse momentum and angular distributions of the decay products. These can be found in figure 1.3.

### 1.3.3 Experimental Signature for $WW$ Production

$W$ boson pair production can manifest itself in three main topologies: those in which both $W$'s decay hadronically, those in which one decays hadronically and the other leptonically, and those in which both decay leptonically. The purely hadronic final state has several advantages. It has the highest branching fraction, being produced 45.6% of the time (summing over all accessible flavors), and it also is the only final state which has fully measured kinematics[4]. The disadvantages suffered by

[4]At hadron colliders, only the transverse kinematics can be reconstructed due to the unknown parton-parton center of mass energy. At $e^+e^-$ machines, full transverse and longitudinal constraints can be applied.

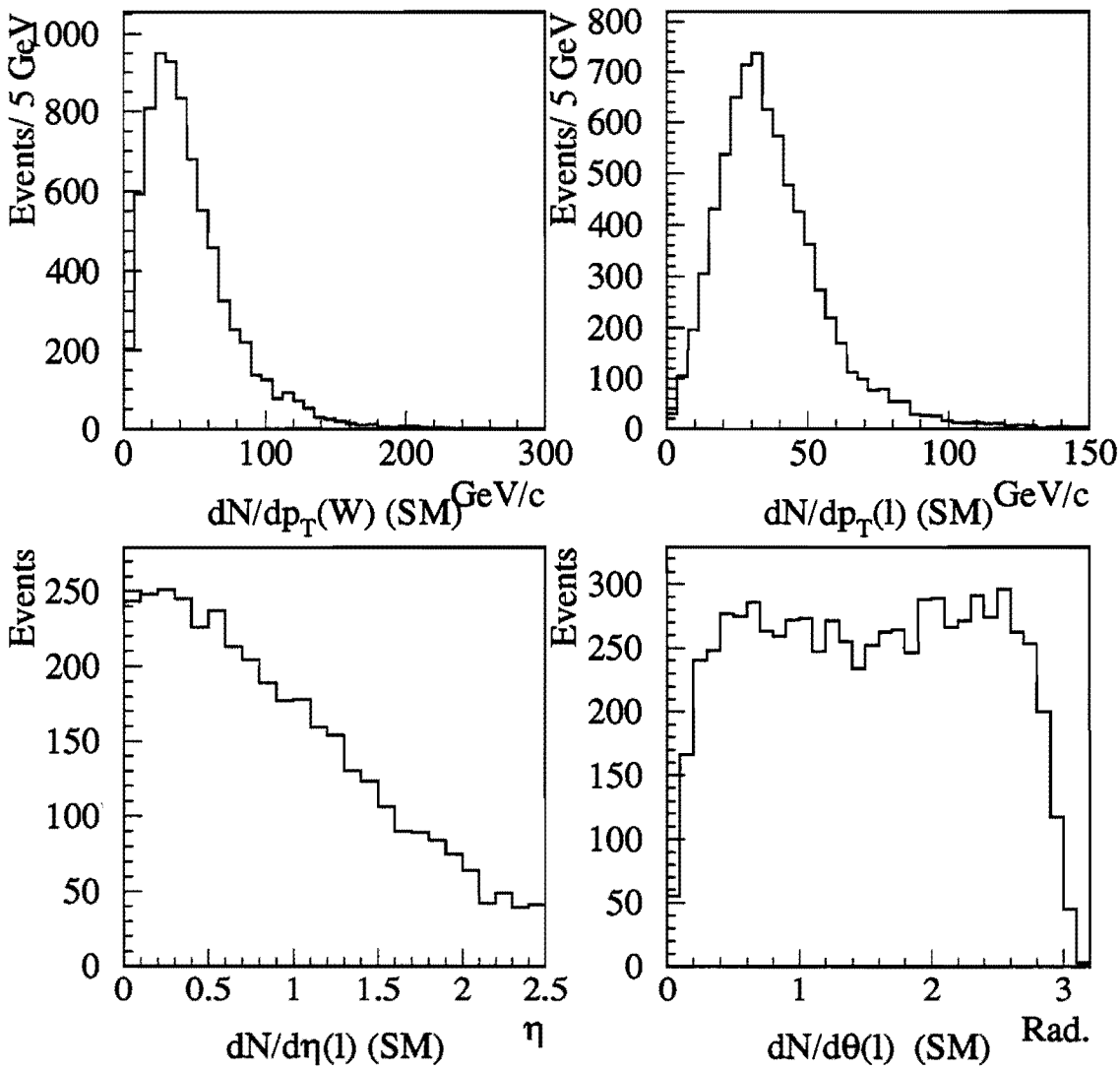


Figure 1.3: Kinematic distributions for Standard Model $W$ pair production.

this final state however, far exceed the advantages. First, the ability to reconstruct which jet comes from which $W$ is limited both by the generally inferior energy resolution of hadronic calorimeters (compared to electromagnetic calorimeters) and by difficulties in charge sign determination of the jets. A further complication due to the limited energy resolution of hadronic calorimeters is the inability to clearly distinguish $W$'s from $Z$'s which decay hadronically, thus making it difficult at best to distinguish $WW$ from $WZ$ production[5]. Finally, this channel suffers from large backgrounds at hadron colliders due to continuum multijet production as well as the production of single $W$ bosons in association with jets.

The mixed hadronic/leptonic topology suffers from lower branching ratio, occuring 29.2% of the time counting electrons and muons, and also has more poorly measured kinematics due to the presence of the neutrino, whose momentum can only be inferred in the transverse direction. This channel also suffers from large QCD backgrounds from both multijet and $W$+jets production. As in the all-jets channel, the mixed topology is also complicated by the "pollution" of the $WW$ final state from $WZ$ final states. Additionally, this topology suffers from large backgrounds similar to those in the all-jets channel. The main (and substantial) advantage of this channel is the ability to unambiguously reconstruct both $W$'s, and to determine via $p_T$ balance the transverse momentum of each $W$. While unsuitable for a cross

[5]Of course this situation only arises at a hadron collider where the leading order production of the $WZ$ final state is possible. For the purposes of studying the boson self couplings, it is a complication rather than a disadvantage because once can simply do a simultaneous analysis for both $WW$ and $WZ$, as both final states rely on the $WWZ$ coupling.

section measurement due to signal to noise considerations, this channel does provide an excellent arena for the measurement of trilinear boson couplings (as will become more apparent later in this chapter).

The purely leptonic topology suffers badly from low branching ratio, occurring only 4.66% of the time (allowing for only electrons and muons - tau's are excluded due to the difficulty in identifying them efficiently). This topology also suffers from very poorly known kinematics due to the presence of two neutrinos. The advantages of this channel come from both a unique diboson signature, and from relatively low backgrounds. Figure 1.4 shows some important kinematic distributions for $W$ pairs in the purely leptonic topology. The particular case shown is for $W^+W^- \rightarrow e^+\nu_e e^-\bar{\nu}_e + X$. These events are characterized by two high $p_T$ leptons, and large missing transverse energy. Because the total $\not{E}_T$ in the event is due to the sum of two neutrinos, it tends to have no angular correlation to the charged leptons. These events also tend to have small amounts of hadronic energy (only higher order QCD correction diagrams for initial state radiation contribute events with jets), and have a broadly distributed range of invariant dilepton mass.

The dilepton + $\not{E}_T$ signature is relatively unambiguous amongst diboson final states. Possible exceptions include $WZ$ production in the trilepton + $\not{E}_T$ topology (in which one of the leptons is not reconstructed), and $ZZ$ production in which one $Z$ decays to neutrinos and the other to charged leptons. Taking into account cross section, branching ratio and detector acceptance, both processes are

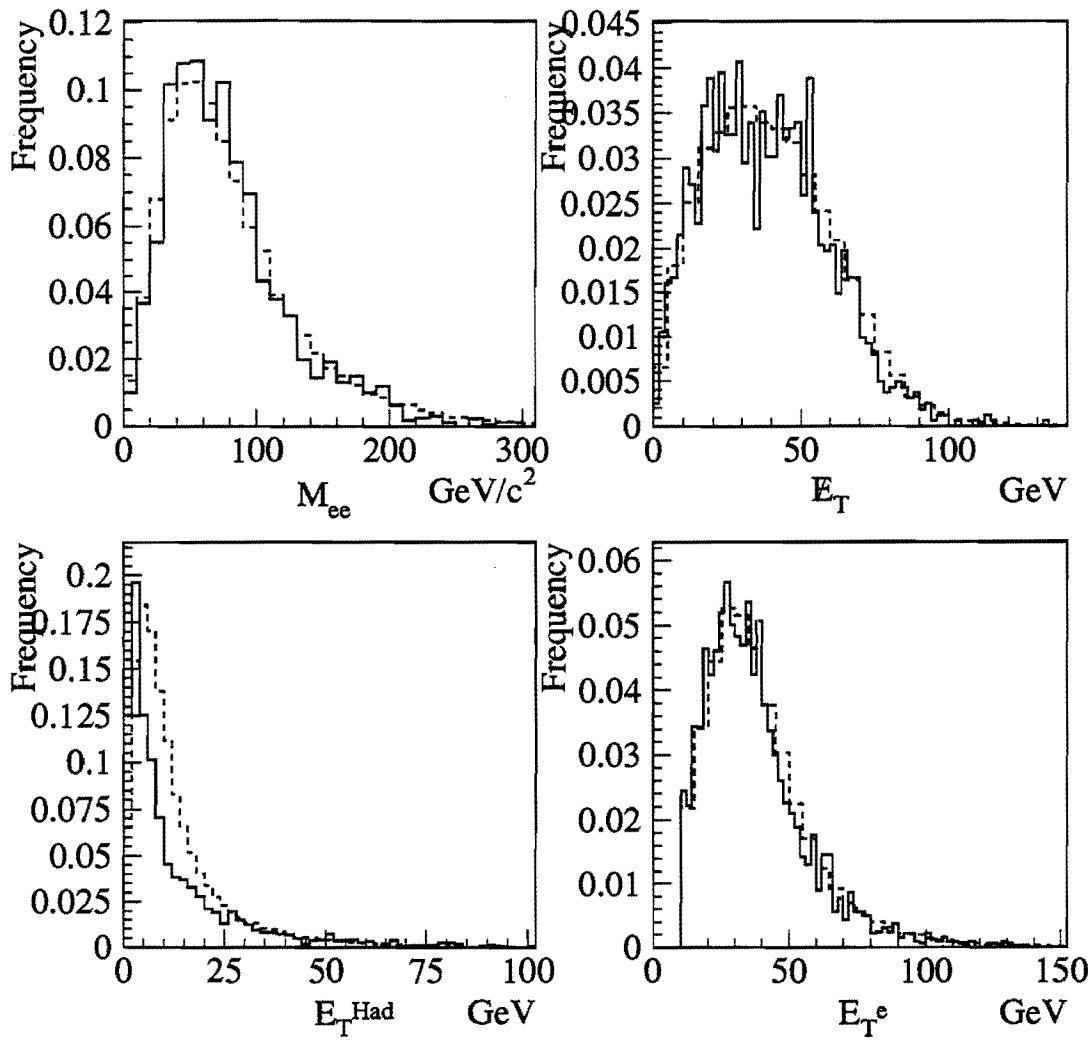


Figure 1.4: Distributions of $e^+e^-$ invariant mass, $\not{E}_T$ , $|\vec{E}_T^{Had}|$, and electron $E_T$ for $W$ pair Monte Carlo events in the dielectron channel. The solid line indicates PYTHIA+ DØGEANT+DØRECO v11.19, the dashed fast Monte Carlo+DIPS. The discrepancy in the $\vec{E}_T^{Had}$ and $\not{E}_T$ distributions is due to the inclusion of underlying event in the fast Monte Carlo.

significantly more rare than purely leptonic $W$ pairs.

The backgrounds to the dilepton topology are small due both to the low relative abundance of the competing background processes (compared to QCD processes), and to the relative ease to with which they can be controlled. For example, $Z \rightarrow \tau\tau$ events typically have a softer electron/muon spectrum than $W$ pair events, and also have smaller $\not{E}_T$ which tends to be correlated angularly with the direction of the charged leptons. These events can be suppressed as a dilepton background by placing higher acceptance cuts on lepton $p_T$ and on the $\not{E}_T$ in the event, or by cutting on the angle between the $\not{E}_T$ and the charged leptons. Similarly, $t\bar{t}$ events typically have one or more high $p_T$ jets resulting from $b$ quark decays. A cut on the transverse hadronic energy in the event substantially reduces this background while resulting in the loss of only higher order QCD correction diagrams for the signal.

As a result of all these factors, the purely leptonic $W$ pair topology provides the best platform on which both to attempt to measure the hadroproduction cross section and to investigate the trilinear vector boson self couplings, and is the subject of the remainder of this dissertation.

## 1.4 $W$ Pairs Beyond the Standard Model

Up to this point, everything that has been discussed has been based on the assumption that the Standard Model is correct. It doesn't have to be. Although

the model has many features which might motivate us to choose it as the correct one, it need not be so. While the Standard Model agrees with all observations as of this writing, there are features of the theory which are unsatisfactory. Problems such as the required fine tuning of quadratic divergences (the issue of "mass hierarchy" [40]) and the ad-hoc nature of the Higgs field motivate the search for a more comprehensive theory. There may be other phenomenological scenarios in which one could construct the observed weak and electromagnetic currents. The Standard Model could simply be another in a line of low energy approximations; good enough at energies that are accessible by today's experiments, but obviously inadequate to describe data which are currently far beyond our reach. Such flaws can possibly be seen at lower energies, but only through precision measurements. Whatever the case, anything that effects the gauge boson sector of the Standard Model will have implications for the pair production of $W$ bosons. In this section, we briefly discuss possible mechanisms for the non-Standard Model production of $W$ pairs. We then introduce a generalized formalism which will allow us to cope with all such scenarios without regard to their specifics. Finally we will discuss the experimental signature of "anomalous" $W$ pair production.

### 1.4.1 Mechanisms for non-SM $WW$ Production

There are many phenomenological scenarios one could imagine which would have direct effects on the pair production of $W$ bosons. The discussion here is not

meant to be a complete survey, but is rather intended to provide a few examples of the types of modifications or extensions to the Standard Model that one could imagine.

One example of a non-SM scenario would be the existence of a heavy $Z$ like gauge boson. Such a particle could well have the same or similar couplings to the $W$ boson. This would necessitate the modification of the $W$ pair cross section calculation to include yet another $s$-channel diagram involving a $WWZ'$ vertex, possibly disrupting delicate gauge cancellation.

Another mechanism for non-SM $W$ pair production would be if either the $W$ or $Z$ bosons were composites. In such a scenario, the simple trilinear couplings of the SM would have to be replaced by new couplings involving the interactions of the constituent particles. This could result in observable anomalous couplings if the energy scale at which the gauge boson compositeness became visible was accessible.

A final mechanism to consider is the presence of particles which alter the gauge coupling by participating in loop diagrams. Additional fermions, higgs bosons or other particles could change the couplings by varying amounts. Some changes might only be of the same order as SM electroweak loop corrections, but others could be larger if new particles coupled strongly to the gauge bosons.

### 1.4.2 Formalism

Given that there are so many possible non-SM mechanisms which could cause measurable effects on the production of $W$ pairs, it is impractical to formulate theories for and test each model. The approach that has been taken is to introduce a set of generic parameters which describe, in the most general way, the allowed forms of the gauge boson vertices. Effectively, what this procedure does is take the s-channel diagrams shown in figure 1.2 and replace them with diagrams (shown in figure 1.5) containing a generalized coupling between the $Z/\gamma$ and the $W$. Because there are

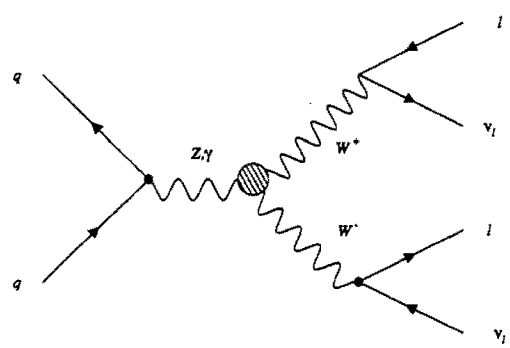


Figure 1.5: Feynman Diagrams involving anomalous couplings for the tree level hadro-production of $W$ pairs decaying into purely leptonic final states.

many possible parameters, it is convenient to first apply an effective Lagrangian approach to define the set of parameters, and then to impose further relationships

between the parameters by assuming certain symmetries are respected.

The most general effective Lagrangian that can be written for the $WWV$ ($V = Z, \gamma$) vertex is [51]

$$\mathcal{L}_{WWV}/g_{WWV} = ig_1^V(W^\dagger_{\mu\nu}W^\mu V^\nu - W^\dagger_\mu V_\mu W^{\mu\nu}) \tag{1.9}$$

$$+i\kappa_V W^\dagger_\mu W_\nu V^{\mu\nu} \tag{1.10}$$

$$+\frac{i\lambda_V}{M_W^2}W^\dagger_{\rho\mu}W^\mu_\nu V^{\nu\rho} \tag{1.11}$$

$$-g_4^V W^\dagger_\mu W_\nu(\partial^\mu V^\nu + \partial^\nu V^\mu) \tag{1.12}$$

$$+g_5^V \epsilon^{\mu\nu\rho\sigma}(\partial_\rho W^\dagger_\mu W_\nu - W^\dagger_\mu \partial_\rho W_\nu)V_\sigma \tag{1.13}$$

$$+\tilde{\kappa}_V W^\dagger_\mu W_\nu \tilde{V}^{\mu\nu} \tag{1.14}$$

$$+\frac{i\tilde{\lambda}_V}{M_W^2}W^\dagger_{\rho\mu}W^\mu_\nu \tilde{V}^{\nu\rho} \tag{1.15}$$

where $W_{\mu\nu} \equiv \partial_\mu W_\nu - \partial_\nu W_\mu$, $V_{\mu\nu} \equiv \partial_\mu V_\nu - \partial_\nu V_\mu$ and $\tilde{V}^{\mu\nu} \equiv \frac{1}{2}\epsilon_{\mu\nu\rho\sigma}V^{\rho\sigma}$. The overall couplings (or normalization factors) are defined to be $g_{WW\gamma} \equiv -e$ and $g_{WWZ} \equiv -e \cot\theta_W$, where $\theta_W$ is the Weinberg angle and $e$ the proton charge. In the Standard Model at tree level, the couplings are given by $g_1^V = \kappa_V = 1$ and $\lambda_V = g_4^V = g_5^V = \tilde{\kappa}_V = \tilde{\lambda}_V = 0$. The 14 (seven each for $Z$ and $\gamma$) general coupling parameters allow for C/P-violating[6] ($g_5^V$) and CP-violating ($g_4^V, \tilde{\kappa}_V, \tilde{\lambda}_V$) terms. These terms are neglected in this and most other studies, resulting in six couplings ($g_1^V, \kappa_V, \lambda_V$) to be measured. Electromagnetic gauge invariance (the photon is massless) requires $g_1^\gamma = 1$, reducing the number of free parameters to five[7]. Thus, deviations from the

[6]ie. C and P are not conserved, but CP is.

[7]Alternatively, this is an expression of the electic charge of the $W$ boson.

Standard Model are given by the anomalous couplings:

$$\Delta g_1^Z \equiv g_1^Z - 1,\ \Delta\kappa_\gamma \equiv \kappa_\gamma - 1,\ \Delta\kappa_Z \equiv \kappa_Z - 1,\ \lambda_\gamma,\ \lambda_Z.$$

To further reduce the number of free couplings we introduce two schemes which impose additional relationships between the couplings. In the first and simplest, we require that the $Z$ and photon couple identically to the $W$. Thus we have $\Delta\kappa = \Delta\kappa_\gamma = \Delta\kappa_Z$ and $\lambda = \lambda_\gamma = \lambda_Z$ ($\Delta g_1^\gamma = \Delta g_1^Z = 1$). This is referred to as the "equal couplings" scheme, and reduces the number of free couplings parameters to two. In the second scheme, the so called HISZ [52] scenario named after the authors, the anomalous couplings are formulated in a framework which explicitly respects the $SU(2)\times U(1)$ gauge invariance of the Standard Model. This also results in a reduction of the number of free couplings to two. The couplings $\Delta\kappa_\gamma$ and $\lambda_\gamma$ are chosen as the free parameters, relating to the $WWZ$ couplings by:

$$\Delta g_1^Z = \frac{1}{2\cos^2\theta_W}\Delta\kappa_\gamma \tag{1.16}$$

$$\Delta\kappa_Z = \frac{1}{2}(1-\tan^2\theta_W)\Delta\kappa_\gamma \tag{1.17}$$

$$\lambda_Z = \lambda_\gamma \tag{1.18}$$

Figure 1.6 shows the total cross section as a function of anomalous couplings for the "equal coupling" and HISZ relations. Figure 1.7 shows the ratio of cross sections.

While the anomalous coupling parameters appear as constants, they can in principal have functional dependency on the energy scale of the interaction since they

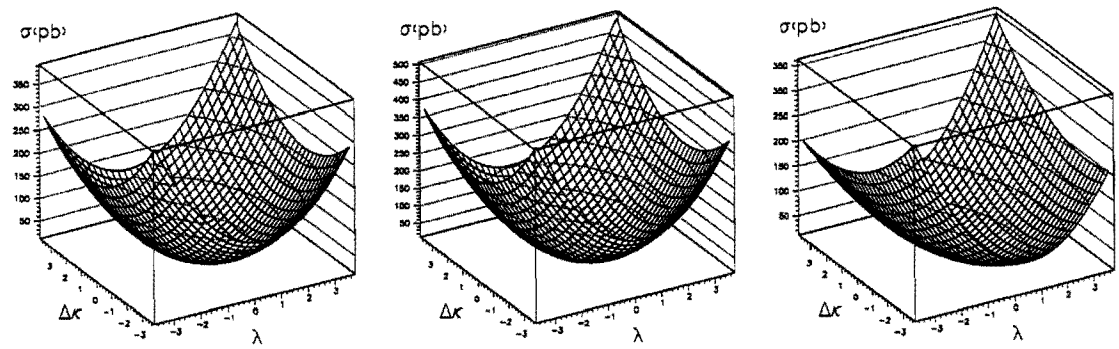


Figure 1.6: The cross section as a function of anomalous couplings for the three sets of events generated. The left figure is for "equal coupling" relations and $\Lambda = 1000$ GeV. The middle figure is for "equal couplings" with $\Lambda = 1500$ GeV. The right figure is for couplings with the HISZ relations and $\Lambda = 1000$ GeV.

must, eventually, depend on the details of the new physics. Additionally, the self consistency of the formalism, requires that unitarity must be respected. This in turn requires that the behavior of the matrix elements (and hence the couplings) must be controlled at high energies. Specifically, since the anomalous couplings participate only in s-channel processes, the $\ell = 0$ term in the partial wave expansion must be explicitly controlled. It can be shown however that for $WW$ production, the $\mathcal{M}_{\pm\pm}$ helicity amplitudes are enhanced by $\hat{s}/m_W^2$ for anomalous values of $\lambda$, and that the $\mathcal{M}_{0,0}$ amplitude is similarly enhanced for anomalous values of $\Delta\kappa$. Non-SM values of $\Delta g_1^Z$ affect $\mathcal{M}_{\pm 0}$ and $\mathcal{M}_{0\pm}$ but only like $\sqrt{\hat{s}}/m_W$[8] Thus the non-SM amplitudes

[8]In fact, all diboson processes show $\hat{s}/m_W^2$ enhancement for anomalous $\lambda$. For $\Delta\kappa$ however, it is only the $W$ pair process which grows as $\hat{s}$. All other diboson processes have their (0,0) amplitudes enhance only as $\sqrt{\hat{s}}$. For $\Delta g_1^Z$ only the (0,0) amplitude of $WZ$ production grows linearly with $\hat{s}$. Thus $W$ pair production is the most sensitive probe available for $\Delta\kappa$, while $WZ$ production is the best for $\Delta g_1^Z$.

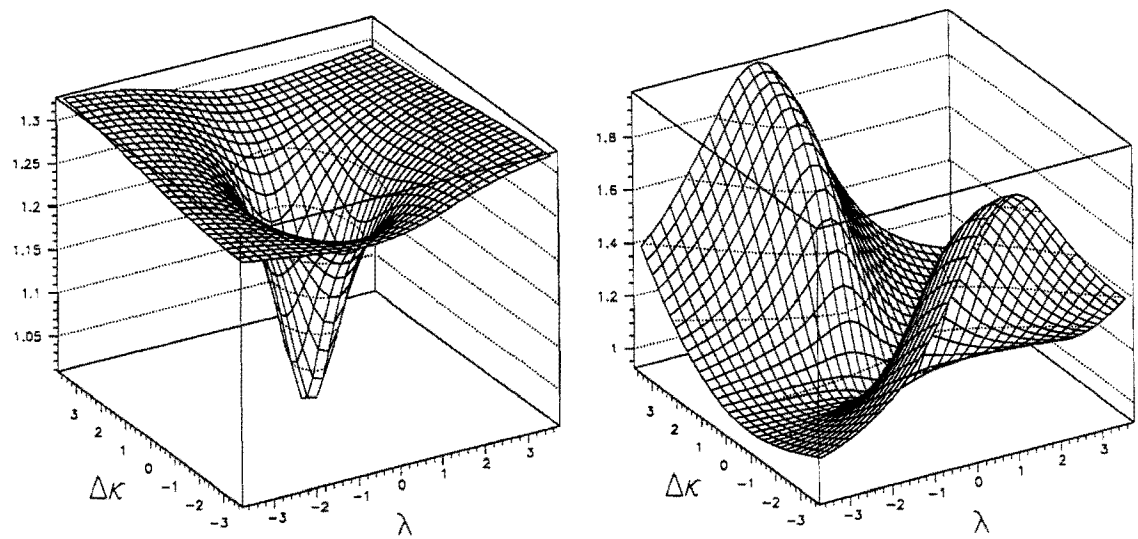


Figure 1.7: The cross section ratio for events generated with the "equal coupling" relations and $\Lambda = 1500$ vs. $\Lambda = 1000$ GeV (left). The cross section ratio for events generated with the "usual couplings" relations and the HISZ coupling relations, both with $\Lambda = 1000$ GeV (right).

rise without limit as $\hat{s}$ increases, eventually violating unitarity [53].

To control the high energy behavior of the scattering amplitudes, the couplings are modified by form factors,

$$\lambda \to \lambda(\hat{s}) = \frac{\lambda}{(1+\frac{\hat{s}}{\Lambda^2})^n} \quad \text{and} \quad \Delta\kappa \to \Delta\kappa(\hat{s}) = \frac{\Delta\kappa}{(1+\frac{\hat{s}}{\Lambda^2})^n}.$$

For the $WWV$ couplings, the choice of $n = 2$ is sufficient to bring the high energy behavior of the matrix elements under control. The parameter $\Lambda$ is the form factor scale, and is related to the scale of new physics (it is effectively the energy scale at which the new physics becomes important). Limits on the couplings are measured

experimentally for an assumed choice of $\Lambda$. Because the anomalous couplings affect only s-channel feynman diagrams, the momentum transfer $q^2$ is interchangeable with the square of the collision energy in the quark-antiquark center of momentum frame $(\hat{s})$.[9]

A consequence of the form factor behavior is that for a choice of scale $\Lambda$, the unitarity condition places constraints on the allowed values of the couplings [54]. The expression [53]

$$\Lambda \leq (\frac{6.88}{(\kappa-1)^2+2\lambda^2})^{\frac{1}{4}} \text{ TeV}$$

derives from the tree level unitarity requirement, and can be solved for a particular value of $\Lambda$ to produce simultaneous unitarity limits on $\Delta\kappa$ and $\lambda$. The surface produced by this expression, and unitarity limits for several values of $\Lambda$ can be found in figure 1.8. Because of this, some care must be taken in the choice of form factor scales. If the choice is too large, the unitarity limits will be more stringent than the experimental bounds. If the scale is chosen to low, the experimental results will be less stringent than the data allow. This would also result in predictions for $W$ and $Z$ properties different than those already observed [55]. Thus the choice of

[9]This situation is entirely analogous to the case of elastic lepton-nucleon scattering. In that case, the form factors found in the high energy differential cross section correspond to the charge distribution inside the nucleon, and $\Lambda$ (the Fourier transform of) the spatial extent of the distribution. The physical interpretation is that as momentum transfers become larger $(-q^2 > \Lambda^2)$ the virtual photon becomes sensitive to the quark substructure of the nucleon, and the nucleon is more easily broken apart. As the elastic process becomes more unlikely, the form factors (and hence the cross section) become smaller, going to zero in the high energy limit. The onset of the non-elastic lepton-nucleon physics is characterized by the scale $\Lambda$. In the case of anomalous couplings, the same story holds true. For $q^2 < \Lambda^2$, the form factors (and hence the scattering amplitudes) are independent of energy, but for higher energies $(q^2 > \Lambda^2)$ the energy dependence of the form factors comes into play, as the sensitivity to the new physics increases.

scale must be made such that the highest possible form factor scale is used that does not result in a unitarity limit more stringent than the experimental limit.

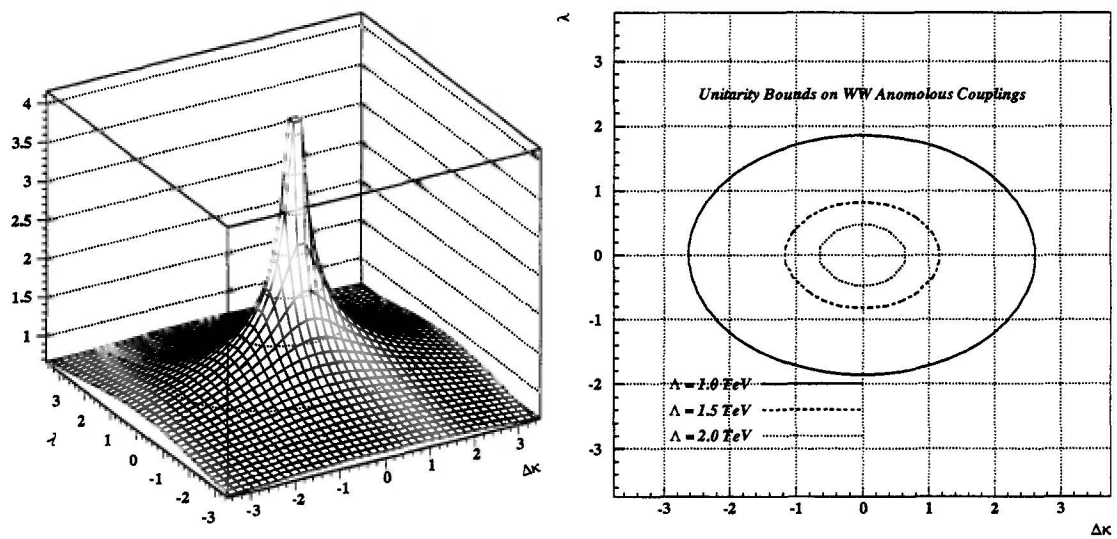


Figure 1.8: Unitarity surface and limit contours. (Right) The surface generated by the unitarity condition on dipole form factors. The vertical scale is $\Lambda$ in units of TeV. (Left) Coupling limit contours from the unitarity condition for various values of $\Lambda$.

To give the anomalous coupling parameters a more familiar frame of reference, it is useful to note that they can be related to the electromagnetic moments of the $W$ boson. Formally, the C and P conserving terms in the effective $WW\gamma$ Lagrangian correspond to the lowest order terms in a multipole expansion of the $W$ - photon interaction: the charge $Q_W$, the magnetic dipole moment $\mu_W$ and the

electric quadrupole moment $q_W$ of the $W^+$ [53]

$$Q_W = eg_1^\gamma \tag{1.19}$$

$$\mu_W = \frac{e}{2m_W}(g_1^\gamma + \kappa_\gamma + \lambda_\gamma) \tag{1.20}$$

$$q_W = -\frac{e}{m_W^2}(\kappa_\gamma - \lambda_\gamma.) \tag{1.21}$$

Expressing the familiar electromagnetic moments of a point particle in terms of the anomalous coupling parameters can give us some insight into how we might expect the various modifications to the Standard Model discussed above to be manifest in the anomalous couplings. If, for example, the $W$ were a composite particle, then the multipole moments would be different from the SM predictions due to the differences in charge configuration between a point particle and a more complicated composite. In any case, by whichever mechanism (if any) reality differs from the Standard Model, the physical observables available to us can in principal be used as a probe of the verity of the model.

### 1.4.3 Experimental Signatures of non-SM $WW$ Production

The presence of anomalous couplings has several consequences which enables their detection. The first is an increase in the total cross section, which is illustrated in figure 1.6. Recall from 2.2.2 that both the $Z$ and $\gamma$ s-channel diagrams are required at their Standard Model strengths to produce the "delicate" gauge cancellation which controls the $WW$ cross section. The presence of anomalous couplings changes

those values and disrupts the cancellation. The larger the difference between the real and SM values, the larger the disruption. The result is that as the size of the anomalous couplings increases, the enhancements to the cross section grow larger and become visible at smaller center of mass energies,

In addition to the total cross section, the differential distributions are also sensitive the presence of non-SM couplings. For large values of $WW$ invariant mass ($\sqrt{\hat{s}}$) the anomalous contributions to the helicity amplitudes dominate the SM contributions. Because the anomalous couplings contribute only in the s-channel, their effects tend to be concentrated in regions of small $W$ rapidity. Thus the transverse momentum of the $W$'s (and hence their decay products) is enhanced by the presence of anomalous couplings, particularly at large transverse momenta [53]. Because the rate of growth of the $W$ pair cross section is largest at hight $p_T^W$, and because the backgrounds tend to be concentrated at smaller values of $p_T$, a fit to the $W$ boson transverse momentum distribution can provide a very sensitive test for the presence of anomalous couplings. Figure 1.9 shows the distribution of $p_T^W$ for several values of anomalous couplings. Because the $W$ transverse momentum cannot be unambiguously reconstructed in the dilepton channels, we also consider the $p_T$ distribution of the $W$ decay products. Figure 1.10 shows the distribution of $E_T^l$ for several values of anomalous couplings.

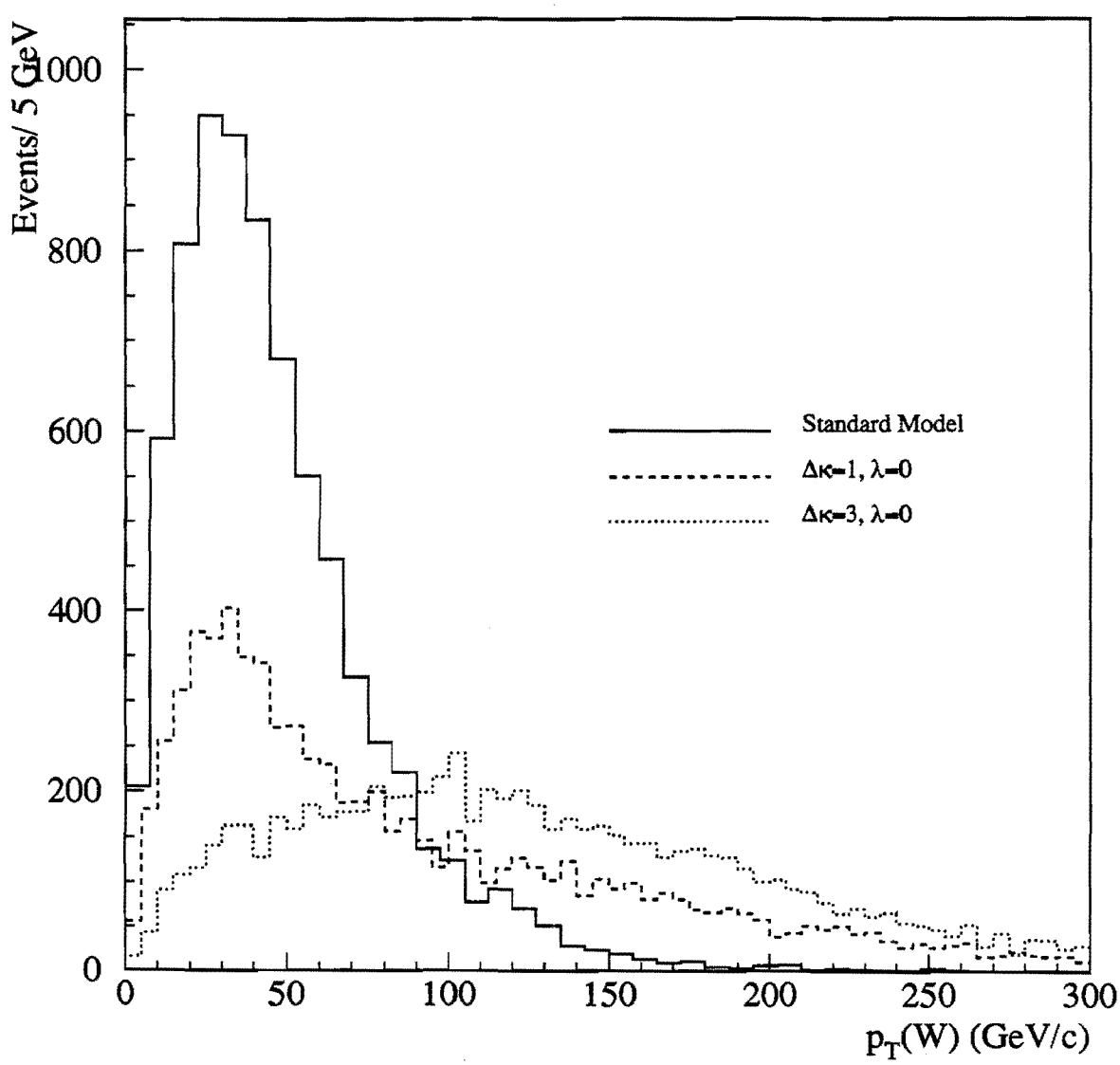


Figure 1.9: $W$ boson transverse momentum distribution for Standard and non-Standard Model Couplings.

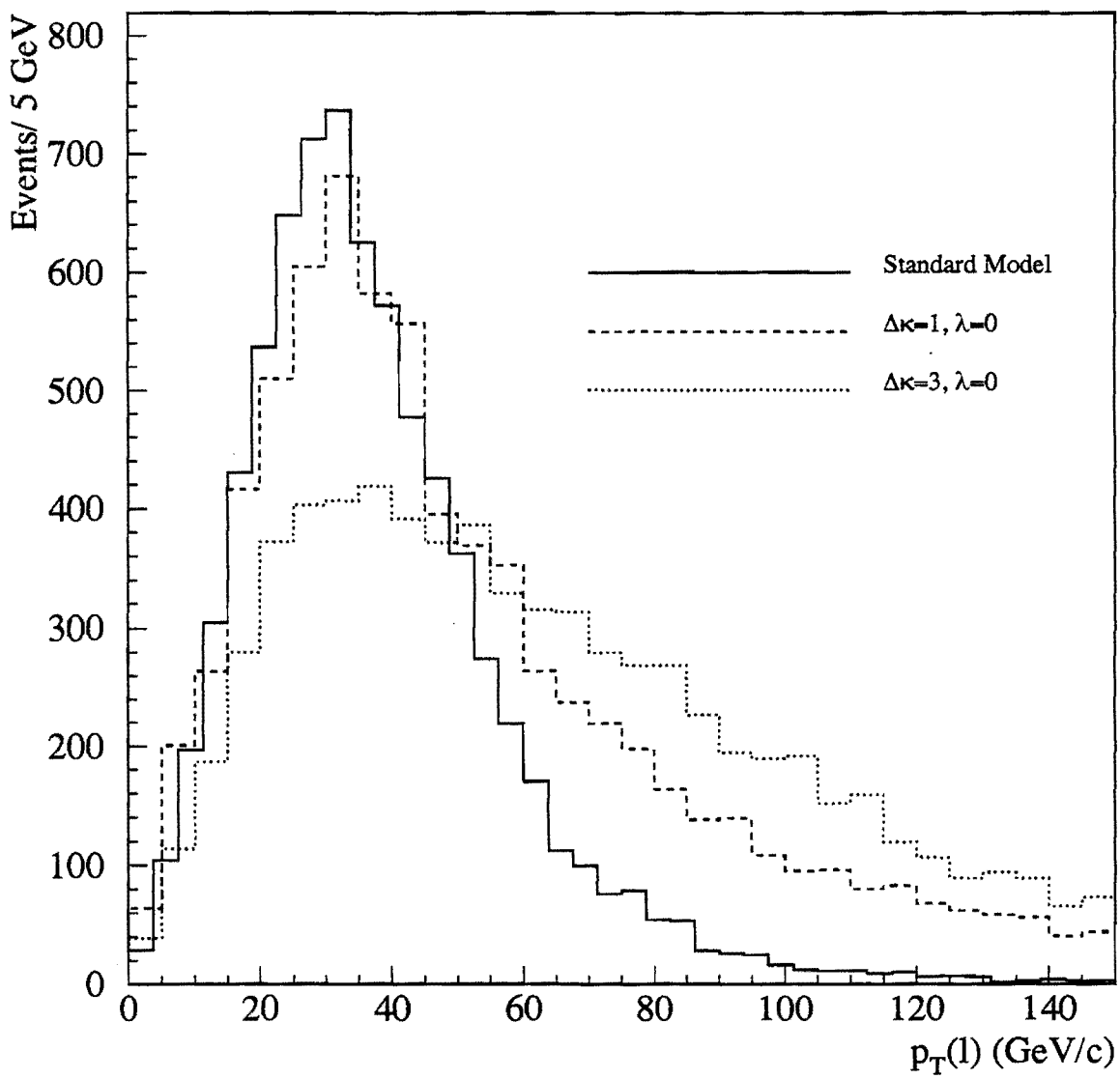


Figure 1.10: Final state lepton transverse momentum distribution for Standard and non-Standard Model Couplings.

## 1.5 Previous Experimental Results

Before proceeding, we pause to present a brief overview of anomalous coupling limits which have already been published. Measurements of the $WW\gamma$ coupling have been made at low energies using decays such as $b \to s\gamma$ [56] which involve the $WW\gamma$ vertex at the level of one loop diagrams (so called "penguins"). At higher energies, the $WW\gamma$ coupling has been measured directly via the $W\gamma$ final state. The first such measurement was performed by the UA2 experiment at CERN, which resulted in limits of [57]

$$-4.5 < \Delta\kappa_\gamma < 4.9\ (\lambda_\gamma = 0);\ -3.6 < \lambda_\gamma < 3.5\ (\Delta\kappa_\gamma = 0).$$

At the Tevatron, CDF reported limits derived from the analysis of their 1992-1993 Run 1a data set (approximately 20 $\text{pb}^{-1}$) of [58]

$$-2.3 < \Delta\kappa_\gamma < 2.2\ (\lambda_\gamma = 0);\ -0.7 < \lambda_\gamma < 0.7\ (\Delta\kappa_\gamma = 0),$$

while DØ has reported limits of [59]

$$-0.93 < \Delta\kappa_\gamma < 0.94\ (\lambda_\gamma = 0);\ -0.31 < \lambda_\gamma < 0.29\ (\Delta\kappa_\gamma = 0),$$

for their full Run 1 data set of approximately 93 $\text{pb}^{-1}$. The Tevatron results assume a form factor scale of 1.5 TeV.

Measurements of the $WW\gamma$ and $WWZ$ couplings have been made directly via the $WW$ and $WZ$ final states. At the Tevatron, CDF reported limits derived from

the simultaneous measurement of the $WW$ and $WZ$ final states in the $\ell\nu jj/\ell\bar{\ell}jj$ ($\ell = e, \mu$) channel of [60]

$$-1.11 < \Delta\kappa < 1.27; (\lambda = 0);\ -0.81 < \lambda < 0.84\ (\Delta\kappa = 0)$$

for the 20 pb$^{-1}$ data sample from run 1a and assuming a form factor scale of 1.0 TeV. In a similar analysis, DØ has reported limits of [61]

$$-.43 < \Delta\kappa < 0.59; (\lambda = 0);\ -0.33 < \lambda < 0.36\ (\Delta\kappa = 0)$$

from $e\nu jj$ final states for the 96 pb$^{-1}$ data sample from run 1 and assuming a form factor scale of 2.0 TeV. CDF has also published coupling limits derived from the measurement of the $WW$ final state in the $\ell\nu\ell'\nu'$ ($\ell, \ell' = e, \mu$) channel of [62]

$$-1.05 < \Delta\kappa < 1.30; (\lambda = 0);\ -0.90 < \lambda < 0.90\ (\Delta\kappa = 0)$$

for the 108 pb$^{-1}$ data sample from run 1, assuming a form factor scale of 1.0 TeV. DØ has reported limits from this channel of [63]

$$-2.6 < \Delta\kappa < 2.8;\ (\lambda = 0); -2.2 < \lambda < 2.2\ (\Delta\kappa = 0)$$

for the 14 pb$^{-1}$ data sample from run 1a, and assuming a 0.9 TeV form factor scale. Additional measurements of the $WW$ final state from the LEP II experiments will be forthcoming in the near future, but at the time of this writing have not yet been published.

The above results provide a framework in which to place this study of the $WWV$ couplings. The purpose of this analysis is to extend the parameter space

explored and to provide confirmation of results seen in other analysis channels. The work presented in the following chapters is an extension of an earlier DØ analysis on a smaller data sample, and seeks to offer improvement due to both the increase in data sample size as well as the techniques used to extract limits on anomalous couplings.

# Chapter 2

# Experimental Apparatus

The production of $W$ pairs requires a large center-of-mass energy, necessitating a colliding-beam experiment. The TeVatron accelerator at the Fermi National Accelerator Laboratory (Fermilab or FNAL), implements this condition via proton-antiproton ($p\bar{p}$) collisions at $\sqrt{s} = 1.8$ TeV. The detection of leptonic $W$ boson pairs requires a general purpose detector capable of identifying and measuring the energies and momenta of electrons, muons, and neutrinos. In this chapter, we describe the FNAL collider complex, tracing a proton's path from $H^+$ ion to collision. We then describe the DØ detector which collected the data used in this analysis. More detailed descriptions of the FNAL accelerators and operations can be found in [64]. The official reference for the DØ detector is [65], and is well complimented by [66].

## 2.1 The FNAL Collider Complex

A series of seven acceleration devices is used to create, store, accelerate and collide protons and antiprotons. Their layout is shown in figure 2.1. Such a system is required due to the fact that different acceleration techniques and device parameters are needed for the various energy regimes the particles must pass through on their way to a final energy of 0.9 TeV.

The proton beam begins with 18 keV $H^-$ ions from a plasma source, which are then accelerated to 750 keV by a Cockroft-Walton electrostatic accelerator. Such accelerator techniques are straightforward, but ultimately limited by the maximum electrode potential attainable before breakdown and arcing occur.

To reach higher energies, a series of potentials must be used to accelerate the particle. Typically this is provided by a radio-frequency (RF) cavity. By arranging the geometry such that the particles are shielded by a conductor while the field is in a de-accelerating configuration, and exposed to the field only at such times as when it is in an accelerating configuration, a net acceleration can be imparted to a charged particle. One such geometry is the *linear accelerator*, in which the conductors are a series of cylinders placed end to end. By coordinating the frequency of the accelerating field with the length of the conductors and gaps, one can ensure that the field is always accelerating the particles as they pass between the conductors. At Fermilab, ions from the Cockroft-Walton accelerator are passed to such a device

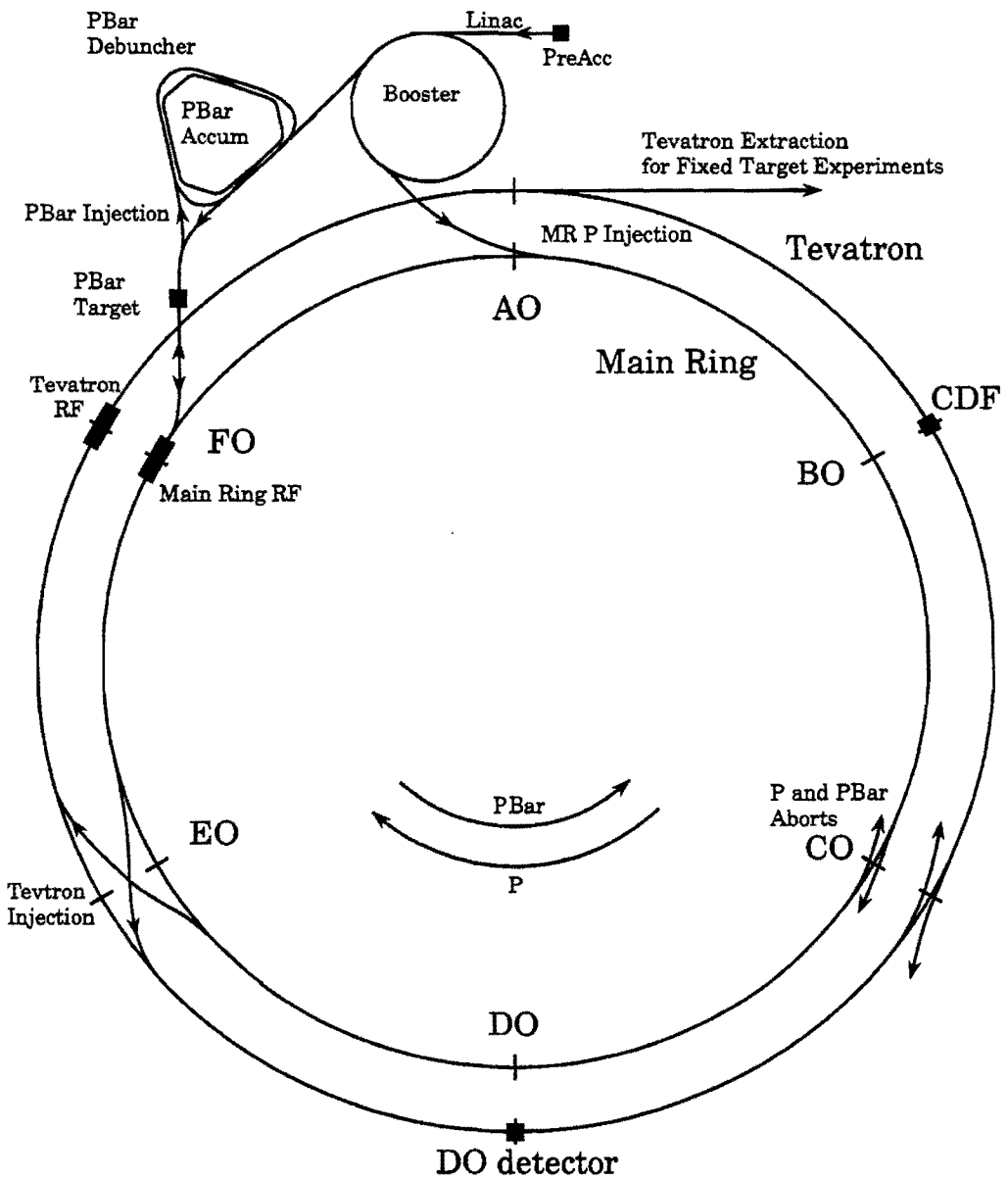


Figure 2.1: Schematic of the FNAL facility (not to scale).

(the Linac), which increases the beam energy to 400 MeV.

Because the energy range of a linear accelerator is limited by its length, a

second class of accelerator devices are employed for all subsequent stages of acceleration. By the skillful arrangement of magnets, it is possible to arrange the series of conductors and accelerating gaps in a circle. Such cyclic accelerators use the same accelerating cavity repetitively to raise the energy of the particles. The simplest and oldest of these configurations is the cyclotron. In such accelerators, the entire particle trajectory takes place in a single region of magnetic field. Inside this region are hollow D-shaped conductors which are separated by a single gap. An alternating field on the D's turns the gap into an accelerating region. The particles within travel in circular orbits, and are accelerated each time they traverse the gap. The frequency of the orbit is constant with particle energy (in the non-relativistic regime), but the radius increases. Because of this, the ultimate energy achievable by a cyclotron is limited to the size of the magnet.[1]

An alternate to the cyclotron is the synchrotron. In such a device, the particles are constrained to orbits of constant radius. This is done by increasing the magnetic field strength as the particles gain energy. The advantage of such a system is that the field need only be applied in the region of the particle orbits, allowing the construction of much larger accelerators capable of reaching much higher energies. Because there is a limit to the range of fields a set of magnets can achieve with accuracy, the dynamic range of a synchrotron is limited. Because of this, Fermilab

[1] Cyclotrons can and have been extended into relativistic energy regimes by various techniques such as shaping the magnetic field to vary with radius, and by varying the RF frequency used. The final limitation is invariably the size of the magnet.

uses three synchrotrons to accelerate particles from linac energies up to 0.9 TeV.

The first of the three synchrotrons is the Booster. This machine has a diameter of 150 m, and accelerates protons from the linac up to 8 GeV after the electrons are stripped from the $H^-$ ions. Next, protons pass to the Main Ring, a 1000 m machine which shares the tunnel with the TeVatron. The accelerator is capable of reaching energies of up to 400 GeV, but needs only accelerate protons and antiprotons to 150 GeV for injection into the TeVatron.

In addition to serving as the injector to the TeVatron, the Main Ring also provides a beam of 120 GeV protons for use in antiproton production. These protons are made to strike a nickel target which is optimized to produce antiprotons with an energy spectrum peaked at 8 GeV (the Main Ring injection energy). One antiproton is made for every $10^5$ protons incident on the target. As the antiprotons are produced, they have a spread in phase space which is determined by the dynamics of the p-Ni collisions. In order to achieve efficient transfer to the Main Ring, the beam must first be 'cooled'. This process takes place in two stages. First, in the Debuncher, the burst of antiprotons are spread into a continuous beam (the antiprotons are produced in pulses which correspond to the RF structure of the Main Ring). This process also serves to lower the momentum spread of the antiprotons. The Debuncher also begins the process of *stochastic cooling*, in which deviations from ideal synchrotron orbits are measured and correction signals applied. Antiprotons can reside in the Debuncher for up to 2.4 s, after which time another batch of

antiprotons arrives from the target. In the second stage, the Accumulator continues the cooling process. This storage ring is designed for long-term storage or *stacking* of antiprotons. As each batch of antiprotons is removed from the Debuncher, it is slowly merged with the previously produced antiprotons in the Accumulator, and the cooling process continues. Once the antiproton stack is large enough, it is transfered into the Main Ring for injection into the TeVatron.

The stacking of antiprotons can be made to take place during TeVatron collisions so that antiprotons are always ready for the next injection cycle. Because of this however, the Main Ring must be in operation while collisions are taking place. This will turn out to have a non-trivial effect on data taking for the DØ detector.

The TeVatron accepts bunches from the Main Ring, and uses superconducting magnets to confine them while accelerating the proton and antiproton beams to 0.9 TeV, providing a center-of-mass collision energy of 1.8 TeV. Table 2.1 lists some important parameters of the TeVatron accelerator. For collider operations, six bunches each of protons and antiprotons counter circulate in the machine. For most of the orbit, they are kept apart by electrostatic separators, but at the BØ (CDF) and DØ regions, special magnets (low beta quadrupoles) reduce the transverse beam sizes to about $50\mu$m, providing high-luminosity collisions.[2] The peak instantaneous luminosity reached in run 1 was $\approx 3 \times 10^{31}$ cm$^{-2}$s$^{-1}$.

[2]More precisely, the low beta quads reduce the $\beta^*$ - the local wavelength of the betatron oscillations about the ideal orbit - at the interaction region. A $\beta^*$ of $\approx$ 25 cm is achieved.

| | |
|---|---|
| Radius | 1000 m |
| Number of dipole magnets | 744 |
| Number of quadrupole magnets | 216 |
| Number of proton bunches | 6 |
| Number of protons/bunch | $\approx 2 \times 10^{11}$ |
| Number of antiproton bunches | 6 |
| Number pf antiprotons/bunch | $\approx 7 \times 10^{10}$ |
| Center-of-mass energy ($\sqrt{s}$) | 1.8 TeV |
| Maximum number $p\bar{p}$ collisions/second | $\approx 10^6$ |
| Maximum instantaneous luminosity | $\approx 3.0 \times 10^{31}$ cm$^{-2}$s$^{-1}$ |

Table 2.1: Selected TeVatron parameters

## 2.2 The DØ Detector

As previously discussed, the purely leptonic $W$ pair final states under study in this analysis contain electrons, muons and neutrinos. The DØ detector was designed to identify and measure the energies and momenta off all these objects. As shown in Figure 2.2, the detector consists of three major subsystems: the central tracker, calorimeter, and muon spectrometer. The design of the detector was optimized to perform high-resolution, hermetic calorimetry as the sole measurement of electromagnetic and hadronic energies. As a consequence, the central tracking volume is small, and there is no magnetic field in the tracking region.

The coordinate system used in discussing the position of objects within the detector is a right-handed system with origin at the center of the detector, positive $z$ axis along the beamline in the direction of proton travel, and positive $y$ in the upward

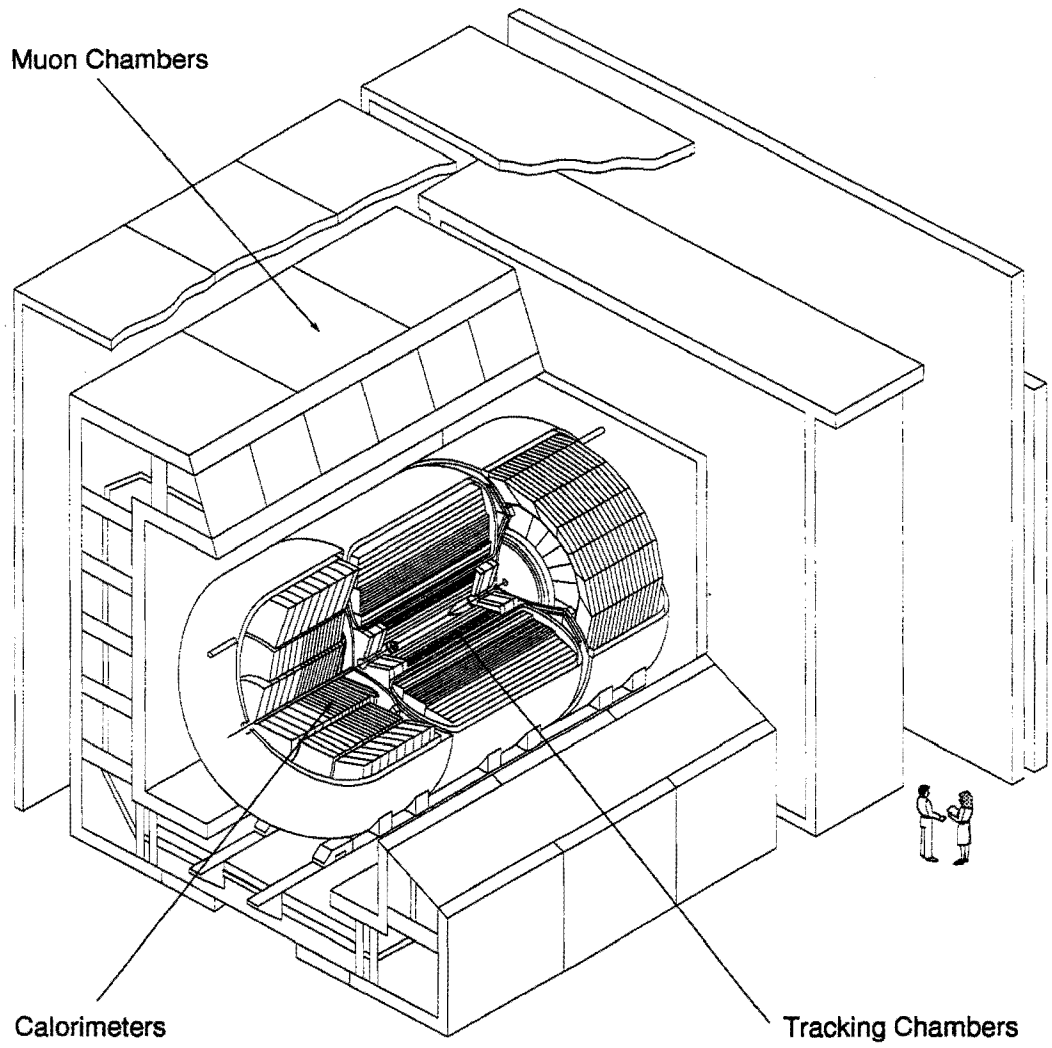


Figure 2.2: Isometric cutaway view of the DØ detector.

direction. Because the detector exhibits approximate cylindrical symmetry, it is also convenient to use coordinates $r$ - the distance from the beamline, $\phi$ - the azimuthal angle with respect to the positive $x$ axis, and $\theta$ - the polar angle with respect to the positive $z$ axis. The polar direction may also be described by the *pseudorapidity*,

define as $\eta = -ln[tan(\frac{\theta}{2})]$. In the limit of $E >> m$, the pseudorapidity approaches the true rapidity of the particle

$$y \approx \frac{1}{2} ln(\frac{E + p_z}{E - p_z}).$$

The polar angle of a particle may then be expressed in terms of the "detector pseudorapidity", denoted $\eta_{det}$, which is computed with respect to $z = 0$. However, since the interaction point has a typical spread of $\sigma_z \approx 30$ cm, $\eta$ and $\eta_{det}$ tend in general to differ slightly for a given particle.

### 2.2.1 Central Detector

The systems of the central detector were designed to non-destructively measure the trajectories of charged particles, and to aid in the identification of electrons. The central detector consists of a vertex drift chamber (VTX), a transition radiation detector (TRD), a set of central (CDC) and forward (FDC) drift chambers, and the forward level-Ø counters. For efficiency reasons, the TRD subdetector is not used in this analysis, and is not discussed here. The level-Ø detector is discussed in 2.2.4.

#### The Basics of Drift Chamber Operation

Drift chambers are designed to detect the ionization liberated by a charged particle passing through a gas-filled region. The total number of ionizations produced (so called *primary ionization electrons*) is given by $n = \frac{\Delta E}{W_i}$, where $\Delta E$ is

the total energy lost by the particle, and $W_i$ is the ionization potential of the gas. Typical values for $n$ range from 10 - 100 per cm of gas traversed.

If there is an electric field across the gas region, these free electrons drift toward the anode. The energy gained by the electrons drifting in the field quickly comes into equilibrium with the losses due to atomic collisions, and the drift velocity becomes a constant[3]. While the drifting electrons will eventually reach the anode, their number is too small to produce an observable signal. If the anode is a thin (typically a few 10's of $\mu$m) wire however, the electric field near the wire is very large. If the field is large enough ($10^4 - 10^5$ V/cm), the energy gained by the electrons between atomic collisions exceeds the ionization potential of the gas, and additional electrons can be liberated. These new electrons will do the same, creating an avalanche of secondaries. The number of such ionizations is typically between $10^4 - 10^6$ times the number of primary electrons. This ratio is called the "gas gain", and is sufficient to produce an observable signal. It is important to note that while the electron avalanche initiates the signal, they are produced so close to the anode that there is little change in the energy of the system as the electrons drift the final distance to the wire. Therefore, the bulk of the signal that is measure is created by the drift of the residual ions towards the cathodes. Because these ions are heavy, and hence slow moving, the time development of the signal results almost entirely

[3]One should note that while the average drift velocity of a cluster of electrons is constant, the velocities of individual electrons will vary due to statistical fluctuations inherent in the collision process. This results in diffusion in the spatial extent of the cluster, and represents a lower bound on the resolution attainable in such devices

from the motion of the ions.

Generally, the gas gain increases with increasing electrical field. For moderate fields, the gain is independent of the number of primary electrons, so the signal is directly proportional to this number (hence this is known as the *proportional* regime). Since $n$ is proportional to the energy lost by the ionizing particle, such a detector enables one to measure $dE/dx$ and hence aid in particle identification. If the field is further increased, the cloud of slow moving positive ions surrounding the anode acts as an increasingly large coulomb screen for additional secondary electrons. This screening results is a gradual loss of proportionality, and culminates in the transition to the so called "saturation" mode of operation. In this mode, the signal size is independent of the amount of primary ionization. While allowing the largest possible signal, no measurement of $dE/dx$ can be made.

While the above holds for all types of ionization counters, one can also make a measurement of the signal timing to measure the distance from the anode to the ionizing particle. This is the unique feature of a drift chamber. If the chamber is constructed so that the electric field is uniform across most of the chamber (not very near the anode, however), then the relation of the drift time to distance is given by

$$z = v_d(t_1 - t_0).$$

To ensure this condition, relatively thick field-shaping wires are placed between the anode wires.

The choice of the gas used in a drift chamber is subject to several constraints. Nobel gases are typically favored; first, because ionization is the only means by which energy can be dissipated, the avalanche condition occurs at lower field strengths than for other gases. Second, there is no chance that a nobel gas will attach to a drifting primary ionization electron and thereby attenuate the signal. Argon is the typical choice of gas. A drawback to argon is that photons emitted by de-exciting atoms are energetic enough to liberate electrons from the metal cathodes (positive ions striking the cathode may also do this). These electrons create their own avalanches, and at relatively low fields, the cycle becomes self perpetuating. To use argon while allowing the use of higher strength fields (and hence more gas gain), small admixtures of polyatomic gases may be added to the argon. These gases, known as "quenchers", have many degrees of freedom and are excellent absorbers of the de-excitation photons. These gases can absorb the photons without liberating additional electrons and interrupt the chain reaction. The drawback to adding such a molecule is that it can break up into simpler molecules which can then polymerize on the anode and cathode surfaces and degrade the chamber performance. A third component is often added to the gas mixture to slow such polymerization and increase the useful lifetime of the chamber.

Finally, readout of such chambers is generally performed by differentiating the signal. The time development of the signal generated by the ions is such that most of the signal develops quickly, mostly in the first $\mu$s or so of the drift. If the

differentiating circuit has a short time constant, a sharp pulse is produced. For additional details on drift chamber principles, see [67]

### Vertex Drift Chamber (VTX)

The component of the detector closest to the interaction region is the Vertex Drift Chamber (VTX). This device is composed of three cylindrical layers of drift chambers covering the region $|z| < 116$ cm and 3.7 cm $< r <$ 16.2 cm. This corresponds to a coverage in pseudorapidity of $|\eta| < 1.0$. The need to detect and resolve tracks this close to the interaction region placed strict demands on the resolution of the chamber. This required a gas with a low electron diffusion constant and a slow drift velocity. For the VTX, a mixture of $CO_2$ (95%) and ethane (5%) was chosen, along with a small admixture of water as a cleansing agent. In order to achieve the required low diffusion constants, the chamber is operated in a voltage regime such that the electron drift velocity is proportional to the drift field. This condition placed stringent requirements on the design of the field shaping components of the detector. As implemented, the drift velocity was 7.3$\mu$m/ns.

A quadrant of the VTX is shown in Figure 2.3. The inner layer is divided into 16 azimuthal readout cells, while the outer two layers have 32 such cells. Each cell contains eight 25$\mu$m diameter NiCoTin sense wires running axially along the beamline to provide $r - \phi$ measurement. These wires are surrounded by various gold plated aluminum field shaping wires. The sense wires have a resistance of

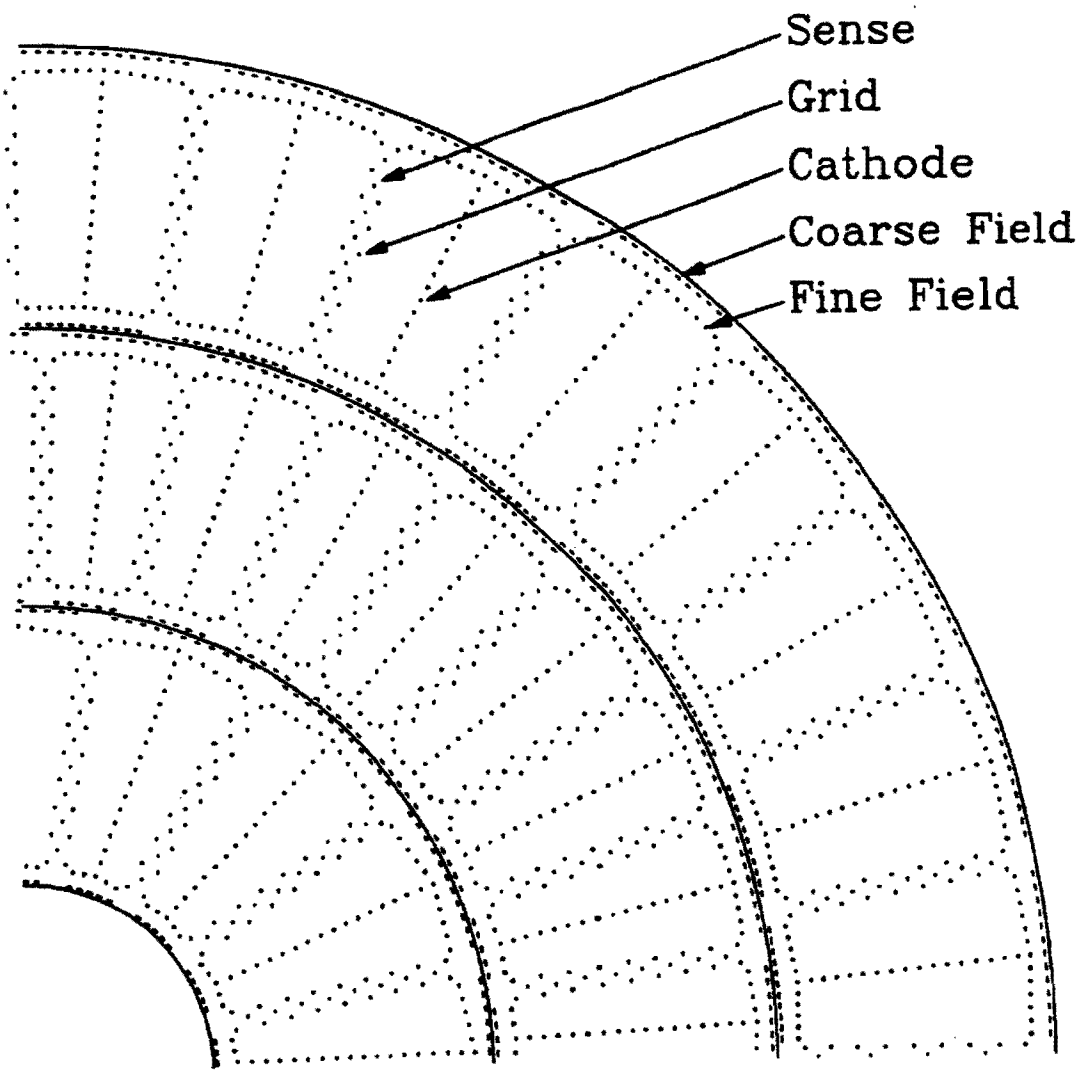


Figure 2.3: End view of one quadrant of the VTX chamber.

1.8 k$\Omega$/m, allowing the measurement of $z$ position by reading out both ends of the sense wire. Test results achieved a resolution of 1% of the wire length. The electric field is such that the drift direction is azimuthal. The drift timing allows the determination of the distance from the primary ionization site to the sense

wire, but carries no information about what side of the wire it was on. The left-right ambiguity was resolved by staggering adjacent sense wires by $\pm 100\mu$m. In test beam data demonstrated an $r - \phi$ resolution which varies between $30 - 60\mu$m, depending on the drift distance, with typical resolutions around $40\mu$m.

Additional information on the VTX can be found in Table 2.2.

| | |
|---|---|
| Maximum length | 116.8 cm |
| Radial position | $3.7 - 16.2$ cm |
| Radial wire spacing | 4.57 mm |
| Maximum drift distance | 16 mm |
| Sense wires per cell | 8 |
| Gas mixture | 95% $CO_2$ + 5% ethane + 0.5% $H_2O$ |
| Gas pressure | 1 atmosphere |
| Drift field | 2.3 kV/cm |
| Sense wire potential | +2.5 kV |
| Gas gain | $4 \times 10^4$ |

Table 2.2: Selected parameters of the Vertex Drift Chamber

### Central Drift Chamber (CDC)

The Central Drift Chamber (CDC) lies radially outside the VTX and the TRD. It consists of four concentric cylinders, covering a range of $|z| < 89.7$ cm and 51.8 cm $< r <$ 71.9 cm. This corresponds to a coverage in pseudorapidity of $|\eta| < 1.2$. The gas used was a combination of argon, methane, carbon dioxide and water. The layout of the CDC is shown in Figure 2.4. Each layer consists of 32

identical azimuthal cells containing seven 30$\mu$m gold plated tungsten sense wires and two delay lines, all running parallel to the beam direction. Adjacent sense wires are staggered by $\pm 200\mu$m to resolve the left-right ambiguity. There are two field wires associated with each anode wire to produce a uniform field across each cell, with a drift field of about 620 V/cm. As in the case of the VTX, the cathode voltage must be increased with radius to maintain a uniform drift field. To accomplish this, resistive strips are printed on the cathode surfaces, allowing the voltage to vary with position.

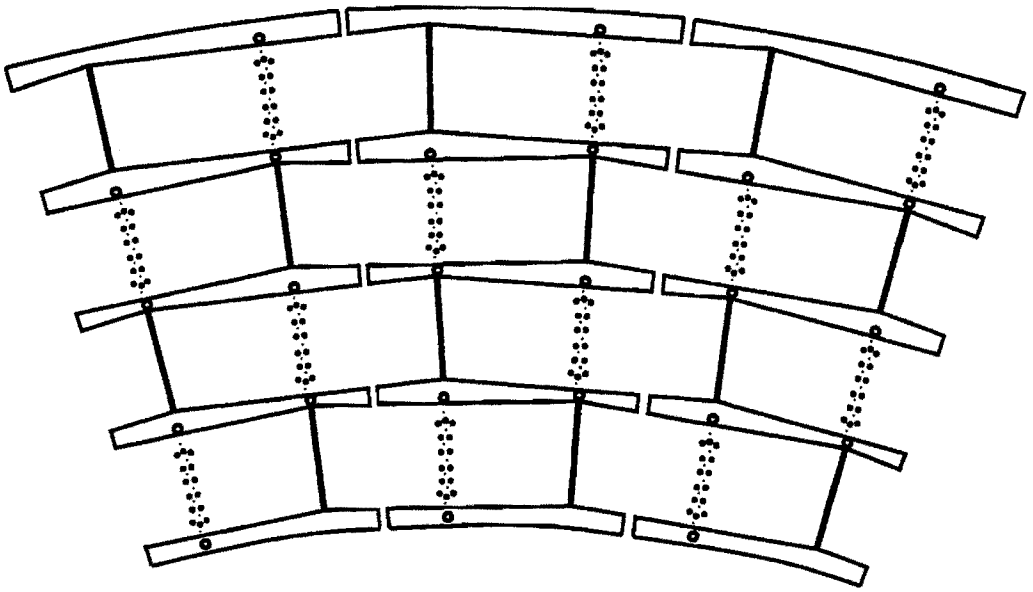

Figure 2.4: End view of three CDC modules. Sense wires are indicated by small dots, guard (field shape) wires by large dots, and delay lines by open circles.

The $r - \phi$ resolution for a single wire varies with drift distance, but is in the

range of $150 - 200\mu$m. The Measurement of the $z$ coordinate is accomplished by measuring the the signal induced on the delay lines by avalanches on nearby anodes. Signals propagate along these lines at $2.4\mu$m/ns, so readying out the delay line at both ends allows a $z$ measurement with a measured resolution of about 4 mm.

For further details on the CDC, see Table 2.3.

| | |
|---|---|
| Maximum length | 179.4 cm |
| Radial position | $51.8 - 71.9$ cm |
| Radial wire spacing | 6 mm |
| Maximum drift distance | 7 cm |
| Sense wires per cell | 7 |
| Gas mixture | 92.5% argon + 4% methane + 3% $CO_2$ + 0.5% $H_2O$ |
| Gas pressure | 1 atmosphere |
| Drift field | 650 V/cm |
| Sense wire potential | +1.5 kV |
| Gas gain | $2 \times 10^4$ (inner sense wires) |
| | $6 \times 10^4$ (outer sense wires) |

Table 2.3: Selected parameters of the Central Drift Chamber

### Forward Drift Chambers (FDC)

The Forward Drift Chamber (FDC) consists of two sets of drift chambers located at the ends of the CDC. These chambers are installed at each end of the cylinder defined by the VTX and CDC. This device provides tracking coverage in the forward region in the pseudorapidities range of $1.4 < |\eta| < 3.1$. The construction

and operation of these chambers are similar to those of the CDC, with the FDC using 163$\mu$m field wires. The gas mixture used is identical.

Each set of FDCs is composed of three chambers: one $\Phi$ chamber between two $\Theta$ chambers. The $\Phi$ module is divided into 36 azimuthal segments, each having 16 layers in $z$ of sense wires. A single grounded field wire between each pair of sense wires and aluminum cathode traces etched onto the cell wall provide the field shaping elements for the cell. As the name suggests, the $\Phi$ chambers provide a measurement of $\phi$. The $\Theta$ Modules are divided into quadrants, and each quadrant into six box shaped cells. These cells contain eight azimuthal sense wires along the $z$ direction, so the drift direction is approximately along $\theta$. Cells in the $\Theta$ modules also contain one delay line similar to those used in the CDC to provide a redundant $\phi$ measurement. To reduce ambiguities, the two $\Theta$ modules are rotated in $\phi$ by 45° to each other. See Figure 2.5 for details on the positioning of the chambers and signal wire directions.

The performance of the FDC is very similar to the CDC. Single-hit resolutions are about 200$\mu$m in the direction measured by the drift time. The delay lines in the $\Theta$ modules have a resolution of about 4 mm. The two track resolution efficiency for a 2 mm separation is about 90%.

Further details of the $\Phi$ and $\Theta$ chambers are given in Tables 2.4 and 2.5.

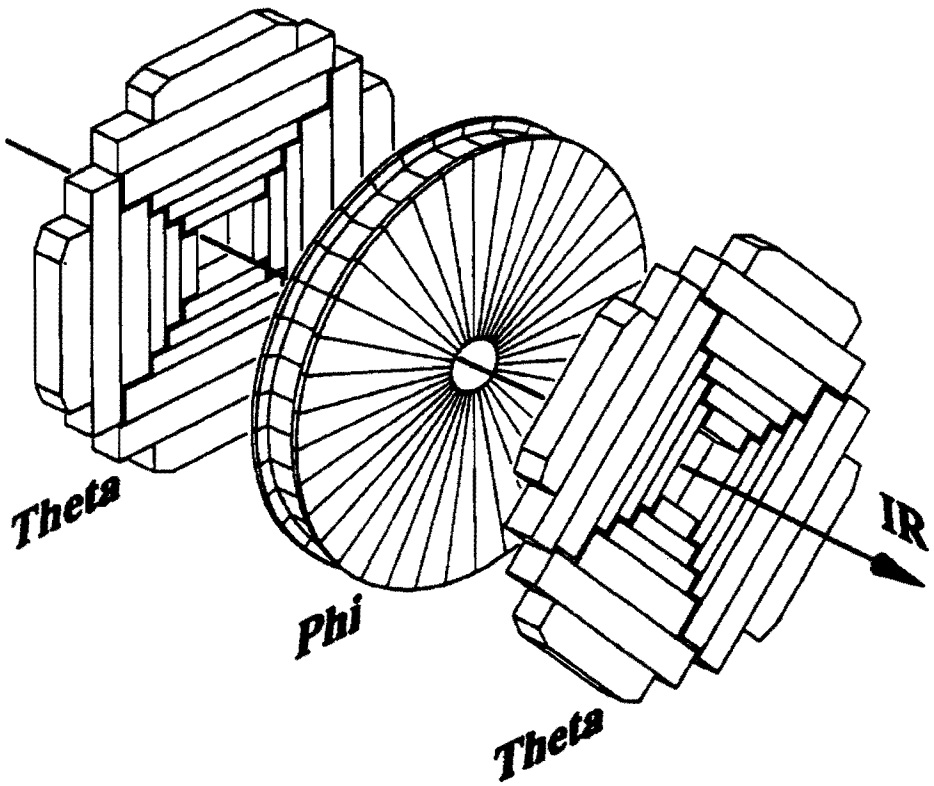


Figure 2.5: Exploded isometric view of one half of the FDC tracking system.

| | |
|---|---|
| $z$ position | 113.0 – 127.0 cm |
| Radial position | 11.0 – 61.3 cm |
| $z$ wire spacing | 8 mm |
| Maximum drift distance | 5.3 cm |
| Sense wires per cell | 16 |
| Gas mixture | 92.5% argon + 4% methane + 3% $CO_2$ + 0.5% $H_2O$ |
| Gas pressure | 1 atmosphere |
| Drift field | 1.0 kV/cm |
| Sense wire potential | +1.5 kV |

Table 2.4: Selected parameters for FDC $\Phi$ modules

| | |
|---|---|
| $z$ position | 104.8 – 111.2 cm and 128.8 – 135.2 cm |
| Radial position | 11.0 – 61.3 cm |
| $z$ wire spacing | 8 mm |
| Maximum drift distance | 5.3 cm |
| Sense wires per cell | 8 |
| Gas mixture | 92.5% argon + 4% methane + 3% $CO_2$ + 0.5% $H_2O$ |
| Gas pressure | 1 atmosphere |
| Drift field | 1.0 kV/cm |
| Sense wire potential | +1.5 kV |

Table 2.5: Selected parameters for FDC $\Theta$ modules

### Detector Readout

All the subsystems of the central detector employ similar readout electronics. The first stage of the readout is performed by surface mounted preamplifiers on the various detectors. These amplifiers also serve to inject test charges onto the sense wires to calibrate the readout chain. Signals from the preamps are carried on about 15 m of coaxial cable to the platform beneath the detector where shaper circuits remove long tails in the signal due to ion drift. The resulting pulse are more symmetric about their peaks, and are optimized for resolving double hits.

After shaping, the signals are carried 45 m to the movable counting house for digitization. This is accomplished using flash analog to digital converters (FADCs), which have an 8-bit dynamic range and operate at 106 MHz. This speed is necessary to allow two hit separation down to small distances. For $dE/dx$ measurement, one desires as large as possible dynamic range. To accomplish this, signals enter an

analog buffer before the FADC which applies an adjustable gain correction to the signal such that small signals are amplified by a factor of 8.5 or less than large signals. This effectively increases the dynamic range of the digitization circuitry to 9.5 bits.

A total of 6080 channels are instrumented for the entire central detector. An attempt to read out every digitization cycle for every channel would result in data rates in excess of 325 Mbytes/s, which would overwhelm the data acquisition system. To reduce this number, zero suppression circuitry is installed after the FADCs. These circuits compare the signal size for each cycle and the difference between adjacent cycles to programmed thresholds. This defines the leading and trailing edges of a signal, with only those cycles lying between the edges being retained for further processing.

### 2.2.2 Calorimeter

The DØ detector was designed to achieve good resolution on the energies of electrons, photons and jets. Since there is no central magnetic spectrometer, this measurement must be provided solely by the calorimetry.

In a calorimeter, incident particles are stopped, and their energy dissipated for measurement. Electrons and Photons interact with material in a substantially different way than do hadrons. Thus the types of calorimetry best suited to measure

their energies are different. DØ accomplishes these two functions in separate modules. The following discussions describe these types of calorimeters in general as well as their implementation at DØ. For further information on calorimetry, see [67, 68]

### Electromagnetic Calorimeter

The calorimeter layers closest to the interaction point are called the electromagnetic (EM) calorimeter because they are optimized for electron and photon measurement. The principal behind this device is that electrons (photons) with energy great than $\approx$ 10 MeV dissipate their energy predominantly through the emission of bremsstrahlung photons. For example, an electron with an energy of several GeV will radiate an energetic photon which in turn will produce an electron-positron pair and so forth, creating a shower of secondary electrons and photons (the process is identical for photons except that the initial step in the shower is the pair production). The parameter used to describe the development of this shower is the "radiation length" $X_0$, which is define by

$$< \frac{dE}{dx} >_{brem} = \frac{E}{X_0}.$$

The critical energy at which the energy loss by ionization is on average equal to that by bremsstrahlung is approximately given by

$$\epsilon_c \approx \frac{580}{Z}(MeV).$$

The mean total track length of ionizing secondaries is an electromagnetic shower is

given by

$$T_d \approx (\frac{4}{3}X_0 + \frac{2}{3}s_0)\frac{E}{\epsilon_c},$$

where $s_0$ is the range of electrons which have the critical energy. This proportionality between $E$ and $T_d$ allows measurement of the total ionization to give a measurement of the incident particle energy.

An EM shower reaches it's maximum multiplicity at a distance of

$$\approx (ln(\frac{E}{\epsilon_c}) - 1)X_0$$

in the calorimeter (for a 100 GeV electron in uranium, this corresponds to about 10 $X_0$), so it is apparent that the amount of material needed scales as the natural log of the incident particle energy. The transverse spread of the shower is determined by the typical angle of bremsstrahlung emission and multiple scattering. This is parameterized in term of the "Moliére radius" $\rho_M \approx 21X_0/\epsilon_c$. About 90% of the shower energy is contained in a cylinder of radius $2\rho_M$.

The accuracy with which a calorimeter can measure a particle's energy is limited by the measurement of the total track length. Ideally, one would use the same material to initiate the shower and to measure the ionization such that the entire track is visible. To allow for a more compact calorimetric volume, it is possible to divide the calorimeter into alternating layers of dense (absorber) and light (sampler) materials. Such a system is called a "sampling calorimeter", since only the part of the ionization which occurs in the sampling layers is measured. The limit on

the resolution for such a scheme is determined by the statistical fluctuations in the amount of ionization occurring in the sampling layers. As such, the fractional uncertainty in the energy measurement will scale as one over the square root of the number of ionizing tracks, or equivalently, $E^{-\frac{1}{2}}$.

At DØ, the absorbing material used is uranium, while the sampling medium used is liquid argon. Some important properties of uranium are shown in Table 2.6. The motivation for this choice of absorber will be discussed later. Liquid argon was chosen as the sampling material because it allows uniform gain over the entire calorimeter, is relatively simple to calibrate, allows flexibility in the segmentation of the readout cells, and is not susceptible to radiation damage. The need to operate at cryogenic temperatures and hence seal the modules inside the cryostat, did impose constraints on design of the detector. To facilitate construction and allow access to the central tracker, the DØ calorimeter modules are divided into three separate cryostats; the central calorimeter (CC) surrounded by two end calorimeters (EC), as shown in Figure 2.2. The CC provides coverage for $|\eta| < 1.1$ and the EC extends the coverage to $|\eta| < 4$, providing the hermeticity needed for good total transverse energy resolution. As will be discussed later, the uninstrumented material between the CC and EC modules means that this region requires special attention.

The layers of the calorimeter closest to the interaction region are optimized for the measurement of electromagnetic showers. The absorbers in these modules are thin (3 and 4 mm in the CC and EC respectively) plates of pure depleted uranium.

| | |
|---|---|
| Density | 18.95 g/cm$^3$ |
| Radiation length ($X_0$) | 6.00 g/cm$^2$ |
| Nuclear interaction length ($\lambda$) | 199 g/cm$^2$ |
| Moliére radius ($\rho_M$) | $\approx$ 1.1 cm |

Table 2.6: Selected properties of uranium

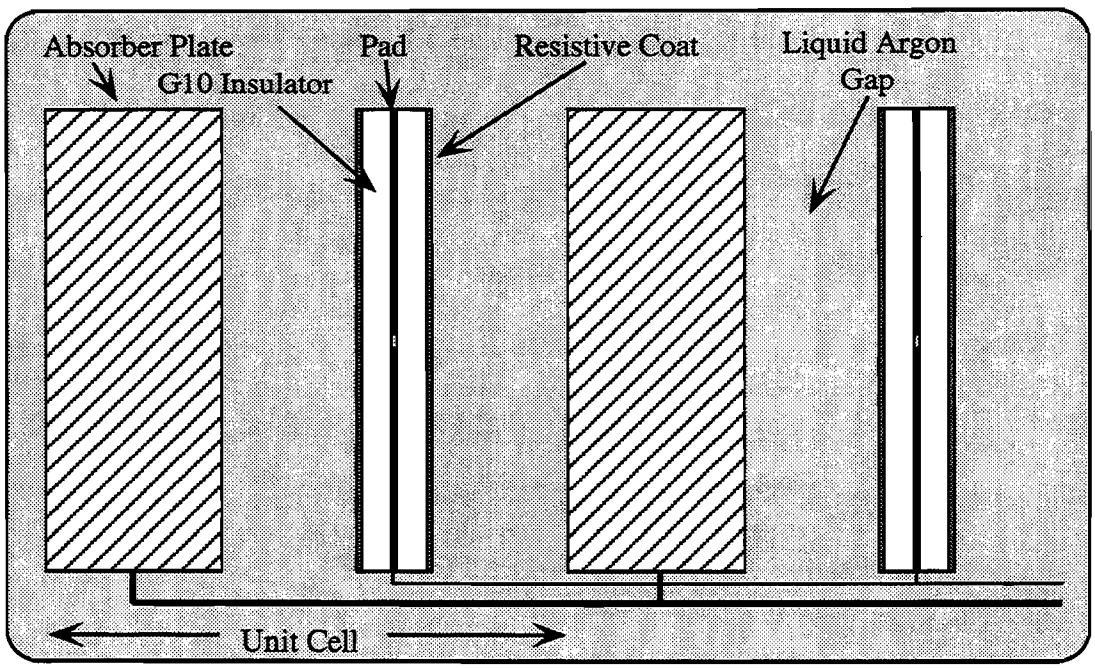


Figure 2.6: Structure of a calorimeter readout cell.

In the space between the adjacent plates there is a single board surrounded by two 2.3 mm liquid argon gaps to form a sampling cell (see Figure 2.6). The signal board is a multilayer printed circuit board, the outer surfaces of which have a resistive epoxy coating, and are connected to positive high voltage. The absorber plates

are held at ground, creating a drift field across the liquid argon gap. Signals are collected on the copper readout pads in the middle layer of the signal boards. The transverse segmentation of the signals is defined by the size of these pads.

Signals from several sampling cells at the same $\eta$ and $\phi$ are ganged together in depth to form one layer for readout. The EM calorimeter is divided into four such layers. In radiation lengths, these cells are 2, 2, 7, and 10 in the CC, and 0.3, 2, 7, and 10 in the EC. The difference in the first EC layer is to account for the additional material which lies in front of the EC modules. The transverse segmentation is $\approx 0.1 \times 0.1$ in $\Delta\eta \times \Delta\phi$ for layers 1, 2 and 4, and is $0.05 \times 0.05$ in the third layer ($0.1 \times 0.1$ for $|\eta| > 2.5$) to allow more accurate measurement of the shower at its maximum, which is important for electron and photon identification.

Signals from various layers are grouped into "pseudo-projective" towers, meaning that the center cells in each layer line up with the nominal interaction point, while their edges are perpendicular to the absorber plane. Details of the segmentation and tower structure can be seen in Figure 2.7. Of importance is the fact that the CCEM was constructed of 32 azimuthal modules, each containing two EM towers. This results in a small uninstrumented crack between each of these modules in which the measurement of showers is likely to be distorted.

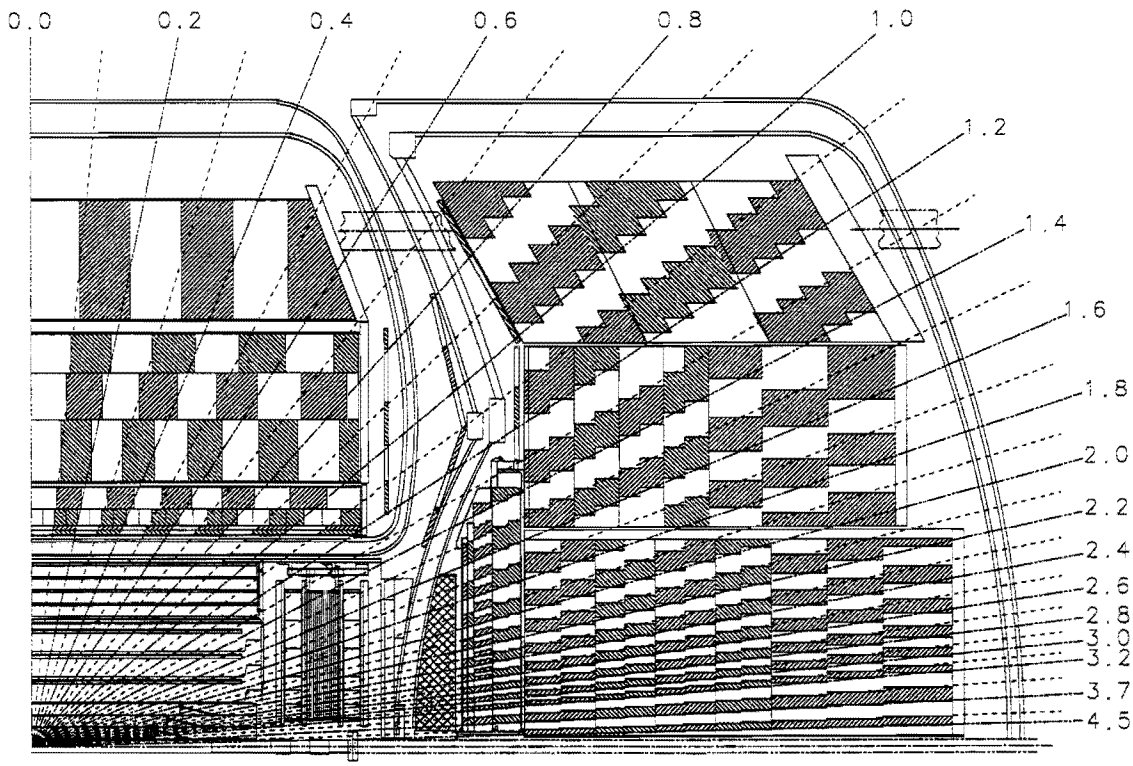


Figure 2.7: Side view of one quadrant of the calorimeter and central detector. The lines of constant pseudorapidity intervals are with respect to $z = 0$.

### Hadronic Calorimeter

The principles of hadronic calorimetry are similar to those of electromagnetic calorimetry. The incident particle collides inelastically with a nucleus in the absorber medium, producing secondary hadrons which repeat the process and form a shower. Because the number and types of processes are far more numerous and complex than in the electromagnetic case, an analytic description is difficult. We can, however, outline some general features.

The appropriate scale for nuclear processes is the nuclear interaction length

$\lambda$, define as

$$\lambda = \frac{A}{\sigma_i N_0 \rho},$$

where $\sigma_i$ is then inelastic nuclear cross section, $N_0$ is Avagadro's number, and $\rho$ is the density of the absorber. The average shower maximum scales as the incident of the particle energy, occurring at $\approx (0.2ln(E) + 0.7)\lambda$ where $E$ is in GeV. For a 100 GeV hadron, this turns out to be about $1.6\lambda$. At a depth of just more than $2.5\lambda$ beyond shower max, 95% of the energy is contained. Typically, the transverse spread of the shower is significantly broader than for the electromagnetic case, with a cylinder radius of about $1\lambda$ required to contain 95% of the energy.

The limit on the energy resolution for a hadronic calorimeter comes form the fluctuations in the shower composition, particularly in the fraction of $\pi^0$'s and $\eta^0$'s produced in the first interaction. Since these particles quickly decay to two photons, they will produce an electromagnetic shower within the hadronic shower, most of the energy of which can be measured. If on the other hand, the interactions produce neutrinos and muons, these will carry away energy which is unlikely to be detected. So typically, the response of a calorimeter to to hadrons is less than for electrons of the same energy. The difference, the "$e/\pi$ ratio", can be corrected for on average, but a ratio that differs from unity will result in variations on a shower by shower basis, depending on the electromagnetic content. An advantage of using uranium as an absorber is that secondary neutrons can cause fission in the uranium nuclei, which produces some detectable energy. This results in an $e/\pi$ ratio that is closer to

unity than is attainable with any other absorber by roughly a factor of two. Because this lower limit tends to be larger than the contributions from sampling statistics and incomplete shower containment, the resolution obtained is close to the above limit.

At DØ, the layers of the calorimeter outside the EM layers form the hadronic calorimeter. In the CC, there are two types of modules: fine hadronic (FH), which lie immediately behind the EM layers and have 6 mm uranium-niobium alloy absorbers, and course hadronic (CH), which have 46.5 mm copper absorbers. The transverse segmentation in all the hadronic modules is $0.1 \times 0.1$. The FH modules are divided into three readout layers (1.3, 1.0, 0.9 $\lambda$ deep) which provide detailed information about shower shape, while the CH modules are treated as a single $3.2\lambda$ deep layer which provides shower containment. In the EC, a greater variety of geometries is required, but the functionality is the same as in the CC. See Figure 2.7 for further details of the segmentation. The total material in the calorimeter ranges from $7.2\lambda$ at $\eta = 0$ to $10.3\lambda$ at the forward most extent of the EC.

### ICD and Massless Gaps

Any particle which crosses the boundary between the CC and EC encounters a substantial amount of material in the cryostat walls. In order to have some sampling in this region, the "massless gaps" and "intercryostat detector" (ICD) were constructed. The massless gaps have the same structure as a typical readout

cell, with the cryostat walls acting as the absorbing plates. These detectors are installed in both the CC and EC as shown in Figure 2.7. ICDs are mounted on the inner surface of the EC and consist of 384 scintillator tiles, each segmented into $0.1 \times 0.1$ cells, and aligned with the towers define by the calorimeter layers. The ICDs are the only calorimeter component in DØ that do not use liquid argon as the sampling medium.

### Calorimeter Readout and Performance

The subdivision of the 5000 towers in the calorimeter into layers brings the number of readout channels to $\approx 47000$. The signals are first processed by preamplifiers, and then sent to base-line subtracter (BLS) circuits on the detector platform. These circuits sample the integrated charge just before and $2.2\mu$s after the beam crossing, and define the signal as the difference. The signal from the BLS is then amplified by 1 or 8 depending on the size, which allows a 15-bit dynamic range using 12-bit ADC's in the movable counting house. To reduce bandwidth, zero-suppression is applied to remove cells which contain no appreciable energy deposition.

In test beam conditions [65], the response to both electrons and pions as a function of energy was found to be good to within 0.5% in the energy range of $10 - 150$ GeV. The measured resolutions can be approximated by:

$$\frac{\sigma(E)}{E} \approx \frac{16\%}{\sqrt{E}} \text{ for electrons}$$

$$\frac{\sigma(E)}{E} \approx \frac{41\%}{\sqrt{E}} \text{ for pions.}$$

These approximations show the expected behavior with $E$ due to the statistical nature of the processes, but ignores the constant terms which would appear from taking into account noise and calibration uncertainties. It should be noted that the resolution for a single hadron is much better than that for a jet which is made of may hadrons.

Because of its importance to particle identification, the position resolution of the EM calorimeter was also measured. This resolution is important due to the need to match calorimeter energy clusters to to central detector tracks when identifying electrons. In test beam studies, the resolution was found to be $0.8 - 1.2$ mm for 100 GeV electrons, and to scale as $E^{-\frac{1}{2}}$, reflecting the statistical nature of the shower.

### 2.2.3 Muon Spectrometer

The outermost detector system at DØ is the muon spectrometer. Muons do not interact via the strong force and are too massive to lose substantial energy via bremsstrahlung, therefore they will not cause hadronic or electromagnetic showers in the calorimeter. Because they have a long lifetime, muons can traverse the entire detector before decaying. They are they only known charged particle with all the above characteristics. Because the typical detector has many interaction lengths of material between the interaction region and the outer edge of the calorimeter (DØ

has at least 7.2 - see Figure 2.8), detectors are constructed outside the calorimeter for the express purpose of detecting muons.

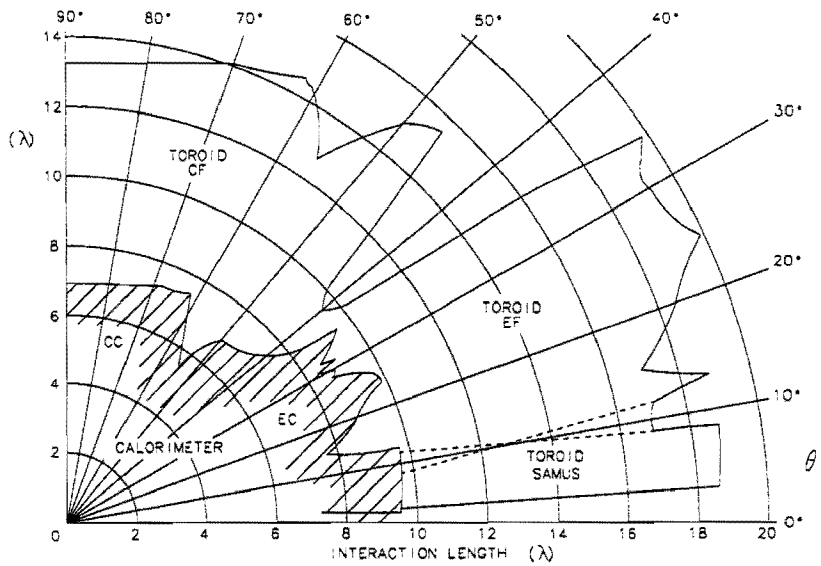


Figure 2.8: Total material in the calorimeter and muon toroid, as a function of polar angle.

Since muons deposit little of their energy in the calorimeter (only that due to ionization), a spectrometer must be constructed to measure their momenta. The DØ muon spectrometer consists of five magnetized iron toroids surrounded by three layers of proportional drift tubes (PDTs). The PDTs measure the particle direction before and after traversing the toroid. This allows a trajectory to be determined, from which the momentum can be inferred. The muon system is divided into two sections, the Wide Angle Muon Spectrometer (WAMUS), and the Small Angle Muon

Spectrometer (SAMUS). The WAMUS provides coverage out to $|\eta| < 1.7$ and is discussed below. The SAMUS extends the muon coverage out to $|\eta| < 3.6$, but is not used in this analysis and hence not discussed here.

### Wide Angle Muon Spectrometer (WAMUS)

The WAMUS is formed from three planes of PDTs, the first (the A layers) mounted on the inner surface of the toroid, the second (B) layer on the outside of the toroid, and the final (C) layer an average of 1.4 m beyond the B layer. The A layer consists of four layers of PDTs, allowing a measurement of the incident muon direction to about 0.6 mrad and position to 100$\mu$m. Additional information from the event vertex, central detector track and muon trace in the calorimeter can improve this measurement. The B and C layers have three layers of PDTs, each of which measure the outgoing position and direction to 0.2 mrad and 0.17 mm.

The toroid itself is divided into three sections. The CF toroid is a square annulus and covers the region of $|\eta| < 1.0$, while the EF toroids cover the region from 1.0 to 2.7. The CF toroid is 1.1 m thick, with its inner surfaces at 317.5 cm from the beamline. The EF toroids are just more than 1.5 m thick, with their inner surfaces at $|z| = 447$ cm. Wire coils carrying 2500 A of current induce a 2T magnetic field in each of the toroids, with field lines running approximately in the azimuthal direction.

The PDT cells are formed from extruded aluminum which has been joined

as shown in Figure 2.9. Each cell is 10.1 cm wide and 5.5 cm high. Cathode pads are inserted at the top and bottom of each cell, and a 50$\mu$m diameter gold-plated tungsten anode wire is strung in the center. During operation, the aluminum walls are held at ground, with the cathodes at +2.3 kV and the anodes at +4.56 kV. The gas mixture consisted of argon (90%), $CF_4$ (5%) and $CO_2$ (5%). The length of each cell varied to suit the detector geometry, with the longest wires begin 6.1 m. All wires were aligned approximately parallel to the magnetic field.

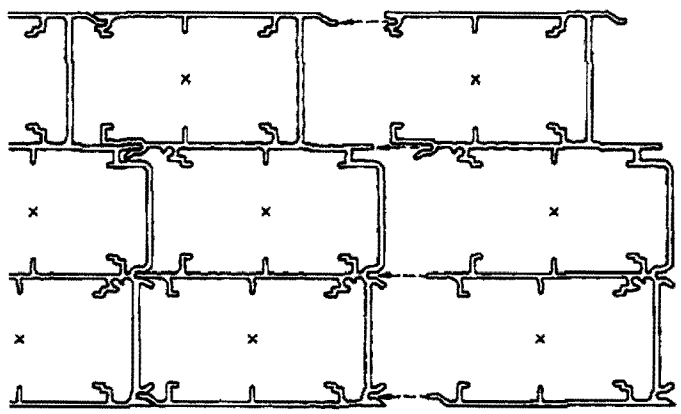

Figure 2.9: End view of the proportional drift tubes used in the muon spectrometer.

As in the central tracker, drift time information is used to measure the track position perpendicular to the wire direction. Both timing and cathode information are used to measure the coordinate parallel to the wire. To simplify the readout electronics, anodes from adjacent cells in the same PDT layer were connected at one

end of the chamber. As as result, muons produced signals on two PDT wires, both in the cell traversed and in the adjacent cell to which it is connected. Noting the timing difference allows a crude placement of the hit position along the wire direction with a resolution of about 10-20 cm. To improve this resolution, the cathode pads were designed with two independent electrodes arranged in a repeating diamond pattern (every 30 cm along the wire direction). Comparing the sizes of the signals induced on the two electrodes allows a determination of the point in the pattern at which the hit occurred with a resolution of 3 mm.

With the exception of the digitization circuitry in the counting house, all the signal processing electronic are located on the chambers themselves. Signals from the cathodes are first sent to pre-amplifiers, and the to baseline subtraction circuitry similar to that used in the calorimeter. A channel is latched for readout if the signal exceeds a specified threshold. Signals from the anodes are sent both to time-to-voltage circuits which measure the drift distance, and $\Delta$time-to-voltage circuits which measure the parallel coordinate. The perpendicular resolution has been measured at about 0.3 mm.

The performance of the system in measuring muon momenta is determined by several factors. First is the geometrical acceptance to hit all three PDT layers. This acceptance is about 60 - 70% for most values of $\eta$, but smaller near the CF - EF boundary. This can obviously be increased by relaxing the condition that all three layers be hit. For a particle which does hit all three layers, the momentum

resolution is determine by the measurement of the original direction, the position resolution of the muon system, and multiple scattering in the toroids. The overall resolution can be parameterized by [69]:

$$\sigma(\frac{1}{p}) = 0.18(p - 2GeV/c)/p^2 \oplus 0.003.$$

### 2.2.4 Trigger

As mentioned in 2.1, the TeVatron produces beam crossings every 3.5$\mu$s. At operating luminosities, this results in at least on $p\bar{p}$ collision in almost every crossing. Data taking at such a rate is impossible. The solution to this problem is to implement a real time processing or "trigger" system to select out the interesting events for recording and analysis. The DØ trigger system is divided into three levels which we discuss below.

#### Level Ø

The Level Ø trigger consists of scintillator hodoscopes mounted between the FDC and the EC, covering a range of $1.9 < |\eta| < 4.3$. These detectors quickly and efficiently (99%) detect the presence of an inelastic collision. In addition to indicating whether or not such a collision took place, the hodoscope signals are also used to determine the $z$ position of the collision. A fast decision is made is based on the analog sum of signals from a subset of the LØ counters, and is used to reject events with $|z| > 100$ cm, which are usually beam-gas events. This fast estimate is

available to the Level 1 trigger for use in the calculation of transverse energies. A second, more accurate determination of $z$ is made by taking into account the timing and total charge on each detector as well as known corrections and calibrations. This result is available to the Level 2 software filter. By calculating the RMS deviation of the time signals for individual counters, the LØ trigger can also tag events which are likely to contain multiple collisions. This information is also made available to higher level triggers.

In addition to its role as primary trigger, the LØ system also serves as the experiment's luminosity monitor [70]. The instantaneous luminosity is given approximately by measuring the rate $R_{L\emptyset}$ of LØ triggers:

$$\mathcal{L}_{meas} = \frac{R_{L\emptyset}}{\sigma_{L\emptyset}} \tag{2.1}$$

where $\sigma_{L\emptyset}$ is the world average $p\bar{p}$ inelastic cross section, corrected for the LØ acceptances and efficiencies as measured from Monte Carlo and data. It's value for the 1994-1995 run was $44.4 \pm 2.3$ mb [71]. The 5.2% uncertainty on this number is dominated by systematic differences between experimental measures of the $p\bar{p}$ cross section, and is overwhelmingly the largest source of uncertainty in the overall luminosity uncertainty.

Equation 2.1 is true only if the assumption the all LØ triggers result from single interaction beam crossings. In the high luminosity environment of run 1B, this was almost never true, and the approximation is very poor. To correct for this,

Poisson statistics must be taken into account. This results in

$$\mathcal{L} = \frac{-ln(1 - \mathcal{L}_{meas}\tau\sigma_{L\emptyset})}{\tau\sigma_{L\emptyset}} \tag{2.2}$$

where $\tau$ is the time between beam crossings. The integrated luminosity is then given by numerical integration of the instantaneous luminosity measurements:

$$\int \mathcal{L} = \sum_{i=1}^{n} \mathcal{L}_i f_{live} \Delta t_i \tag{2.3}$$

where $f_{live}$ is the live fraction measured using a dedicated trigger bit.

### Level 1 (1.5)

The next level of triggers is a hardware based network which reduces the event rate to about 200 Hz. Most decisions are made within the time between beam crossings, but some events required additional processing in a somewhat slower network known as the Level 1.5 trigger, which takes up to several beam crossings.

The L1 framework [72] is an AND-OR network with 256 input bits provided by the calorimeter and muon systems, and mapped out into 32 output trigger bits. The system is programmable, and allows the downloading of both thresholds to fire various AND-OR terms, and the patterns of AND-OR terms which allow a trigger bit to fire. Additionally, there are "prescale" factors that can be define for triggers whose rate would otherwise overload the available bandwidth.

The calorimeter trigger takes its input from fast analog pickoffs from the baseline subtraction circuits. The analog sum of energies in $\Delta\eta \times \Delta\phi$ trigger towers

of $0.2 \times 0.2$ is computed separately for electromagnetic and fine hadronic layers of the calorimeter. The analog input is digitized and weighted by the sine of the trigger tower polar angle, thus giving an approximate transverse energy (exact for $z_{vert} = 0$). This information plus the fast LØ vertex $z$ are used in a lookup table which returns the $E_T$. Once trigger tower $E_T$s are known, the AND-OR terms are define by comparing such quantities as total event $E_T$, $E_T$ imbalance, and the electromagnetic and hadronic $E_T$s in each tower, to some thresholds which have been downloaded.

For most calorimeter information, the above is sufficient. The fact that some electromagnetic showers share their energy between two trigger towers, however, implies that electron and photon triggers can benefit from a crude clustering algorithm, which is applied at L1.5 [73]. The clustering sums the electromagnetic energies from two adjacent towers, and also calculates the total energy in a $3 \times 3$ grid of towers centered on the trigger tower in order to calculate the isolation of the object.

The muon trigger takes its input from the latch bits of the WAMUS and SAMUS cells. This information gives the bend direction coordinate with a granularity of 10 cm. By combining information from multiple layers, a centroid is defined as the center of the half-cell which was most probably hit. The OR of three chambers adjacent in the bend direction to the one being hit is sent to the coarse centroid trigger, which ORs the information by another factor of 4 to create a 60 cm wide trigger road. If a hit pattern in the A, B or C layers is consistent with the passage

of a muon, the L1.5 trigger is invoked.

At Level 1.5, the trigger passes information on all centroids to octant cards. These cards compare possible combinations of hit centroids in the three layers to those expected from tracks above some programmable $p_T$ threshold. This processing reduces the muon trigger rate by about 10-20 times at the cost of about 1% deadtime. The overall effect of the L1.5 trigger is to reduce the trigger rate from about 800 Hz passing level 1 to about 200 Hz input to Level 2.

**Level 2**

The L2 trigger is a software filter which uses digitized information from the event to perform a fast reconstruction. This allows the use of more sophisticated criteria in the event selection decision. The L2 system was a farm of 32 VAX model 4000/60 and 16 VAX model 4000/90 processors running in parallel, which reduces the event rate to about 4 Hz which is written to tape. Each event was roughly 0.5 Mbytes, so the detector typically wrote about 2 Mbytes/s.

During collider operations, a supervisor processor directs incoming events to idle nodes. The event filter software was built around a collection of "tools", each of which had a specific task such as particle identification, or global event characteristic. Which tools were invoked, and the order of their application was controlled by the Level 1 bits. It was possible for a single Level 1 bit to cause the firing of multiple Level 2 filters. There were a total of 128 Level 2 filter bits.

### 2.2.5 Main Ring Effects and Beam Vetos

The trigger system was also responsible for flagging events that were contaminated by Main Ring activity [74]. As described above, the Main Ring passes through the coarse hadronic calorimeter, and is usually active as part of antiproton generation during collider operations. Beam loss from the Main Ring was capable of causing spurious signals in the coarse hadronic calorimeter (affecting the missing $E_T$ resolution) and in the muon system.

Large beam losses occurred from the Main ring during injection (every 2.4 seconds) and during transition (0.3 seconds later). A gate known as `MRBS_LOSS` was raised at the time of proton injection, and remained for 0.4 seconds until the beam had passed through transition, and the muon high voltage system recovered.

During the remainder of the Main Ring cycle, losses were significant only when the passage of the proton beam through the detector coincides with a TeVatron beam crossing. A second gate, known as `MICRO_BLANK`, was raised if a Main Ring beam transit occurred within $\pm$800ns of a $p\bar{p}$ crossing.

The LØ counters measure the fraction of crossings which occur during these gates, allowing the correct luminosity to be calculated by those using any combination of the above vetoes. The beam veto which rejected events occurring in either of the above conditions was known as `GOODBEAM`. During typical operation, this resulted in a loss of about 25% of the recorded luminosity.

### 2.2.6 Data Acquisition

The data acquisition system (DAQ) runs parallel to the operation of the trigger. Once a L1 trigger is passed (with L1.5 confirmation if necessary), the supervisor processor directs the event to a L2 node, and notifies the Sequencer to begin digitization of the event. The front-end crates require about 1 ms to fully digitize an event. Data is then read out on eight cables which correspond to different detector systems. These cables can transmit 40 Mbytes/s and are connected to input boards on the L2 nodes. The node selected to process the event receives the data. If the event passes any L2 filter, it is transfered to the host computer, which writes the event to a disk buffer. Once about 500 events are written to a file, the file is closed and written to tape. A schematic of the DAQ can be seen in Figure 2.10.

## 2.3 Detector Operation and Data Collection

As mentioned earlier in this chapter, a TeVatron store typically lasted about 20 hours, during which time the detector was active and recording data. As the beams circulate, they slowly dissipate, resulting in lower luminosities. This change in running conditions meant that the set of prescale factors which were optimized for the beginning of the store were no longer able to fill the available bandwidth, resulting a lost opportunity for data taking. To maintain the maximum data taking rate, data taking was periodically paused to allow the downloading of a new set of

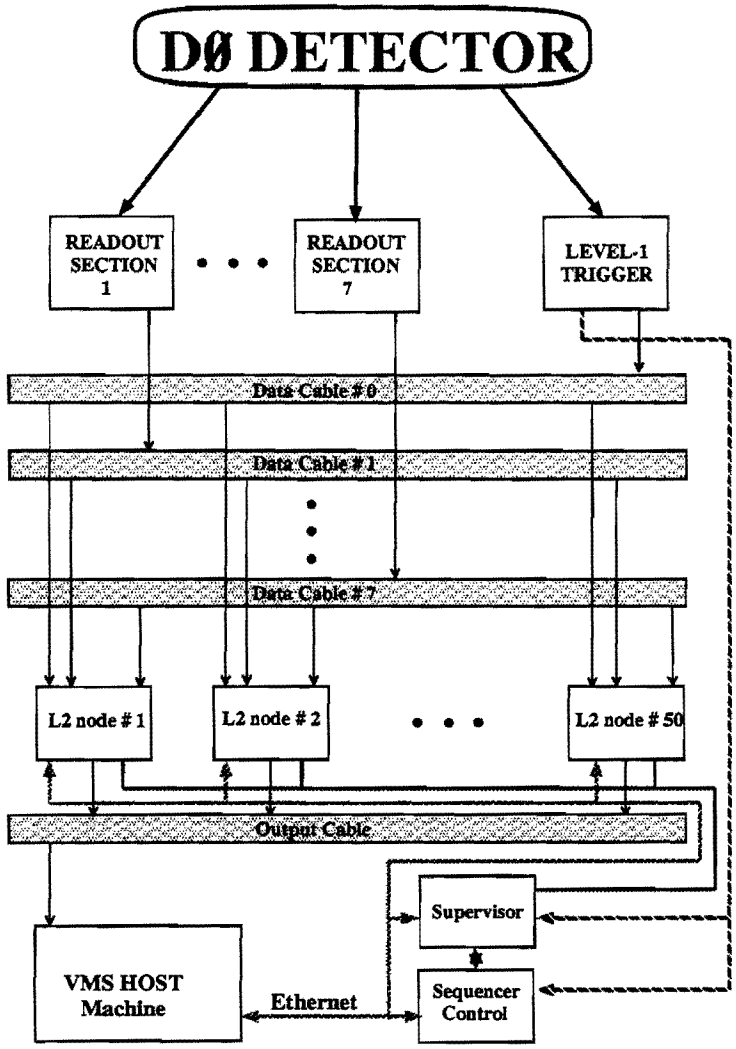


Figure 2.10: Schematic of data acquisition at DØ.

prescales which were optimized for the current beam conditions. The time in which a given set of prescales was in place and the detector in continuous operation is called a "run". Each run would typically last about four hours. Events passing a L2 filter were labeled sequentially, so each each event was uniquely labeled by a run and event number.

# Chapter 3

# Event Reconstruction and Particle Identification

The data from $p\bar{p}$ collisions recorded by DØ consists of ADC counts from the hit channels in the central tracker and calorimeter, as well as both digital and analog signals from the muons system. This information is not immediately useful to humans, and the quantities which these data represent are not clearly interpreted as meaningful physical quantities. It is the job of the reconstructor program, DØRECO, to process the raw data into objects which are recognizable as the signature of high energy physics processes and are more suitable for further analysis. In this chapter, we describe the workings of DØRECO. We then describe the additional techniques used to identify electrons, muons and missing $E_T$.

## 3.1 DØRECO

The DØRECO program performs three major tasks. The first task is hit finding. Signals from each sense wire of the tracking chambers (including muon PDTs) are converted into the spatial location of hits, and signals from each calorimeter cell are converted into an energy deposition. In the second task, tracking chamber hits are combined to form tracks, while calorimeter energy deposits are combined to form energy clusters. In the final task, tracking and calorimetric information is combined to reconstruct jets, and identify electron, photon and muon candidates.

### 3.1.1 Tracking Reconstruction

The reconstruction of tracking information begins with the identification of hits. In the central tracker, special algorithms are used to identify the leading and trailing edges of pulses coming from sense wires and delay lines. These algorithms remove spurious pulses due to bad FADC bits and discharges, and they reduce the sensitivity to fluctuations in pedestals. Once the edges of the pulse have been found, the pulse size is used to determine $dE/dx$ and the timing is used to calculate the hit position. The processes in the muon system is essentially the same, with only the timing information to compute the hit locations in each of the layers being of relevance.

Once the hits are found, segments are defined which connect the hits. These

segments are then combined to form tracks. In the central detector, segments are build on a layer by layer basis within each chamber, with up to two sense wires allowed to be missing a hit in a given segment. The connection of segments into tracks begins in the outermost layer of the chamber. Each segment in the outer layer is compared to segments in the next layer within a predefined distance in $\phi$. The best match is added to the track, and the process continues until the track extends through all the layers, with one layer allowed to be missing. After the $r\phi$ fitting is done, $z$ information from the delay lines is added. Overall, this results in typical resolutions of 2.5 mrad in $\phi$ and 28 mrad in $\theta$ [75]. For additional information, see [76, 77].

In the muon system, hits from the A layer are joined into segments (A segments) , while hits from both the B and C layers are formed into segments (BC segments). This is accomplished using a linear least squares fit in $r - z$ and $r - \phi$ separately. BC segments must have four of six possible hits, while A segments must have two of four possible hits. All segments are required to point to with 5 m of the central detector. Once the segments in the separate views are formed, only those with the same hits are retained. The connection of segments into tracks begins by extending the BC segment to the midplane of the toroid. The A segment which points most closely to the BC segment intersection with the toroid midplane is added to the track. If no A segment matches sufficiently well, the pre-toroid direction is defined by the line between the primary vertex and the mid-toroid point.

### 3.1.2 Vertex Determination

As mentioned earlier, the $z$ position of the event vertex varies on an event by event basis and is roughly Gaussian in its distribution, with a width of $\sigma_z \approx 30$ cm. It is essential to make an accurate determination of the vertex $z$ in order to make good measurements of the azimuthal angle of final state objects and hence assign good energy vector components to those objects. To accomplish this, the reconstructor takes all CDC tracks which have an impact parameter in the $xy$ plane with respect to the beam of less than 2.5 cm. These tracks are projected to $x = y = 0$, and their $z$ positions at that point histogrammed. The peak of this histogram is used as the event vertex, with a resolution of about 1.2 cm. Additional vertices from multiple interactions are distinguished as secondary peaks in the histogram, provided they are at least 7 cm away from the primary vertex.

The $xy$ position of the vertex is tightly constrained by the small transverse size of the beam spot (about $50\mu$m). For a given store, the $xy$ position of the interaction point is quite stable, so the measurement of the $xy$ vertex is done on a store by store basis. For this measurement, the first $\approx 500$ events at the start of the store are processed. CDC and VTX tracks are matched to give improved resolution. All matched tracks are then extrapolated to either $x = 0$ or $y = 0$, and the orthogonal coordinate histogrammed. The peak of each histogram gives the mean $x$ and $y$ interaction point for the store.

### 3.1.3 Calorimeter Reconstruction

The reconstruction of calorimeter data begins with the conversion of recorded ADC counts into deposited energy values. This conversion is accomplished by using the results of test beam runs performed prior to detector installation in which calorimeter modules were exposed to electron and pion beams of known energies. Because the conditions of these test did not perfectly reproduce operating conditions, further in-situ calibrations are necessary. These are describe in 3.1.8. As in tracking hit reconstruction, the calorimeter signals are corrected for time dependent changes in readout channel gains and pedestals. Special runs between stores were taken to determine these corrections.

Once the energy deposition in each cell is determined, signals from all cells with the same $\eta$ and $\phi$ indices are summed into towers. In the computation of this sum, it is assumed that each cell represented a massless particle, with a resulting four-vector of $(E, E\sin\theta\sin\phi, E\sin\theta\cos\phi, E\cos\theta)$ where E is the signal in the cell, and $(\theta,\phi)$ determined by the cell centroid and the vertex $z$. The tower energy four-vector is then given by the sum of cell four-vectors. With this four-vector, the $\phi$, $\theta$, and $\eta$ for the tower are then trivially calculated. These towers form the basis for jet reconstruction, while electromagnetic only versions of the towers form the basis for electron and photon reconstruction.

### 3.1.4 Electron Reconstruction

The reconstruction of electrons and and photons begins with the grouping of electromagnetic towers into clusters of energy [78]. Beginning with the highest-$E_T$ tower, all neighboring towers with more than 50 MeV of $E_T$ are added to the cluster. This process repeats until no neighboring towers satisfy the energy requirement. A new cluster is then begun from the tower with the highest remaining $E_T$ not already in a cluster.

Any cluster in the calorimeter with more than 90% of its energy in the electromagnetic calorimeter and more than 40% in a single tower is identified by the reconstructor program as an electron/photon candidate. Because the typical hadronic jet is broad and deposits only about 10% of its energy in the EM layers, this cut removes most hadronic clusters from consideration while retaining more than 99% of true electrons and photons. If there is a CDC or FDC track within a $0.1 \times 0.1$ $\Delta\eta \times \Delta\phi$ road defined by the cluster center of gravity and the event vertex, the cluster is defined to be an electron candidate. This criterion in the sole distinction between reconstructed electrons and photons.

### 3.1.5 Muon Reconstruction

The reconstuction of muons begins with the construction of tracks in the muon spectrometer PDTs (see 3.1.1). Once a track has been found, the muon

momentum is determined by the angle between the A and BC segments, corrected for energy losses in the calorimeter. A global fit for the momentum is then performed to further enhance this measurement. This fit makes use of 16 parameters:

- The $x$ and $y$ event vertex positions
- The slope and intercept of the matching CDC track in the $r - z$ and $r - \phi$ views
- The two angles representing the mismatch of the CDC track and calorimeter track directions
- The slope and intercept of the A and BC segments in the $r - z$ and $r - \phi$ views.

The fit returns seven parameters: four for the CDC track, two representing the multiple scattering in the calorimeter, and the momentum of the track.

### 3.1.6 Missing $E_T$ Reconstruction

Because neutrinos do not interact in the detector, their presence must be inferred from an imbalance in the energy in the event. Since the longitudinal energy is not well measured due to beampipe losses and the lack of far-forward hermeticity in the calorimeter, only the transverse energy (for which the hermeticity is excellent) imbalance in the event can be used. The missing transverse energy ($\not\!\!E_T$ ) is

determined by summing the transverse energy components of all calorimeter and ICD cells:

$$\not{E}_T{}_x^{cal} = \sum_{i=1}^{N_{cells}} E_{xi},$$

$$\not{E}_T{}_y^{cal} = \sum_{i=1}^{N_{cells}} E_{yi}.$$

The magnitude of $\not{E}_T{}^{cal}$ is obtained by summing the components in quadrature, and represents the energy carried away by any particles which do not interact in the calorimeter. As mentioned above, the near hermeticity of the detector for transverse energy results in excellent resolution for this variable. Based on the $\not{E}_T$ distribution in "minimum bias" data (events which need only pass the LØ trigger), this can be parameterized as [75]:

$$\sigma(\not{E}_T) = 1.08 \text{ GeV} + 0.019 \times \sum_{Cells} E_T.$$

In order to isolate the $\not{E}_T$ due only to neutrinos, the contributions from muons to $\not{E}_T{}^{cal}$ must be subtracted:

$$\not{E}_T{}_x = \not{E}_T{}_x^{cal} - \sum_{i=i}^{N_{muons}} p_x^{mu_i},$$

$$\not{E}_T{}_y = \not{E}_T{}_y^{cal} - \sum_{i=i}^{N_{muons}} p_y^{mu_i}.$$

Again, with the magnitude of $\not{E}_T$ obtained as the sum in quadrature of the components.

### 3.1.7 Jet Reconstruction

The process of jet reconstruction is different than that for electrons or muons, because there is no unambiguous way to define a jet. In the process of hadronization, a parton may emit gluons at sufficiently large angles to produce distinct clusters of energy. Because the boundary of such clusters is define by the observer, there is no clear demarcation. The standard practice is to define an algorithm which associates energy deposits with jets.

The standard algorithm used at DØ was the "cone" algorithm [79]. First, an $E_T$ ordered list of calorimeter towers was made. For every tower with $E_T > 1$ GeV, a precluster was formed from that tower and all of its neighbors also meeting this condition. The $E_T$ weighted $\eta$ and $\phi$ of each precluster was stored as a jet finding starting point.

The jet algorithm proceeded by looping over all preclusters, and summing the energy from all towers within $\sqrt{(\Delta\eta)^2 + (\Delta\phi)^2} < R$ from the precluster center. Typical values of $R$ used were 0.3, 0.5 and 0.7, with 0.5 chosen for this analysis. In creating this sum, the calorimeter energy vectors were added vectorially, and a new $\eta - \phi$ centroid calculated. If the new centroid was different from the old, the cone summation was repeated using the new centroid coordinates. This was repeated until the jet direction became stable to within $\Delta R$ of 0.001.

If the jet overlapped with a jet that had previously been reconstructed, the

shared $E_T$ was compared to the $E_T$ of the softer jet. If the shared $E_T$ was greater, the jets were merged, if not, they were split. If two jets were reconstructed with $\Delta R < 0.01$ and $\Delta E_T < 10$ MeV, the second jet was discarded rather than being split or merged. Finally, in order to suppress random noise fluctuations, only jets with $E_T > 8$ GeV were retained.

### 3.1.8 Energy Calibrations

The calibration of the calorimeter began with the electromagnetic modules. First, corrects were applied for known differences between the test beam and running conditions. These included differences in the readout electronics, the liquid argon purity and the gap voltage, and account for roughly a 5% offset. In additional module by module variations were measured and corrected for by taking advantage of the $\phi$ symmetry of the physics measured in the data. This resulted in an RMS deviation between modules of 1.3%, with a maximum deviation of about 5%.

Once this was done, the overall scale of the calibration needed to be set. The linearity observed in the beam tests allowed the inference of a linear relationship between the measured and true electromagnetic energies:

$$E^{True} = \alpha E^{Meas} + \delta. \tag{3.1}$$

Reconstructing the invariant mass of spectrum of any particle which decays to electrons or photons is sufficient to constrain such a calibration. Three such particles

were used; the $Z$ boson, the $J/\psi$ and the $\pi^0$. These measurements restricted the values of $\alpha$ and $\delta$ to [80],

$$\alpha = 0.9537 \pm 0.00086$$

$$\delta = -0.16^{+0.03}_{-0.21}\ \text{GeV}.$$

Given this determination, it was possible to determine the jet energy calibration.

The jet energy calibration is necessarily complicated due to the ambiguities of the definition of a jet. Because this analysis relies only minimally on the precision reconstruction and measurement of jets[1], the calibration is not discussed at length here. The purpose of the jet energy calibration is to enable the relationship of measured energy depositions to the energy of the partons which formed the jet. This process takes place in two steps. In the first, applied by the post-RECO package called CAFIX [81], corrections are applied so that the jet energy is on average that of the final state particles contained within the jet cone. In the second step, applied after CAFIX, so called out of cone corrections are made to account for gluon emission which can occur at large angles and carry final state parton energy away from the jet cone.

[1]Jet reconstruction and calibration enter in two places. First, directly in the isolation requirement imposed on muons (see 3.2.2), and second, indirectly in the computation of the CAFIX corrected $\not\!\!E_T$ .

## 3.2 Particle Identification

The criteria applied by DØRECO in selecting particle candidates are quite loose. Further offline processing results in substantial rejection of spurious electrons and muons.

### 3.2.1 Electron Identification

There are two primary background processes which can mimic an electron. Both are driven by the same two mechanisms. First, a photon produces an electromagnetic cluster. A track is then provided either by the random overlap of a low energy charged hadron, or by the conversion of the photon into an $e^+e^-$ pair early in the tracking system. With no magnetic field in the tracking volume, the low $p_T$ of a random overlap track cannot be used to reject its match to the high $E_T$ calorimeter cluster. Similarly, with no central magnetic field, both particles resulting from the conversion continue on nearly the same trajectory resulting in tracks that are too close together to be resolved. Because of this, leptonic $W$ pairs can suffer substantial background from the production of single leptonic $W$'s in association with jets (which contain $\pi^0$'s and $\eta$'s which decay to two photons) and photons which, as will be discussed in 6.1.2 and 6.1.1, have much larger cross sections than does the $W$ pair process.

In order to suppress these backgrounds while retaining the maximum possible efficiency with which electrons are identified, we employ an "electron likelihood" method developed at DØ for electron identification [82, 83]. This method takes the "standard" DØ electron identification variables for both calorimeter and tracking information, and convolutes them into an inverse likelihood function. Both the standard variables, as well as the electron likelihood and determination of the associated identification efficiency are discussed below.

### Standard Electron Identification Variables

The typical DØ analysis considers some or all of the following six variables to describe the quality of an electron candidate: the "isolation" - $f_{iso}$, electromagnetic energy fraction - $f_{EM}$, "$H$ matrix $\chi^2$", "track-match significance" - $\sigma_{trk}$, track ionization - $dE/dx$, and the TRD response - $\epsilon$. All these quantities except TRD $\epsilon$ (which is not discussed here) were used as part of the electron identification process in this analysis.

The isolation of the electromagnetic cluster is defined by comparing the electromagnetic energy in a cone of radius $\sqrt{(\Delta\eta)^2 + (\Delta\phi)^2} = 0.2$ centered on the cluster (EM(0.2)), to the total energy contained within a concentric cone of radius 0.4 (E(0.4)). The fractional isolation is define as:

$$f_{iso} \equiv \frac{E_{\rm tot}(0.4) - E_{\rm EM}(0.2)}{E_{\rm EM}(0.2)}$$

Any cluster with $f_{iso}$ greater than 0.1 is rejected. This cut differentiates between electromagnetic and hadronic showers via their transverse development, and is 98% efficient. It significantly reduces the background from random track overlaps as well as semileptonic heavy quark decays (which tend to produce electrons embedded in jets). Distributions of $f_{iso}$ for electrons from $Z \rightarrow ee$ candidate events, and from highly electromagnetic showers found in multijet events can be found in figure 3.1.

The remaining four variables are all convoluted into the electron likelihood. The first two involve information from the calorimeter, the second two from the tracker. The first of these is the electromagnetic energy fraction, defined as

$$f_{EM} = E_{EM}/E_{tot}.$$

In the selection of any electron or photon candidate, $f_{EM}$ is implicitly cut on, as the reconstructor requires that an energy cluster have $f_{EM} > 0.9$ in order to be such a candidate. This variable differentiates electromagnetic and hadronic showers via their longitudinal development.

The $H$ matrix $\chi^2$ [84] is a measure of a detailed comparison between the shape of a candidate cluster with the expected shape of an electromagnetic shower. The expected shape is characterized by a covariance matrix devolved from a sample of Monte Carlo electrons:

$$M_{ij} = \frac{1}{N}\sum_{n=1}^{N}(x_i^n - \bar{x}_i)\cdot(x_j^n - \bar{x}_j)$$

where $N$ is the total number of electrons in the sample, and the $x_i$ are the variables

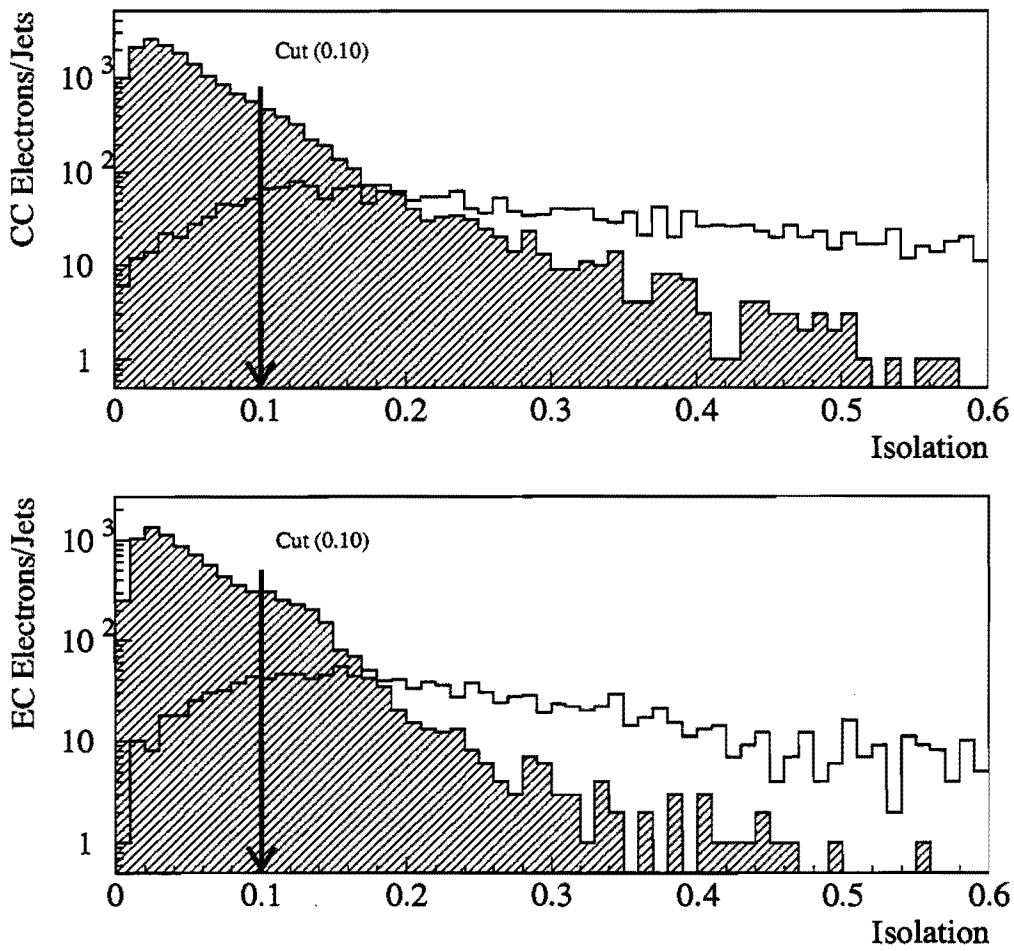


Figure 3.1: Fractional Isolation Distributions. (a) CC distributions of fractional energy isolation for electrons from $Z \rightarrow ee$ candidate events (hashed) and highly electromagnetic showers from multijet events. (b) EC distributions of fractional energy isolation for electrons (hashed) and jets. The electrons are from the dielectron data used in $WW \rightarrow e^+e^-$ search, while the jets are from the multijet data sample used to study the electron fake probabilities.

used which define the shower shape. A total of 41 variables are use:

- The fraction of the total energy contained in the first, second and fourth layers of the EM calorimeter
- The fraction of the total energy contained in each cell of a $6 \times 6$ array around the shower center in the third layer
- The logarithm of the total energy
- the z position of the primary vertex.

The matrix $M$ is calculated individually for towers at different $\eta$, with symmetry in $\phi$ assumed. Reflection symmetry is also assumed for positive and negative values of $\eta$, resulting in 37 distinct matrices.

Once $M$ has been calculated, the measure of agreement between the candidate shower and the Monte Carlo ideal is given by:

$$\chi^2 = \sum_{i,j=1}^{41} (x_i - \bar{x}_i) H_{ij} (x_j - \bar{x}_j)$$

where $H$ is the inverse of $M$.[2] In order to reduce the sensitivity to possible differences between data and Monte Carlo electrons, the $H$ matrix is diagonalized and an upper limit is placed on the elements of the diagonalized matrix.

The first of the tracking variables is the "track-match significance" ($\sigma_{trk}$). This quantity is a measure of the consistence between the direction of the central

[2]It should be noted that since the individual variables are not in general Gaussian distributed, the overall measure is not distributed as a true $\chi^2$.

track, and the centroid of the shower, and serves to reject random track overlaps. The centroid of the shower is defined as:

$$\vec{x}_{cog} = \frac{\sum_i w_i \vec{x}_i}{\sum_i w_i}$$

where the sum is over the cells in the shower, $\vec{x}_i$ is a vector from the vertex to the cell centroid, and

$$w_i = \mathrm{Max}(0, w_0 + \ln(E_i/E)).$$

The logarithmic weighting reflects the logarithmic development of the shower, and the $w_0$ are chosen empirically to optimize the position resolution. The azimuthal resolution of the center of gravity was measured at about 2.5 mm.

The track match significance for a cluster is defined as:

$$\sigma_{trk} = \sqrt{\frac{(\Delta x_L)^2}{\sigma^2_{\Delta x_L}} + \frac{(\Delta x_T)^2}{\sigma^2_{\Delta x_T}}}$$

where $\Delta x_L$ and $\Delta x_T$ are the differences in the longitudinal and transverse directions of the cluster-track projection. The variables $\sigma_{\Delta x_L}$ and $\sigma_{\Delta x_T}$ are the resolutions of the mismatch measurement. This measurement is illustrated in Figure 3.2.

The last variable we consider here is the track ionization, $dE/dx$. This variable is used to discriminate between prompt electrons and those coming from photon conversions. The $dE/dx$ measurement is made using all but the third of the wires in the CDC (FDC) which have the largest signals. This is done to reduce the sensitivity to Landau fluctuations due to delta rays.

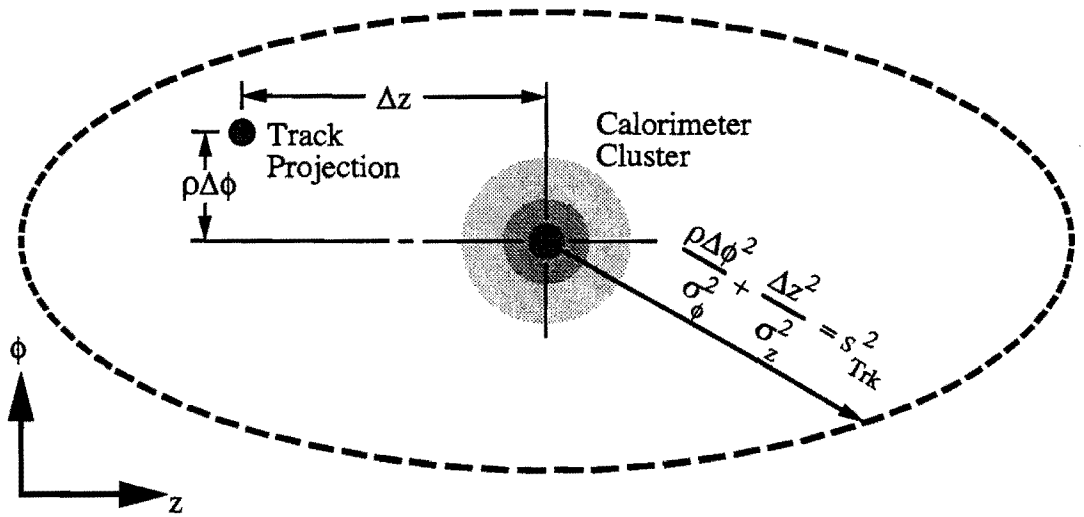


Figure 3.2: Definition of the track match significance in terms of the cluster centroid in EM3 and the projection of a track to this radius. Track projects which fall within the indicated ellipse are considered good matches.

### Electron Likelihood

The electron likelihood is a multi-variable Neymann-Pearson likelihood test which compares the value of several parameters for a given electron candidate to distributions of those parameters from known samples of electrons, photon conversions, and hadronic overlaps. The result of this test is an inverse likelihood which is close to zero for a good electron, and large for a fake. More technically, the variables, combined into a vector $\mathbf{x}$, are assumed to be uncorrelated probability distributions such that the probability of the cluster in question arising from a hypothesis $H$ is:

$$p(\mathbf{x}|H) = p(dE/dx|H)p(\chi^2|H)p(\sigma_{trk}|H)p(f_{EM}|H)$$

where the possible hypotheses are electron ($H = e$), hadron overlap ($H = h$), and photon conversion ($H = ee$). Next, the variable $\mathcal{R}$ is defined as:

$$\mathcal{R}(f_h) = \frac{p(\mathbf{x}|b)}{p(\mathbf{x}|e)} = \frac{f_h p(\mathbf{x}|h) + (1 - f_h)p(\mathbf{x}|ee)}{p(\mathbf{x}|e)}$$

where $f_h$ is the fraction of hadronic overlaps in the background. A cut is then placed on $\mathcal{R}(f_h)$, and clusters with values below the cut are taken to be electrons. The probability densities and the values for $f_h$ were determined from the data [82, 83]. $f_h$ was found to be 0.53 in the CC, and 0.62 in the EC. Distributions of $\mathcal{R}$ for both electron and jet samples, can be found in Figure 3.3.

The choice for the value of the likelihood cuts used in this analysis was made by maximizing the ratio of the electron identification efficiency to the predicted number of background events in the dielectron decay channel due to jets being misidentified as electrons. The efficiency is based on the distribution of electrons in Monte Carlo $W$ pair events, 0.5989, 0.3587, 0.0424 for CC/CC, CC/EC and EC/EC events respectively, and the identification efficiency for electrons in the CC and EC. Details of the determination of the identification efficiency for electrons in each of the fiducial regions can be found below. The background from jet misidentifications was determined entirely from the data. Details of this calculation can be found in 6.1.2. The distribution of this ratio (effectively signal to noise) can be found in figure 3.4

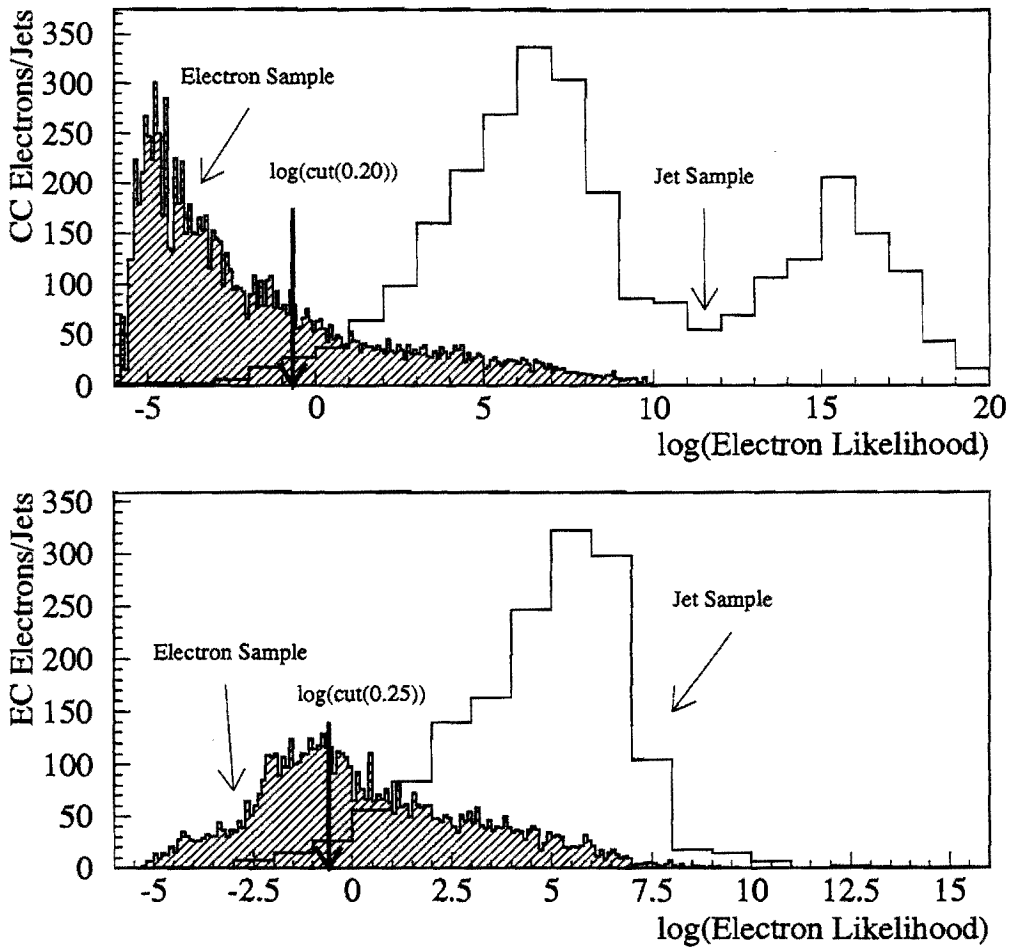


Figure 3.3: Electron Likelihood Distributions. (a) 4-variable electron likelihood for CC electrons from $Z \rightarrow ee$ candidate events (hashed) and highly electromagnetic showers from multijet events. (b) 4-variable electron likelihood for EC electrons (hashed) and jets. The electrons are from the dielectron data used in $WW \rightarrow e^+e^-$ search, while the jets are from the multijet data sample used to study the electron fake probabilities.

We thus require the following of electron candidates:

- $|\eta_{det}| < 1.1$ (CC) or $1.5 < |\eta_{det}| < 2.5$ (EC),

  $|\Delta\phi(\text{cluster}, \text{crack})| > 0.01$ in the CC

  We cut on the position in the calorimeter of the shower center of gravity to ensure that the shower will be fully contained in the fiducial volume of the electromagnetic calorimeter. Additionally, we require that the shower occur where the EM3 segmentation is best, and that the shower be separated from the CCEM module cracks. This increases the probability that the electron will be well measured.

- Electron likelihood ($\mathcal{R}$) $< 0.20$ (0.25) in the CC (EC)

  We cut on a four variable electron likelihood, based on $f_{EM}$, $\chi^2$, $\sigma_{trk}$, and $dE/dx$. This cut selects cluster-track combinations which have the characteristics of electrons. Because $f_{iso}$ depends not only on the development of the shower, but also on the event topology, it was not included in the likelihood function used in this analysis.

- $f_{iso} < 0.10$

  We cut on the isolation of candidate electrons to differentiate between EM and hadronic showers via their transverse development, and to assist in choosing event topologies with minimal jet activity.

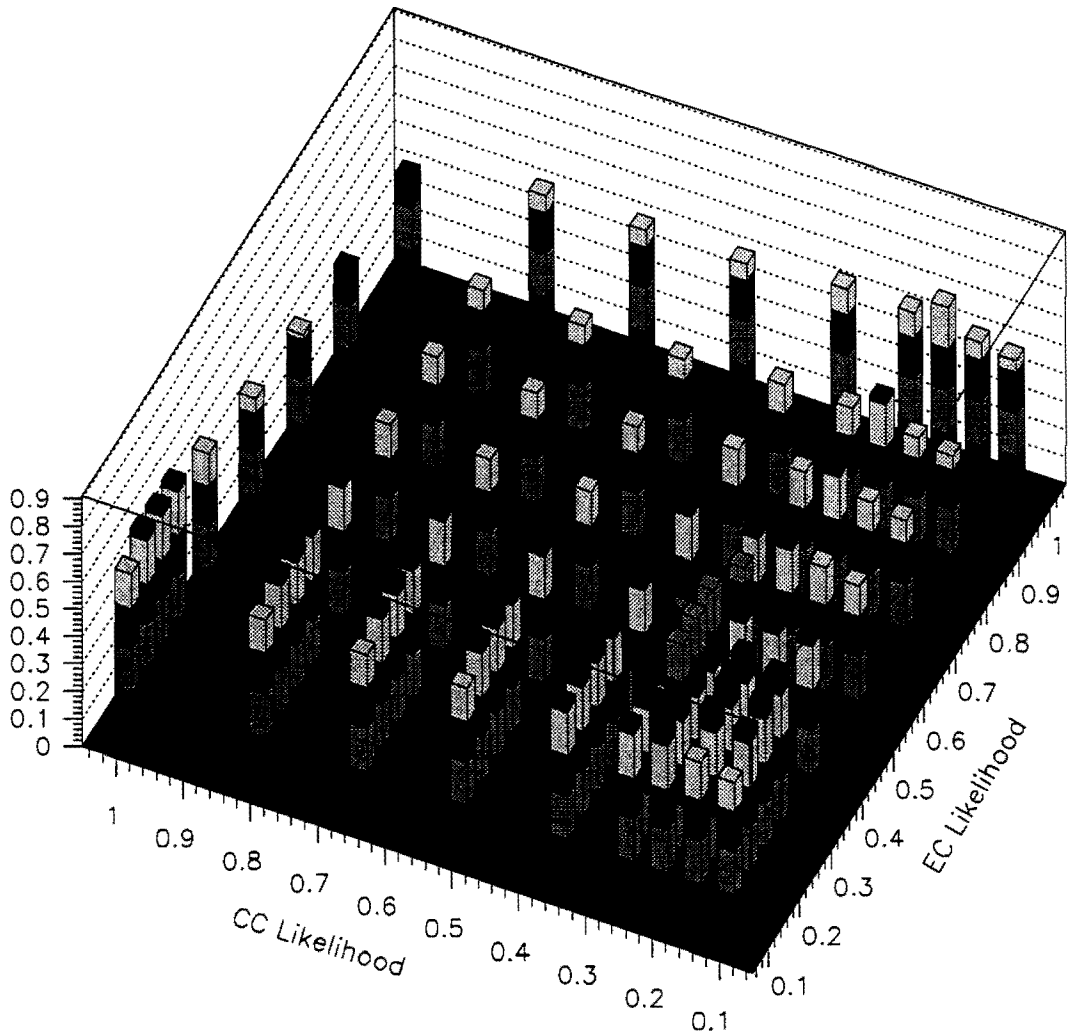


Figure 3.4: Ratio of weighted electron ID efficiency to background event yield for jets misidentified as electrons.

### Electron Identification Efficiency

The TeVatron provides a convenient source of high-$p_T$ electrons through the process $Z \rightarrow e^+e^-$, which is ideal for the study of electron identification efficiencies. The data-based technique used for the efficiency measurement relies on the fact that a dielectron event can be identified or "tagged" as a $Z$ boson candidate using the invariant mass of the pair. The change in the number of candidates in the mass peak for different cuts allows the relative efficiency to be determined. The relative efficiency of a cut "a" to a (looser) cut "b" is given by

$$\epsilon_{ab} = S_{ab}/S_b$$

where $S_{ab}$ and $S_b$ denote the number of background-subtracted events in the mass peak for cuts "a" and "b" together, and for cut "b" alone. The precision of such an estimate is limited statistically by the number of available $Z$ events, and systematically by the uncertainty in the true number of background events in the mass peak.

The efficiency for the above set of cuts was determined based on a sample of $Z \rightarrow e^+e^-$ events. Candidate events were required to pass the `EM2_EIS2_HI` level 2 filter, which contains the same L2 electron term as the trigger used in the search in electron decay modes, and the `GOOD_BEAM` veto. Because the electron likelihood can only be applied to reconstructed electrons, the identification efficiency is given by:

$$\epsilon_{\rm ID}^{\rm electron} = \epsilon_{\rm track-in-road} \times \epsilon_{\mathcal{R}+f_{iso}}.$$

$\epsilon_{\text{track-in-road}}$ is the efficiency for finding a track in an $\eta \times \phi$ road of $0.1 \times 0.1$ projected from the primary reconstructed vertex to the calorimeter cluster in question. The efficiency for reconstructing a 20 GeV cluster under the above fiducial cuts is 100%, so the reconstruction efficiency for an electron in this analysis is simply the efficiency for reconstructing the accompanying track. Once reconstructed as an electron, the candidate must further pass the likelihood and isolation cuts. $\epsilon_{\mathcal{R}+f_{iso}}$ is the combined efficiency for an electron to pass both the likelihood and isolation cuts. Thus the total identification efficiency is the product of the efficiency for reconstructing the electron and the efficiency for that electron to pass the likelihood test and isolation cut.

The track-in-road efficiency was determined using two different methods. In the first [85] , we define four exclusive subsamples of the dielectron data described above, based on whether or not a track is found to accompany the cluster:

1. cc/cc, track/track
2. cc/cc, track/no-track
3. cc/ec, track/track
4. cc track/ec no-track.

To remove background contamination, the method of sideband subtraction is used. In this method, three regions in the invariant mass of the dielectron system are defined; $61 < m_{ee} < 71$ GeV, $81 < m_{ee} < 91$ GeV, and $111 < m_{ee} < 121$ GeV. The background in the middle (*signal*) region is estimated to be the average of the number of events in the upper and lower (*sideband*) regions. After performing

sideband subtraction, the efficiencies are given by the following expressions:

$$\frac{N_1}{N_1+N_2} = \frac{\epsilon_{\rm trk}^{\rm cc}}{2-\epsilon_{\rm trk}^{\rm cc}} \qquad \frac{N_3}{N_3+N_4} = \epsilon_{\rm trk}^{\rm ec}.$$

Table 3.1 lists the relevant parameters of this method along with statistical uncertainties.

| $N_1$ | $N_2$ | $N_3$ | $N_4$ | $\epsilon^{\rm CC}_{\rm track-in-road}$ | $\epsilon^{\rm EC}_{\rm track-in-road}$ |
|---|---|---|---|---|---|
| 1914 | 897 | 1665 | 287 | $0.8102 \pm 0.0057$ | $0.8530 \pm 0.0080$ |

Table 3.1: Track-in-road efficiency, method 1

In the second method [86], we use the standard electron identification method of applying a tagging cut to one electron in the event, and if it passes, asking whether the second, now unbiased, electron also passes. Each event may be used twice. Sideband subtraction is used to remove background contamination. The efficiencies are given by the following expression:

$$\epsilon_{\rm trk}^{\rm cc(ec)} = \frac{\#w/track}{\#w/track + \#w/no-track}.$$

Table 3.2 lists the relevant parameters from this method, along with statistical uncertainties.

The final track-in-road efficiency is computed by taking the mean of the two methods. The systematic uncertainty is estimated to be the average of the difference

| $N^{CC}_{w/track}$ | $N^{CC}_{total}$ | $N^{EC}_{w/track}$ | $N^{EC}_{total}$ | $\epsilon^{CC}_{track-in-road}$ | $\epsilon^{EC}_{track-in-road}$ |
|---|---|---|---|---|---|
| 4653 | 5650 | 1906 | 2231 | $0.8235 \pm 0.0051$ | $0.8543 \pm 0.0075$ |

Table 3.2: Track-in-road efficiency, method 2

between the final efficiency and the efficiencies of each method. Table 3.3 shows the final track in road efficiency with systematic and statistical uncertainties. It should be noted that the track-in-road efficiency is measured to be higher in the forward region than in the central. This is an artifact of the higher track density found at larger values of $|\eta|$.

| Cryostat | $\epsilon_{track-in-road}$ |
|---|---|
| CC | $0.8169 \pm 0.0054\ (stat) \pm 0.0067\ (sys)$ |
| EC | $0.8537 \pm 0.0078\ (stat) \pm 0.0007\ (sys)$ |

Table 3.3: Combined track-in-road efficiency

The efficiency of the likelihood and isolation cuts was determined using standard electron identification procedure as described in reference [86]. A tagging cut is applied to one electron in the event, leaving the other unbiased. Several tagging cuts are used to estimate a systematic uncertainty. Since the likelihood efficiency was being studied, only events with both showers reconstructed as electrons were considered. Sideband subtraction was used to remove background contamination in

the signal region. Efficiencies are given by the following expression:

$$\epsilon^{cc(ec)}_{\mathcal{R}+f_{iso}} = \frac{electrons\ passed}{total\ electrons}.$$

Table 3.4 lists the tagging cuts used, and the likelihood efficiency for each set of cuts, including statistical uncertainty. Table 3.5 lists the final likelihood efficiencies. Table 3.6 lists the final electron ID efficiencies.

| Cryostat | Likelihood Cut | Isolation Cut | Tagging Cut | $\epsilon_{\mathcal{R}+f_{iso}}$ |
|---|---|---|---|---|
| CC | 0.20 | 0.1 | 1.00 | $0.7312 \pm 0.0064$ |
| CC | 0.20 | 0.1 | 0.25 | $0.7358 \pm 0.0069$ |
| EC | 0.25 | 0.1 | 1.00 | $0.5605 \pm 0.0116$ |
| EC | 0.25 | 0.1 | 0.25 | $0.5419 \pm 0.0137$ |

Table 3.4: Likelihood + isolation efficiencies

| Cryostat | Likelihood Cut | Isolation Cut | $\epsilon_{\mathcal{R}+f_{iso}}$ |
|---|---|---|---|
| CC | 0.20 | 0.1 | $0.7335 \pm 0.0067(stat) \pm 0.0023(sys)$ |
| EC | 0.25 | 0.1 | $0.5512 \pm 0.0127(stat) \pm 0.0093(sys)$ |

Table 3.5: Final likelihood + isolation efficiencies

| Cryostat | Likelihood Cut | Isolation Cut | $\epsilon^{\text{electron}}_{\text{ID}}$ |
|---|---|---|---|
| CC | 0.20 | 0.1 | $0.5992 \pm 0.0068(stat) \pm 0.0053(sys)$ |
| EC | 0.25 | 0.1 | $0.4706 \pm 0.0117(stat) \pm 0.0079(sys)$ |

Table 3.6: Combined electron ID efficiencies (per electron)

### 3.2.2 Muon Identification

The principal backgrounds to muon candidates in this analysis come from cosmic rays, tracks formed from random noise hits in the muons chambers, muons from the semileptonic decays of charm and bottom quarks, and other sources of hadronic muon production. The contribution from hadrons punching through the calorimeter and toroid is negligible except at the very edge of the CF toroid. To suppress these backgrounds, several variables are defined and cut upon. We discuss these variables, the cuts made, and the resulting particle identification efficiency below.

#### Muon Identification Variables and Cuts

We have used the following variables and cuts for muon identification:

- $|\eta| < 1.0$

  Only muons in the CF region of the WAMUS are considered in this analysis. This restriction virtually eliminates punch trough and noise hit combinatorics as sources of background.

- IFW4 $\leq 1$

  This variable is a word representing the quality of the muon track fit. Tracks with perfect fits have an IFW4 of 0, those with one failure have IFW4 of 1, and all others have IFW4 of 2. This cut increases the probability that the

muon will be well measured

- HFRAC $\geq 0.70$

  As the muon traverses the calorimeter, it deposits energy through ionization. These energy depositions can be used to form a track. HFRAC is the fraction of all possible hadronic layers which had energy deposition consistent with the passage of a minimum ionizing particle. This cut requires such deposition in all but one of the hadronic calorimeter layers, and is useful in rejecting muons due to noise hits.

- |xy Impact Parameter| $\leq 25$ cm

  Tracks which do not pass near the beam position are likely to be cosmic rays. Impact parameters in the bend ($r - z$ plane) and non-bend ($xy$ plane) views are calculated, along with a three-dimensional impact parameter.

- Floating time offset ($|t_0^{\mathrm{float}}|$) $\leq 200$ ns

  The time of the hits in the track are allowed to float in the fit, and the difference between the best-fit time and the beam crossing time is calculated. This cut rejects cosmic ray muons, whose timing is independent of the beam activity

- $\int \vec{B} \cdot \vec{dl} \leq 0.6$ GeV

  This quantity is a measure of the integrated magnetic field a muon traverses in its passage through the toroid. This cut is effectively a geometrical cut as

it rejects muons mainly in the region near the CF-EF toroid boundary, and rejects muons in this region, which tend to have poorly measured momenta.

- $\Delta R(\mu, jet) \geq 0.5$, $E_T^{jet} > 10$ GeV

  This isolation cut is designed to remove background muons which may come from pions, kaons or heavy quark jets. $\Delta R$ is the separation distance in $\eta \times \phi$ space. The threshold of the jets is slightly higher than the jet reconstruction threshold in order to reduce dependence on the reconstruction efficiency for low $E_T$ jets.

### Muon Identification Efficiency

The identification efficiency for the above set of cuts can be expressed as:

$$\epsilon_{\mathrm{ID}}^{\mathrm{muon}} = \epsilon_{(\mathrm{RECO+IFW4+}\int \mathrm{Bdl})} \times \epsilon_{\mathrm{HFRAC}} \times \epsilon_{\mathrm{t_0}} \times \epsilon_{\mathrm{ImpactParameter}} \times \epsilon_{\mathrm{Isolation}}.$$

The reconstruction efficiency is well modeled by the combination of DØGEANT and MUSMEAR (see 4.2.1). This is because the GEANT simulation has detailed information about the fiducial acceptances of the detector, and the MUSMEAR package has similar information about the measured resolutions and efficiencies of the muon PDTs. Similarly, the IFW4 and $\int Bdl$ variables are well modeled by the Monte Carlo, as these tend to be closely related to the geometry of the detector. Because the efficiencies for these cuts depend strongly on the rapidity distributions of the muons in the event, and because the reconstruction cut is implicit in all event

selection the efficiencies for these cuts are incorporated into the overall kinematic + fiducial efficiency, and are determined on a process by process basis. The isolation cut efficiency was also determined from Monte Carlo, because the efficiency of the muon isolation cut depends on the distributions of muons and jets in the process.

The efficiency for the HFRAC cut was derived from scanned events. This is a process by which events are viewed manually for the signs of a muon, and whether or not a muon was actually reconstructed and if that muon was accompanied by the appropriate calorimeter information. The impact parameter and $t_0$ efficiencies were determined from the data. This was done by measuring the ratio of "double tight" to "tight + loose" events in a sample of $Z \rightarrow \mu\mu$ events. This sample was composed of dimuon events with muon $p_T > 15$ GeV/c. Here "loose" refers to reconstructed muons passing the IFW4 and HFRACT cuts, while "tight" refers muons passing IFW4, HFRAC and the cut under study. This procedure is identical to the one used to study the likelihood + $f_{iso}$ efficiency for electrons. Details on the derivation of the HFRAC, impact parameter and $t_0$ efficiencies can be found in [87] .

An added complication to the determination of the muon identification efficiency is that the operating conditions of the muons system changed significantly over the course of Run 1B. In the "pre-shutdown" period (Runs 65000 - 89000), some chambers became inefficient due to the buildup of polymers on the anode wires. This effect was particularly severe in the EF region, and around the Main Ring. In the "post-shutdown" period (Runs 89000 - end), most of the chambers were cleaned to

remove the polymers, and the efficiency in those chambers restored. Because of the way in which the high voltage is ganged for the muon chambers, some chambers which were not cleaned became totally inefficient due to the lower operating potentials needed by the cleaned chambers. While the effect of the differing operating conditions is primarily on the muon momentum resolution and acceptance, the effect on the muon identification efficiency is not negligible for some of the variables.

Table 3.7 lists the various measured efficiencies as well as the overall muon identification efficiency. These efficiencies are for the entire 1B run. Pre and post-shutdown efficiencies have been combined in a luminosity weighted average.

| Cut | CF Efficiency |
|---|---|
| HFRAC | $0.964 \pm 0.013$ |
| impact parameter | $0.99 \pm 0.01$ |
| $t_0^{\mathrm{float}}$ | $0.98 \pm 0.01$ |
| isolation | $0.75 \pm 0.03$ |
| combined | $0.701 \pm 0.031$ |

Table 3.7: Muon ID efficiencies (per muon)

# Chapter 4

# Event Modeling

In order to optimize selection cuts to be efficient for selecting leptonic $W$ pair events, and for rejecting background, one needs a model of the final states which are expected to arise from both signal and background events. For some backgrounds, it is often possible to make use of the data itself as such a model, for example the background arising from the misidentification of jets as electrons. Most backgrounds however, and certainly the signal, must be simulated using Monte Carlo programs which model both the physics of the event, and the detector response. In this chapter we describe the event generators and the detector simulations used.

## 4.1 Monte Carlo Event Generators

The first step in modeling either the $W$ pair signal or any of the backgrounds is to model the physical process. This is the task for which event generators are written. These programs use random numbers to simulate processes of interest. Two types of generators were used in this analysis; "standard" event generators, which fully simulate physics events, and "fast" event generators, which model only the hard scatter.

### 4.1.1 Full Event Generators

In "standard" event generators, physics events are fully modeled via factorization theorems which state that any process can be broken up into several independent steps; the elementary hard process, initial and final state gluon emission, and formation of final state hadrons. The hard process is the interaction of initial state partons which results in the final state particles of interest - two $W$ bosons or a competing background. This is entirely calculable in perturbative QCD. The simulation of initial and final state QCD radiation involves both the perturbative radiation of gluons and non-perturbative corrections. The formation of final state hadrons is entirely non-perturbative. The resulting events are full simulations of physics events including the "underlying event" as well as the hard process. Three such Monte Carlo generators were used in this analysis; PYTHIA, ISAJET and

HERWIG. The differences between these generators lies primarily with the way in which they handle the last two steps of the event generation, and primarily in the models used to simulate the hadronization of final state partons. These generators were used to model the backgrounds from $Z \rightarrow \tau\tau$, Drell-Yan, $W\gamma$ and $t\bar{t}$ production. The PYTHIA generator was also used as a cross check for the Standard Model $W$ pair detection efficiency calculation.

### 4.1.2 Fast Event Generators

We refer to the second type of event generator used as "fast Monte Carlo" generators. In these programs, physics events are simulated using only the hard parton subprocess (step one from above). The resulting output of these simulations is typically a list of four-vectors describing only the products of the hard scatter (for instance, the electrons of a $Z \rightarrow ee$ decay). While producing events with less detail than "standard" generators, "fast" generators are able to produce large numbers of events while requiring relatively little computing resources. This is helpful in cases where very large numbers of events are necessary. Two such Monte Carlo generators were used in this analysis. The first is the CMS Monte Carlo [88]. This program was developed for the $W$ boson mass analysis, and incorporates an event generator designed to model leading order intermediate vector boson production based on the theoretical model of Ladinsky and Yuan [89]. This generator is modified to produce high $p_T$ $Z$ bosons using the model of Arnold and Kaufman [90]. The CMS program

also contains a detector simulation which is not used in this analysis. This program was used to model the background from the high $p_T$ production of $Z$ bosons in the $ee$ and $\mu\mu$ channels.

The second fast generator used was the $W$ pair Monte Carlo by the authors of [48]. This program is a leading order event generator which models hadroproduction of $WW$ and $WZ$ events for Standard and non-Standard model trilinear gauge boson couplings. In addition to providing the four-vectors of the final state leptons, the code also provides the cross section for the set of couplings chosen. For the cross section calculation, a k-factor of 1.335 [91] was used to simulate the additional cross section due to higher order diagrams. The method used to account for the kinematic effect of higher order diagrams on the four-vectors is described in the next section. This program was used as the primary model for the calculation of the Standard Model $W$ pair detection efficiency, and as the sole model for the calculation of the non-Standard Model $W$ pair detection efficiency.

## 4.2 Detector Simulation

Once the physics event of interest has been modeled, the next step is to model the response of the detector to that event. The result of this step is to produce a sample of events with the same biases as the data. In this analysis, two types of simulations were used to model the response of the DØ detector; "first principle"

simulations and "parametric" simulations.

### 4.2.1 First Principle Detector Simulation

In "first principle" simulations, the detector response is a simulation of the low level physical processes which occur in each detector element. Trajectories of final state particles are evolved through the various detector elements through which they pass. Ionization in the tracking chambers, and the formation of electromagnetic and hadronic showers in the calorimeter are simulated in great detail. The program which implements this procedure is called GEANT [93], and the DØ implementation DØGEANT.

Because such a detailed simulation is very CPU intensive, a library of electromagnetic and hadronic showers was created to reduce the computing needs for large event samples. This library consists of 1.2 millions tracks at various values of vertex $z$, $\eta_{det}$, $\phi$ and particle momentum. In the course of detector simulation, an appropriate choice of shower is made from this library for each electron/photon, hadron and muon in the event.

In addition to the GEANT simulation, it is also necessary to model the efficiency and the resolution of the muon system, both of which are overestimated by DØGEANT. This implemented by the MUSMEAR [92] package, which runs after GEANT. This routine smears the hit timing information simulated by GEANT so that the Monte Carlo hit position resolution matches that seen in the data.

MUSMEAR also randomly discards hits to model the chamber inefficiency, and modifies the geometry file that describes the muon system in order reproduce the measured momentum resolution.

After the detector response has been simulated in this way, the events are stored in a format identical to the raw data. The events are then processed by DØRECO to reconstruct the various particles. The only difference between the reconstruction of Monte Carlo and the data is that the vertex determination done for the data is not applied to the Monte Carlo because the events are generated with a distribution of vertices similar to that found in the data. The reconstruction makes use of the generated vertex[1]. Two different versions of DØRECO are used for data modeling in this analysis. For dielectron Monte Carlo, version 11.19 is used. For all other standard Monte Carlo, version 12.20 is used. The primary difference between version 11 and 12 lies in the muon reconstruction, thus the version 11 reconstructor is sufficient for cases where muons were not present or unimportant.

In this analysis, all events generated using the "standard" generators were passed through the combination of DØGEANT+MUSMEAR+DØRECO.

[1]Because the data contains events with multiple vertices, the reconstruction of data can differ systematically from the Monte Carlo due to the possibility of misidentifying the primary event vertex in the data, whereas no such ambiguity exists in a generated event. Choosing the wrong vertex during reconstruction results in mismeasurement of calorimeter cluster $E_T$'s and muon $p_T$'s (and hence the $\not{E}_T$ ). No such mismeasurement occurs in the Monte Carlo

### 4.2.2 Parametric Detector Simulation

The second type of detector simulation used in this analysis is the "parametric" simulation. The approach of such a simulation differs from "first principle" simulations in that the goal is to model the macroscopic response of the detector in as simple and accurate a way as possible. The significant advantage of this technique is that it is much less CPU intensive than a GEANT simulation (even after the improvement from using the shower library).

The input to the simulation (known as DIPS [94]) consists of a list of final state four-vectors. If it is desired, the kinematic effects of NLO contributions can be simulated. This was done in the case of $W$ pairs by selecting a transverse momentum for the $WW$ system from the distribution of $p_T^{WW}$ taken from the PYTHIA event generator. This $p_T$ is used as a transverse boost for all the final state four-vectors.

For each event a vertex $z$ is chosen from a Gaussian distribution centered at $z \approx 0$ with a 30 cm width to reflect the distribution seen in the data. This position is used to project where each of the observed final state particles will enter the calorimeter or muon system. The geometrical acceptance for calorimeter objects is cut upon as discussed in 3.2. The acceptance for muons is determined from a map generated with a large sample of single muons which were run through a full detector simulation including MUSMEAR and DØRECO. Maps were generated using both the pre and post-shutdown versions of MUSMEAR, and combined using a luminosity

weighted average.

The energies and momenta of the particles are then smeared according to Gaussian distributions parameterized by

$$(\sigma_x/x)^2 = C^2 + S^2/x + N^2/x^2$$

where $x = E$ for electrons, photons and hadrons, and $x = \frac{1}{p}$ for muons. $C$, $S$, and $N$ correspond to constant, sampling and noise terms respectively. For electromagnetic objects, these terms are taken from test beam data [65] and further tuned to $Z \rightarrow ee$ Monte Carlo simulated using DØGEANT+DØRECO. For hadronic objects, the parameters are taken from test beam data. For muons, the smearing parameters are tuned using a large sample of single muons which were simulated with DØGEANT+MUSMEAR+DØRECO. After all the observed particles are smeared, the total transverse energy of the event is re-summed, and the missing $E_T$ is calculated. An additional contribution to the $\not\!\!E_T$ is added due to the underlying event. This contribution is sampled from a distribution of $\not\!\!E_T$ observed in minimum bias data.

Figures 4.1 and 4.2 show comparisons of kinematic quantities between $Z \rightarrow ee$ and $Z \rightarrow \mu\mu$ events from data, standard Monte Carlo (ISAJET + DØGEANT + MUSMEAR + DØRECO) and fast Monte Carlo (CMS+DIPS). These distributions show that that both forms of Monte Carlo are well matched to each other, and to the data. For variables depending on the $\not\!\!E_T$ of the event, the fast simulation is a

better match to the data due to the inclusion of the underlying event, which is not well simulated in the standard generators.

In addition to determining the kinematic and fiducial acceptance of a particle, DIPS also provides the means to include trigger and particle identification efficiencies. Trigger efficiencies are measured from the data, and a probability for a given particle to cause a trigger is generated on a particle by particle basis. For the identification efficiency for electrons, the procedure is the same as for the trigger efficiency, with the efficiency being measured from the data, and the probability for an electron to pass the identification criteria being generated on a particle by particle basis. For muon identification, the efficiencies were a combination of those measured in the data, and for the efficiency as measured in the Monte Carlo acceptance map.

Finally, a user routine is provided in which the entire set of selection cuts - trigger, particle identification, geometric, kinematic, and topological - can be placed on each event. A ratio of events passed by this routine to the total number of events simulated is a measure of the detection efficiency for the process and set of cuts.

In this analysis, high $p_T$ $Z$ boson events and $W$ boson pair events were simulated using this technique.

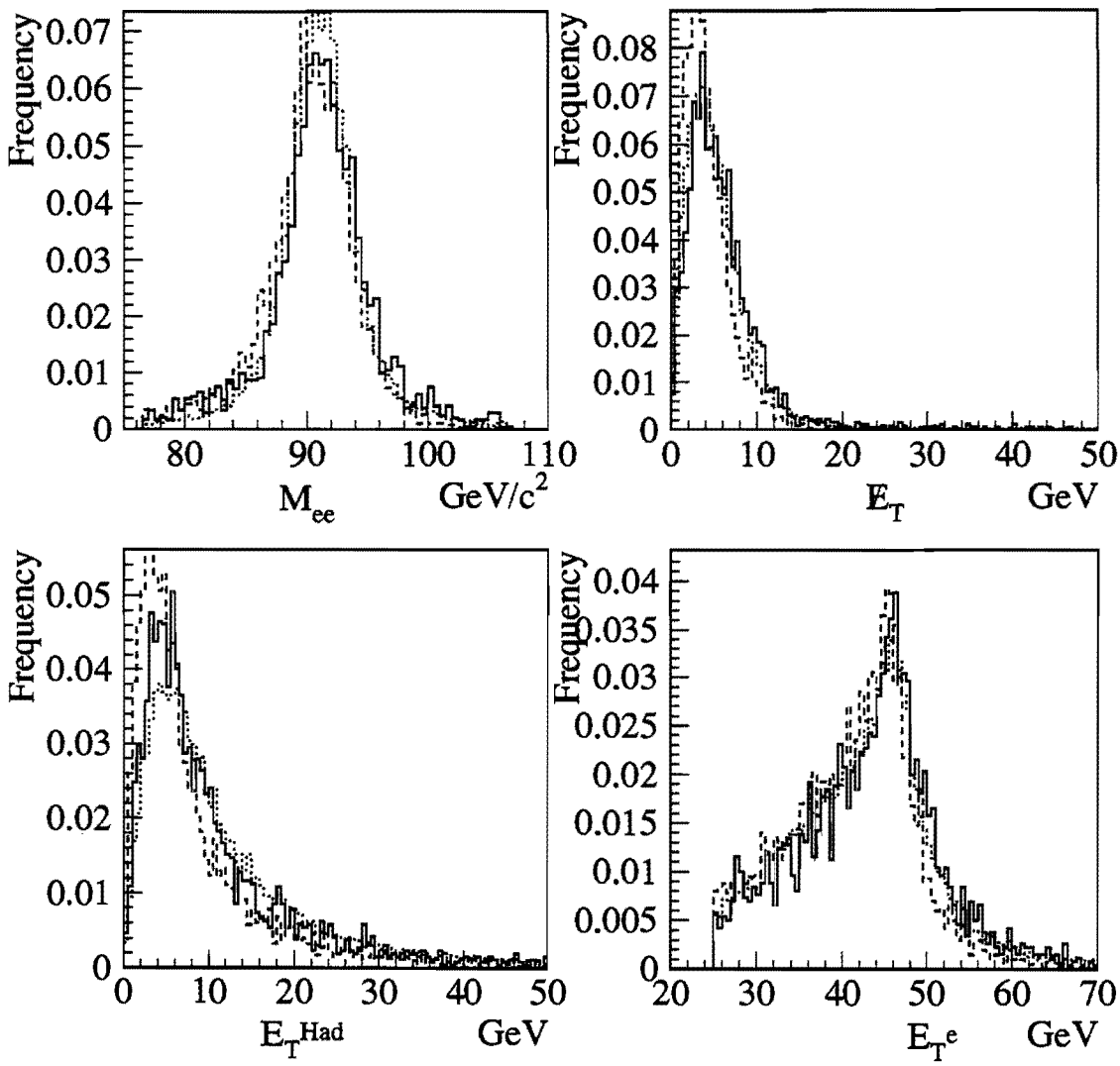


Figure 4.1: Distributions of Dielecton mass, $\not{E}_T$ , $\vec{E}_T^{Had}$ and Electron $E_T$ for $Z \rightarrow e^+e^-$ events from Data (solid), Standard (ISAJET, DØRECO v11.19) (dashed) and Fast Monte Carlo (dotted).

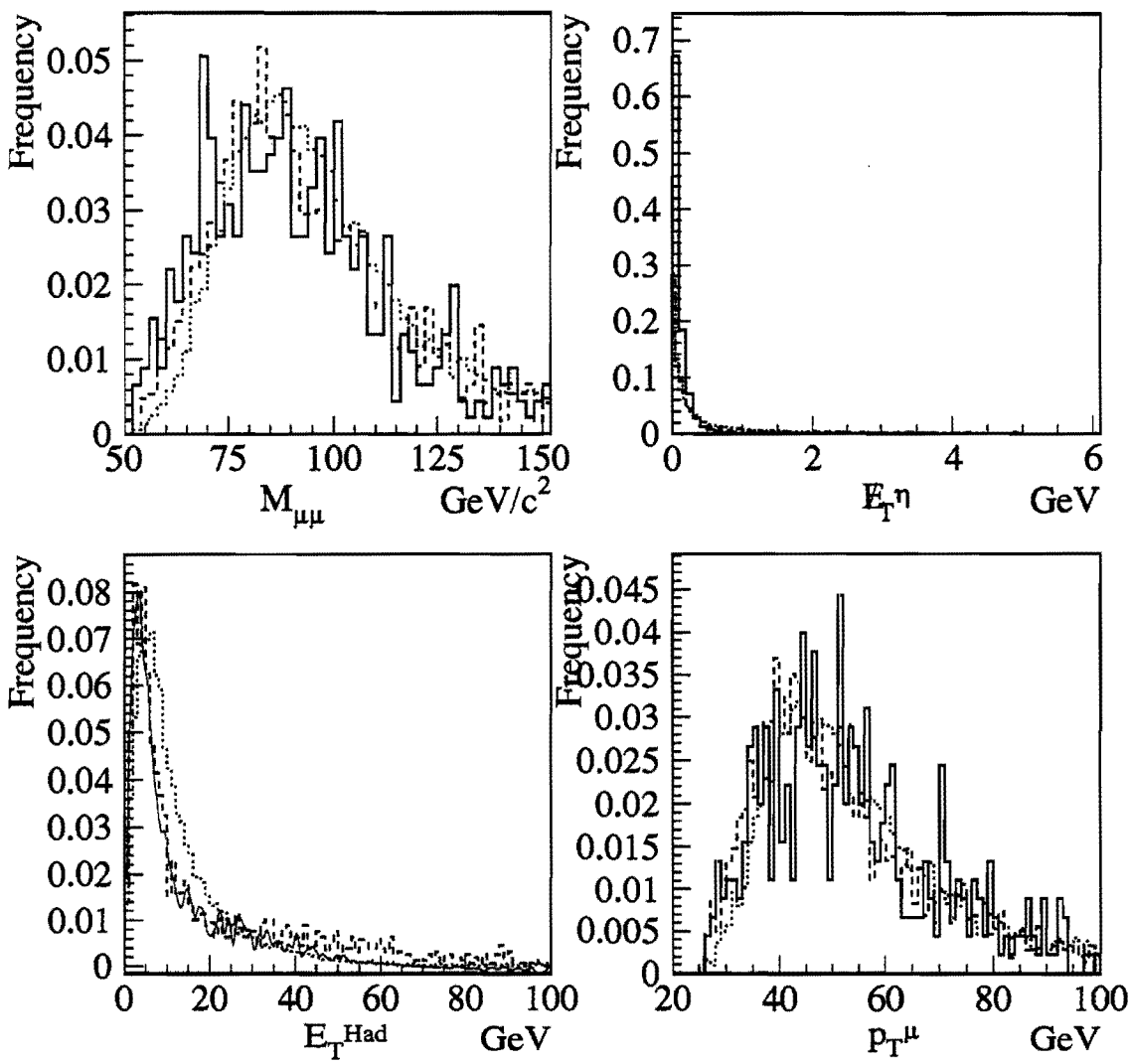


Figure 4.2: Distributions of Dimuon mass, $E_T^{\eta}$, $\vec{E}_T^{Had}$ and Muon $p_T$ for $Z \rightarrow \mu^+\mu^-$ events from Data (solid), Standard (ISAJET, DØRECO v12.20) (dashed) and Fast Monte Carlo (dotted). The data have been background subtracted.

# Chapter 5

# Event Selection and Detection Efficiencies

As discussed in 1.3.3, $W$ pair production in purely leptonic decay modes is characterized by final states containing two high $p_T$ leptons and large missing energy. There are, however, other physical processes which, by themselves, or with the addition of instrumental mismeasurment, may produce similar final states. Therefore, we must design event selection criteria, both off and on-line, to efficiently detect $W$ pair signal events, while reducing contamination from background sources. In this chapter, we describe the data sets and selection criteria used in the search for purely leptonic $W$ pair events. We then report the estimate of the efficiency of these cuts, and present expectations for Standard Model event yields.

## 5.1 Data Samples

The data for both the Dielectron and $e - \mu$ searches were taken from the $W \rightarrow e\mu$ data stream produced by the $W/Z$ group. This stream is a collection of all events passing a Level 2 $W/Z$ electromagnetic filter, and containing at least one electromagnetic object with $E_T > 15$ GeV, and $\not{E}_T > 15$ GeV. The data for the Dimuon search was taken from the $WZ \rightarrow \mu$ data stream. This stream is a collection of all events passing a Level 2 $W/Z$ muon filter, and containing at least one muon with $p_T > 8$ GeV. Both these data streams existed as disk resident micro-dst files, and were processed into ntuple format for subsequent use.

## 5.2 Event Selection

Event selection for $W$ pair candidates took place in two stages. In the first, cuts are applied to the online event criteria. These were conditions that were present during the actual data taking. In this analysis, these conditions included the choice of trigger, and use of a beam veto. In the offline event selection, the particle identification criteria discussed in 3.2 were applied to candidate events. Additionally, kinematic and topological cuts are also applied.

### 5.2.1 Online Event Selection and Luminosity

Two online selection criteria were applied in the search for $W$ pair candidates. In the Dielectron and $e - \mu$ analyses, candidate events were required to pass the EM1_EISTRKCC_MS Level 2 filter. At Level 1, this filter requires the presence of at least one electromagnetic calorimeter tower with $E_T > 12$ GeV. At level two, the filter requires one electromagnetic object with and $E_T > 20$ GeV, and missing $E_T > 15$ GeV. The EM shower is subject to online shape and isolation cuts which are looser than those used in particle identification. This trigger was unprescaled in all but the highest instantaneous luminosity runs during the 1B data taking, and the runs which were prescaled amounted to less than 1% of all runs.

The efficiency for this filter was derived from the data. To estimate these efficiencies, "mark and pass" data from so call "monitor" triggers was used. Such triggers record data regardless of the decisions made by other triggers (although they are highly prescaled). The ratio of the number of events which pass both the selection trigger and the monitor trigger to the number of events that pass the monitor trigger is a measure of the trigger efficiency. By binning this process in electron $E_T$ and $\not{E}_T$ we can generate trigger turn-on curves. These curves are shown in figure 5.1. It should be noted that these curves are for the L2 terms in the trigger only, the L1 efficiency is assumed to be 100% [95].

From these curves we have estimated the trigger efficiency for events with

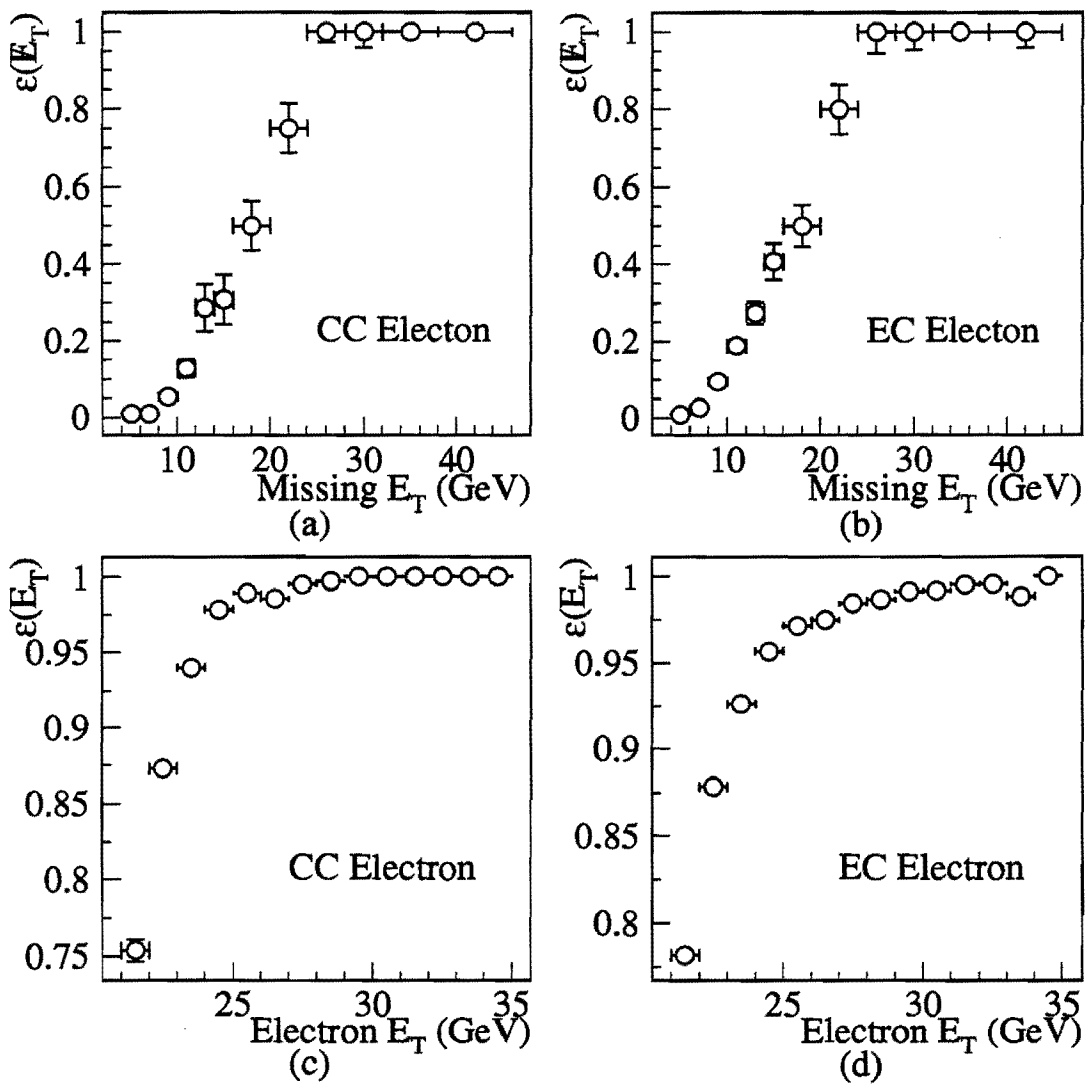


Figure 5.1: Level 2 trigger turn-on curves. (a) Missing $E_T$ turn on for events with an electron in the CC with $E_T > 25$ GeV. (b) Missing $E_T$ turn on for events with an electron in the EC with $E_T > 25$ GeV. (c) Electron $E_T$ turn for CC electrons in events with $\not\!\!E_T > 25$ GeV. (d) Electron $E_T$ turn for EC electrons in events with $\not\!\!E_T > 25$ GeV.

one electron with $E_T > 25$ GeV, and $\not{E}_T > 25$ GeV to be $0.99^{+0.01}_{-0.03}$. The uncertainty listed is statistical only.

In the dimuon analysis, candidate events were required to pass one of two filters, depending on the run number. Before run 87,800 events were required to pass the `MU_1_MAX` filter, while after 87,800 they were required to pass the `MU_1_CENT_MAX` filter. At Level 1, both filters require a WAMUS muon with the addition that there is energy deposition associated with the muon in the calorimeter, and that there are no hits in the cosmic cap scintillator tiles. At Level 1.5, they require that the muon have $p_T > 7$ GeV. At Level 2, the muon is required to have $p_T > 15$ GeV, and have good tracking, calorimeter energy deposition, and no hits in the cosmic cap scintillator. The only difference between the filters is that `MU_1_MAX` allows muons in the entire WAMUS ($|\eta| < 1.7$) whereas `MU_1_CENT_MAX` allows muons only in the CF. This combination of filters was made to obtain the maximum possible integrated luminosity. Being single muon triggers, both filters were necessarily prescaled, resulting in a lower integrated luminosity than the electron trigger.

The efficiency for this combination of triggers was derived from the data for use in the $W \rightarrow \mu\nu_\mu$ cross section analysis [96]. Table 5.1 lists the trigger efficiencies for a single muon with $p_T > 20$ and 25 GeV respectively for the running period before and after run 89000. These efficiencies include factors for L1, L1.5 and L2. Because our selection criteria will require one muon at each threshold, these efficiencies must be combined appropriately. The results are also shown in table 5.2.

| Single Muon Trigger Efficiency | $p_T > 20$ GeV/c | $p_T > 25$ GeV/c |
|---|---|---|
| Pre-shutdown | $0.435 \pm 0.012$ | $0.440 \pm 0.013$ |
| Post-Shutdown | $0.440 \pm 0.019$ | $0.444 \pm 0.020$ |

Table 5.1: Single muon trigger efficiencies. Uncertainties are statistical only.

| | Trigger Efficiency | Integrated Luminosity $pb^{-1}$ |
|---|---|---|
| Pre-Shutdown | $0.684 \pm 0.014(stat) \pm 0.055(sys)$ | 31.00 |
| Post-Shutdown | $0.689 \pm 0.022(stat) \pm 0.055(sys)$ | 34.18 |
| Combined | $0.687 \pm 0.018(stat) \pm 0.055(sys)$ | $65.18 \pm 3.45$ |

Table 5.2: Dimuon trigger efficiencies and luminosities.

In addition to the trigger requirement, candidates in all channels were required to pass the `GOOD_BEAM` veto (see 2.2.5). This veto rejects data taken during the `MRBS_LOSS` and `MICROBLANK` gates. Application of this beam veto served to remove the main ring as a source of spurious muons and calorimeter energy deposition (thus maintaining the missing $E_T$ resolution).

The integrated luminosities for the above filters were calculated by the $W/Z$ group, taking into account data losses due to prescales and beam vetos. For the Dielectron and $e-\mu$ analyses, the integrated luminosity was calculated to be $82.27 \pm 4.36$ pb$^{-1}$, while the for the Dimuon analysis, the calculation yielded a luminosity of $65.18 \pm 3.45$ pb$^{-1}$ [97]. The 5.3% uncertainty is a primarily due to the uncertainty on the inelastic $p\bar{p}$ cross section, which is measured by the LØ trigger.

### 5.2.2 Offline Event Selection

The offline event selection criteria can be divided into three categories; particle identification, kinematic, and topological cuts. Particle identification cuts are discussed in 3.2. These cuts simultaneously reduce the detection efficiency for both the signal and most background processes, but substantially reduce background from 'fake' processes. Kinematic cuts are primarily designed to select signal events. The requirement of two high $E_T$ ($p_T$) leptons and large $\not\!\!E_T$ efficiently selects $W$ pair events. Additional cuts such as restricting the dielectron invariant mass serve to reject sources of background (in this case, $Z \rightarrow ee$ events). Topological cuts such as cutting on the angle between the leptons and $\not\!\!E_T$ in the transverse plane serves to reject $Z \rightarrow \tau\tau$ background as well as direct $Z$ boson decays with mismeasured lepton momenta. The selection cuts for each channel are summarized in Table 5.3.

| | $e\mu$ | $ee$ | $\mu\mu$ |
|---|---|---|---|
| Leptons | $E_T(e) > 25$ GeV<br>$p_T(\mu) > 15$ GeV/c | $E_T(e) > 25, 20$ GeV | $p_T(\mu) > 25, 20$ GeV/c |
| $\not\!\!E_T$ (GeV) | $> 25$ (Cal)<br>$> 20$ (Tot) | $> 25$ | $> 30$ ($E_T^{\eta}$) |
| $M_{ll}$ (GeV/$c^2$) | - | $\lvert M_{ll} - M_Z \rvert > 15$ | - |
| $\Delta\phi$ (degrees) | $20 < (\mu, \not\!\!E_T) < 160$ | $20 < (e_2, \not\!\!E_T) < 160$ | $(\mu_1, \not\!\!E_T) < 160$ |
| $\lvert \vec{E}_T^{Had} \rvert$ (GeV) | $< 40$ | $< 40$ | $< 40$ |
| $\Delta$R(l,l) | $> 0.5$ | - | - |

Table 5.3: Kinematic and topological event selection cuts

In the dielectron channel, two high $E_T$ electrons are required. The threshold on the leading electron is set in order to avoid bias from the trigger requirement on the electron. The second electron threshold is lower to increase acceptance, but must remain relatively high in order to avoid introducing additional background from electron fakes from jets (see section 6.1.2). The requirement on the $\not\!\!E_T$ is set in order to avoid trigger bias. This cut also serves to reject $Z \rightarrow ee$ events with mismeasured electron or recoil system energies. The requirement on the dielectron invariant mass is also designed to reject $Z$ boson events. The angular cut between the second electron and $\not\!\!E_T$ is designed to reduce background from $Z$ bosons decaying through $\tau$'s. This cut is released for events with very large $\not\!\!E_T$ in order to restore detection efficiency for non-SM $W$ pair production (see figure 5.2). Finally, we introduce the variable $\vec{E}_T^{Had}$ [98] which is defined as the vector sum of the leptonic energy (including neutrinos) in the event:

$$\vec{E}_T^{Had} = -(\vec{E}_T^{l_1} + \vec{E}_T^{l_2} + \vec{\not\!\!E}_T\ ).$$

This variable is designed to reject $t\bar{t}$ events, which are always accompanied by at least two jets, and is applied in all the search channels. While reducing the background from top production, this cut also results in the loss of detection efficiency for $W$ boson pair events from higher order diagrams.

In the $e - \mu$ channel, the requirements on the electron $E_T$ and calorimeter $\not\!\!E_T$ are the same as in the $ee$ channel. The calorimeter $\not\!\!E_T$ is defined as the missing

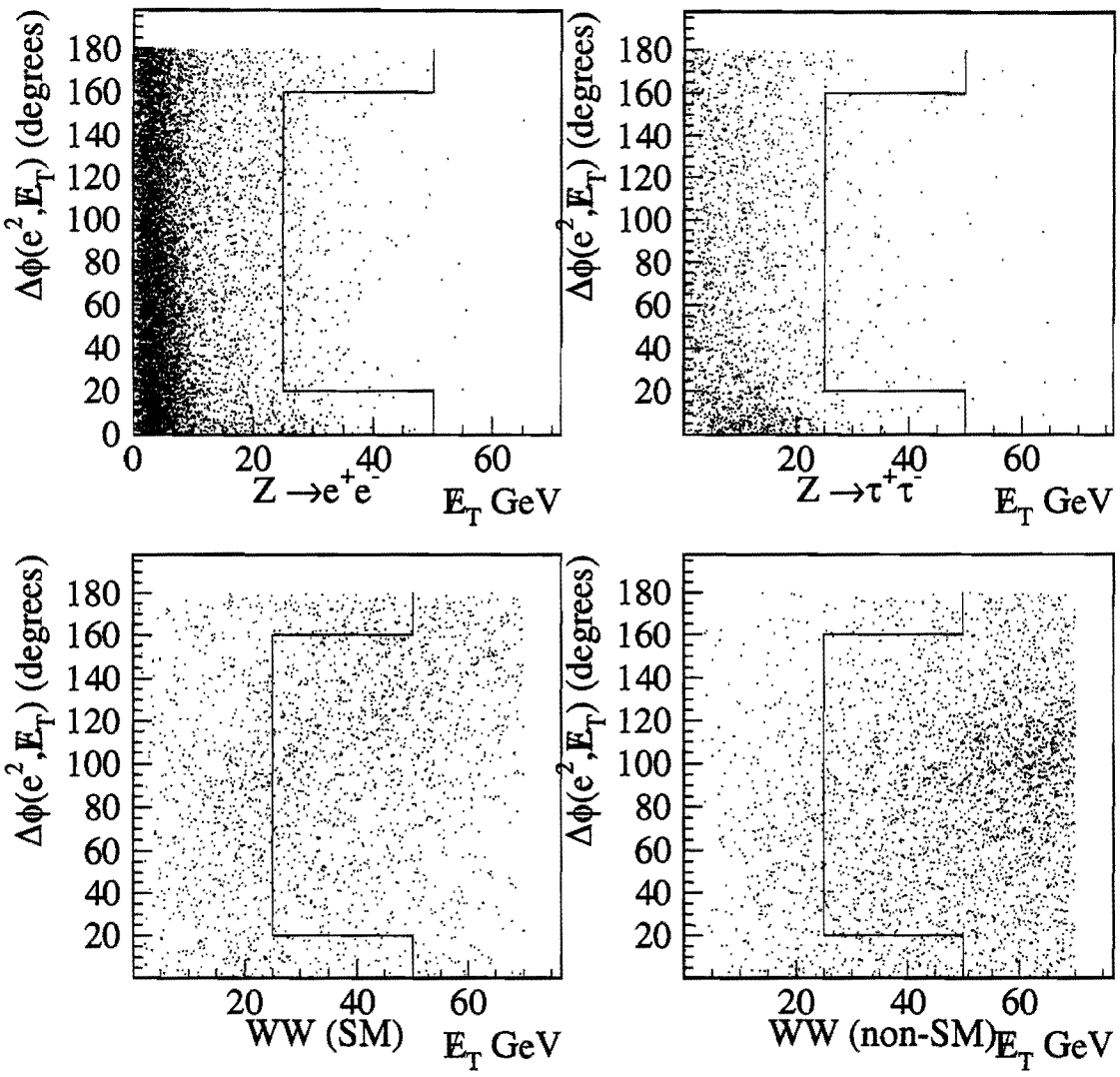


Figure 5.2: Distributions of $\Delta\phi(E_T^{e_2}, \not{E}_T)$ vs $\not{E}_T$ for $Z$, $Z \to \tau^+\tau^-$, Standard Model $W$ pair (PYTHIA, DØRECO v11.19) and non-Standard Model $W$ pair (fast Monte Carlo, DIPS) events in the dielectron channel.

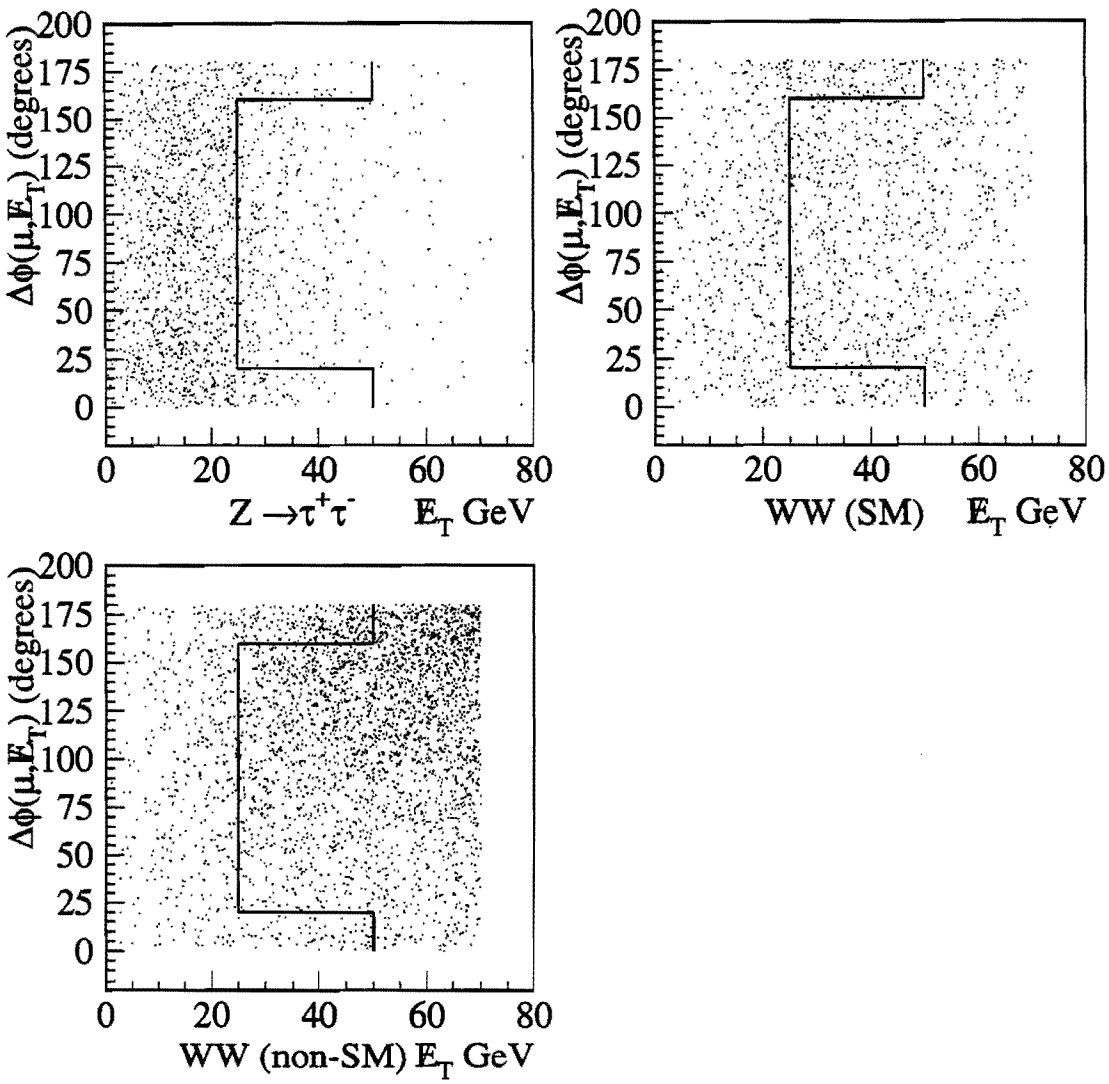


Figure 5.3: Distributions of $\Delta\phi(p_T^{\mu}, \not{E}_T)$ vs $\not{E}_T$ for $Z \to \tau^+\tau^-$, Standard Model $W$ pair (PYTHIA, DØRECO v12.20) and non-Standard Model $W$ pair (fast Monte Carlo, DIPS) events in the $e - \mu$ channel.

$E_T$ calculated using only calorimeter hits. These thresholds are set to avoid trigger biases. The requirements on the muon $p_T$ as well as the total (corrected for the muon) $\not{E}_T$ are looser to increase acceptance. Similar to the dielectron channel, the cut on the angle between the muon and the total $\not{E}_T$ is used to reduce background from $Z \rightarrow \tau\tau$ (see figure 5.3). The muon is used here because it is more likely to be mismeasured than the electron. The isolation cut between the muon and electron is applied to remove background from partially reconstructed cosmic ray muons which emit a brehmstrallung photon.

In the dimuon channel, both muons are required to have relatively high $p_T$. The thresholds are set to increase the trigger efficiency, and to reduce the background from low $p_T$ dimuon production from sources like $b\bar{b} \rightarrow \mu\mu$. Because the muon momentum resolution is poor, the $\not{E}_T$ is subject to large mismeasurement. Similarly, the dimuon invariant mass is also subject to large mismeasurement. To serve the purpose of both of these cuts, we define the variable $E_T^{\eta}$ as the projection of the $\not{E}_T$ onto the bisector of the muons in the transverse plane. This variable is much less sensitive to the muon momentum resolution. In addition to confirming the presence of real $\not{E}_T$ from a possible $W$ pair event, the cut on $E_T^{\eta}$ also serves to reject $Z \rightarrow \mu\mu$ events with missing $E_T$ due to mismeasurement of the muon momenta. The angular cut used is similar to the one used in the other two channels (see figure 5.4), but differences are made to account for the reduced resolution in this channel. The leading muon is chosen in this case because it is most likely to

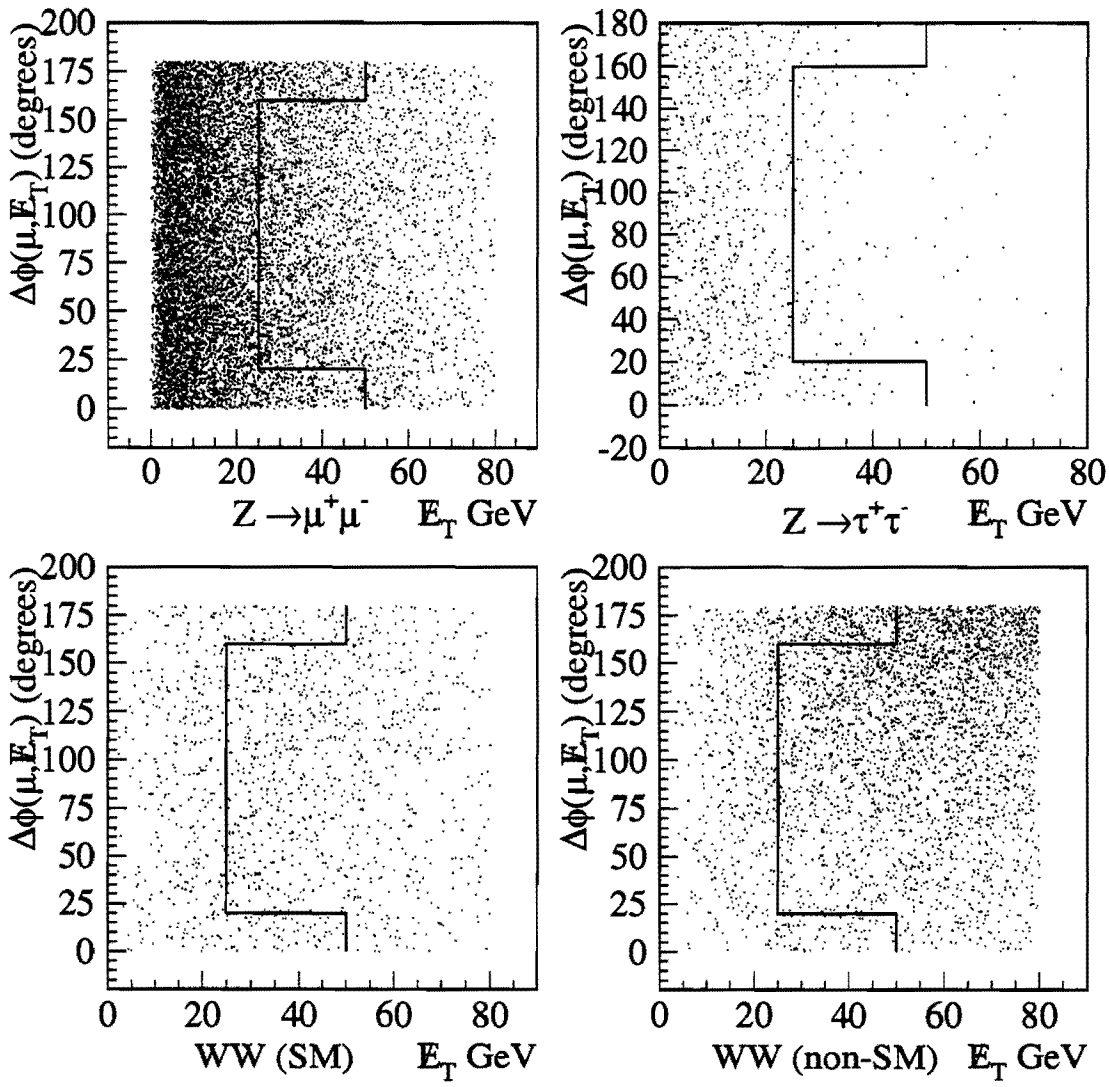


Figure 5.4: Distributions of $\Delta\phi(p_T^{\mu 2}, \not{E}_T)$ vs $\not{E}_T$ for $Z$, $Z \to \tau^+\tau^-$, Standard Model $W$ pair (PYTHIA, DØRECO v12.20) and non-Standard Model $W$ pair (fast Monte Carlo, DIPS) events in the dimuon channel.

have been mismeasured, as muon mismeasurements tend to inflate the value of the momentum. The $\not\!\!E_T$ escape is not applied in this channel due to the poor resolution on $\not\!\!E_T$ .

Four dilepton $W$ pair candidates were identified in the Run 1B data set. The characteristics of these candidates can be found in Tables 5.4, 5.5, 5.6 and 5.7. Event displays of these candidates can be found in appendix A.

| Run 84634 Event 15628 | Electron 1 | Electron 2 |
|---|---|---|
| $E_T$ (GeV) | 26 | 22 |
| $\eta$ (rad) | -0.81 | -1.84 |
| $\phi$ (rad) | 2.80 | 6.12 |
| Electron Likelihood | 0.028 | 0.042 |
| Isolation | 0.062 | 0.042 |
| $M_{ee} = 50$ GeV/c$^2$ | $\lvert\vec{E}_T^{Had}\rvert = 32$ GeV | |
| $\not\!\!E_T = 26$ GeV | $\Delta\phi(E_T^{e_2}, \not\!\!E_T) = 135°$ | |

Table 5.4: Characteristics of dielectron candidate

| Run 85858 Event 29918 | Electron | Muon |
|---|---|---|
| $E_T$ (GeV) / $p_T$ (GeV/c) | 49 | 20 |
| $\eta$ (rad) | 0.02 | 0.24 |
| $\phi$ (rad) | 1.63 | 5.30 |
| Electron Likelihood / IFW4 | 0.005 | 0 |
| Isolation / HFRAC | 0.016 | 1.00 |
| xy Impact Parameter (cm) | | 5.61 |
| $\lvert t_0^{\text{float}}\rvert$ (ns) | | 8.76 |
| $\int Bdl$ (GeV) | | 0.64 |
| $\not\!\!E_T{}^{Cal} = 42$ GeV | $\lvert\vec{E}_T^{Had}\rvert = 10$ GeV | |
| $\not\!\!E_T{}^{Tot} = 29$ GeV | $\Delta\phi(p_T^{\mu}, \not\!\!E_T) = 38°$ | |

Table 5.5: Characteristics of $e - \mu$ candidate one.

| Run 89545 Event 9149 | Electron | Muon |
|---|---|---|
| $E_T$ (GeV) / $p_T$ (GeV/c) | 34 | 16 |
| $\eta$ (rad) | 0.71 | -0.98 |
| $\phi$ (rad) | 3.47 | 1.32 |
| Electron Likelihood / IFW4 | 0.006 | 1 |
| Isolation / HFRAC | 0.073 | 1.00 |
| xy Impact Parameter (cm) | | -1.49 |
| $\lvert t_0^{\mathrm{float}} \rvert$ (ns) | | 117 |
| $\int Bdl$ (GeV) | | 0.84 |

$\not{E}_T{}^{Cal} = 34$ GeV $\quad |\vec{E}_T^{Had}| = 11$ GeV
$\not{E}_T{}^{Tot} = 33$ GeV $\quad \Delta\phi(p_T^{\mu}, \not{E}_T) = 75°$

Table 5.6: Characteristics of $e - \mu$ candidate two.

| Run 92217 Event 2858 | Muon 1 | Muon 2 |
|---|---|---|
| $p_T$ (GeV/c) | 30 | 28 |
| $\eta$ (rad) | -0.52 | 0.16 |
| $\phi$ (rad) | 0.31 | 1.97 |
| IFW4 | 0 | 0 |
| HFRAC | 1.00 | 1.00 |
| xy Impact Parameter (cm) | 3.42 | 3.86 |
| $\lvert t_0^{\mathrm{float}} \rvert$ (ns) | 13.2 | 52.3 |
| $\int Bdl$ (GeV) | 0.71 | 0.65 |

$E_T^{\eta} = 42$ GeV $\quad |\vec{E}_T^{Had}| = 6$ GeV
$\Delta\phi(p_T^{\mu_1}, \not{E}_T) = 142°$

Table 5.7: Characteristics of dimuon candidate

## 5.3 Detection Efficiencies and Standard Model Expectations

In order to either measure or place limits on the $W$ pair cross section, it is necessary to know the detection efficiency for the set of selection cuts used. In this analysis, the detection efficiency for the signal is estimated using Standard Model $W$ pair events generated by the Monte Carlo of, and simulated by the DIPS parametric detector simulation. The geometric and kinematic efficiencies were cross checked using PYTHIA events which were fully simulated. Trigger and particle identification efficiencies measured from the data were input to the DIPS simulation, and the overall detection efficiency was given by the ratio of the number of simulated events passing all the cuts to the number of events generated. Tables 5.8, 5.9 and 5.10 list the detection efficiencies, along with statistical and systematic uncertainties, for each channel.

| Region | Fraction of Events in Region | Detection Efficiency in Region |
|---|---|---|
| CC/CC | 0.4274 | 0.1037 |
| CC/EC | 0.2041 | 0.0684 |
| EC/EC | 0.0303 | 0.0684 |
| All | 1.00 | $0.0603 \pm 0.0010(stat) \pm 0.0035(sys)$ |

Table 5.8: Detection efficiencies for the dielectron channel

| Region | Fraction of Events in Region | Detection Efficiency in Region |
|---|---|---|
| CF/CC | 0.3634 | 0.1130 |
| CF/EC | 0.0971 | 0.0673 |
| All | 1.00 | $0.0476 \pm 0.0009(stat) \pm 0.0048(sys)$ |

Table 5.9: Detection efficiencies for the $e - \mu$ channel

| Region | Fraction of Events in Region | Detection Efficiency in Region |
|---|---|---|
| CF/CF | 0.3808 | 0.0313 |
| All | 1.00 | $0.0119 \pm 0.0005(stat) \pm 0.0018(sys)$ |

Table 5.10: Detection efficiencies for the dimuon channel.

The statistical uncertainty on the detection efficiencies are due to the number of events generated. The systematic uncertainties come from a variety of sources, and are listed in Table 5.11. The "Monte Carlo" uncertainty is included to cover the small discrepancies between the standard and fast detector simulation.

| Source | Fractional Uncertainty |
|---|---|
| Electron Trigger Efficiency | 2.0% |
| Muon Trigger Efficiency | 8.4% |
| Electron Identification Efficiency (CC) | 1.4% |
| Electron Identification Efficiency (EC) | 3.0% |
| Muon Identification Efficiency | 7.5% |
| Monte Carlo | 5% |

Table 5.11: Sources of systematic uncertainty for the prediction of $WW \rightarrow$ dilepton detection efficiencies.

To compute expected Standard Model event yields, we use the following expression:

$$N_{exp} = \sigma \cdot BR \cdot \epsilon_{det} \cdot \mathcal{L},$$

where $BR$ is the branching ratio, $\epsilon_{det}$ is the detection efficiency, and $\mathcal{L}$ is the integrated luminosity for a given the channel. The detection efficiencies and luminosities for each of the three search channels in this analysis have been discussed above. The branching ratio for $WW \rightarrow \ell\bar{\nu}_\ell\bar{\ell}\nu_\ell$ is given by the square of the $W \rightarrow \ell\bar{\nu}_\ell$ branching ratio. In the most recent world average, $BR(W \rightarrow \ell\bar{\nu}_\ell) = (10.8 \pm 0.4)\%$ [39]. The theoretical prediction for the cross section is 9.4 pb, as discussed in 1.3.2

Using the above parameters, we have calculated predictions for purely leptonic $WW$ events based on SM efficiencies. These predictions are shown in table 5.12. The statistical uncertainty is due entirely to the number of events generated in the determination of the detection efficiency. The systematic uncertainty includes contributions from the $W \rightarrow l\bar{\nu}_l$ branching ratio, and a 5% uncertainty in the $W$ pair cross section calculation due to choice of PDF and evolution scale. The luminosity uncertainty is as discussed above.

| Decay Channel | $N^{SM}_{expected}$ |
|---|---|
| $ee$ | $0.544 \pm 0.001(stat) \pm 0.043(sys) \pm 0.029(lum)$ |
| $e\mu$ | $0.858 \pm 0.016(stat) \pm 0.087(sys) \pm 0.045(lum)$ |
| $\mu\mu$ | $0.085 \pm 0.003(stat) \pm 0.013(sys) \pm 0.004(lum)$ |

Table 5.12: Predicted event yields for Standard Model $WW$ production.

# Chapter 6

# Backgrounds

As discussed earlier, there are sources other than leptonic $W$ pairs which can produce dilepton + $\not\!\!E_T$ final states. In order to make a meaningful comparison between theoretical predictions and experimental observation, it is necessary to estimate the fraction of observed candidates which are not due to $W$ pair production. Although there are many possible sources of background, they all may be estimated in one of two ways. If the background mechanism is well known, and the production cross section reliably calculated or well measured, it is possible to estimate its contribution to the final sample using methods similar to those employed to estimate the expected signal. If this is not possible, data-based techniques must be used to estimate the background contribution. In this chapter, we describe the estimation of the background contribution to the observed dilepton + $\not\!\!E_T$ signal from two classes of background sources: instrumental and dilepton.

## 6.1 Instrumental Backgrounds

We define instrumental backgrounds as processes which fake the dilepton + $\not\!\!E_T$ signature of $W$ pair production via the production of a "fake" lepton. For electrons, this can occur either via a jet or a photon which mimics or "fakes" the response expected from an electron. It is possible, for example, for a jet to hadronize such that it fragments into a leading $\pi^0$ which then decays into $\gamma\gamma$. If the $\pi^0$ is of sufficient transverse energy ($E_T > 10$ GeV), the spatial resolution of the calorimeter will be inadequate to distinguish the resulting electromagnetic shower as resulting from two particles. If either of the photons were to convert, or if there were a random track overlap of a low $E_T$ charged hadron either from the underlying event or from the remainder of the jet, the resulting shower + track would be difficult to distinguish from that of a true electron. A single photon could also be misidentified in a like manner.

The possibility for a jet being misidentified as an electron leads to background from multijet production (in which two jets must fake electrons) and more importantly, from single $W$ production (where the $W$ decays leptonically) in association with jets (one of which must fake the electron). Similarly, the possibility of a photon being misidentified as an electron leads to background from $W\gamma$ production. Backgrounds from $W$+jets, and $W\gamma$ are discussed below.

For muons, the "fake" does not result from the misidentification of a muon,

but because a real muon may be produced as a decay product within a jet at an angle such that it passes the isolation cut ($\Delta R(\mu, jet) < 0.5$) designed to reject such muons. For example, a jet may hadronize such that a kaon with substantial $E_T$ is produced within the jet. The kaon could then decay into a muon produced at a sufficient angle away from the rest of the jet such that it passes the muon/jet isolation cut. Such muons are also possible (and more probable) in jets resulting from heavy quark decays. The possibility of such muon fakes leads to background from single $W$ production (again, decaying leptonically) in association with jets, and also from $b\bar{b}$ production. Backgrounds from isolated hadronically produced muons are also discussed below.

### 6.1.1 Misidentification of Photons as Electrons

The cross section $\times$ branching ratio for $W\gamma \rightarrow l\gamma$ is two orders of magnitude larger than that for leptonic $W$ pairs. If the photon is misidentified as an electron, then an $e\gamma + \not{E}_T$ ($\mu\gamma + \not{E}_T$) final state becomes an $ee + \not{E}_T$ ($e\mu + \not{E}_T$) final state, faking the $W$ pair signal. It is therefore important to understand how often such a misidentification can occur.

For a photon to be misidentified as an electron in this analysis, it must first be misreconstructed as an electron. This can occur via two mechanisms; photon conversion into $e^+e^-$ pair, or the random overlap of a track from a low $E_T$ charged hadron. The photon conversion probability has been determined from Monte Carlo

photons which have been passed through full detector simulation and reconstructed. This probability depends strongly on the amount of material traversed by the photon, and is well suited to be evaluated from Monte Carlo. For photons in the CC (EC), the average conversion probability was determined to be 0.102 (0.268). The random track overlap probability was determined from the data [99]. Electromagnetic clusters from $Z \rightarrow ee$ candidate events were rotated by an arbitrary angle in $\phi$, and the event examined to see if a track could be found in the required $\Delta\eta \times \Delta\phi$ road (based on the new cluster location). Because this probability depends on the distribution of hadrons from the underlying event (which is not well modeled by Monte Carlo generators), the data provides the only accurate means of determining this probability. For photons in the CC (EC), the average random track overlap probability was measured to be 0.139 (0.161). The sum of the conversion and overlap probabilities gives the probability for the photon to be misreconstructed as an electron.

Once the photon has been misreconstructed, it must further pass the likelihood and isolation cuts. The efficiency of the isolation cut for photons is assumed to be the same as that for electrons, hence any rejection of such photons by the electron identification cuts will be achieved through the likelihood cut. Each of the mechanisms responsible for electrons originating from photon misreconstructions can be distinguished by one of the variables used in the calculation of the electron

likelihood. Conversions will have $dE/dx$ peaked around two MIPS[1] instead of one for real electrons. Random track overlaps will have a distribution of track match significance which is essentially flat, rather than one which is peaked near zero. To measure the rejection due to the likelihood cut, the likelihood function was used to evaluate input for simulated conversions and overlaps. To simulate conversions, the $dE/dx$ distribution for conversions used by the likelihood function was sampled as input for the likelihood calculation. The values for the remaining variables were chosen by sampling from the distributions of good electrons used by the likelihood. Similarly, to simulate random track overlaps, the track match significance distribution which the likelihood function uses for hadron overlaps was sampled as input for the likelihood calculation, with the remaining variables being provided as above. 10000 each of converted and overlaped photons were examined, along with 10000 electrons taken entirely from the good electron distributions used in the likelihood function. Table 6.1 shows the relative efficiencies of the likelihood cuts. Each ratio carries a fractional uncertainty (combined statistical and systematic) of 3%. Given

| Cryostat | $\epsilon_{conversion}/\epsilon_e$ | $\epsilon_{overlap}/\epsilon_e$ |
|---|---|---|
| CC | 0.357 | 0.164 |
| EC | 0.488 | 0.717 |

Table 6.1: Relative electron ID efficiencies for photons with tracks

[1]A MIP is defined as the most probable $dE/dx$ deposited by an ultra-relativistic particle. The $dE/dx$ of such a particle is independent of it's mass.

these parameters, the efficiency for a photon to be misidentified as an electron is given by

$$\epsilon_{\rm eID} \times (P(conversion) \times \epsilon_{conversion}/\epsilon_e + P(overlap) \times \epsilon_{overlap}/\epsilon_e).$$

To estimate the dielectron background event yield due to $W\gamma$ production, 2494 PYTHIA $W\gamma \rightarrow e\gamma$ events were generated, simulated and reconstructed. The fiducial, kinematic and topological event selection criteria were applied to the sample, with 20 events passing all the cuts. The resulting passing fraction was multiplied by the electron identification (including the above modified efficiency for photons) and trigger efficiencies to give the total detection efficiency. Along with the DØ measured cross section for $W\gamma \rightarrow l\gamma$ [59], this resulted in a background estimate of

$$N^{ee}_{background}(W\gamma \rightarrow e\gamma) = 0.179^{+0.072}_{-0.042} \pm 0.040(sys) \pm 0.009(lum)\ events.$$

The statistical uncertainty in this estimate results from the numbers of generated and passing events, the systematic uncertainty results from those sources (as appropriate) listed in table 5.11 in addition to the uncertainties on the relative efficiencies for electron identification applied to the photon, and the uncertainty in the $W\gamma$ cross section.

To estimate the $e - \mu$ background event yield due to $W\gamma$ production, 1299 (1299) PYTHIA $W\gamma \rightarrow \mu\gamma$ events were generated, simulated and reconstructed using pre (post) shutdown MUSMEAR parameterizations. The fiducial, kinematic and topological event selection criteria were applied to the sample, with 10 (11)

events passing all the cuts in the pre (post) shutdown sample. The resulting passing fractions were multiplied by the appropriate particle identification (including the above modified efficiency for photons) and trigger efficiencies to give the total detection efficiency. Along with the DØ measured cross section for $W\gamma \rightarrow l\gamma$, this resulted in a background estimate of

$$N^{e\mu}_{background}(W\gamma \rightarrow \mu\gamma) = 0.346^{+0.142}_{-0.081} \pm 0.080(sys) \pm 0.018(lum)\ events.$$

The uncertainties are as above.

### 6.1.2 Misidentification of Jets as Electrons

The cross section $\times$ branching ratio for $W+$ jets production is four orders of magnitude larger than that for leptonic $W$ pairs. If a jet is misidentified as an electron, then an $ej + \not{E}_T$ ($\mu j + \not{E}_T$) final state becomes an $ee + \not{E}_T$ ($e\mu + \not{E}_T$) final state, faking the $W$ pair signal. This process is potentially the largest background to the $W$ pair signal, and therefore must be studied carefully to determine how often such misidentifications occur.

To estimate the fraction of the $e\ell + \not{E}_T$ ($\ell = e, \mu$) final state due to misidentified jets in a specific process (such as multijets), it is necessary to know the frequency with which jets mimic electrons as well as the cross section for that process. Although the cross sections for some of the possible background processes are measured at DØ, the details of the jet fragmentation are not. Instead, we turn to a

data based technique to measure the background. This method is independent of the physical origin of the background, and includes contributions from multijets as well as $W$+jets.

First, the misidentification frequency of jets as electrons is measured using data samples collected using triggers based only on calorimeter towers. Such samples are overwhelmingly dominated by multijet production. Thus any electrons identified in the samples are likely due to jet misidentifications. Details of the measurement of the jet misidentification probability are given in appendix B. These "fake rates" depend not only on the electron selection criteria (as expected), but also on the jet transverse energy. The measured transverse energy dependences are approximately linear, so the fake rate $P(E_T)$ can be parameterized as

$$P = a_0 + a_1 E_T,$$

where $a_0$ and $a_1$ are measured by fitting the data. Table 6.2 summarizes the measurements. The dominant statistical uncertainty is due to the limited number of electron candidates remaining after imposing cuts. It should be noted that the fit parameters are strongly anticorrelated. The covariance matrices and correlation coefficients were obtained from MINUIT [100], and the correlation coefficient for the CC (EC) fit was found to be -0.87 (-0.93). The systematic uncertainty is dominated by the uncertainty in the amount of direct photon contamination in the multijet data sample. This uncertainty is not reflected in the fit parameters, but is *estimated*

for the entire background by calculating the background using fake rates with and without the correction for the photon content. The systematic uncertainty is then assigned to be half the difference between the two results.

| Cryostat | $a_0 \times 10^5$ | $a_1 \times 10^6$ |
|---|---|---|
| CC | $-0.017 \pm 4.681$ | $1.857 \pm 1.550$ |
| EC | $6.187 \pm 13.750$ | $1.771 \pm 4.695$ |

Table 6.2: Jet misidentification probabilities for electrons. Uncertainties are statistical (fit) only.

Given the fake probabilities, the background is estimated by assembling a sample of all events containing $e(\mu)j + \not\!\!E_T$ (the fake candidate sample) and applying the fake probability to the jet $E_T$ spectrum of events passing all selection criteria except electron identification on the jet (would be electron).[2] Integration of the resulting distribution results in the background event estimate.

In the dielectron channel, the fake candidate sample is composed of all events which contain an electron, $\not\!\!E_T$ and at least one jet. All on and off-line event selection criteria are applied to this sample with the exception of electron identification criteria on the jet (the would-be second electron). Events with two or more jets may contribute to the final sample more than once, providing that the event passes all cuts for the choice of a given jet as the fake electron candidate. Figure 6.1 shows the

[2]Events with any numbers of jets are allowed in the sample. However, events with more than one jet would be much more likely to fail the $\vec{E}_T^{Had}$ cut.

jet $E_T$ distributions for events which pass all the selection cuts. This distribution is convoluted with the $P(j \rightarrow e)$ distribution and integrated. This results in a fake background estimate of

$$N^{ee}_{background}(ej + \not{E}_T\ ) = 0.195 \pm 0.133(stat) \pm 0.021(sys)\ events.$$

The statistical uncertainty here includes the bin by bin uncertainty on the number of events in the fake background candidate sample, and the statistical uncertainty on the fake rate fit parameters, taking into account their strong anti-correlation. The systematic uncertainty is as described above.

The estimate of the fake electron background to the $e-\mu$ channel follows the same steps as the dielectron calculation. The fake candidate sample is composed of all events which contain a muon, $\not{E}_T$ and at least one jet. These events must pass all the off-line selection cuts with the exception of electron identification on the jet. The difference from the dielectron channel is in the application of the on-line cuts. Because there is no real electron in the event, demanding that the event pass an L2 filter with an electron trigger term would bias the sample. Instead, we must trigger on another object in the event. The muon is the best choice for this, and the combination of the `MU_1_MAX` and `MU_1_CENT_MAX` filters used in the dimuon analysis was chosen. Because of this choice for trigger, the background calculation must be scaled to account for the relative differences in efficiency and luminosity between the two sets of triggers. As in the dielectron channel, events with two or more jets may

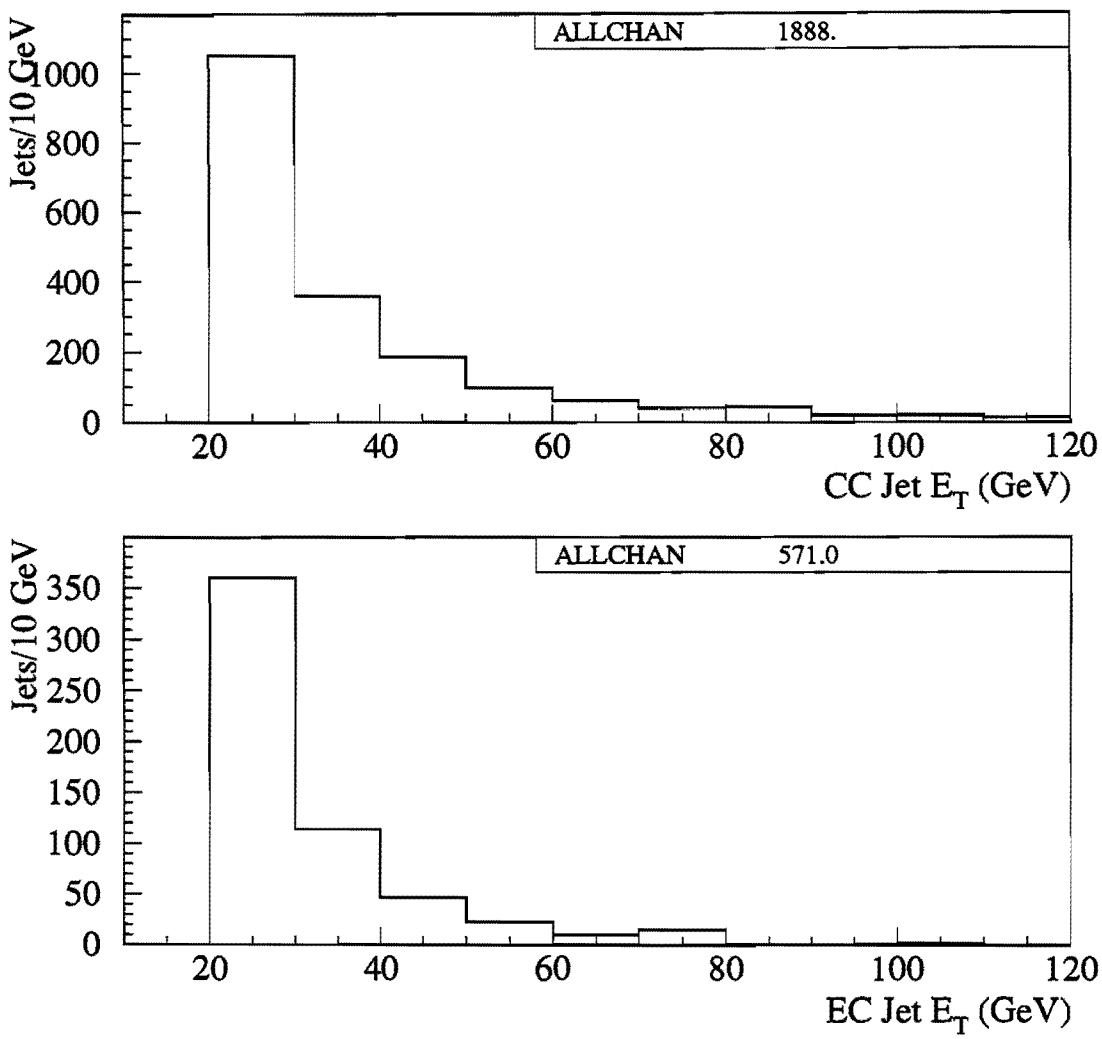


Figure 6.1: Jet $E_T$ distribution for dielectron fake candidate sample events passing all selection cuts.

contribute to the final sample more than once, provided that the event passes all cuts for the choice of a given jet as the fake electron candidate. Figure 6.2 shows the jet $E_T$ distributions for events which pass all the selection cuts. The ratios of the pre and post shutdown luminosities for the various filters, along with the relative trigger efficiencies for a muon with $p_T > 15$ GeV/c are shown in table 6.3. Convoluting the jet $E_T$ distribution with the $P(j \rightarrow e)$ rates, and scaling by the relative luminosities and trigger efficiencies gives a background estimate of

$$N^{e\mu}_{background}(\mu j + \not{E}_T\ ) = 0.396 \pm 0.279(stat) \pm 0.039(sys) \pm 0.021(lum)\ events.$$

The statistical uncertainty is as above. The systematic uncertainty is also as above, with the additional uncertainty due to the relative trigger efficiencies. There is also a luminosity uncertainty due to the scaling of one trigger to the other.

| | $\int \mathcal{L}(\mu/e)$ | $\epsilon_{trig}(\mu)/\epsilon_{trig}(e)$ |
|---|---|---|
| Pre-shutdown | $0.821 \pm 0.044$ | $0.334 \pm 0.036$ |
| Post-shutdown | $0.768 \pm 0.041$ | $0.308 \pm 0.045$ |

Table 6.3: Relative luminosities and trigger efficiencies for $e - \mu$ fake candidate sample.

### 6.1.3 Production of Isolated Muons in Association with Jets

The final type of instrumental background to consider is the background resulting from hadronically produced muons which pass the jet isolation criterion.

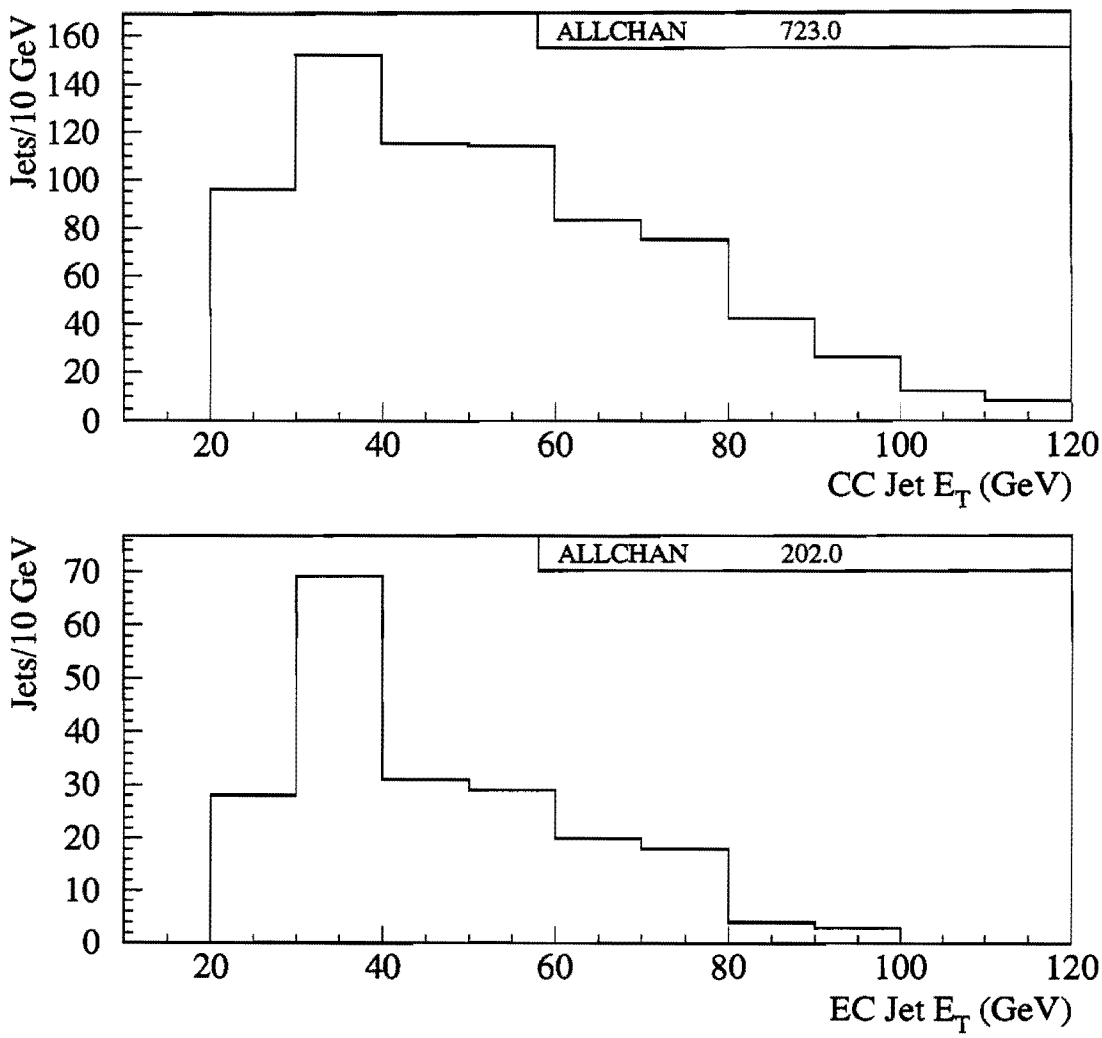


Figure 6.2: Jet $E_T$ distribution for $e - \mu$ fake electron candidate sample events passing all selection cuts.

Again, since the cross sections for $W$+jets and heavy quark production are several orders of magnitude larger than that for $W$ pairs, it is necessary to understand how often these processes can mimic the signal. To estimate the fraction of the $e(\mu)+\not\!\!E_T$ background due to such muons, we follow the example of the background study for jets misidentifications as electrons, determining the frequency with which the fake can occur, and then applying that probability to a fake candidate sample.

The first step is to determine the frequency with which muons from various hadronic sources pass the jet isolation cut. This is much simpler than in the study of jets faking electrons because we don't need to be concerned with trigger turn-ons or direct photon contamination (see appendix B. The only cut applied to the sample is the removal of events with large $\not\!\!E_T$ in order to suppress contamination from $W$+jets events, where the $W$ decays to a muon. We then need only ask what is the ratio of number of muons passing all identification criteria to the number of jets (with $E_T > 10$ GeV) in the sample (the starting sample is the same sample used for the fake electron study). Because this number turns out to be very small, and because there is an ambiguity as to which jet a muon may have originated from, we express the answer as an integrated ratio, rather than a probability distribution as a function of jet $E_T$. The results of this study are shown in table 6.4 for muon $p_T$ thresholds of 15 and 20 GeV/c. Based on the variation of the number of passing muons with $p_T$ threshold, we assign a systematic uncertainty of 10% to the number of passing muons. There is also a 1.8% statistical uncertainty due to the limited

number of muons found.

| $p_T$ cut (GeV/c) | # Muons Passing | # Jets ($E_T > 10$ GeV | Ratio Muons/Jets |
|---|---|---|---|
| 15 | 29 | 1,990,355 | $1.46 \times 10^{-5}$ |
| 20 | 20 | 1,990,355 | $1.00 \times 10^{-5}$ |

Table 6.4: Secondary muons surviving all cuts.

While the above study is sufficient for typical jets produced in association with $W$'s, we must take care when considering jets resulting from heavy quark production. Such jets will have a higher fake probability because heavy quarks can decay semileptonically into muons. To more accurately estimate the background contribution from such processes, we repeat the above study on a sample of jets whose heavy flavor content has been enhanced. To do this, we require the presence of a muon on the away side of the leading (highest $E_T$) jet in the event, in addition to the other selection criteria described above. The results of this study are shown in table 6.5. As expected, the fake probabilities are in excess of a factor of ten larger than in the unenhanced case. As above, we assign a systematic uncertainty of 10%, but a statistical uncertainty of 2.1%.

With fake rates in hand, we consider the possible backgrounds in each channel to determine what the fake background candidate sample is. In the $e-\mu$ channel, we are primarily concerned with background coming from $W(e\nu)$+jets. These jets

| $p_T$ cut (GeV/c) | # Muons Passing | # Jets ($E_T > 10$ GeV | Ratio Muons/Jets |
|---|---|---|---|
| 15 | 20 | 80,054 | $2.50 \times 10^{-4}$ |
| 20 | 12 | 80,054 | $1.49 \times 10^{-4}$ |

Table 6.5: Secondary muons surviving all cuts (heavy quark enhanced).

rarely contain charm or bottom, so the fake rates are best described by the unenhanced version of the muon fake probability. The background candidate sample for these event includes all events with an electron, $\not\!\!E_T$ , and at least one jet (the source of the would-be fake muon). The event must pass all on and off-line event selection criteria, except for muon identification (there need not be an actual muon in the event). This sample is identical to the fake sample used in the determination of the fake electron background to the dielectron channel. The jet $E_T$ distribution is shown in figure 6.1. Scaling this distribution by the probability for a typical jet to produce a high $p_T$, isolated muon, and then integrating yields a background prediction of

$$N^{e\mu}_{background}(ej + \not\!\!E_T\ ) = 0.036 \pm 0.001(stat) \pm 0.004(sys)\ events.$$

The statistical uncertainty on this calculation is due to the statistical uncertainty on the muon fake rate, and the statistics of the fake background candidate sample. The systematic uncertainty is due entirely to the systematic uncertainty on the muon fake rate.

Processes involving heavy quark ($b\bar{b}$) production could also, in principle, be a source of background to the $e - \mu$ channel. However, the source of significant

missing $E_T$ in such events is usually due to a mismeasured muon. So while the total $\not\!\!E_T$ in such an event may be large, the calorimeter $\not\!\!E_T$ will be small as there is no high $E_T$ electron neutrino in the event. As such, these events are efficiently rejected by the calorimeter missing $E_T$ requirement, and no detailed study was made of this background. We assign a conservative upper limit on the background from $b\bar{b}$ production as

$$N^{e\mu}_{background}(b\bar{b}) < 10^{-3}\ events.$$

In the dimuon channel, we proceed in the same manner as in the $e-\mu$ channel. Here we are interested in two processes which provide the major source of fake background in this channel. The first is similar to the background in the $e-\mu$ channel. Here, the production of $W(\mu\nu)$+jets becomes a potential background if the jets are accompanied by high $p_T$, isolated muons. The background candidate sample for this background consists of event which contain and muon, $\not\!\!E_T$ , and one or more jets. The event must pass all the on and off-line selection cuts, with the exception of muon identification (again, there need not be a second muon in the event). This sample is similar to the sample used to determine the fake electron background to the $e-\mu$ channel, but the $p_T$ threshold on the muon is higher. The jet $E_T$ distribution for the sample is shown in figure 6.3. Multiplying this distribution by the fake muon probability for typical jets, and integrating, yields a background

prediction of

$$N^{\mu\mu}_{background}(\mu j + \not{E}_T\ ) = 0.016 \pm 0.001(stat) \pm 0.002(sys)\ events.$$

Statistical and systematic uncertainties are as above.

Unlike the $e-\mu$ channel, $b\bar{b}$ production provides a non-negligible background to the dimuon channel. To estimate this background, it is worthwhile to note that any $b\bar{b}$ event with one badly mismeasured muon will look very much like a $W(\mu\nu)$+jets event. This in fact results in a sizeable background for the $W$ cross section analysis in the muon channel [101]. Thus, any $b\bar{b}$ event which fakes a $W \rightarrow \mu\nu$ event will already be in the fake background sample used in the above estimate. To estimate this background then, we proceed as in the above with two exceptions. First, instead of using the fake probability derived from the full multijet data, we must use the probability from the heavy quark enhanced sample. Second, because the background candidate sample is primarily real $W$'s, we must estimate the acceptance of our cuts on "fake" $W$'s. We estimate this acceptance to be 6% - the same as the QCD background fraction estimated for the $W \rightarrow \mu\nu$ cross section analysis [101]. Thus, while a fake $W$ has a higher probability of mimicking our signal, there are fewer of these events in the background candidate sample. We thus estimate the background event yield for this process as

$$N^{\mu\mu}_{background}(b\bar{b}) = 0.010 \pm 0.001(stat) \pm 0.001(sys)\ events,$$

with statistical and systematic uncertainties as above.

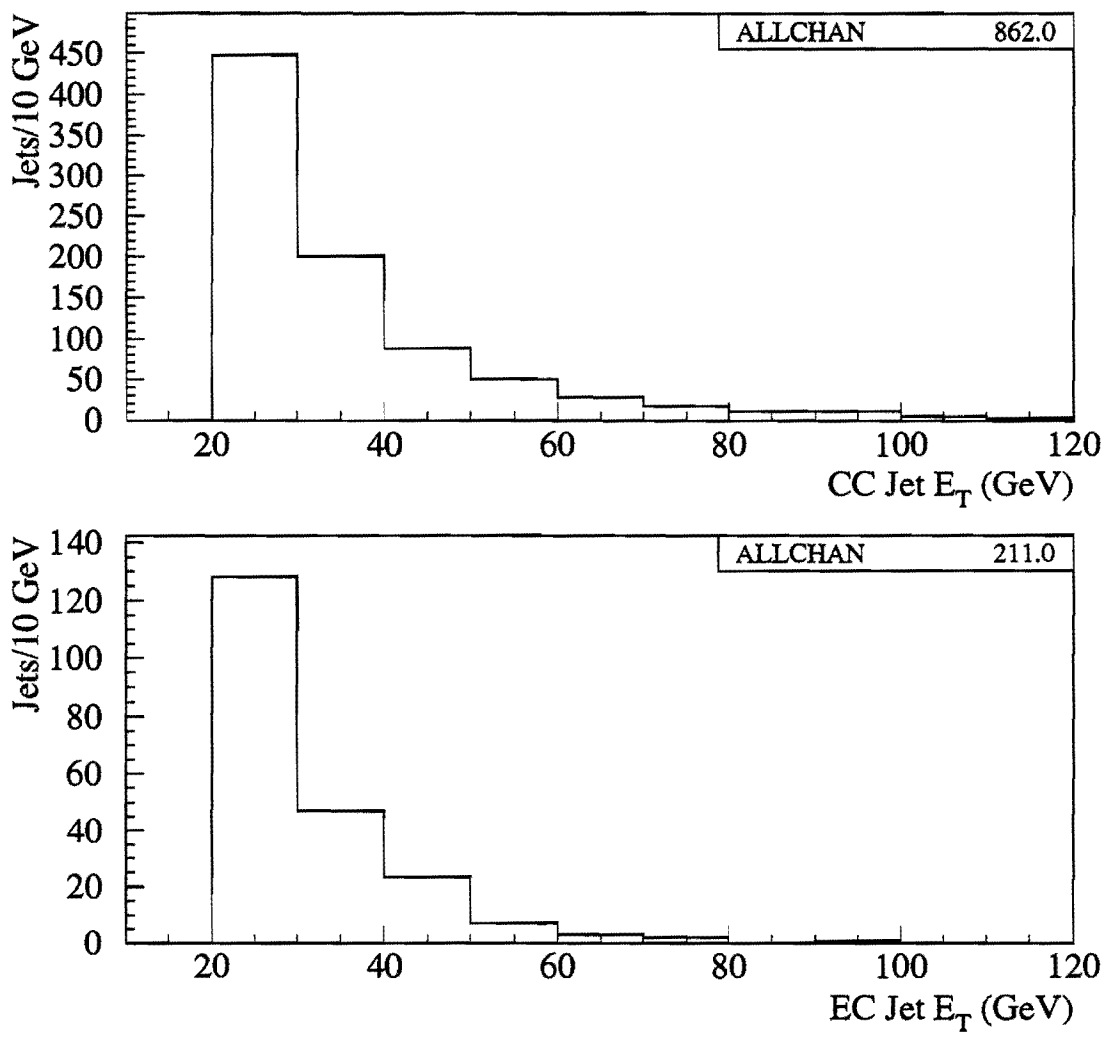


Figure 6.3: Jet $E_T$ distribution for dimuon fake candidate sample.

## 6.2 Dilepton Backgrounds

We define dilepton backgrounds as processes in which two leptons are produced with $\not\!\!E_T$ due either to neutrinos or to the mismeasurement of the transverse energies of the objects in the event. For example, a $Z$ boson decaying directly into electrons will typically produce the necessary dilepton signature of $W$ pairs, but will lack the true $\not\!\!E_T$ typical of $W$ pair production. If the $Z$ is produced at substantial $p_T$ however, the recoil system (one or more jets) may be mismeasured resulting in a net $\not\!\!E_T$ in the event. Backgrounds from direct $Z$ decays, high mass Drell Yan dileptons, $Z$'s decaying through $\tau$'s, and $t\bar{t}$ production are discussed below.

### 6.2.1 $Z \rightarrow ee, \mu\mu$

As discussed above, $Z$ bosons which decay directly into electrons or muons can be a source of background to leptonic $W$ pairs. Although the probability for such events to produce large $\not\!\!E_T$ is small, the cross section $\times$ branching ratio for $Z \rightarrow \ell\ell$ is four orders of magnitude larger than the SM prediction for $W$ pairs ($10^3$ pb vs $10^{-1}$ pb). Because the primary source of $\not\!\!E_T$ (or $E_T^{\eta}$) in such events is expected to be the mismeasurement of the hadronic recoil system, it is necessary to examine $Z$ bosons with very large transverse momenta (and hence with recoil systems with large $E_T$). This, in addition to the large number of events required due to the relative sizes of the cross sections, called for the use of fast Monte Carlos

instead of the standard approach.

To estimate the dielectron background from $Z \rightarrow ee$, 1,549,755 $Z$ boson events were generated with the CMS fast Monte Carlo generator. These events ranged from $0 < p_T^Z < 300$ GeV. Detector simulation was performed by the DIPS fast simulator, treating the entire recoil system as a single hadronic energy deposition (jet) which was then appropriately smeared. After the application of all event selection criteria, 23 events remained. As a cross check, the same cuts (except particle identification and trigger), were applied to a sample of 10,000 ISAJET $Z \rightarrow ee$ events which were fully simulated with DØGEANT and reconstructed. The number of events surviving (one) was consistent with the fast Monte Carlo result. When combined with the DØ measurement of the $Z \rightarrow ee$ cross section $\times$ branching ratio of 218 pb [102], this results in a background estimate of

$$N_{background}(Z \rightarrow ee) = 0.266 \pm 0.056(stat) \pm 0.025(sys) \pm 0.014(lum)\ events.$$

The statistical uncertainty in this estimate results entirely from the number of events generated and passing the cuts. The systematic uncertainty results from those sources (as appropriate) listed in table 5.11, with an additional 5.19% due to the uncertainty on the cross section measurement added in quadrature.[3]

For the dimuon background from $Z \rightarrow \mu\mu$, the same events generated for

[3]In all cases where measured cross sections from DØ were used to compute a background event yield, the systematic uncertainty in that measurement was taken to be the sum in quadrature of the statistical and systematic uncertainty. The luminosity uncertainty was exclude to avoid double counting.

use in the dielectron study were used. The detector simulation proceeded as above, with the exception that the $Z$ decay products were simulated as muons rather than electrons. After the application of all event selection criteria, 43 events remained. As a cross check, the same cuts (except particle identification and trigger) were applied to a sample of 20,000 ISAJET $Z \rightarrow \mu\mu$ events which were fully simulated and reconstructed. The number of events surviving [ 2 (1) using pre-shutdown (post-shutdown) MUSMEAR parameterizations] was consistent with the fast Monte Carlo result. When combined with the DØ cross section $\times$ branching ratio measurement, this resulted in a background estimate of

$$N_{background}(Z \rightarrow \mu\mu) = 0.394 \pm 0.060(stat) \pm 0.064(sys) \pm 0.021(lum)\ events.$$

The statistical and systematic uncertainties are as above.

### 6.2.2 Drell Yan Dileptons

A dilepton background which is very similar to the $Z \rightarrow ee$ $(\mu\mu)$ is the background from high mass Drell-Yan dileptons. The process $q\bar{q} \rightarrow Z^*/\gamma^* \rightarrow ee$ $(\mu\mu)$ can mimic the $W$ pair signature if the leptons are of high enough $p_T$ such that their mismeasurement can lead to sufficient $\not{E}_T$ , or if the Drell-Yan pair is produced with large initial state QCD radiation which is mismeasured. To study this background, 2000 ISAJET Drell-Yan dielectron and dimuon events were generated, simulated and reconstructed in each of four equal ranges of dilepton invariant mass from 100

to 300 GeV/$c^2$. Fiducial, kinematic and topological event selection cuts were applied to each sample. Table 6.6 lists the numbers of events passed in each sample, along with the cross section (from the Monte Carlo) of that sample. Passing fractions were multiplied by the appropriate particle identification and trigger efficiencies to give the total detection efficiency. This resulted in background estimates of

$$N_{background}(Drell - Yan\ ee) = 0.030^{+0.062}_{-0.023} \pm 0.003(sys) \pm 0.002(lum)$$

and

$$N_{background}(Drell - Yan\ \mu\mu) < 10^{-3}\ events.$$

The statistical uncertainty of this estimate is due to the numbers of events generated and passing. The systematic uncertainty is due to the sources (as appropriate) listed in table 5.11.

| $M_{DY}$ (GeV/$c^2$) | $\sigma_{DY}$ (pb) | # Passing ($ee$) | # Passing ($\mu\mu$) |
|---|---|---|---|
| 100 - 150 | 7.7 | 0 | 0 (0) |
| 150 - 200 | 0.61 | 3 | 0 (0) |
| 200 - 250 | 0.0173 | 10 | 0 (0) |
| 250 - 300 | 0.0062 | 10 | 0 (0) |

Table 6.6: Parameters for Drell-Yan backgrounds. For the dimuon channel, the number of passing events is for pre (post) shutdown MUSMEAR parameterizations.

### 6.2.3 $Z \rightarrow \tau\tau$

Unlike the direct decay of $Z$'s into electrons and muons, $Z$'s decaying though $\tau$'s into electrons and muons contain neutrinos and hence real $\not\!\!E_T$ . The leptons from such events, however, tend to have a softer $p_T$ spectrum because they result from $\tau \rightarrow \nu_\tau \ell \nu_\ell$ decays ($\ell = e, \mu$). If the $Z$ is produced at sufficient $p_T$, the additional boost can make these leptons hard enough to pass the selection cuts. To estimate the event yield due to this background, PYTHIA $Z \rightarrow \tau\tau \rightarrow \ell\ell$ ($\ell = e, \mu$) events were generated, simulated and reconstructed in two $p_T^Z$ ranges; 17495 events with $0 < p_T^Z < 25$ GeV, and 28134 events with $p_T^Z > 25$ GeV. Using the DØ measurements of the $Z$ cross section [102] and $p_T^Z$ spectrum [103], along with the ratios for $\tau$ decays [39], the cross sections for these samples are $23.4 \pm 3.0$ pb and $3.19 \pm 0.40$ pb respectively [104].

Fiducial, kinematic and topological event selection criteria for each search channel were applied to the two samples. Table 6.7 lists the numbers of events passing in each channel. The resulting passing fractions were then multiplied by the appropriate particle identification and trigger efficiencies to give the total detection efficiency. This resulted in background estimates of

$$N_{background}(Z \rightarrow \tau\tau \rightarrow ee) = 0.104^{+0.093}_{-0.036} \pm 0.015(sys) \pm 0.006(lum),$$

$$N_{background}(Z \rightarrow \tau\tau \rightarrow e\mu) = 0.212^{+0.099}_{-0.047} \pm 0.028(sys) \pm 0.011(lum),$$

| Channel | # passing, $p_T^Z < 25$ GeV | # passing, $p_T^Z > 25$ GeV |
|---|---|---|
| $ee$ | 1 | 20 |
| $e\mu$ | 3 (2) | 27 (30) |
| $\mu\mu$ | 0 (0) | 0 (0) |

Table 6.7: Number of events passing selection cuts in $Z \to \tau\tau \to \ell\ell$ Monte Carlo samples. For the $e - \mu$ and $\mu\mu$ channels, the first number is for pre-shutdown and the second for post-shutdown MUSMEAR parameterizations respectively.

and

$$N_{background}(Z \to \tau\tau \to \mu\mu) < 10^{-3}\ events.$$

Statistical uncertainties are based on the number of events generated and passed. Systematic uncertainties are as in table 5.11, with the uncertainty on the cross section for each sample added in quadrature.

### 6.2.4 $t\bar{t}$ production

The case of $t\bar{t}$ production is a special case of dilepton background to $W$ pairs. Because it's mass is greater than $m_b + m_W$, the top quark's preferred decay is $t \to W + b$. Thus every $t\bar{t}$ production event contains a pair of $W$ bosons. The distinguishing factor between the top pair production and $W$ pair production comes from the $b$ quarks associated with top decay. Because the top quark is so massive, the typical $t\bar{t}$ event will contain two high $p_T$ bottom quarks, each of which will then decay into jets. These jets distinguish the $t\bar{t}$ final state from the leptonic $W$ pair signature. To take advantage of this, the $\vec{E}_T^{Had}$ variable was designed as a measure

of the hadronic energy in the event (see 5.2.2). Dilepton + $\not{E}_T$ events with large hadronic energy will typically be the result of $t\bar{t}$ production, while such events with small hadronic energy will typically be the result of $W$ pair production.[4] Figure 6.4 shows the distribution of $\vec{E}_T^{Had}$ for both $W$ pair and $t\bar{t}$ Monte Carlo events.

To determine the background from $t\bar{t}$ production, a sample of 10,000 ISAJET $t\bar{t} \rightarrow \ell\ell$ ($\ell = e\mu$) events were generated, simulated and reconstructed. Only 9000 of the events were usable in version of the sample used for the dielectron study which was not processed by the MUSMEAR package. Fiducial, kinematic and topological event selection criteria for each channel were applied to the sample. Table 6.8 lists the number of events passing the selection cuts in each channel. The resulting passing fractions were then multiplied by the particle identification and trigger efficiencies to give the total detection efficiency. Using the DØ $t\bar{t}$ cross section of $5.5 \pm 1.8$ pb [105] results in background estimates of

$$N_{background}(t\bar{t} \rightarrow ee) = 0.130 \pm 0.012 \pm 0.046(sys) \pm 0.007(lum),$$

$$N_{background}(t\bar{t} \rightarrow e\mu) = 0.176^{+0.010}_{-0.009} \pm 0.063(sys) \pm 0.009(lum),$$

and

$$N_{background}(t\bar{t} \rightarrow \mu\mu) = 0.015 \pm 0.003(stat) \pm 0.004(sys) \pm 0.001(lum)\ events.$$

[4]It should again be noted that $W$ pair production due to higher order diagrams can also r in rather large amounts of hadronic energy - primarily due to initial state QCD radiation. diagrams represent about 35% of the total $W$ pair cross section - some of which will be re by this cut. The overall loss to the $W$ pair signal is about 10%. It is of some interest t that should the $W$ have an strongly interacting component, then the amount of QCD ra present in $W$ pair events would be expected to be enhanced. The cut on hadronic energy this analysis would result in a significant loss of sensitivity to such anomalous couplings.

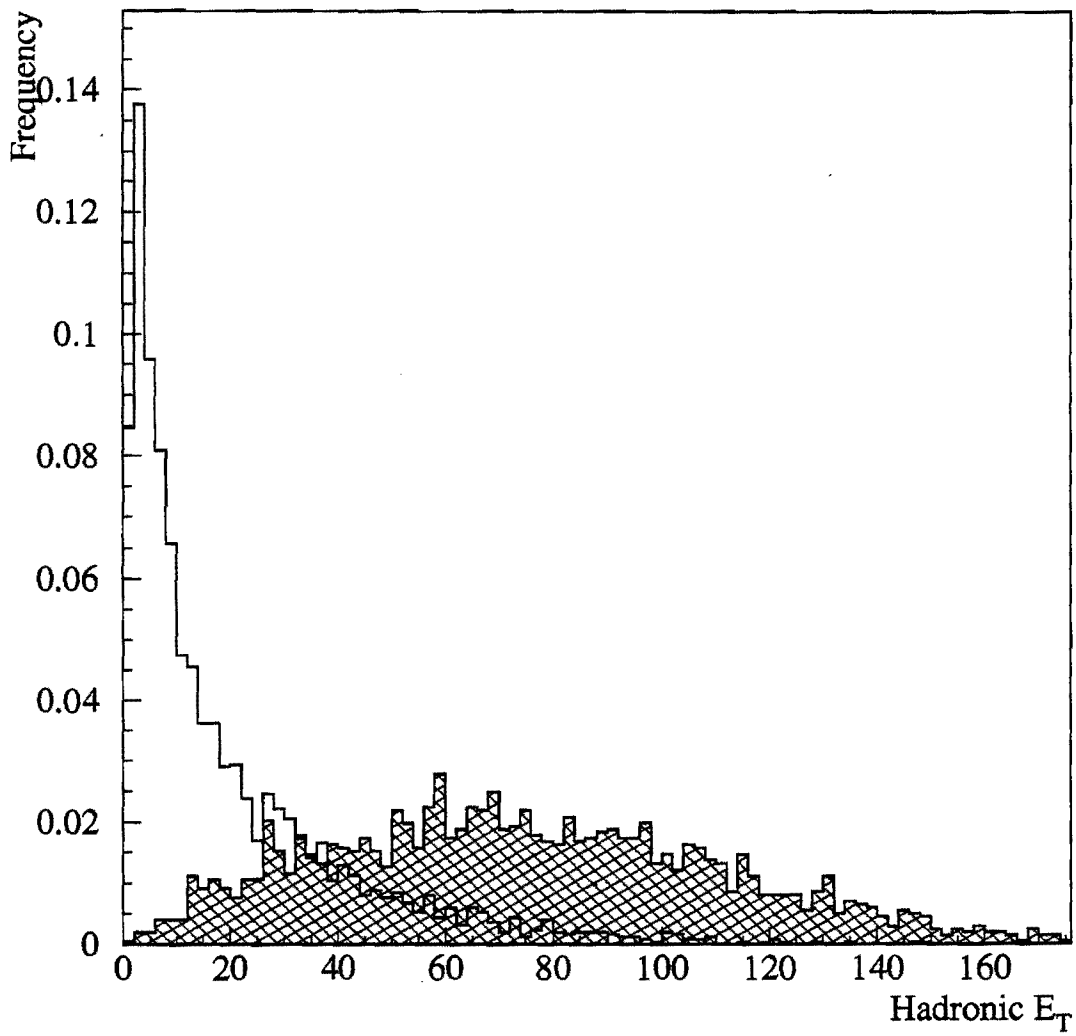


Figure 6.4: Transverse hadronic energy distributions for $t\bar{t}$ (shaded) and $W$ pair events in dilepton channels. The samples are from generator level Monte Carlo.

Statistical uncertainties are based on the number of events generated and passed. Systematic uncertainties are as in table 5.11, with the uncertainty on the $t\bar{t}$ cross section added in quadrature.

| Channel | # events passing selection cuts |
|---|---|
| $ee$ | 124 |
| $e\mu$ | 149 (163) |
| $\mu\mu$ | 21 (20) |

Table 6.8: Number of events passing selection cuts in $t\bar{t} \rightarrow \ell\ell$ Monte Carlo sample. For the $e-\mu$ and $\mu\mu$ channels, the first number is for pre-shutdown and the second for post-shutdown MUSMEAR parameterizations.

## 6.3 Background Summaries

Tables 6.9, 6.10 and 6.11 summarize the background estimates for the $ee$, $e\mu$ and $\mu\mu$ channels respectively. The systematic uncertainties in the total backgrounds takes into account the correlation of some of the uncertainties in the individual background estimates.

| Background Process | Background Event Yield Estimate |
|---|---|
| $Z \rightarrow ee$ | $0.266 \pm 0.056(stat) \pm 0.025(sys) \pm 0.014(lum)$ |
| Drell Yan Dileptons | $0.030^{+0.062}_{-0.023} \pm 0.003(sys) \pm 0.002(lum)$ |
| $Z \rightarrow \tau\tau$ | $0.104^{+0.093}_{-0.036} \pm 0.015(sys) \pm 0.006(lum)$ |
| $t\bar{t}$ | $0.130 \pm 0.012 \pm 0.046(sys) \pm 0.007(lum)$ |
| $W\gamma$ | $0.179^{+0.072}_{-0.042} \pm 0.040(sys) \pm 0.009(lum)$ |
| QCD | $0.195 \pm 0.133(stat) \pm 0.021(sys)$ |
| Total Background | $0.904^{+0.195}_{-0.157} \pm 0.078(sys) \pm 0.038(lum)$ |

Table 6.9: Background summary for dielectron channel.

| Background Process | Background Event Yield Estimate |
|---|---|
| $Z \rightarrow \tau\tau$ | $0.212^{+0.099}_{-0.047} \pm 0.028(sys) \pm 0.011(lum)$ |
| $t\bar{t}$ | $0.176^{+0.010}_{-0.009} \pm 0.063(sys) \pm 0.009(lum)$ |
| $W\gamma$ | $0.346^{+0.142}_{-0.081} \pm 0.080(sys) \pm 0.018(lum)$ |
| QCD | $0.432 \pm 0.229(stat) \pm 0.039(sys) \pm 0.021(lum)$ |
| Total Background | $1.166^{+0.328}_{-0.294} \pm 0.118(sys) \pm 0.059(lum)$ |

Table 6.10: Background summary for $e - \mu$ channel.

| Background Process | Background Event Yield Estimate |
|---|---|
| $Z \rightarrow \mu\mu$ | $0.394 \pm 0.060(stat) \pm 0.064(sys) \pm 0.021(lum)$ |
| Drell Yan Dileptons | $< 10^{-3}$ |
| $Z \rightarrow \tau\tau$ | $< 10^{-3}$ |
| $t\bar{t}$ | $0.015 \pm 0.003(stat) \pm 0.004(sys) \pm 0.001(lum)$ |
| QCD | $0.026 \pm 0.001(stat) \pm 0.002(sys)$ |
| Total Background | $0.435^{+0.062}_{-0.060} \pm 0.065(sys) \pm 0.022(lum)$ |

Table 6.11: Background summary for dimuon channel.

# Chapter 7

# Results

The detection efficiency and background calculations of the previous chapters allow for the quantitative comparison between theoretical predictions and the data. In the sections that follow, the number of observed events and the predicted backgrounds and detection efficiencies are used to place a limit on the $W$ pair cross section. Via that cross section limit, we then place limits on deviations from Standard Model predictions for the trilinear vector boson couplings. In addition, we also use the kinematic properties of the observed candidate events (as well as those of the predicted background) to place additional constraints on the trilinear couplings. Finally, we present the limits resulting from the combination of the run 1a and 1b analyses.

## 7.1 $p\bar{p} \rightarrow W^+W^- + X$ Cross Section

The cross section, number of observed candidates, estimated background, and detection efficiency are related by the following expression:

$$\sigma = \sum_i \frac{N_i^{observed} - N_i^{background}}{Br_i \epsilon_i \mathcal{L}_i},$$

where the sum is over the $ee$, $e\mu$ and $\mu\mu$ channels. $\mathrm{Br}_i$, $\epsilon_i$ and $\mathcal{L}_i$ are the branching ratio, detection efficiency and integrated luminosity in the $i$th channel. $N_i^{observed}$ is the number of observed candidate events, while $N_i^{background}$ in the estimated background event yield. The difference $N_i^{observed} - N_i^{background}$ is the observed $W$ pair signal.

Using the results from the previous chapters, the the $W \rightarrow \ell\nu$ branching ratio [39], and $1\sigma$ (69.2% confidence level interval) Poisson distributed statistics for the uncertainty on the number of candidate events, we obtain a result of

$$\sigma(p\bar{p} \rightarrow WW) = 9.44^{+23.84}_{-15.48} \pm 1.80(sys) \pm 0.50(lum).$$

The asymmetric statistical uncertainty is due both to the limited number of observed candidate events and the statistical uncertainty on the background predictions. The systematic uncertainty is due both to the systematic uncertainty on the detection efficiencies and on the background estimates. Because the lower statistical uncertainty interval encloses zero, we must conclude that this analysis lacks the statistical significance to provide an actual observation of the $W$ pair production process.

Although we cannot quote a central value, we can use the results of this analysis to place an upper limit on the $W$ pair cross section. For a given confidence level, one can calculate the largest allowed value for the number of observed $W$ signal events based on the detection efficiencies, backgrounds, and their associated uncertainties. Based on this number, one can then calculate the upper limit on the cross section. This calculation was performed using the TOP_LIMIT [106] software package developed at DØ. Using the results discussed in chapters 6 and 7, we place an upper limit on the Standard Model $W$ pair cross section of

$$\sigma_{WW}^{SM}(95\%CL) < 44.06\ pb.$$

## 7.2 Coupling Limits from the $W$ Pair Cross Section

As was discussed in chapter 1, the total $W$ pair cross section rises with increasing anomalous coupling values. Therefore, an observed limit on that cross section provides information on the allowed values of the anomalous couplings. The procedure for setting anomalous coupling limits in this fashion involved three steps. In the first, samples of $W$ pair events were generated with sets of couplings selected at appropriate points in a two-dimensional $\Delta\kappa$ and $\lambda$ grid for both the "equal" and HISZ coupling relations discussed in chapter 2. For the HISZ relations the form

factor scale $\Lambda = 1000$ GeV was used. For the "equal" relations $\Lambda = 1000$ and $\Lambda = 1500$ GeV were both used. Figure 7.1 shows the 61 point grid in $\Delta\kappa$ and $\lambda$ used in generating the events with the "equal" coupling relations and the 43 point grid used in generating the events with the HISZ relations.

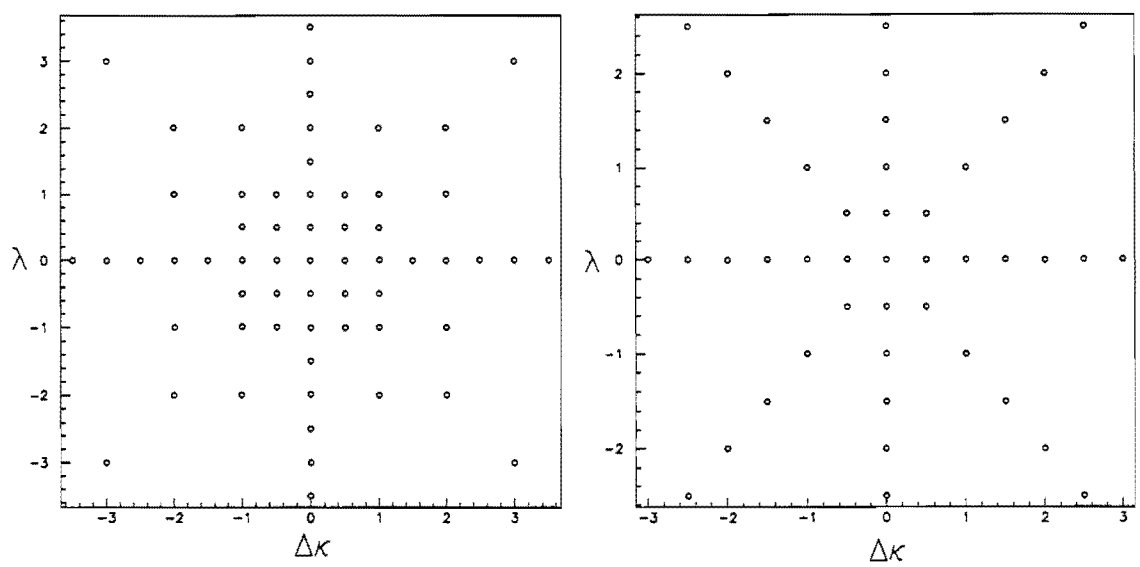


Figure 7.1: The grids in $\lambda$ and $\Delta\kappa$ for the events generated with the "equal" coupling relations (left) and the HISZ coupling relations (right).

In the second step, the generator cross section and 95% confidence level limit on the cross section were determined at the selected points on the $(\Delta\kappa, \lambda)$ grid. Because the kinematic properties of $W$ pair events change with anomalous couplings, the detection efficiency is expected to vary with the values of the anomalous coupling

parameters. Since the detection efficiencies vary (while the backgrounds and number of candidates will not), the limit on the cross section will also vary. At each point on the grid, the detection efficiency was evaluated using the fast Monte Carlo and DIPS detector simulation. The 95% confidence level limit on the cross section was calculated using the TOP_LIMIT package.

In the final step, the surfaces of $\sigma_{WW}^{95\%CL}$ and $\sigma_{WW}^{MC}$ were fit using a combination of polynomials and exponentials. Figure 7.2 shows the Monte Carlo generator cross section for the various grids of anomalous couplings studied. Figure 7.3 shows the $\sigma_{WW}^{95\%CL}$ surfaces for the "equal" ($\Lambda = 1.0$ and 1.5 TeV) and HISZ coupling relations ($\Lambda = 1.0$ TeV).

Coupling limit contours were produced via the intersection of the experimental cross section limit and the Monte Carlo cross section surfaces. Figures 7.4 through 7.6 show the resulting limit contours. The dashed line in the figures is the limit placed on the couplings by unitarity. As discussed in chapter 1, this limit is obtained by solving the expression

$$\Lambda \leq (\frac{6.88}{(\kappa - 1)^2 + 2\lambda^2})^{\frac{1}{4}} \text{ TeV},$$

which is derived from the requirement of tree-level unitarity. Table 7.1 shows the on-axis coupling limits for the various coupling schemes and scale factors tested. Because the 1.5 TeV experimental contour is less strict than the corresponding unitarity contour, limits for a 1.5 TeV form factor cannot be meaningfully interpreted

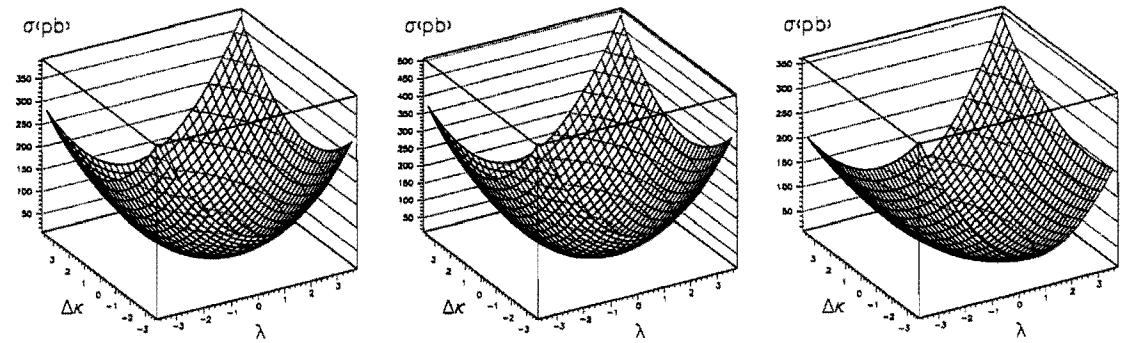


Figure 7.2: $W$ pair cross section as a function of anomalous couplings for the three sets of events generated. The left figure is for couplings with the "equal" relations and $\Lambda = 1000$ GeV. The middle figure is for couplings with the "equal" relations and $\Lambda = 1500$ GeV. The right figure is for couplings with the HISZ relations and $\Lambda = 1000$ GeV.

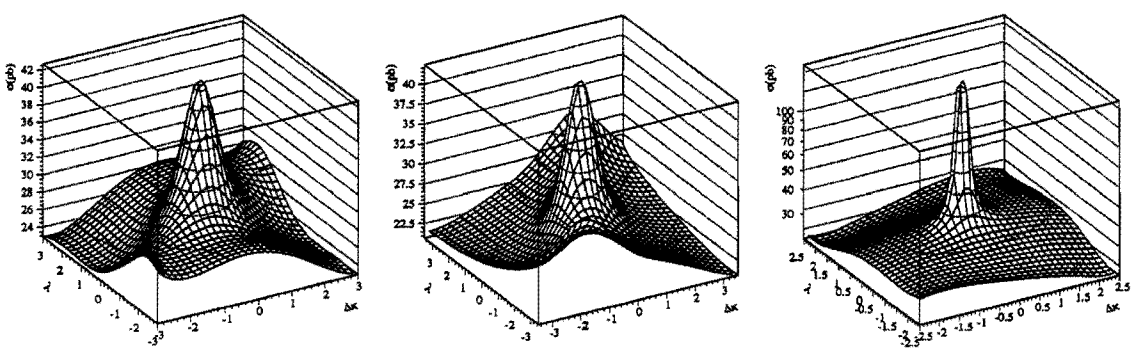


Figure 7.3: Surfaces of 95% confidence level Limit $WW$ cross section. The left figure is for couplings with the "equal" relations and $\Lambda = 1000$ GeV. The middle figure is for couplings with the "equal" relations and $\Lambda = 1500$ GeV. The right figure is for couplings with the HISZ relations and $\Lambda = 1000$ GeV.

from the cross section limit.

| Coupling Scheme | $\Lambda$ (TeV) | $\lambda = 0$ | $\Delta\kappa = 0$ |
|---|---|---|---|
| "equal" | 1.0 | $-1.3 < \Delta\kappa < 1.5$ | $-1.1 < \lambda < 1.1$ |
| "equal" | 1.5 | Looser than | unitarity limit |
| HISZ | 1.0 | $-1.9 < \Delta\kappa_\gamma < 2.2$ | $-1.1 < \lambda_\gamma < 1.1$ |

Table 7.1: Anomalous coupling limits for various coupling schemes

## 7.3 Coupling Limits from the Candidate Lepton Spectrum

While we can place good limits on $\Delta\kappa$ and $\lambda$ from the above method, more stringent limits are possible by exploiting the kinematic properties of the candidate events. Recall from chapter 1 that it is high $p_T^W$ part of the cross section which is most sensitive to the presence of anomalous couplings. Since high $p_T$ $W$'s will result in high $p_T$ leptons, a maximum likelihood fit to the spectra of the candidate event leptons can provide limits on anomalous couplings which are more sensitive than a fit to the total cross section [107, 108].

The first step in performing a fit is the choice of binning. The $E_T$ (or $p_T$) of the two leptons in each event are correlated. This correlation grows stronger with increasing anomalous couplings because the $W$'s produced are boosted by the same $p_T$ in the opposite directions. To respect this correlation, two dimensional bins in

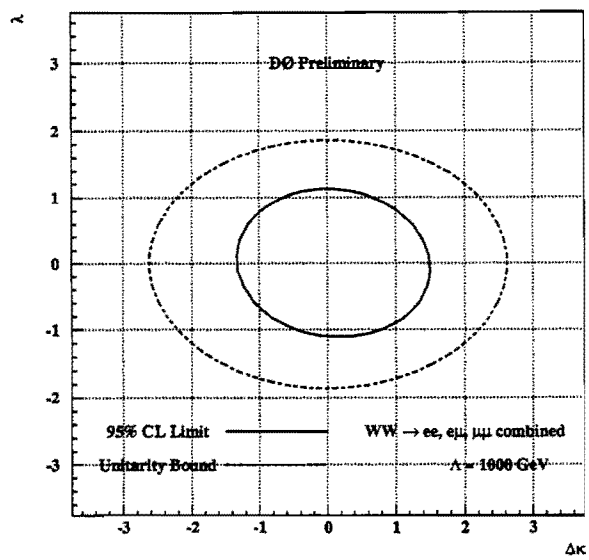


Figure 7.4: Anomalous coupling limit contour for "equal" couplings with $\Lambda = 1000$ GeV.

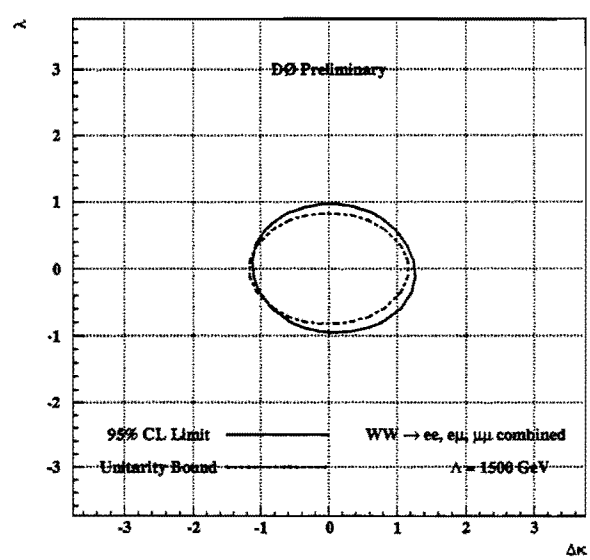


Figure 7.5: Anomalous coupling limit contour for "equal" couplings with $\Lambda = 1500$ GeV.

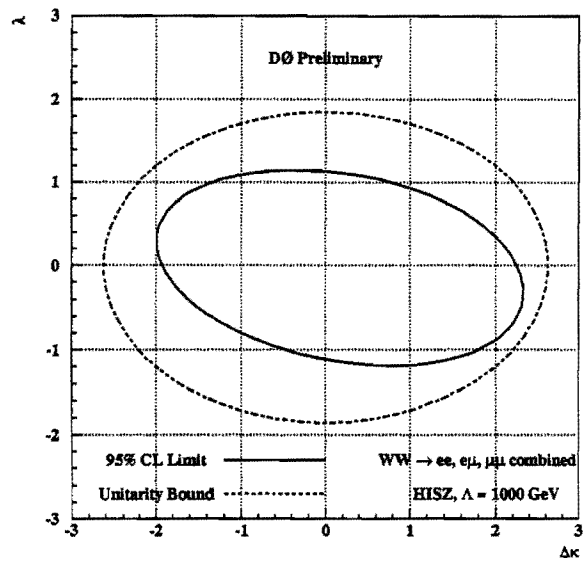


Figure 7.6: Anomalous coupling limit contour for HISZ couplings with $\Lambda = 1000$ GeV.

$E_T$ (or $p_T$) space were used. One axis in this space represents the $E_T$ (or $p_T$) of the first lepton, the other axis the second lepton. The details of the binnings used are shown in tables 7.2, 7.3 and 7.4.

| | $E_T^{e2}$ GeV | |
|---|---|---|
| $E_T^{e1}$ (GeV) | 20-40 | 40-500 |
| 25-40 | Bin 1 | - |
| 40-500 | Bin 2 | Bin 3 |

Table 7.2: Binning for $ee$ channel lepton spectrum fit.

The second step is to generate the expected signal spectrum. For each grid

| | $p_T^\mu$ GeV | |
|---|---|---|
| $E_T^e$ (GeV) | 15-40 | 40-500 |
| 25-50 | Bin 1 | Bin 2 |
| 50-500 | Bin 3 | Bin 4 |

Table 7.3: Binning for $e\mu$ channel lepton spectrum fit.

| | $p_T^{\mu 2}$ GeV/c | |
|---|---|---|
| $p_T^{\mu 1}$ (GeV/c) | 20-40 | 40-500 |
| 25-40 | Bin 1 | - |
| 40-500 | Bin 2 | Bin 3 |

Table 7.4: Binning for $\mu\mu$ channel lepton spectrum fit.

point shown in figure 7.1, the Monte Carlo generated leptons were binned as described above. The expected numbers of leptons in each bin were fitted using a second order polynomial function of $\Delta\kappa$ and $\lambda$:

$$N(\Delta\kappa, \lambda) = a_0 + a_1 \cdot \Delta\kappa + a_2 \cdot \Delta\kappa^2 + a_3 \cdot \lambda + a_4 \cdot \lambda^2 + a_5 \cdot \Delta\kappa \cdot \lambda.$$

The expected numbers of events from the Monte Carlo generation was normalized to the luminosity of the appropriate data sample. The results for the "equal" coupling fits are listed in tables 7.5, 7.6 and 7.7. The uncertainty in the fit was calculated using the error matrix from the fit and found to be less than 2% at all points. The uncertainty on the expected number of events was determined by adding in quadrature the luminosity, theoretical and detection efficiency uncertainties. This

results in an uncertainty on the number of expected events of 18.1%.

| | $a_0$ | $a_1$ | $a_2$ | $a_3$ | $a_4$ | $a_5$ |
|---|---|---|---|---|---|---|
| Bin 1 | $1.97\times10^{-1}$ | $9.30\times10^{-3}$ | $3.71\times10^{-2}$ | $1.58\times10^{-2}$ | $5.20\times10^{-2}$ | $1.55\times10^{-2}$ |
| Bin 2 | $2.28\times10^{-1}$ | $-5.04\times10^{-2}$ | $2.81\times10^{-1}$ | $-5.95\times10^{-2}$ | $8.09\times10^{-1}$ | $1.38\times10^{-1}$ |
| Bin 3 | $1.46\times10^{-1}$ | $-1.06\times10^{-1}$ | 1.11 | $-6.92\times10^{-2}$ | 1.58 | $1.45\times10^{-1}$ |

Table 7.5: Fitted parameters for the number of expected $ee$ signal events with "equal" couplings.

| | $a_0$ | $a_1$ | $a_2$ | $a_3$ | $a_4$ | $a_5$ |
|---|---|---|---|---|---|---|
| Bin 1 | $3.48\times10^{-1}$ | $2.11\times10^{-2}$ | $1.08\times10^{-1}$ | $1.85\times10^{-2}$ | $9.50\times10^{-2}$ | $7.36\times10^{-2}$ |
| Bin 2 | $2.33\times10^{-1}$ | $-5.00\times10^{-2}$ | $3.76\times10^{-1}$ | $-8.76\times10^{-2}$ | $8.17\times10^{-1}$ | $1.14\times10^{-1}$ |
| Bin 3 | $7.40\times10^{-2}$ | $-3.78\times10^{-2}$ | $1.83\times10^{-1}$ | $-3.23\times10^{-2}$ | $5.10\times10^{-1}$ | $8.55\times10^{-2}$ |
| Bin 4 | $1.76\times10^{-1}$ | $-1.21\times10^{-1}$ | 1.55 | $-9.09\times10^{-2}$ | 1.90 | $3.68\times10^{-1}$ |

Table 7.6: Fitted parameters for the number of expected $e\mu$ signal events with "equal" couplings.

| | $a_0$ | $a_1$ | $a_2$ | $a_3$ | $a_4$ | $a_5$ |
|---|---|---|---|---|---|---|
| Bin 1 | $2.70\times10^{-2}$ | $2.90\times10^{-5}$ | $7.10\times10^{-3}$ | $1.67\times10^{-3}$ | $4.73\times10^{-3}$ | $-4.77\times10^{-3}$ |
| Bin 2 | $4.10\times10^{-2}$ | $-1.84\times10^{-2}$ | $4.70\times10^{-2}$ | $-1.32\times10^{-2}$ | $1.22\times10^{-1}$ | $-1.16\times10^{-2}$ |
| Bin 3 | $2.90\times10^{-2}$ | $-3.14\times10^{-2}$ | $1.47\times10^{-1}$ | $-2.71\times10^{-3}$ | $2.05\times10^{-1}$ | $-8.73\times10^{-2}$ |

Table 7.7: Fitted parameters for the number of expected $\mu\mu$ signal events with "equal" couplings.

The third step is to determine the lepton spectrum of the predicted background. For both data and Monte Carlo based background estimates, the numbers of background events in each bin were determined using the techniques described

in chapter 6. Figure 7.7 shows the predicted spectra for signal and background, as well as the observed candidate spectrum. With predicted and observed spectra in hand, it is now possible to perform the maximum likelihood fit.

The probability $P_i$ for observing $N_i$ events in a given bin of a kinematic variable can be expressed by:

$$P_i = \frac{(b_i + n_i)^{N_i}}{N_i} e^{-(b_i+n_i)},$$

where

$$n_i = \mathcal{L}\epsilon\sigma_i(\lambda, \Delta\kappa).$$

In this expression $b_i$ is the estimated background, $n_i$ the expected signal, $\mathcal{L}$ the integrated luminosity, $\epsilon$ the detection efficiency, and $\sigma_i$ is the theoretical cross section as a function of anomalous coupling parameters $\Delta\kappa$ and $\lambda$. The joint probability for all the kinematic bins that are fitted is given by the product of the individual probabilities in each bin.

Since the values of $b_i, \mathcal{L}_i, \epsilon$ and $\sigma_i$ are measured quantities with some uncertainty, the joint probability must include Gaussian smearing around the central values of these quantities,

$$P' = \int \mathcal{G}_{f_n} df_n \int \mathcal{G}_{f_b} df_b \prod_{i=1}^{N_{bin}} \frac{e^{(f_n n_i + f_b b_i)}(f_n n_i + f_b b_i)^{N_i}}{N_i},$$

where $\mathcal{G}_{f_b}$ and $\mathcal{G}_{f_n}$ are Gaussian functions with an rms $\sigma_b$ and $\sigma_n$ for the background and signal respectively. The integration was performed between $-3\sigma$ and $+3\sigma$. For convenience, the log-likelihood, $L = -logP'$, is used in this study.

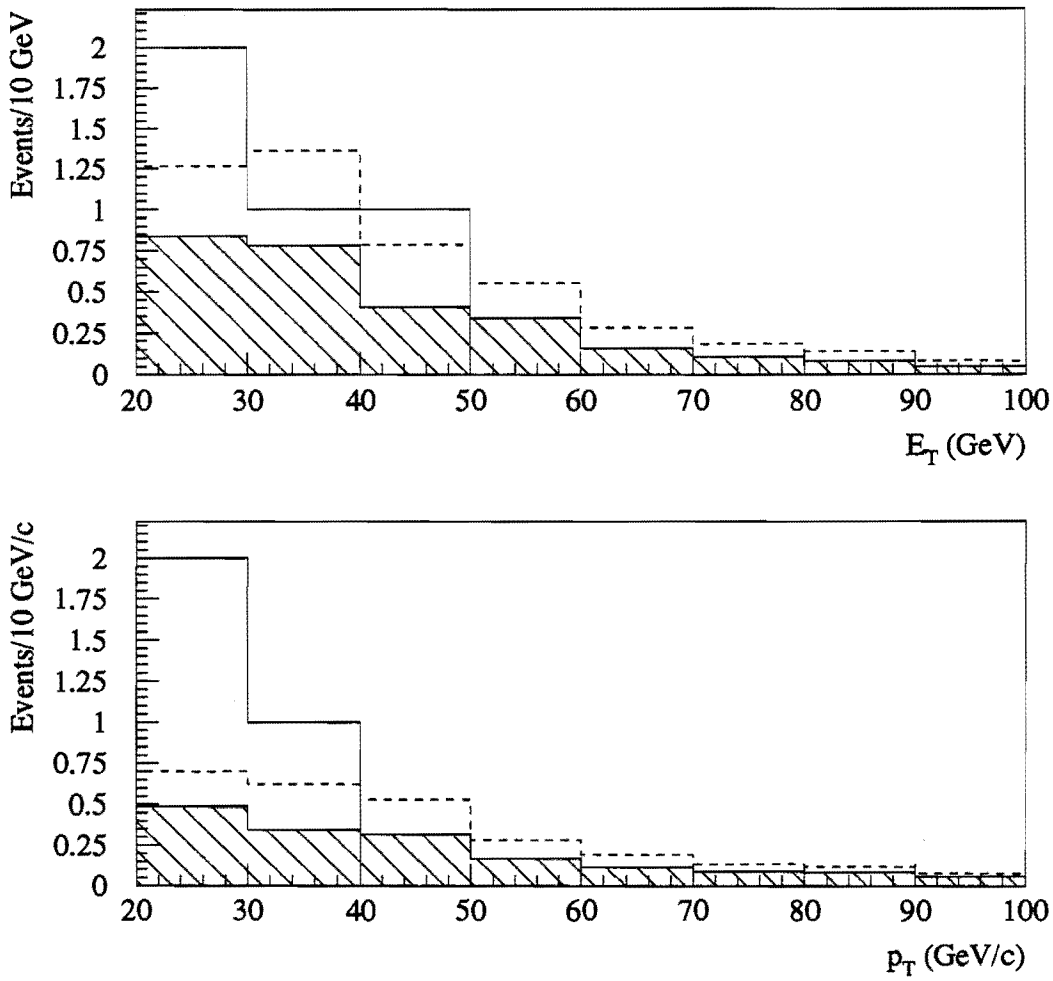


Figure 7.7: Lepton Spectra for the $W$ pair signal and background. The solid histograms are the candidates, the shaded histograms are the estimated background, and the dashed are the sum of the SM signal prediction plus background.

Once the surface of the log-likelihood has been formed on the $(\Delta\kappa, \lambda)$ grid, limits on the coupling parameters can be set. The anomalous coupling limit contour

is defined as the intersection of the log-likelihood function and a surface of constant likelihood, $L = \delta$. The dimensionality of these surfaces is determined by the number of free parameters in the fit. If we are interested in the on-axis limits for the couplings (similar to those listed in table 7.1) then only one parameter is actually free. If we are interested in the full limit contour (in which both couplings may vary) then there are two free parameters. For one free parameter (or degree of freedom) $\delta = 1.92$. For two free parameters, $\delta = 3.00$ [109]. Figure 7.8 shows both the one and two degree of freedom contours for the "equal" and HISZ coupling relations. In each case of form factor scale of $\Lambda = 1.5$ TeV was used. The one degree of freedom contour results in axis coupling limits of

$$-0.68 < \Delta\kappa < 0.83\ (\lambda = 0);\ -0.57 < \lambda < 0.62\ (\Delta\kappa = 0)$$

for the "equal" coupling relations, and axis coupling limits of

$$-1.02 < \Delta\kappa_\gamma < 1.30\ (\lambda_\gamma = 0);\ -0.60 < \lambda_\gamma < 0.62\ (\Delta\kappa_\gamma = 0)$$

for HISZ coupling relations.

## 7.4 Results from the Combined Run 1 Analysis

While the analysis described in this dissertation covers the bulk of the data collected at DØ during run 1, it is not the entire data set. A similar analysis was performed on the approximately 14 pb$^{-1}$ of data collected during run 1a [98]. This

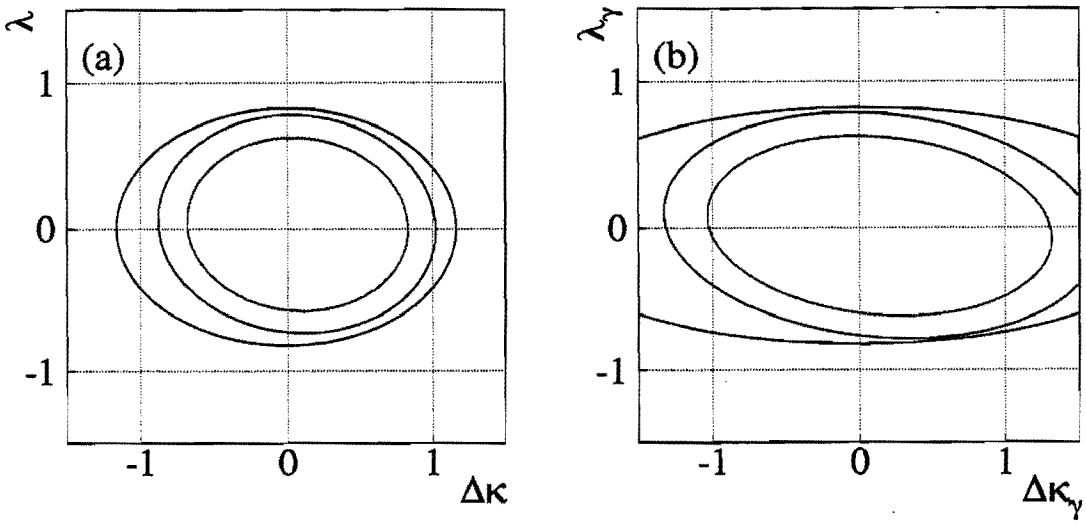


Figure 7.8: Run 1b anomalous coupling limits. a) Limits for the "equal" coupling relationships with $\Lambda = 1.5$ TeV. b) Limits for the HISZ coupling relationships. For each plot, the innermost contour is the 1 degree of freedom contour, the middle is the 2 degree of freedom contour, and the outermost contour the unitarity limit.

analysis is summarized in table 7.8. Because the 1a analysis represents a relatively small amount of data relative to the 1b data set (approximately $\frac{1}{6}$ the integrated luminosity), it's inclusion is not expected to make any significant improvement in the cross section or anomalous coupling limits. We show the combined limits for the sake of completeness.

| Channel | Background (events) | Detection Efficiency | Observed Candidates |
|---|---|---|---|
| $ee$ | $0.22 \pm 0.08$ | $0.094 \pm 0.008$ | 1 |
| $e\mu$ | $0.25 \pm 0.10$ | $0.092 \pm 0.010$ | 0 |
| $\mu\mu$ | $0.075 \pm 0.025$ | $0.033 \pm 0.003$ | 0 |

Table 7.8: Summary of Run 1a $WW \rightarrow$ dilepton analysis.

Repeating the procedures described in the previous sections on the combined data set results in a run 1 cross section limit of

$$\sigma_{WW}^{SM}(95\%CL) < 37.13\ pb,$$

and anomalous coupling limits (based on a fit to the lepton spectra) summarized in table 7.9. Figure 7.9 shows the corresponding coupling limit contours.

| Coupling Scheme | $\Lambda$ (TeV) | $\lambda = 0$ | $\Delta\kappa = 0$ |
|---|---|---|---|
| "equal" | 1.5 | $-0.62 < \Delta\kappa < 0.77$ | $-0.52 < \lambda < 0.56$ |
| HISZ | 1.5 | $-0.9 < \Delta\kappa_\gamma < 1.2$ | $-0.5 < \lambda_\gamma < 0.5$ |

Table 7.9: Anomalous coupling limits for various coupling schemes using Run 1a+1b data.

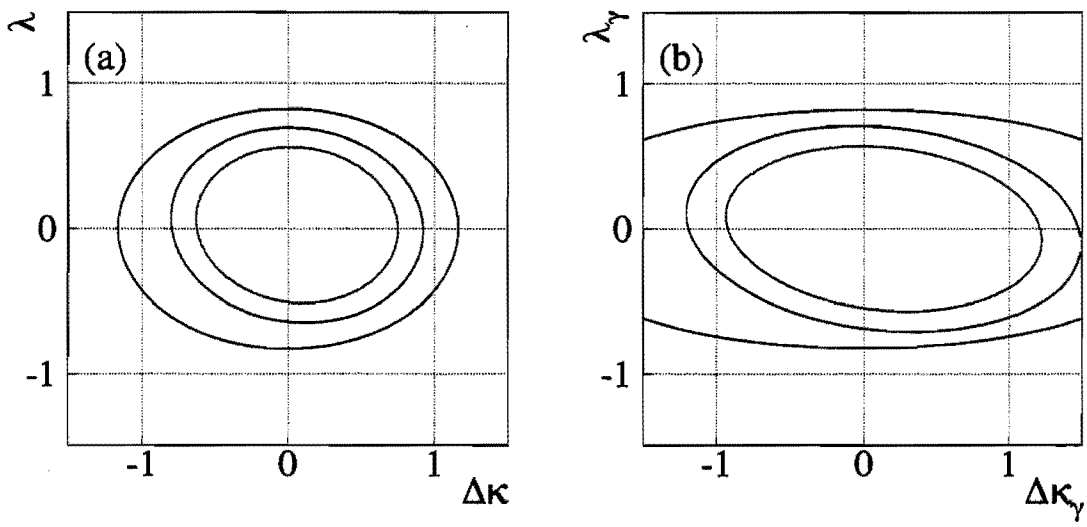


Figure 7.9: Run 1 anomalous coupling limits. a) Limits for the "equal" coupling relationships with $\Lambda = 1.5$ TeV. b) Limits for the HISZ coupling relationships. For each plot, the innermost contour is the 1 degree of freedom contour, the middle is the 2 degree of freedom contour, and the outermost contour the unitarity limit.

# Chapter 8

# Conclusions

We conclude this study with a summary of results and a comparison to other relevant measurements. Prospects for further study of the $WWZ$ and $WW\gamma$ vertices at future experiments are also discussed

## 8.1 Summary

A search for anomalous $WWZ$ and $WW\gamma$ interactions has been carried out by studying the inclusive reaction $p\bar{p} \rightarrow \ell\bar{\nu}_\ell\bar{\ell}'\nu_{\ell'}+$ X $(\ell, \ell' = e, \mu)$ at $\sqrt{s} = 1.8$ TeV, leading to an upper limit on the cross section for the hadroproduction of $W$ boson pairs of 44.06 pb at the 95% confidence level. The results of this search have been presented within the context of a generalized framework in which deviations from the Standard Model predictions for the $WWZ$ and $WW\gamma$ interactions are

parameterized by couplings which exhibit dipole form-factor behavior to maintain the self consistency of the model. In this study we have focused our attention on two sets of relationships between the couplings. In the first, we have made the assumption of equal $Z$ and $\gamma$ couplings. In the second, we have assumed a more complicated relationship derived from the requirement that the framework explicitly respect the gauge symmetry of the Standard Model. Form factor scales of both 1.0 and 1.5 TeV are assumed. Within these assumptions, limits on anomalous couplings are extracted from the data using both a fit to the total cross section, and a fit to the lepton transverse energy/momentum distribution of observed candidate events. These limits are summarized in table 8.1.

| Couplings | Method Used | $\Lambda$ (TeV) | $\lambda = 0$ | $\Delta\kappa = 0$ |
|---|---|---|---|---|
| Equal | Cross Section | 1.0 | $-1.3 < \Delta\kappa < 1.5$ | $-1.1 < \lambda < 1.1$ |
| Equal | Lepton $E_T(p_T)$ | 1.5 | $-0.68 < \Delta\kappa < 0.83$ | $-0.57\lambda < 0.62$ |
| HISZ | Cross Section | 1.0 | $1.9 < \Delta\kappa_\gamma < 2.2$ | $-1.1 < \lambda_\gamma < 1.1$ |
| HISZ | Lepton $E_T(p_T)$ | 1.5 | $-1.02 < \Delta\kappa_\gamma < 1.30$ | $-0.60 < \lambda_\gamma < 0.62$ |

Table 8.1: Summary of anomalous coupling limits.

A total of four dilepton + $\not\!\!E_T$ events were observed in a data set corresponding to an integrated luminosity of 82 pb$^{-1}$. This is in excellent agreement with the SM predicted signal of $1.5 \pm 1.1$ events and an estimated background of $2.5 \pm 0.4$ events. The channel by channel breakdown of these numbers is shown in table 8.2,

and the agreement with the SM on a channel by channel basis is also quite good. Within the statistical limitations of this analysis, no deviations from SM predictions can be inferred.

| Channel | N Observed | SM Prediction | Background Prediction |
|---|---|---|---|
| $ee$ | 1 | $0.544 \pm 0.052$ | $0.904 \pm 0.196$ |
| $e\mu$ | 2 | $0.858 \pm 0.099$ | $1.166 \pm 0.338$ |
| $\mu\mu$ | 1 | $0.085 \pm 0.014$ | $0.435 \pm 0.092$ |

Table 8.2: Summary of decay channels. Errors are combined in quadrature.

## 8.2 Comparison With Other Results

It is of interest to compare these results with those results previously obtained both by DØ and by other experiments. Two other measurements or limits on the $W$ pair hadroproduction cross section have been published. The first is the run 1a cross section limit from DØ [63]. This analysis provided a cross section limit of 91 pb. The cross section limit present in this analysis provides the expected improvement from the 1a analysis for the relative increase in luminosity and a comparable signal to noise ratio.

The second publication is the CDF run 1 $WW \rightarrow$ dilepton analysis [62]. This analysis had sufficient statistical significance to report evidence for the observation

of the $W$ pair process, and measures the cross section $\sigma(p\bar{p} \rightarrow WW) = 10.2^{+6.3}_{-5.1} \pm 1.6(sys)$ pb. Because the CDF analysis has a better signal to noise ratio, and is based on a larger data sample (about 20% more integrated luminosity for the same running period), the analysis presented here is consistent with the CDF result.

For anomalous coupling limits, there are many relevant results with which to compare. The CDF dilepton $W$ pair analysis is perhaps the most obvious choice for comparison, however the authors of that publication have chosen to use only the total cross section technique to extract coupling limits. Also very relevant are limits from the run 1 DØ analyses of $p\bar{p} \rightarrow WW/WZ \rightarrow e\nu jj + X$ [61], which sets limits on both the $WWZ$ and $WW\gamma$ couplings, and $p\bar{p} \rightarrow W\gamma \rightarrow \ell\nu\gamma + X$ ($\ell = e, \mu$) [59] which sets limits only the the $WW\gamma$ coupling. These are summarized in table 8.3.

Finally, limits are now being set by the LEP II experiments, which are measuring the process $e^+e^- \rightarrow WW$ in dilepton, lepton jets, and all jets channels. The LEP II machine operates above the center of mass energy threshold for the production of $W$ pairs, so the various experiments will have large samples of candidate events. The results from LEP will differ from the Tevatron results in several ways. Because the processes being studied are occurring at a fixed energy (verses the variable energy at the $p\bar{p}$ collider) no form factor ansatz is required for the couplings. Thus, while couplings (at the fixed energy) can be measured with precision, the high energy behavior implicit in the form factor construction cannot be probed. In this way, the measurements from LEP and the Tevatron are complementary in

nature. Axis limits from preliminary OPAL [110] and ALEPH [111] analyses are also summarized in table 8.3.

| Analysis | $\Lambda$ (TeV) | $(\lambda = 0)$ | $(\Delta\kappa = 0)$ |
|---|---|---|---|
| DØ run 1b $WW \to \ell\nu\ell'\nu'$ | 1.5 | $-0.68 < \Delta\kappa < 0.83$ | $-0.57 < \lambda < 0.62$ |
| DØ run 1 $WW \to \ell\nu\ell'\nu'$ | 1.5 | $-0.62 < \Delta\kappa < 0.77$ | $-0.52 < \lambda < 0.56$ |
| CDF run 1 $WW \to \ell\nu\ell'\nu'$ | 1.0 | $-1.05 < \Delta\kappa < 1.30$ | $-0.90 < \lambda < 0.90$ |
| DØ run 1 $WW/WZ \to e\nu jj$ | 2.0 | $-0.43 < \Delta\kappa < 0.59$ | $-0.33 < \lambda < 0.36$ |
| DØ run 1 $W\gamma \to \ell\nu\gamma$ | 1.5 | $-0.93 < \Delta\kappa < 0.94$ | $-0.31 < \lambda < 0.29$ |
| OPAL $WW$ | - | $-0.90 < \Delta\kappa < 1.12$ | $-0.78 < \lambda < 1.19$ |
| ALEPH $WW$ | - | $-1.74 < \Delta\kappa < 2.41$ | $-0.88 < \lambda < 1.13$ |

Table 8.3: Summary of anomalous coupling limits. All results assume equal couplings.

## 8.3 Future Prospects

The future offers many opportunities for the improved measurement of the trilinear gauge boson couplings. Perhaps the most obvious source of improvement comes from the collection of additional data. If all other things are equal (detection efficiencies, signal to noise ratios), coupling limits can be expected to improve by $\approx \mathcal{L}^{\frac{-1}{4}}$. The upcoming Tevatron run 2 is expected to result in the collection of 1-10 fb$^{-1}$ of data, resulting in an improvement of between a factor of 2 and 3 if all else remains the same. Another way to increase the size of the data set is to include additional decay modes. By adding channels in which one of the leptons may be a tau, the

branching ratio accessible to the dilepton analysis is doubled (although $\tau$'s will likely have much lower detection efficiencies than electrons or muons). Additional improvement will come in the form of detector upgrades which are now ongoing. These upgrades will likely improve the detection efficiencies and acceptances for leptons, and also provide added ability to reject background. As larger data sets become available, it will also become possible to employ more advanced analysis techniques. Multivariate kinematic fitting can be used to distinguish between $t$ and $s$ channel $W$ pair production, and to further constrain the boson self couplings

In the longer term, ongoing data collection at LEP II, the Tevatron, LHC, and a possible NLC (next linear collider) will all add to our ability to measure the boson self couplings, both by increasing the size of data sets, and by extending the kinematic range at which the couplings can be probed.

## 8.4 Final Remarks

The sensitivity of this analysis is constrained by the limited size of the data set, low detection efficiencies and small branching ratios. Nevertheless, the result rules out gross deviations from the Standard Model, and finds no evidence for new physics. Further improvement in the measurement will require more statistically significant data samples. An improved understanding of the backgrounds and systematics, particularly theoretical uncertainties, will be required to reap the full

benefit of additional data. The goal of observing coupling limits down to the order of Electroweak loop corrections will provide the ultimate probe of this sector of the Standard Model, and remains as the long term objective for this program of measurements.

# Appendix A

# Candidate Event Displays

This appendix contains event displays of each of the four Run 1B dilepton $W$ pair candidates. For each event there is a display showing the $R-Z$ and $R-\phi$ views of the detector, as well as a lego plot of the event.

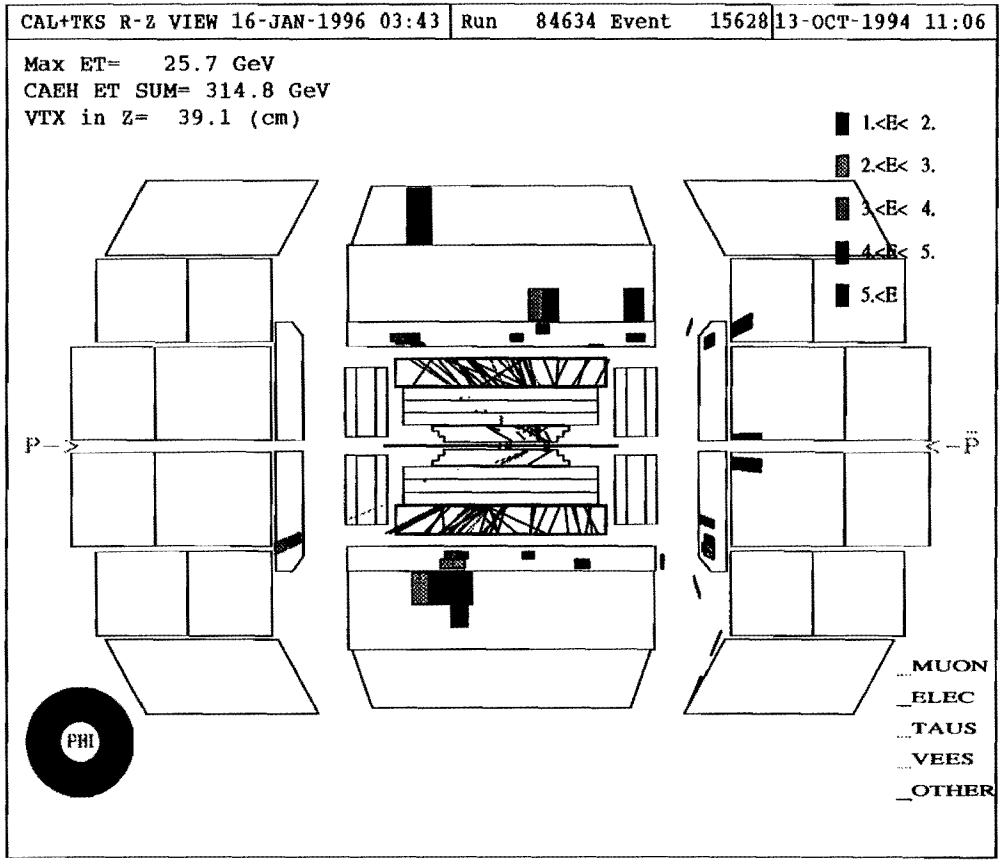


Figure A.1: $R - Z$ View of Dielectron Candidate.

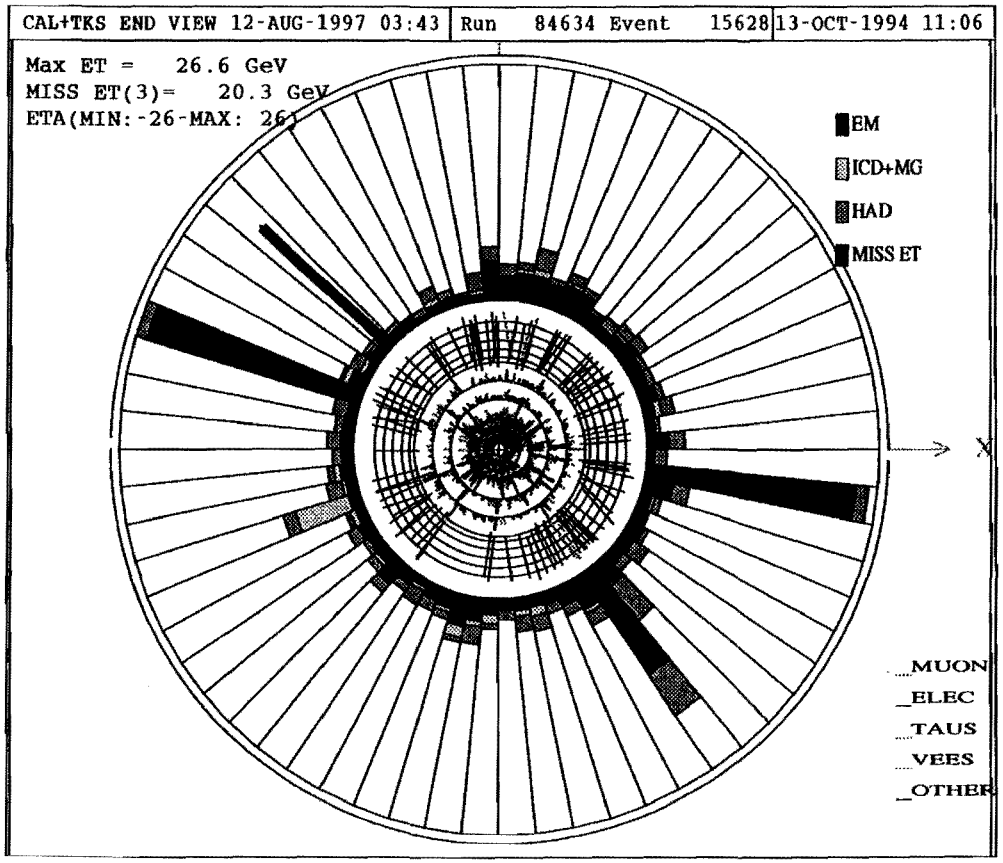


Figure A.2: $R - \Phi$ View of Dielectron Candidate.

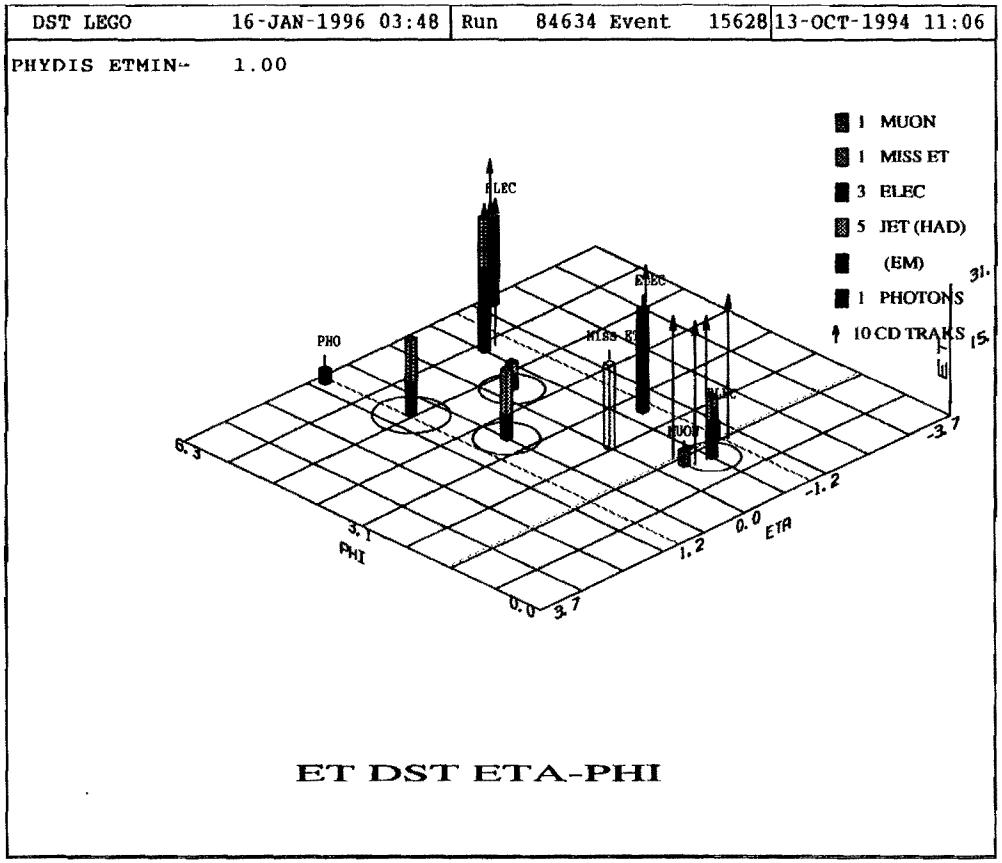


Figure A.3: Lego Display of Dielectron Candidate.

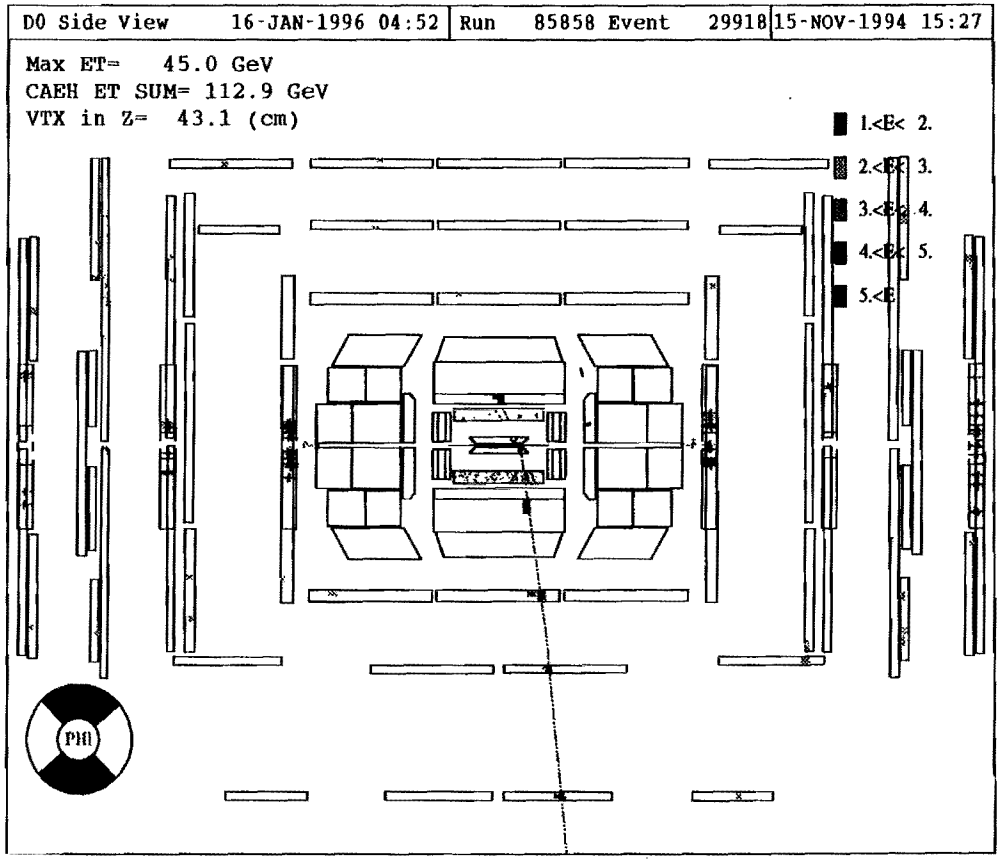


Figure A.4: $R - Z$ View of $e\mu$ Candidate One.

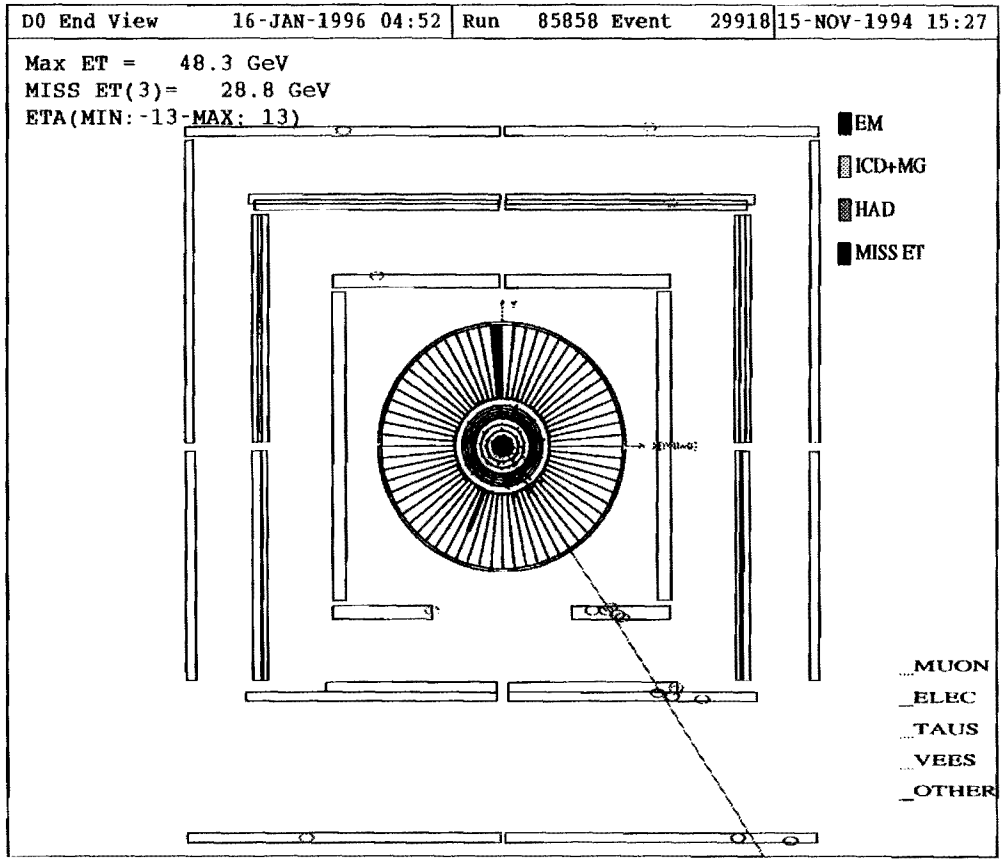


Figure A.5: $R - \Phi$ View of $e\mu$ Candidate One.

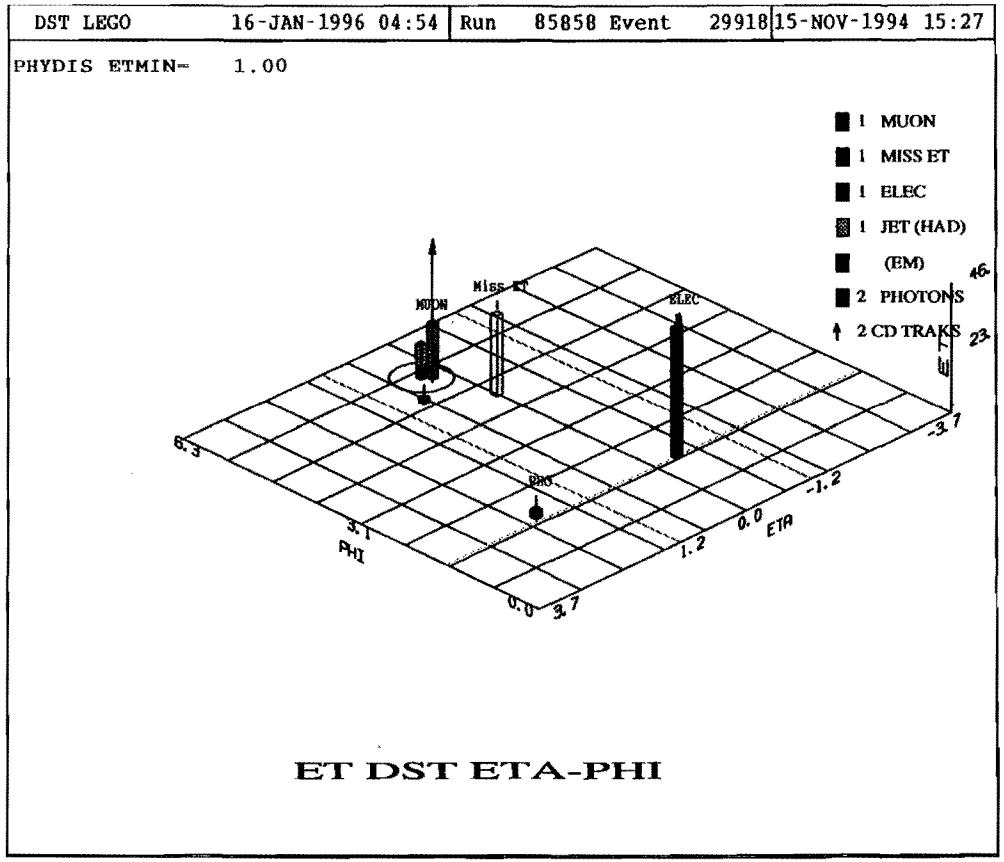


Figure A.6: Lego Display of $e\mu$ Candidate One.

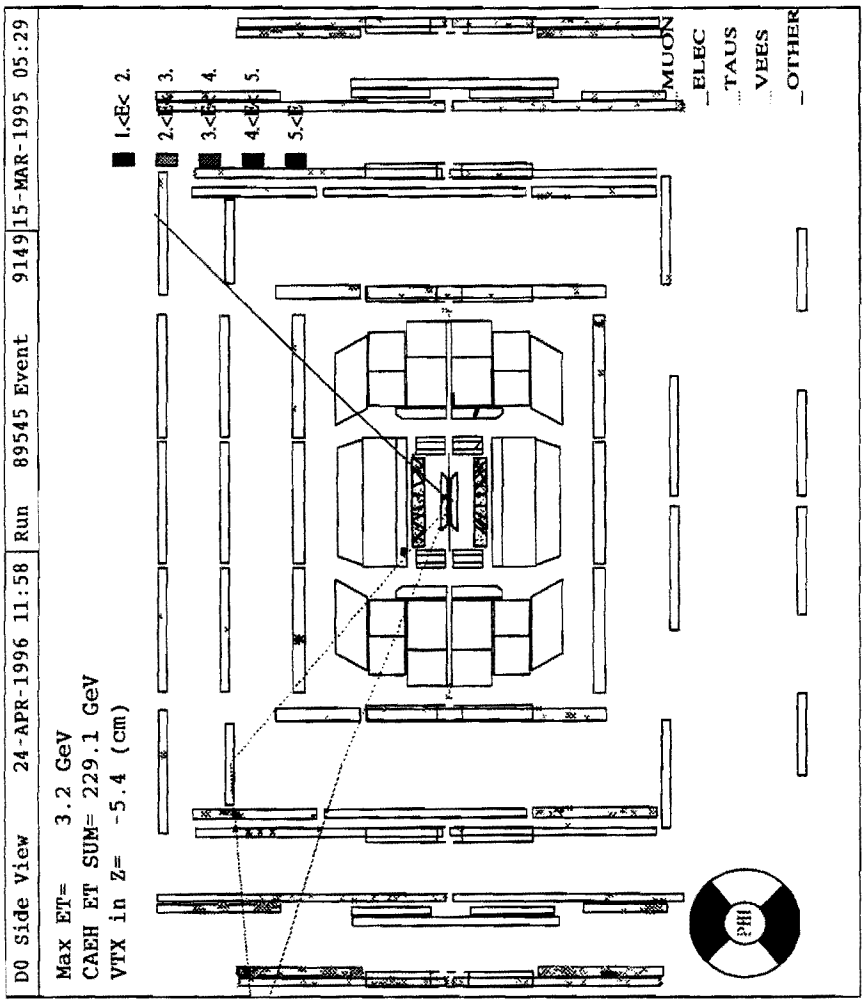


Figure A.7: $R-Z$ View of $e\mu$ Candidate Two. The muon in the upper right quadrant is the primary muon associated with the $W$ pair candidate. The remaining two muons (upper left) are low pt (see lego of this candidate) and result from either the underlying event, or combinatoric fakes associated with the WAMUS EF region.

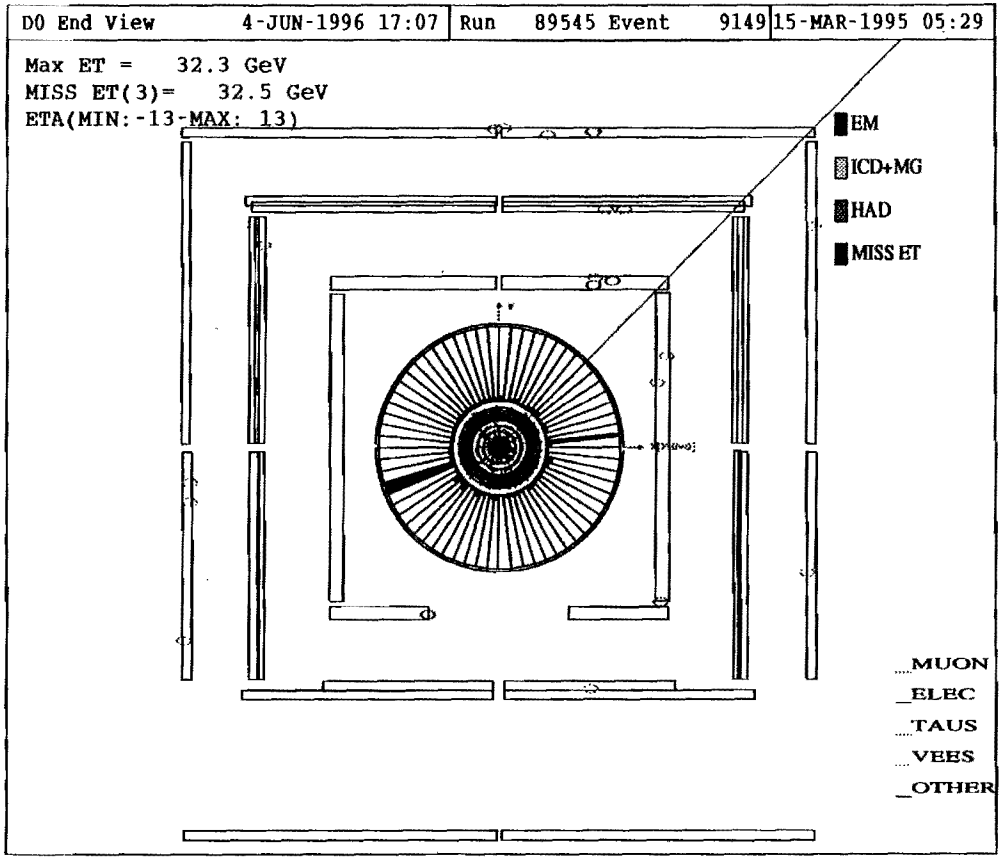


Figure A.8: $R - \Phi$ View of $e\mu$ Candidate Two.

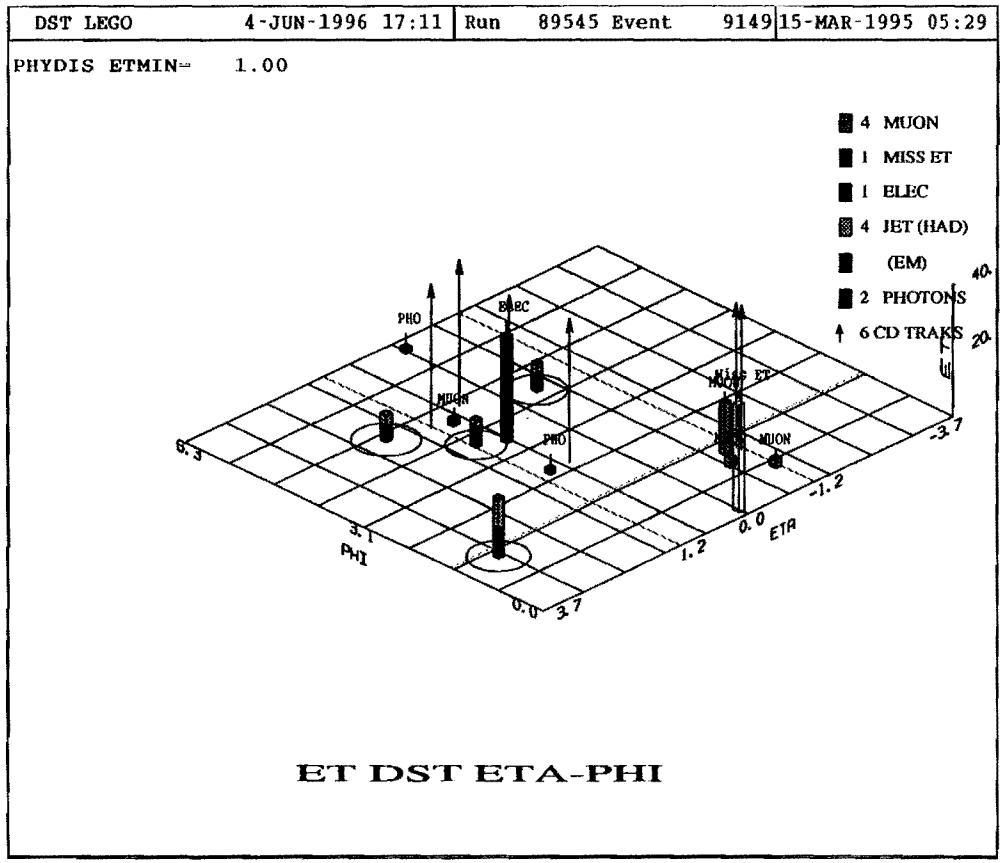


Figure A.9: Lego Display of $e\mu$ Candidate Two.

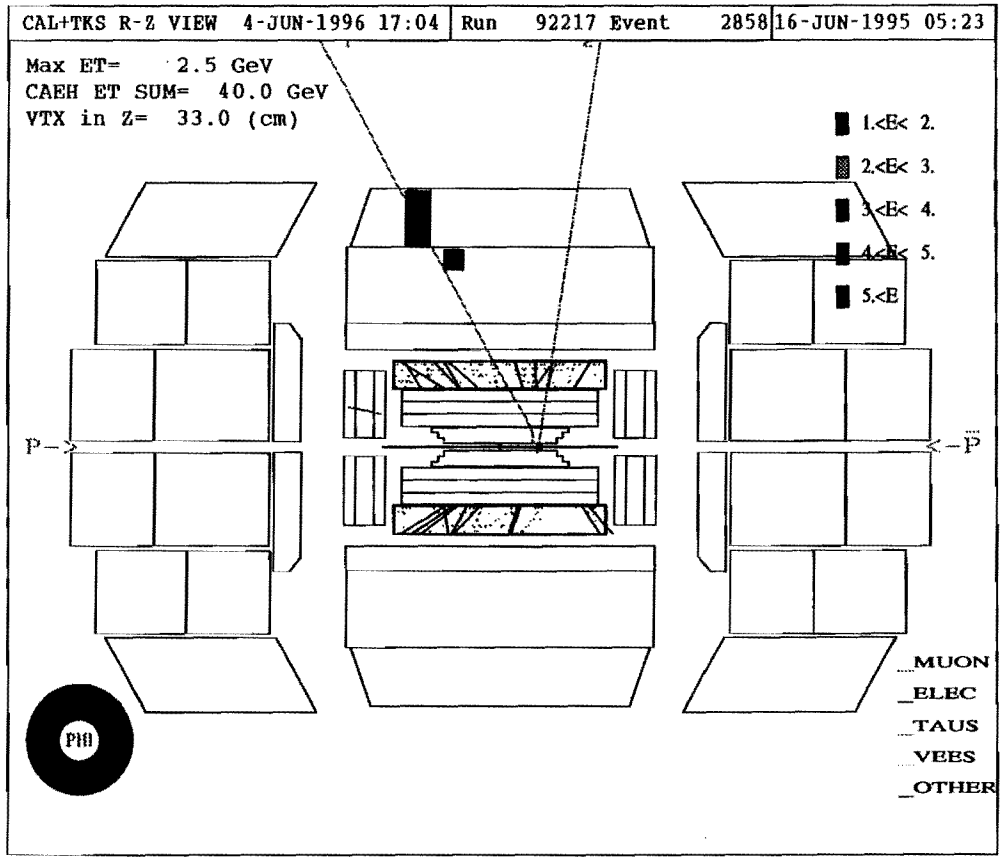


Figure A.10: $R-Z$ View of Dimuon Candidate.

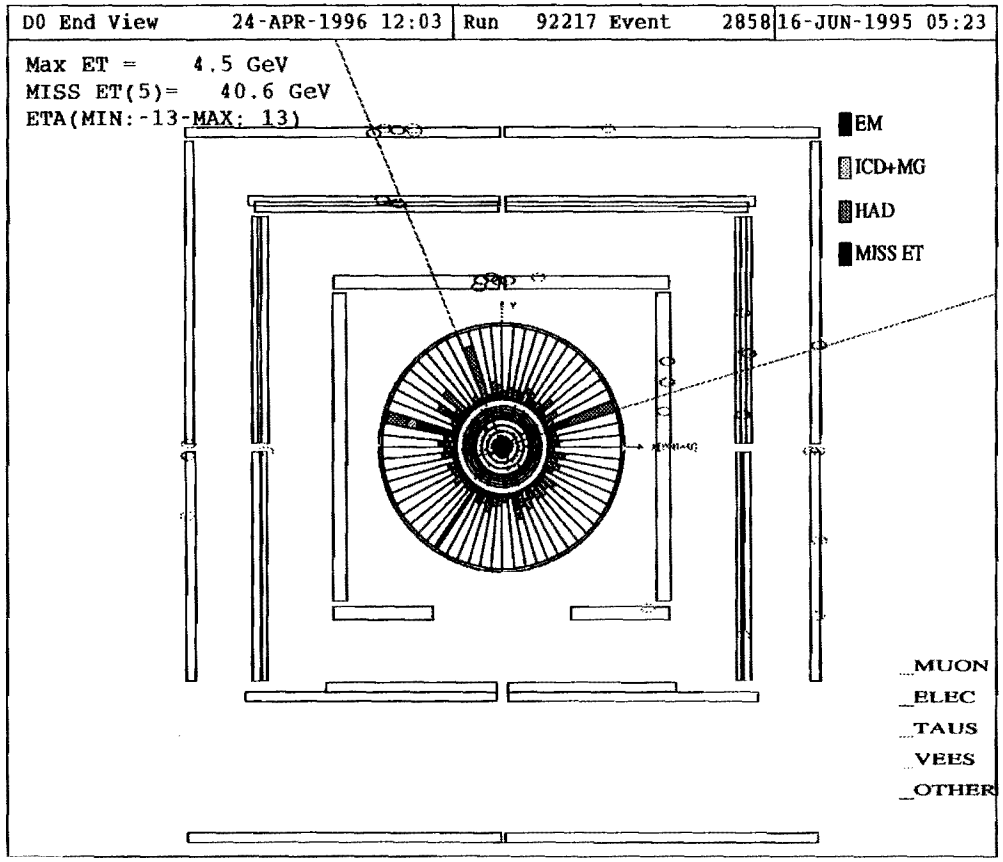


Figure A.11: $R - \Phi$ View of Dimuon Candidate.

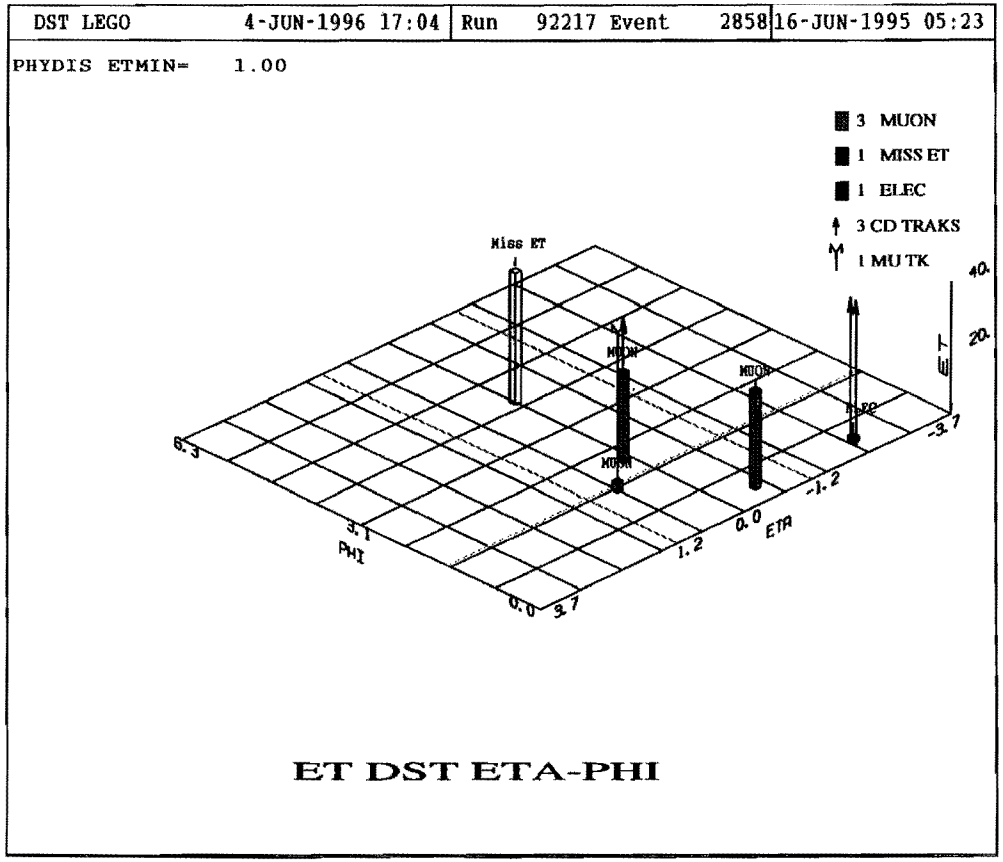


Figure A.12: Lego Display of Dimuon Candidate.

# Appendix B

# Measurement of $P_{j\to e}$

Diboson processes involving electrons and photons in the final state are plagued by potentially large QCD backgrounds from $W$'s or $Z$'s produced in association with jets. The typical procedure for estimating these backgrounds involves counting jets in inclusive $W$ or $Z$ samples and weighting by the probability that a jet is misidentified as an electron or photon. Previous studies [112, 113, 114, 115, 116] with DØ data indicate these probabilities are of order $10^{-3}$, and that the probabilities measured from the data roughly agree with Monte Carlo predictions from ISAJET [38]. This appendix is intended to detail the measurement of jet misidentification rates for the electron selection criteria used in this analysis.

## B.1 Introduction

At transverse energies greater that $\approx$ 10 GeV/c, the granularity of the DØ calorimeter is insufficient to distinguish between an isolated $\pi^0/\eta \to \gamma\gamma$ and and single electron based on transverse shower shape (which dominates the H-Matrix $\chi^2$) or isolation requirements. Consequently, when a jet fragments primarily into an isolated $\pi^0$ or $\eta$, it will be misidentified as the electromagnetic show due to an electron or photon. Because the DØ detector has a non-magnetic tracking system, photon conversion to an $e^+e^-$ pair, or the presence of a soft charged hadron [1] from either the associated jet or the underlying event near the shower will provide the requisite tracking information required by electrons. This will lead to the misidentification of the jet as an electron.

In this study, fake probabilities are measured from a data sample collected from six single jet L2 filters: `jet_20_noLØ`, `jet_30`, `jet_50`, `jet_80` and `jet_max`. To good approximation, the fake probability is given by the ratio of the electron population to the jet population:

$$P_{j\to e} \equiv N_e/N_j$$

where $N_e$ and $N_j$ are the number of electrons and jets found in the sample. These objects are restricted to the same region of phase space. Generally, this ratio depends on the transverse energy of the objects in question, so it must be calculated in bins

[1] The overlapping hadron must be of relatively low energy, or the prospective electron fake will fail the isolation requirement.

of $E_T$. The dependence on the jet/electron $E_T$ also comes into play in the trigger requirements placed on the data sample. This dependence is discussed more fully below. Angular effects are assumed to be accounted for by calculating the ratios for the CC and EC fiducial regions separately. Finally the correction procedure to account for the contamination of the jet sample by direct photon production also produces an $E_T$ dependent effect. This is also discussed below.

## B.2 Data Sample and Event Selection Criteria

To faithfully measure and quantify the probability with which jets are misidentified as electrons, it is necessary to start with a data sample which is free of genuine electrons. Because the cross sections for QCD jet processes are orders of magnitude larger than processes which produce real electrons, data collected with jet triggers (ie. calorimeter tower triggers) have almost no authentic electron content. The data collected for this study are from the `jet_20_noLØ`, `jet_30`, `jet_50`, `jet_80` and `jet_max` filters from runs 87804 to 93115, with the additional requirement that the `GOOD_ BEAM` veto also be applied (to remain consistent with the $W$ pair event selection). Events passing any one of these triggers were reconstructed with DØRECO versions 12.15 through 12.20, with jets being reconstructed with a cone size of $R = 0.5$. Jets in these events were then subject to the following requirements:

- $E_T > 10$ GeV
- $|\eta_{det}| < 1.1$ or $1.5 < |\eta_{det}| < 2.5$
- $\phi < 1.1$ or $\phi > 1.2$
- Coarse Hadronic (CH) energy ¡ 40% of total energy
- $E_1/E_2 < 10.0$ GeV, where $E_1$ and $E_2$ are the two highest energy cells in the cluster.

The first two criteria restrict jets to the same phase space as the electrons considered in this analysis. The cut on $\phi$ eliminates objects near the Main Ring, which may be caused by Main Ring activity. The last two cuts remove contributions from "hot cells" in the calorimeter. Finally, the missing transverse energy in the event was required to be less than 15 GeV to eliminate $W \to e\nu$ as a possible source of electron contamination.

Electrons were identified using the requirements discussed in chapter 3

## B.3 Trigger Bias

Because the energy resolutions and corrections for electromagnetic and hadronic showers differ, triggers can induce a source of bias to the measurement of $P(j \to e)$. Because the superior resolution of the electromagnetic calorimeter, an event near a trigger threshold will more likely to cause a trigger if the leading object

in the event is isolated from hadronic energy, and contained primarily in the EM calorimeter. As a result, the populations of electrons and photons are inflated relative to jet populations near a trigger threshold. These changes in relative population can induce bumps in the ratio for $P(j \rightarrow e)$. As a result it is necessary to impose kinematic restrictions on the reconstructed objects in the event to minimize trigger bias. This is done by rejecting events which have leading objects with transverse energy less than some minimum $E_T$ associated

To minimize the induced bias, it is necessary to impose kinematic requirements on the reconstructed objects. Events with leading objects having transverse energy less than a threshold $E_T^{Min}$ associated with an L2 filter the event has passed are rejected. This threshold was chosen such that the trigger is fully efficient for both electromagnetic and hadronic showers. Table B.1 summarizes various thresholds used in this measurement.

| L2 filter | L1 $E_T$ | L2 $E_T$ | $E_T^{\mathrm{Min}}$ |
|---|---|---|---|
| jet_20 | 10 | 20 | 30 |
| jet_30 | 15 | 30 | 50 |
| jet_50 | 15 | 50 | 90 |
| jet_85 | 35 | 85 | 150 |
| jet_max | 45 | 115 | 200 |

Table B.1: Summary of $E_T$ thresholds used in measuring fake rates. Units are GeV.

## B.4 Direct Photon Subtraction

Since multijet cross sections are orders of magnitude larger than $W/Z$ cross sections, one expects that the above data sample be composed nearly exclusively of QCD jets, with any electrons found in that sample being the result of jets faking electrons. However, the direct photon cross section is relatively large compared to electroweak processes, and it increases relative to the multijet cross section at high $p_T$. primarily due to running of the electromagnetic and strong couplings constants. Since the showers produced by photons and electrons are indistinguishable by standard electron identification techniques, these photons provide a potentially large source of fake electrons in the multijet sample, and their contribution must be subtracted before forming $P(j \to e)$.

In run 1A, it was shown [117] that the fraction of the inclusive isolated photon sample due to $\pi^0$ or $\eta$ meson production could be parameterized by

$$f_{\gamma\gamma} = a \times e^{-b \times E_T}$$

where $a$ and $b$ are constants. The meson fraction was measured by comparing the longitudinal shower profile of candidates to predictions from GEANT detector simulations[2] The results of this analysis were:

$$a = 1.14 \pm 0.05$$

[2]Single photons are less likely to deposit energy in the first layer of the calorimeter than are two photons.

and

$$b = 0.0177 \pm 0.0021 \mathrm{GeV}^{-1}$$

for photons in the CC[3]. More recent results [118] show that the meson fraction in the forward region is similar to the central region, so it is assumed that the above parameterization is valid for the EC as well.

Once a direct photon is produced, it may fake an electron by the mechanisms discussed in 6.1.1. The following procedure was used to estimate the number of fake electrons in that sample which will arise to due direct photons. First, the meson fraction $f_{\gamma\gamma}$ was used to estimate the fraction of electromagnetic objects in the event (as a function of $E_T$ which were due to direct photons. This distribution was then scaled by the combined conversion and random-track-overlap probabilities to produce the direct photon contribution to the fake electron content of the sample.

## B.5 Fake Probabilities

Once the correction for direct photons has been applied, the fake probabilities may be calculated. These are shown in figure B.1. The error bars displayed are Gaussian approximations to the binomial uncertainties on the population ratios. From the figure, it is evident that the probability for a jet to fake an electron

[3]The selection criteria for photons in that analysis differed primarily due to a different shower isolation requirement. It is assumed that the parameterization is a close approximation to the results which would be obtained using the isolation requirement used in this analysis.

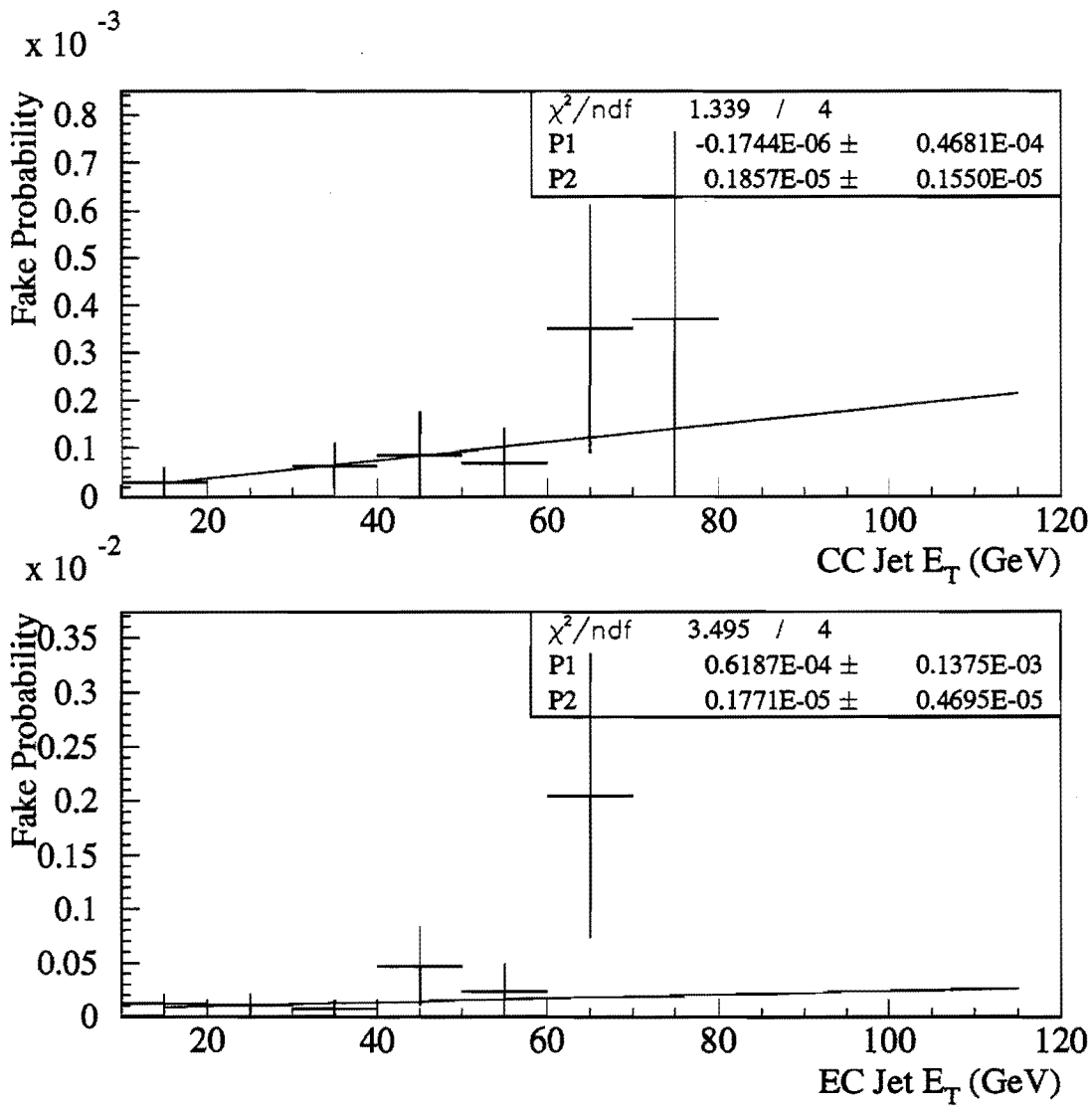


Figure B.1: Distributions of jet misidentification as electron probability - direct photon subtraction applied. (a) Fake probability in the CC for a likelihood cut of 0.20 (b) Fake probability in the EC for a likelihood cut of 0.25.

increases with jet $E_T$. One explanation of this would be that the soft charged hadrons required for a random track overlap are more likely to be produced in the fragmentation process as the $\pi^0/\eta$ parent parton energy increases[4]

Because the systematic uncertainty due to the meson fraction is large where the most fake candidates exist (around 20% at $E_T = 20$ GeV), the assignment of the systematic error is somewhat troublesome. We have chosen to assign a systematic error by computing $P(j \rightarrow e)$ with and without the direct photon subtraction, and assigning half the difference in background event yield using the two fake rates to be the systematic uncertainty. The fake probabilities without the direct photon subtraction are shown in figure B.2.

For additional information the validity of these procedures, see [116]

[4]conversely, fake probabilities for photons can be shown [116] to decrease with $E_T$ for the same reasons.

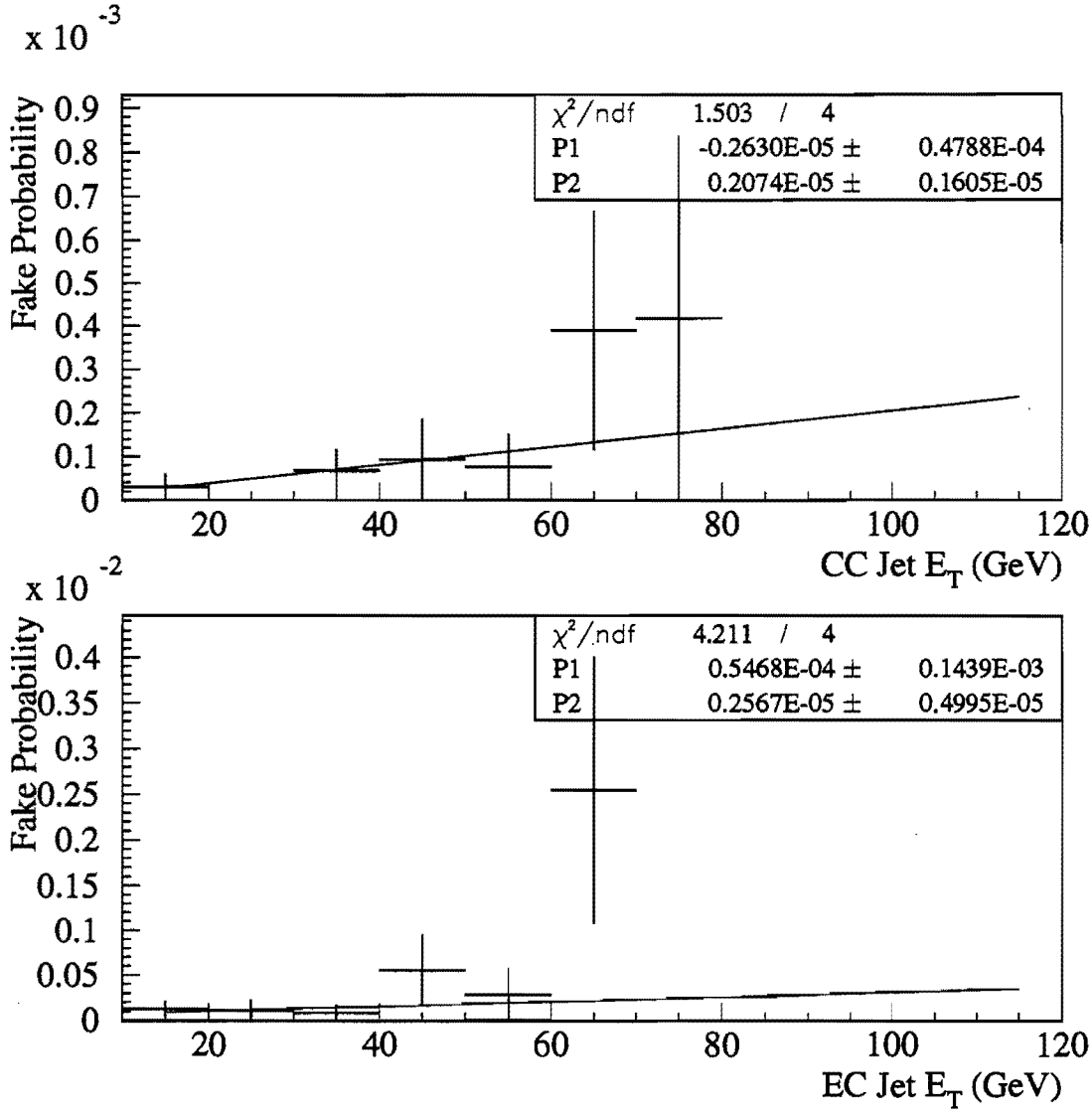


Figure B.2: Distributions of jet misidentification as electron probability - no direct photon subtraction. (a) Fake probability in the CC for a likelihood cut of 0.20 (b) Fake probability in the EC for a likelihood cut of 0.25.

# Appendix C

# Cross Check of the $ee$ Background from Jet Fakes

The fake electron background to the dielectron channel can be estimated in a manner which is independent of the study performed in 6.1.2. This method was used in the $W$ pair analysis performed on the run 1a data [98], and can be extended to the 1b data with minimal modification.[1] Two subsamples are derived from the ELE_EM1_MON L2 filter (with the GOOD_BEAM beam veto applied). As a monitor trigger, the events passed by this filter are totally unbiased by any particle identification cuts. The first or "good" subsample, similar to the data sample, contains two electrons which pass all the identification cuts (see 3.2.1). The second, "fake" or "bad"

[1]Only in the dielectron channel however. This method is not readily applicable to the $e - \mu$ channel due to additional difficulties with trigger bias deriving from the presence of a muon in the event.

subsample contains events in which one or both electrons pass *anti*-quality cuts; Electron Likelihood > 0.20 (0.25) in the CC (EC), and Isolation > 0.10 (the electron must still pass the fiducial cuts). Figure C.1 shows the $\not\!\!E_T$ distributions of each sample. A normalization factor (F) of the fake sample relative to the good sample is calculated using the numbers of events with $\not\!\!E_T$ < 15 GeV (thus removing events containing real $W \rightarrow e$ decays). All the kinematic and topological event selection cuts are then applied to the fake sample, and the number of surviving events (N) counted. Because the monitor triggers are heavily prescaled, N must be multiplied by the relative luminosity between the `ELE_EM1_MON` and `EM2_EIS2_HI` filters. The `EM2_EIS2_HI` filter is the L2 filter used in analyses involving $Z \rightarrow ee$ events. It requires two high $E_T$ electrons, using the same electron term in the trigger as does the `EM1_EISTRKCC_MS` filter. The $Z$ trigger is used as an intermediate step because it (like the monitor trigger) has no $\not\!\!E_T$ requirement. The relative luminosity between the two filters is determined by counting $Z \rightarrow ee$ events (based on a standard, loose set of cuts) in each sample. A further correction is then necessary to account for the difference in luminosities between the `EM2_EIS2_HI` and `EM1_EISTRKCC_MS` filters because `EM2_EIS2_HI` was never prescaled, whereas `EM1_EISTRKCC_MS` was at the highest instantaneous luminosities. Finally, the number of fake background events is estimated by multiplying the scaled number of surviving events by the good to bad normalization. Relevant parameters are listed in table C.1. This calculation

leads to a background estimate of

$$N^{ee}_{background}(\text{jet fakes}) = 0.392^{+0.193}_{-0.136}\ (\text{stat}) \pm 0.020\ (\text{sys})\ \text{events}.$$

The statistical uncertainty is based on the 8 events observed, and on the total numbers of events in the good and bad samples. The systematic uncertainty was estimated by noting the change in the normalization (F) as the cutoff between the quality and anti-quality cuts was varied. Within uncertainties, this estimate is consistent with the dielectron fake electron background calculated in 6.1.2.

| | |
|---|---|
| # of Bad events passing | 8 |
| Good/Bad with $\not{E}_T < 15$ GeV | $0.00682 \pm 0.00037\ (stat) \pm 0.00034\ (sys)$ |
| $Z$'s in ELE_EM1_MON/EM2_EIS2_HI | 0.138 |
| EM1_EISTRKCC_MS/EM2_EIS2_HI $\mathcal{L}$ | 0.99 |

Table C.1: Parameters in Fake Background Calculation

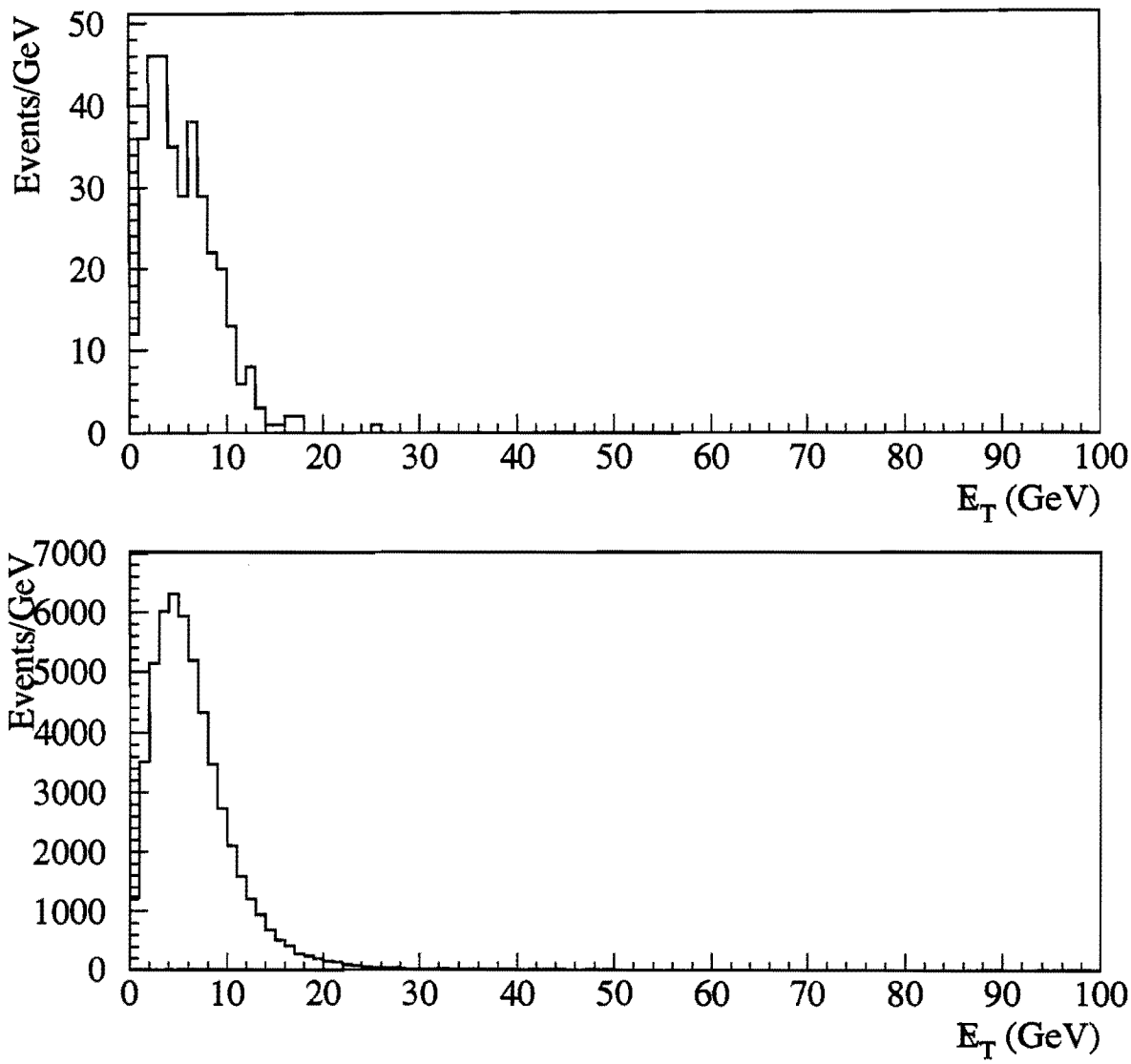


Figure C.1: $\not\!\!E_T$ distributions for Good (top) and Fake (bottom) dielectron samples.

# Appendix D

# Physics at a Hadron Collider

The accelerator apparatus used for the work that follows is the Tevatron. It is a proton antiproton collider which operates at a center of mass energy of 1.8 TeV (Trillion electron volts), which is currently the highest energy available in the world. In the quest to produce higher and higher collision energies using today's collider techniques, it becomes necessary to use heavier particles, with proton-proton and proton-antiproton colliders being the most suitable choices. This is necessary primarily because lighter electrons have a much larger charge to mass ratio than do protons. For electrons, this leads to large amount of synchrotron radiation when they are placed in high energy storage rings. This radiation carries away energy from the beam which must be constantly replaced, and solutions to this problem tend to be very costly. Because protons are about two thousand times heavier than electrons but carry the same amount of charge, such radiation is not a problem for

any foreseeable collider.

This does lead to one rather messy complication: protons are not fundamental particles. Any collision of two hadrons is really the result of the collision of two of the hadron constituents (quarks and gluons), which are generally referred to as partons. In order to make a relevant calculation, one must have knowledge of the parton densities, that is, what kind of partons are present and what fraction x of the proton's momentum they are carrying. These densities have been inferred from experimental data by the authors of reference [49], and [50]. Figure D.1 shows the results of these analyses. In figure D.1a, parton density functions (pdf's) are plotted as functions of the proton momentum fraction $x$ for the up ($u$), down ($d$), gluon ($g$) and sea ($S$) constituents, where the "sea" refers to the virtual quarks which exist in the proton at any given instant. Typical $W$ and $Z$ production at the Tevatron is sensitive to pdf's in the region of x around 0.2.

An additional complication is that the data used to infer the pdf's is taken from a variety of experiments at different energies. To make use of these results at Tevatron energies, it is necessary to 'evolve' the distributions to energy scales appropriate for those energies. The choice of this scale is somewhat arbitrary (somewhere around $M_Z$) and introduces theoretical uncertainty into any calculation done with

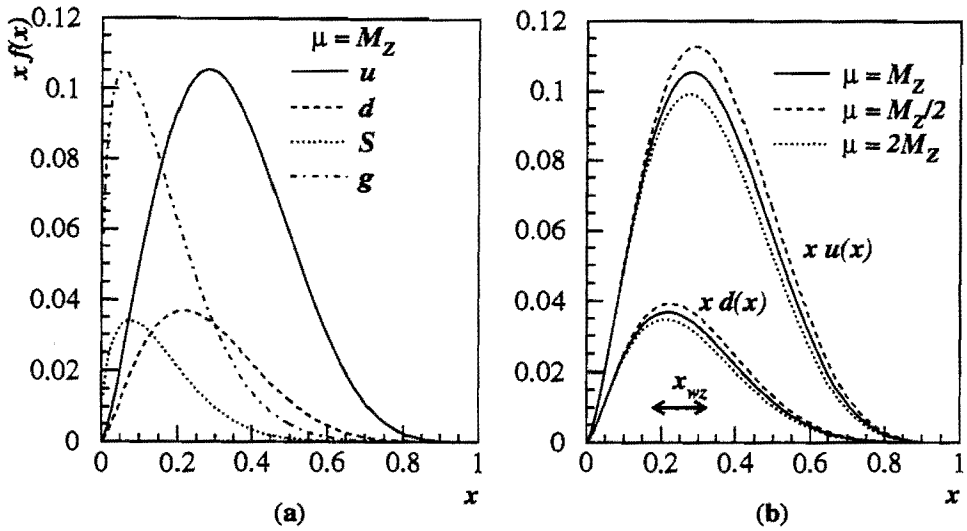


Figure D.1: (a) Parton distributions from the MRSD'_ set evaluated at $\mu = M_Z$. (b) Sensitivity of the up and down quark distributions to the scale $\mu$. Typical $x$ values for gauge boson production are indicated by $x_{WZ}$.

them.[1] Figure D.1b shows the variation on the up and down distributions for different choices of scale. The uncertainty due to choice of scale is typically evaluated by varying the scale over some range, and observing the change in the pdf's. A similar uncertainty due to the choice of pdf's (there are many), can also be obtained. With parton densities in hand, one can calculate cross sections for hadronic collisions, as in figure D.2, for example. Combining the information in pdf's with calculations from the SM allows one to make theoretical predictions about quantities which one wishes to measure in experiment.

[1]Technically this dependence on scale is a result of truncating the perturbation sequence used in the calculation. If the calculation could be performed to all orders, the scale dependence would vanish.

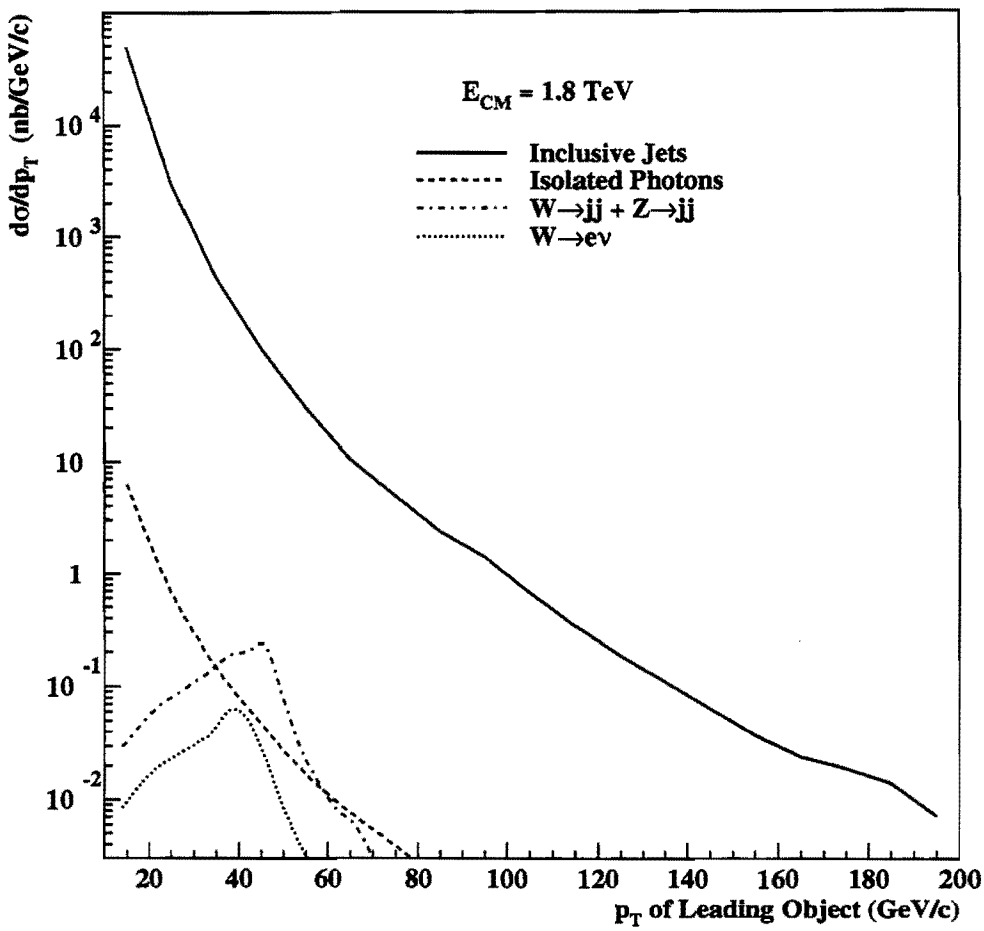


Figure D.2: Cross sections for various processes at the Tevatron as predicted by the ISAJET Monte Carlo.

# Bibliography

[1] J.D. Bjorken and S.D. Drell, *Relativistic Quantum Mechanics and Relativistic Quantum Fields.*, McGraw Hill, (1964).

[2] I.J.R. Atchison and A.J.G. Hey, *Gauge Theories in Particle Physics.*, Institution of Physics Publishing, (1989).

[3] L.H. Ryder, *Quantum Field Theory.*, Cambridge University Press, (1991).

[4] T.P. Chen and L.F. Li, *Gauge Theories of Elementary Particle Physics.*, Oxford University Press, (1984).

[5] F. Halzen and A. Martin, *Quarks and Leptons.*, John Wiley & Sons, (1984).

[6] C.N. Yang, *Elementary Particles.*, Princeton University Press, (1961).

[7] F.E. Close, *The Cosmic Onion.*, Heinemann Educational Books, (1983).

[8] A. Pais, *Inward Bound.*, Clarendon Press, (1986).

[9] Particularly illuminating is chapter one of D. Griffiths, *Introduction to Elementary Particles.*, John Wiles & Sons, (1987).

[10] O. Chamberlain, *et al.*, *Physical Review* **100**, 947, (1955).

[11] B. Cork, *et al.*, *Physical Review* **104**, 1193, (1956).

[12] An excellent bibliography on the neutrino can be found in L. Lederman, *American Journal of Physics* **38**, 129, (1970).

[13] F. Reines and C.L. Cowan, Jr., *Physical Review* **92**, 8301, (1953).

[14] G. Danley, *et al.*, *Physical Review Letters* **9**, 36, (1962).

[15] R. Davis and D.S. Harmer, *Bulletin of the American Physical Society* **4**, 217, (1959).

[16] M. Gell-Mann, *Physical Review* **92**, 883, (1953).

[17] See for example M. Gell-Mann and Y. Ne'eman, *The Eightfold Way.*, Benjamin, (1964).

[18] See for example D.B. Lichtenberg and S.P. Rosen, eds., *Developments in the Quark Theory of Hadrons.*, Hadronic Press, (1980)

[19] D.H. Coward *et al.*, *Physical Review Letters* **20**, 292, (1968).

[20] J.J. Aubert, *et al.*, *Physical Review Letters* **33**, 1404, (1974).

[21] J. E. Augustin, *et al.*, *physical Review Letters* **33**, 1406, (1974).

[22] S.L. Glashow, J. Iliopoulos and L. Maiani, *Physical Review* **D2** 1285, (1970).

[23] E.G. Cazzoli, *et al.*, *Physical Review Letters* **34**, 1125, (1975).

[24] G. Goldhaber, *et al.*, *Physical Review Letters* **37**, 255, (1976).

[25] R. Brandelik, *et al.*, *Physics Letters* **B70**, 132, (1977).

[26] M. Perl, *et al.*, *Physical Review Letters* **35**, 1489, (1975).

[27] S.W. Herb, *et al.*, *Physical Review Letters* **39**, 252, (1977).

[28] S. Abachi, *et al.* (DØ Collaboration), *Physical Review Letters* **74**, 2632, (1995).

[29] F. Abe, *et al.* (CDF Collaboration), *Physical Review Letters* **74**, 2626, (1995).

[30] D. Decamp *et al.* (ALEPH Collaboration), *Physics Letters* **B235**, 399 (1990)

[31] S.L. Glashow, *Nuclear Physics* **22**, 579, (1961).

[32] S. Weinberg, *Physical Review Letters* **19**, 1264, (1967).

[33] A. Salam, *Proceedings of the Eighth Nobel Symposium,* ed. by N. Svartholm, Almqvist & Wiskell, Stockholm, (1968).

[34] UA1 Collaboration, *Physics Letters* **B122**, 103, (1983).

[35] UA2 Collaboration, *Physics Letters* **B122**, 476, (1983).

[36] UA1 Collaboration, *Physics Letters* **B126**, 398, (1983).

[37] UA2 Collaboration, *Physics Letters* **B129**, 130, (1983).

[38] F. Paige and S. Protopopescu, *ISAJET: A Monte Carlo Event Generator for pp and $p\bar{p}$ Reactions.*, Fermilab program library.

[39] Particle Data Group, "Review of Particle Properties." *Physical Review* **D54**, (1996).

[40] V. Barger and R. Phillips, *Collider Physics.* Frontiers In Physics Lecture Note Series, Addison-Wesley, (1987).

[41] P.W. Higgs, *Physics Letters* **12**, 132, (1964).

[42] M. Kobayashi and T. Maskawa, *Progress in Theoretical Physics* **49**, (1973).

[43] C.N. Yang and R.L. Mills, *Physical Review* **96**, 191, (1954).

[44] E. Commins and P. Bucksbaum, *Weak Interactions of Leptons and Quarks.* Cambridge University Press, (1983).

[45] G. 't Hooft, *Nuclear Physics* **B33**, 173, (1971); *ibid* **B35**, 167 (1971).

[46] T. Sjostrand, *Computational Physics Communications* **82**, 74, (1994).

[47] G. Marchesini, *Computational Physics Communications* **67**, 465 (1992).

[48] K. Hagiwara, J. Woodside and D. Zeppenfeld, *Physical Review* **D48**, 2113 (1990).

[49] A. Martin, W. Stirling, and R. Roberts, *Physical Review* **D47**, 867, (1993).

[50] A. Martin, W. Stirling, and R. Roberts, *Physics Letters* **B306**, 145, (1993).

[51] K. Hagiwara, R.D. Peccei, D. Zeppenfeld and K. Hikasa, *Nuclear Physics* **B282**, 253 (1987).

[52] K. Hagiwara, S. Ishihara, R. Szalapski and D. Zeppenfeld, *Physical Review* **D48**, 2182 (1993); *Physics Letters* **B283**, 353 (1993).

[53] H. Aihara *et al.*, Preprint Fermilab-Pub-95/031, (1995).

[54] U. Baur and D. Zeppenfeld, *Physics Letters* **B201**, 383, (1988).

[55] C. Burgess and D. London, *Physical Review Letters* **D69**, 3428, (1992)

[56] M.S. Alam *et al.* (CLEO Collaboration), *Physical Review Letters* **74**, 2885 (1995).

[57] J. Alitti *et al.* (UA2 Collaboration), *Physics Letters* **B277**, 194 (1992).

[58] F. Abe *et al.* (CDF Collaboration), *Physical Review Letters* **74**, 1936 (1995); *ibid.* **75**, 1017 (1995).

[59] S. Abachi *et al.* (DØ Collaboration), *Physical Review Letters* **78**, 3634 (1997).

[60] F. Abe *et al.* (CDF Collaboration), *Physical Review Letters* **74**, 1936 (1995).

[61] B. Abbott *et al.* (DØ Collaboration), *Physical Review Letters* **79**, 1441 (1997).

[62] F. Abe *et al.* (CDF Collaboration), *Physical Review Letters* **78**, 4537 (1997).

[63] S. Abachi *et al.* (DØ Collaboration), *Physical Review Letters* **75**, 1023 (1995).

[64] J. Thompson, DØ internal report No. 2367, FERMILAB-TM-1909, (1994).

[65] S. Abachi, *et al.* (DØ Collaboration), *Nuclear Instruments and Methods* **A388**, 185, (1993).

[66] S. Snyder, DØ internal report No. 2500 (Unpublished).

[67] R. Fernow, *Introduction to Experimental Particle Physics.* Cambrige Press, (1986).

[68] C. Fabjan in *Experimental Techiques in High-Energy Physics*, ed. T. Ferbel, pages 79-188, Addison-Wesley (1987).

[69] C. Gerber *et al.*, DØ internal report No. 2140 (Unpublished)

[70] J. Bantly, *et al.*, DØ internal report No. 1966 (Unpublished)

[71] J. Bantly, *et al.*, Fermilab-TM-1995, February 1997 (Unpublished)

[72] M. Abolins, *et al.*, *Nuclear Instruments and Methods* **A289**, 543, (1990).

[73] J. Bantly, *et al.*, DØ internal report No. 2147 (Unpublished).

[74] J. Butler, DØ internal report No. 1682 (Unpublished).

[75] S. Abachi *et al.* (DØ Collaboration), *Physical Review* **D52**, 4877 (1995).

[76] T, Behnke, Ph.D. Dissertation, State University of New York at Stony Brook, 1989 (Unpublished).

[77] D. Pizzuto, Ph.D. Dissertation, State University of New York at Stony Brook, 1991 (Unpublished).

[78] S. Youssef, *Computational Physics Communications* **45**, 423 (1987).

[79] N. Hadley, DØ internal report No. 904 (Unpublished).

[80] S. Abachi *et al.*, Proceedings of the 28th International Conference on High Energy Physics, Warsaw, Poland, July 1996.

[81] R. Kehoe, DØ internal report No. 2052, 1994 (Unpublished). R. Kehoe and R. Astur, DØ internal report No. 2908, 1996 (Unpublished).

[82] U. Heintz and M. Narain, DØ internal report No. 2355, 1994 (Unpublished).

[83] U. Heintz *et al.*, DØ internal report No. 2386, 1994 (Unpublished).

[84] M. Narain, In the proceedings of DPF92, ed. C. Albright *et al.*, 1678, World Scientific (1992).

[85] U. Heintz and M. Narain, DØ internal report No. 1814, 1993 (Unpublished).

[86] P. Grudberg, DØ internal report No. 2316, 1994 (Unpublished).

[87] P. Quintas, DØ internal report No. 2865, 1996 (Unpublished).

[88] B. Abbott *et al.* (DØ Collaboration), Preprint Fermilab-PUB-97/422-E, Submitted to *Physical Review* **D**.

[89] G. Ladinsky and C.P. Yuan, *Physical Review* **D50**, 4239, (1994).

[90] P. Arnold and R. Kauffman, *Nuclear Physics* **B349**, 381 (1991). The Monte Carlo grid was provide by Dylan Casey.

[91] J. Ohnemus, *Physical Review* **D44**, 1403 (1991); *ibid.* **D44**, 3477 (1991).

[92] The `MUSMEAR` program was written by T. Diehl and P. Quintas.

[93] F. Carminati *et al.*, `GEANT` *Users Guide*, CERN Program Library Long Writeup WS0113 (1993) (Unpublished).

[94] S. Glenn, DØ internal report 2846, 1996 (Unpublished).

[95] M. Tartaglia, DØ internal report No. 1333 (Unpublished).

[96] P. Quintas, DØ internal report No. 2712, 1995 (Unpublished).

[97] J. Thompson, Private Communication.

[98] H. Johari, Ph.D. Dissertation, Northeastern University, 1995 (Unpublished).

[99] S. Glenn, Private Communication.

[100] F. James, MINUIT *Reference Manual.* CERN program Library Long Writeup D506, Version 92.1, 1992.

[101] T. Hu. Ph.D. Dissertation, State University of New York at Stony Brook, 1996 (Unpublished).

[102] S. Abachi *et al.* (DØ Collaboration), *Physical Review Letters* **75**, 1456 (1995).

[103] D. Puseljic, DØ internal report No. 2737 (Unpublished).

[104] J. Cochran, Private Communication.

[105] S. Abachi *et al.* (DØ Collaboration), *Physical Review Letters* **79**, 1203 (1997).

[106] R. Partridge, Private Communication.

[107] T. Yasuda and P. Bloom, DØ internal report No. 2391, 1997 (Unpublished).

[108] T. Yasuda, Private Communication. The actual implementation of the lepton fit was performed by Taka Yasuda. The calculation was based entirely on the results discussed in chapters 5 and 6.

[109] R. Barlow, *Statistics: A Guide to the Use of Statistical Methods in the Physical Sciences.* Wiley & Sons, 1989.

[110] K. Ackerstaff *et al.* (OPAL Collaboration), Preprint CERN-PPE/97-125, (1997).

[111] R. Barate *et al.* (ALEPH Collaboration), Preprint CERN-PPE/97-166, (1997).

[112] D. Chakrobarty and M. Fatyga. "QCD Backgrounds to Electroweak Signals: A Study of Electron and Fake Photon Probability" DØ Note 1753, (unpublished)

[113] M. Fatyga, "A Comparison of Fake Electron Rates in Data and the ISAJET Monte Carlo. A Comparison of Multi-Jet Triggers with ISAJET Monte Carlo". DØ Note 1850, (unpublished)

[114] M. Kelly, "Jet Faking Photon/Electron Study". DØ Note 1659, (unpublished)

[115] M. Kelly, "The Doomsday Study of QCD Flakes for $W\gamma$ in RECO 11". DØ Note 2215, (unpublished)

[116] S. Glenn, DØ internal report No. 2937, 1996 (Unpublished).

[117] S. Fahey, "Direct Photon Production at $\sqrt{s} = 1.8$ TeV". Ph.D. thesis, (unpublished), 1995

[118] S. Abachi *et al.* (DØ Collaboration), *Physical Review Letters*, **77**, 5011 (1996)